FILE COPY

(1)

AD-A216 226

DTIC
S ELECTE D
DEC 29 1989
B

A STUDY OF FAILURE CHARACTERISTICS IN
THERMOPLASTIC COMPOSITE LAMINATES DUE
TO AN ECCENTRIC CIRCULAR DISCONTINUITY

THESIS

John A. Daniels
Capt, USAF
AFIT / GAE / ENY / 89D-06

DEPARTMENT OF THE AIR FORCE
AIR UNIVERSITY
AIR FORCE INSTITUTE OF TECHNOLOGY

Wright-Patterson Air Force Base, Ohio

DISTRIBUTION STATEMENT A
Approved for public release;
[illegible]

89 12 29 028

①

AFIT / GAE / ENY / 89D-06

A STUDY OF FAILURE CHARACTERISTICS IN THERMOPLASTIC COMPOSITE LAMINATES DUE TO AN ECCENTRIC CIRCULAR DISCONTINUITY

THESIS

John A. Daniels
Capt, USAF
AFIT / GAE / ENY / 89D-06

DTIC
ELECTE
DEC 29 1989
S B D

Approved for public release; distribution unlimited

AFIT / GAE / ENY / 89D-06

A STUDY OF FAILURE CHARACTERISTICS IN THERMOPLASTIC COMPOSITE LAMINATES DUE TO AN ECCENTRIC CIRCULAR DISCONTINUITY

THESIS

Presented to the Faculty of the School of Engineering
of the Air Force Institute of Technology
Air University
In Partial Fulfillment of the
Requirements for the Degree of
Master of Science in Aeronautical Engineering

John A. Daniels, B.S.
Captain, USAF

December 1989

Approved for public release; distribution unlimited

Acknowledgements

Completing this thesis could best be described as a "team effort." Without the support of any person listed in this section, this thesis would not have been successfully completed. I was fortunate enough to have two very knowledgeable advisors who provided enthusiastic support and guidance. Dr. Anthony Palazotto, my AFIT advisor, kept me pointed in the "right" direction, and was always available to answer my naive questions. I also had the privilege of working, on a daily basis, with Dr. R.S. Sandhu of the Flight Dynamics Laboratory. Dr. Sandhu provided me with an insight into composite materials, and testing techniques, that will benefit me for a lifetime. To both of these individuals, I'm deeply indebted.

The Structures Division, of the Flight Dynamics Laboratory, provided additional support through the efforts of the following people.

(1) Patty Lachey and Kevin Spitzer, of the Composites Group, who insured that my specimens were properly fabricated and completed on time.

(2) Clifford Hitchcock, Wendy Choate, and David Heart, of the Instrumentation Group, who spent hour upon hour gluing and wiring hundreds of strain gages.

(3) Don Cook, Larry Bates, and Harold Stalnaker, of the Fatigue, Fracture, and Reliability Group, who tested *numerous* composite coupons.

(4) Gene Maddux, Bruce Cox, and Don Webb, of the Photomechanics Facility, who provided photographic support and photoelastic expertise.

To AFIT's School of Engineering, many thanks go to Mr. Nick Yardich for providing both supply and photographic support. Also, to Mr. Jack Tiffany and Mr. Joe Hofele, AFIT Model Shop, for their support in the fabrication of an experimental test fixture.

Finally, I wish to express my sincere thanks to my wife (Annette) and children (Jonathan and Sharon). Their patience, support, and understanding, for the past eighteen months, made AFIT a bearable assignment.

DTIC
COPY
INSPECTED
1

For
☑
☐
☐
on
n/
ty Codes
and/or
Dist Special
A-1

Table of Contents

List of Figures

List of Tables

AFIT / GAE / ENY / 89D-06

Abstract

The purpose of this thesis was to determine (both experimentally and analytically) the initiation and progression of failure, stress-strain response, and the failure loads of Graphite/Polyetheretherketone (Gr/PEEK) laminates, incorporating an eccentric 0.4 inch circular discontinuity, loaded in axial tension at room temperature. The ply lay-ups of these specimens were $[0^o{}_{16}]$, $[90^o{}_{16}]$, $[\pm45^o]_{4s}$, and $[0^o/\pm45^o/90^o]_{2s}$. For each of these ply ~~lay-~~ (lay-up ~~ups~~, three values of eccentricity were considered (the three values of eccentricity were determined by the hole location within each specimen). In addition, experimentation was conducted to study the effects of boundary conditions on the failure characteristics of the Gr/PEEK laminates; this was accomplished through the use of a special mounting fixture which allowed in-plane rotation of the specimens. Finally, experimentation was conducted, using photoelasticity, to verify the "gross" stress states of the Gr/PEEK laminates predicted by the analytical study.

Analytically, a nonlinear material finite element program was used to predict the initiation and progression of failure, stress-strain response, and the failure loads of the Gr/PEEK laminates. In addition, the effects of boundary conditions on the failure modes of the Gr/PEEK laminates was studied analytically. And finally, the "gross" stress states of the Gr/PEEK laminates were considered in the analytical portion of this thesis. (ICR)

The experimental and analytical results were then compared. The initiation and progression of failure, stress-strain response, and the failure loads of the (Gr/PEEK) laminates compared quite well for the $[0^o{}_{16}]$, $[90^o{}_{16}]$, and $[0^o/\pm45^o/90^o]_{2s}$ laminates. For the $[\pm45^o]_{4s}$ laminates, the analytical predictions for the failure loads underestimated (from 16.6% to 40.5%) the experimentally obtained failure loads. Furthermore, it was observed (both experimentally and analytically) that the failure modes and failure loads for the Gr/PEEK laminates were not appreciably affected by the boundary conditions caused

through the use of the mounting fixture (in-plane rotation allowed). Finally, there was good agreement between the experimental and analytical predictions of the "gross" stress states of the Gr/PEEK laminates.

Since eccentricity effects on the failure modes and failure loads of the Gr/PEEK laminates were of interest in this study, the analytical study attempted to predict the behavior of the Gr/PEEK laminates due to an eccentric circular discontinuity. The eccentric circular discontinuity created a centroid (area) shift in the Gr/PEEK laminates. This shift in centroid, combined with the axial loading, created a bending moment which varied depending on the eccentricity of the circular discontinuity. The analytical study was able to accurately predict the failure modes and failure loads resulting from eccentricity effects. Although the final failure mode, and failure load, was available from experimentation, the failure progression resulting from eccentricity effects was not observed during expermentation. All experimentation was recorded on video tape for post failure analysis. However, failure was too rapid to observe failure progression (by viewing the video tape frame-by-frame).

A STUDY OF FAILURE CHARACTERISTICS IN THERMOPLASTIC COMPOSITE LAMINATES DUE TO AN ECCENTRIC CIRCULAR DISCONTINUITY

I. Introduction

In weight-sensitive applications, such as aircraft design, accurate strength and failure characteristics must be ascertained before composite materials can be used to their full advantage. Therefore, future design advancements rely heavily upon our ability to accurately predict strength and failure characteristics of composite materials.

Fiber reinforced resin composites typically have high strength-to-weight and stiffness-to-weight ratios. For this reason. they have become important in the aerospace industry. As more demands are made upon new generation aircraft, we must continue to develop new composite materials with desirable strength characteristics. To this end, Gr/PEEK has been developed. This polyether based thermoplastic material has shown several advantages over graphite epoxy (Gr/Ep). Among these advantages are: ease of fabrication, lower weight (per part), higher operating temperatures, increased resistance to delamination, and higher fracture toughness [9].

Past research on Gr/PEEK laminates, containing circular discontinuities, has shown that the nonlinear relationships between stress and strain must be considered [10,13,17]. Therefore, a nonlinear material finite element program [23,25] was employed in this study.

A. Purpose.

The purpose of this thesis was to determine (both experimentally and analytically) the initiation and progression of failure, stress-strain response, and the failure loads of Gr/PEEK laminates containing an eccentric 0.4 inch circular discontinuity. These Gr/PEEK laminates were loaded in axial tension at room temperature. The ply lay-ups of the laminates were $[0^\circ_{16}]$, $[90^\circ_{16}]$, $[\pm 45^\circ]_{4s}$, and $[0^\circ/\pm 45^\circ/90^\circ]_{2s}$. For each of these ply lay-ups, three values of eccentricity were considered (the three values of eccentricity were determined by the hole location within each specimen).

The experimental and analytical objectives of this study were as follows:

(1) Investigate the initiation and progression of failure, and the failure loads of the Gr/PEEK laminates.

(2) Investigate the boundary condition effects on the failure characteristics of the Gr/PEEK laminates.

(3) Determine the "gross" stress states of the Gr/PEEK laminates.

(4) Compare the experimental and analytical results.

B. Background and Overview.

Composite materials contain two or more materials and have been in use for centuries.

> Prehistoric civilizations used straw in mud bricks; plywood existed in early Egyptian construction; and medieval knights used combinations of various metals in their swords [13].

For the purposes of this thesis, a composite material is a material consisting of continuous reinforcing fibers in a matrix material. The fibers and matrix are considered, on a macroscopic scale, to form a useful material which acts as a single structural element. One advantage of composite materials over "typical" isotropic materials (aluminum, steel, etc.) is that the composite material can be optimized (tailored) to meet a specific application. Therefore, the fibers of a composite material are typically oriented so that the directional dependence of strength and stiffness of the composite matches the loading environment.

In recent years, the term "advanced composite material" has been used to describe composites with very high strength and stiffness fibers. These advanced composites typically use a plastic (epoxy) or metal matrix. The Gr/PEEK used in this study is considered to be an advanced composite material. Gr/PEEK consists of continuous AS-4 graphite fibers in a polyetheretherketone (PEEK) matrix.

Since composite materials can be tailored to match the loading environment, they usually have high strength and low weight. Therefore, as previously mentioned, composite materials have found widespread use in the fabrication of component parts for the aerospace industry. Examples of some of these components include the wings of the X-29 aircraft, and the horizontal and vertical stabilizers of the F-15 and F-16 aircraft.

These aircraft components are usually connected to other components through adhesive bonds, mechanical fastners (such as bolts), or a combination of adhesive bonds and mechanical fastners. Since mechanical fastners require fastner holes, successful designs rely heavily upon the ability to analytically predict the stress distribution around these holes which result from service loads. The analytical predictions of load redistribution around a fastner hole, in composite materials, is not a simple task.

Although there are many techniques for predicting the ultimate strength in composites, in general, two techniques are commonly used. These include a fracture mechanics approach [3,12,28] and a finite element (damage zone) approach [6,21,22,23,25].

Several commonly used fracture models for predicting the strength of composites containing circular holes are reviewed by [3]. In this reference, "serious questions are raised as to the applicability of classical fracture mechanics to composites [3]." Fracture models typically do not address the failure modes of composites, and as discussed by [3]:

> Semi-empirical fracture models which attempt to predict the notched strength of composites do not address, but rather by-pass, the micro- and macro-failures associated with the crack extension process [3].

Furthermore, typical fracture models require correction factors which are often arbitrary and subject to question [20]. Therefore, as previously mentioned, the analytical portion of this study made use of finite element (damage zone) methods.

For several reasons, the nonlinear material finite element program which was used in this thesis, was ideally suited to study the Gr/PEEK laminates considered in this study. First the nonlinear stress-strain response of the Gr/PEEK laminates was modeled by piecewise cubic spline interpolation functions. The use of piece-wise cubic spline interpolation functions to represent the experimental stress-strain data for Gr/PEEK laminates [13], provided "smoothness" (continuity of slope) over the entire range of the stress-strain curves. Secondly, the finite element program (unlike fracture methods) properly modeled the damage accumulation process of the Gr/PEEK laminates. This damage accumulation (failure progression) was modeled as areas of failure (element failures) within the finite element model. And finally, the geometry of the specimens including the physical dimensions, boundary conditions, and ply orientations of the laminates were all easily modeled through finite element techniques. The numerical portion of this study (including the development of the finite element models) is discussed in detail in Section III.

As mentioned previously, numerous failure theories are available for use with finite element methods. Over 30 failure theories exist for composites, with another 12 theories used to predict post-failure behavior of composites [10]. Some of these theories may be used only in special cases, and some are not valid for use with composite materials [10]. This study made use of a total strain energy failure criterion [21,22,23,25] which was incorporated in the nonlinear material finite element program. This total strain energy criterion is discussed in detail in Section II D.

In addition to the analytical study, experimentation was also conducted to verify the analytical predictions of initiation and progression of failure, stress-strain response, failure loads, and the "gross" stress states of the Gr/PEEK laminates studied. The experimental portion of this study is described in Section IV.

Section VI presents the results from the analytical and experimental studies, and the conclusions from this thesis are summarized in Section VI.

II. Theory

This thesis made use of the following theories: mechanics of composite materials, linear finite element theory, nonlinear constitutive relationships, and a strain energy failure theory for composite laminates [21,22,23,25].

The mechanics of composite materials can encompass both micromechanics and macromechanics. This thesis was primarily directed toward the macromechanical behavior of laminates. However, for completeness, the micromechanics of composites, as it applies to this thesis, will be discussed.

Linear finite element theory will be discussed briefly as a "building block" to a discussion of the nonlinear relationships between stress and strain. Finally, a discussion of the failure criteria and the unloading options utilized by the nonlinear finite element program will be discussed.

A. Mechanics of Composite Materials.

(1) Micromechanical Behavior of Composite Materials.

The term micromechanics is often used to describe the behavior of composites wherein the interaction of the constituent materials is considered on a microscopic scale. However, since this thesis utilized a macromechanical approach, only the applicable portion of the theory of micromechanics will be discussed. In particular, the transfer of load between fibers is of primary concern.

An aromatic polymer composite (APC) is a composite which is constructed with a polyaromatic resin combined with continuous fibers [13]. The Gr/PEEK used in this study was APC-2 and consisted of a polyetheretherketone (PEEK) matrix containing Hercules AS-4 graphite fibers. For Gr/PEEK to resist externally applied loads, the fiber and matrix must function in an integrated manner. This requires that the load be transferred from fiber to fiber throughout the matrix as well as through the fiber-matrix interface [4,26]. In a typical composite lamina with unidirectional fibers, the fibers are surrounded by the adjacent matrix material as depicted in Figure 2-1. The fibers in Gr/PEEK are the principal load-carrying agent. The matrix serves several purposes including fiber support, protection of fibers, and transmitting load between fibers. When fiber failure occurs, the capability of the matrix to transfer load between fibers is very important. One model which describes the transfer of load after fiber failure is depicted in Figure 2-2 [12]. In this model, load transfer is accomplished by shearing stress which develops in the matrix material. When composites are subjected to high temperatures and/or humidity, this interfacial shear strength can be reduced. Therefore, the fiber-matrix interface is often times considered to

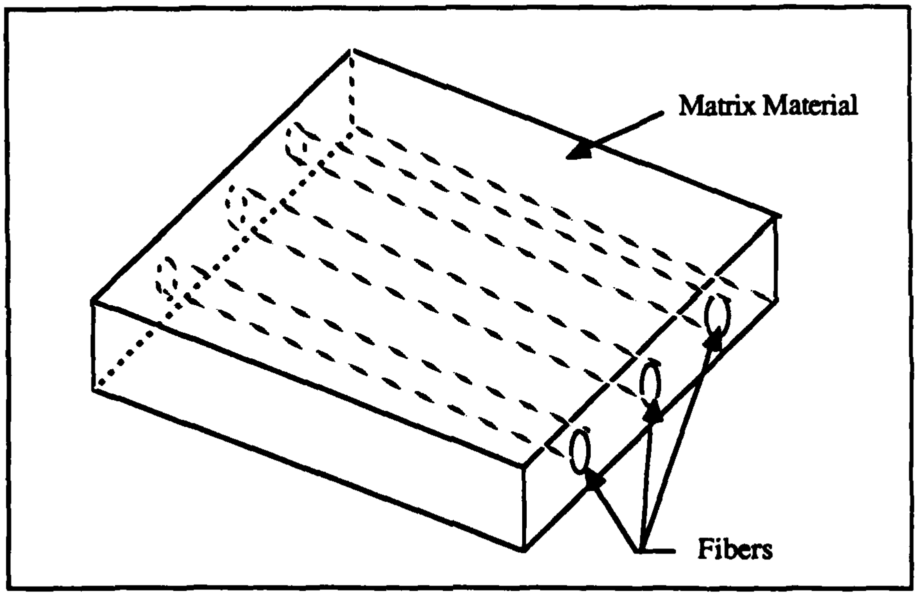

Figure 2-1. Lamina with Unidirectional Fibers

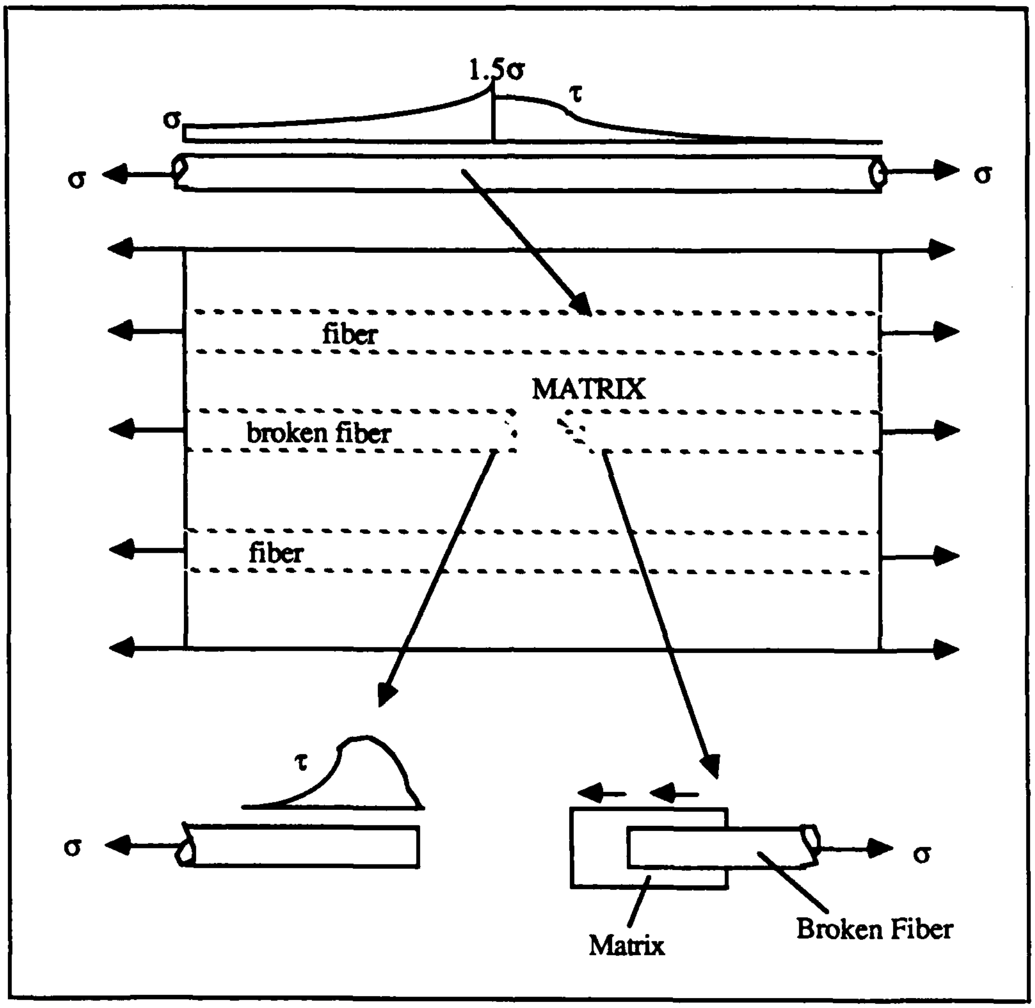

Figure 2-2. Broken Fiber Effects

be the weak link in a composite lamina. Numerous theories have been implemented on how load transfer between fibers is achieved. Two of these theories are the "shrink-fit" theory and "chemical coupling" theory, both of which are discussed by [26].

Finally, from a micromechanics point of view, the properties of a composite depend upon the individual properties of its constituents. Typically, "the composite stress and strain are defined as the volume averages of the stress and strain fields, respectively, within the representative volume element [27]." Therefore, it is necessary to find relations between the composite stresses in terms of the properties of the constituents. A major problem with micromechanics is the inability to accurately describe the boundary conditions which exist between each constituent within the material. An exact analysis based on micromechanics is therefore difficult at best. For this reason, this thesis made use of the theory of macromechanics.

(2) Macromechanical Behavior of Composite Materials.

Since composite materials are normally nonhomogeneous and anisotropic, the theories and formulas with which we have dealt with isotropic materials cannot generally be utilized. The macromechanics approach concerns itself with "gross" composite material behavior. This approach does not recognize the individual constituent materials and the composite material is considered to be anisotropic.

> Since most practical composites are uniformly constructed (at least within each layer, if laminated), each layer of the material can usually be assumed to be quasi-homogeneous on the macro scale [1].

The individual layers within a composite laminate, as depicted in Figure 2-3, are bonded together to act as a single structural element. Typically, the laminae principal material directions are oriented so that the structure is capable of resisting load in several directions. The stacking sequence of laminae can therefore be used to "tailor the directional dependence of strength and stiffness of a material to match the loading environment of the structural element [12]." The complexity arising in composite laminates is the introduction of shear stresses between layers. These interlaminar shear stresses develop due to the tendency of each individual ply to deform according to its respective material properties. These shearing stresses are largest at the edges of the laminate and often lead to delamination. Additionally, the transverse and normal stresses which arise from uniaxial loading can also lead to delamination [12]. Therefore, the stacking sequence of laminae not only affects

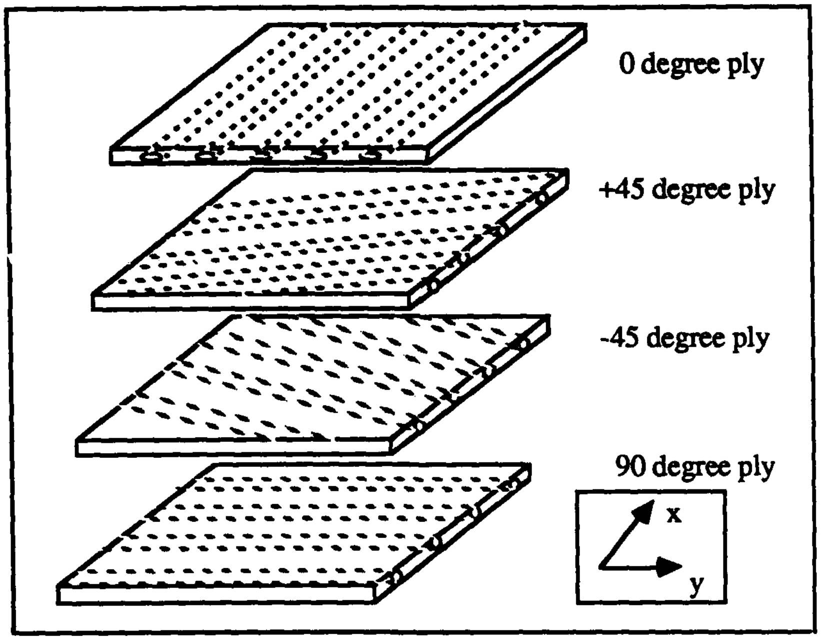

Figure 2-3. Laminate Construction

directional dependence of strength, but also affects the interlaminar stresses [28].

To understand the behavior of a laminated composite, it is essential to understand the behavior of a lamina. Linear elastic behavior is typically assumed with the macromechanical approach. In this study, the nonlinear material behavior of Gr/PEEK has been modeled as increments of linear behavior. Therefore, the macromechanical approach is applicable.

If we start with the most general case of the stress strain relations for an anisotropic material, we can make use of the generalized expression for Hooke's Law (equation 1).

$$\sigma_i = C_{ij}\,\varepsilon_j \qquad i,j = 1,\cdots,6 \qquad (1)$$

where:

σ_i = stress components
C_{ij} = stiffness matrix
ε_j = strain components

The convention for this contracted notation is the same as that used by [12]. For clarity, the following relationships between the tensor notation and the contracted notation are given.

TENSOR NOTATION	CONTRACTED NOTATION
σ_{11}	σ_1
σ_{22}	σ_2
σ_{33}	σ_3
τ_{23}	σ_4
τ_{31}	σ_5
τ_{12}	σ_6
ε_{11}	ε_1
ε_{22}	ε_2
ε_{33}	ε_3
$\gamma_{23} = 2\varepsilon_{23}$	ε_4
$\gamma_{31} = 2\varepsilon_{31}$	ε_5
$\gamma_{12} = 2\varepsilon_{12}$	ε_6

where:

γ_{ij} = engineering shearing strain
ε_{ij} = tensor shearing strain

The linear strain-displacement relationships in contracted notation can be formally defined as:

$$\varepsilon_1 = \frac{\partial u}{\partial x} \qquad \varepsilon_2 = \frac{\partial v}{\partial y} \qquad \varepsilon_3 = \frac{\partial w}{\partial z}$$

$$\gamma_{23} = \frac{\partial v}{\partial z} + \frac{\partial w}{\partial y} \qquad \gamma_{31} = \frac{\partial w}{\partial x} + \frac{\partial u}{\partial z} \qquad \gamma_{12} = \frac{\partial u}{\partial y} + \frac{\partial v}{\partial x}$$

where: u,v, and w are x,y, and z displacements

The stiffness matrix (C_{ij}) has 36 constants. These 36 constants are not independent and for elastic materials the stiffness matrix is found to be symmetric. Therefore, only 21 of the constants are actually independent. The stress-strain relations for an anisotropic material (21 independent constants) can therefore be expressed as:

$$\begin{Bmatrix} \sigma_1 \\ \sigma_2 \\ \sigma_3 \\ \tau_{23} \\ \tau_{31} \\ \tau_{12} \end{Bmatrix} = \begin{bmatrix} C_{11} & C_{12} & C_{13} & C_{14} & C_{15} & C_{16} \\ C_{12} & C_{22} & C_{23} & C_{24} & C_{25} & C_{26} \\ C_{13} & C_{23} & C_{33} & C_{34} & C_{35} & C_{36} \\ C_{14} & C_{24} & C_{34} & C_{44} & C_{45} & C_{46} \\ C_{15} & C_{25} & C_{35} & C_{45} & C_{55} & C_{56} \\ C_{16} & C_{26} & C_{36} & C_{46} & C_{56} & C_{66} \end{bmatrix} \begin{Bmatrix} \varepsilon_1 \\ \varepsilon_2 \\ \varepsilon_3 \\ \gamma_{23} \\ \gamma_{31} \\ \gamma_{12} \end{Bmatrix} \quad (2)$$

Equation (2) is the most general form of the stress-strain relations of an anisotropic material with no planes of material symmetry. Equation (2) can be simplified for materials which have symmetry of material properties. For orthotropic materials there are three orthogonal planes of material symmetry. Therefore, equation (2) can be simplified as shown in equation (3). For the orthotropic case, there are nine independent constants, and there is no interaction between normal stresses and shearing strains and vice versa.

$$\begin{Bmatrix} \sigma_1 \\ \sigma_2 \\ \sigma_3 \\ \tau_{23} \\ \tau_{31} \\ \tau_{12} \end{Bmatrix} = \begin{bmatrix} C_{11} & C_{12} & C_{13} & 0 & 0 & 0 \\ C_{12} & C_{22} & C_{23} & 0 & 0 & 0 \\ C_{13} & C_{23} & C_{33} & 0 & 0 & 0 \\ 0 & 0 & 0 & C_{44} & 0 & 0 \\ 0 & 0 & 0 & 0 & C_{55} & 0 \\ 0 & 0 & 0 & 0 & 0 & C_{66} \end{bmatrix} \begin{Bmatrix} \varepsilon_1 \\ \varepsilon_2 \\ \varepsilon_3 \\ \gamma_{23} \\ \gamma_{31} \\ \gamma_{12} \end{Bmatrix} \quad (3)$$

If we choose to invert equation (1) and write an equivalent strain-stress relationship, we must use the compliance matrix (S_{ij}) as follows:

$$\varepsilon_i = S_{ij}\sigma_j \qquad i,j = 1, \cdots, 6 \tag{4}$$

For most test purposes, the compliance matrix components (S_{ij}) are more easily determined than the components of the stiffness matrix (C_{ij}). This is due to the fact that simple tests are performed with a single known load condition [12]. Therefore, it is common to write equation (3) in terms of the compliance matrix (S_{ij}) as shown in equation (5).

$$\begin{Bmatrix} \varepsilon_1 \\ \varepsilon_2 \\ \varepsilon_3 \\ \gamma_{23} \\ \gamma_{31} \\ \gamma_{12} \end{Bmatrix} = \begin{bmatrix} S_{11} & S_{12} & S_{13} & 0 & 0 & 0 \\ S_{12} & S_{22} & S_{23} & 0 & 0 & 0 \\ S_{13} & S_{23} & S_{33} & 0 & 0 & 0 \\ 0 & 0 & 0 & S_{44} & 0 & 0 \\ 0 & 0 & 0 & 0 & S_{55} & 0 \\ 0 & 0 & 0 & 0 & 0 & S_{66} \end{bmatrix} \begin{Bmatrix} \sigma_1 \\ \sigma_2 \\ \sigma_3 \\ \tau_{23} \\ \tau_{31} \\ \tau_{12} \end{Bmatrix} \tag{5}$$

For an orthotropic material, the compliance matrix (S_{ij}) can be written in terms of engineering constants. These constants are obtained from uniaxial tension and compressions tests as well as shear tests. These engineering constants include Young's moduli, Poisson's ratios and the shear moduli. Therefore, for an orthotropic material, the compliance matrix can be written as shown in equation (6).

Since the specimens dealt with in this thesis were essentially thin plates, a state of plane stress was assumed. In order to make this assumption, one assumes that through the thickness normal stresses may be neglected. Without such an assumption, a three-dimensional finite element analysis would be required. This study attempted to accurately model failure of Gr/PEEK laminates with a two-dimensional model. It is important to

$$[S_{ij}] = \begin{bmatrix} \frac{1}{E_1} & \frac{-\nu_{21}}{E_2} & \frac{-\nu_{31}}{E_3} & 0 & 0 & 0 \\ \frac{-\nu_{12}}{E_1} & \frac{1}{E_2} & \frac{-\nu_{32}}{E_3} & 0 & 0 & 0 \\ \frac{-\nu_{13}}{E_1} & \frac{-\nu_{23}}{E_2} & \frac{1}{E_3} & 0 & 0 & 0 \\ 0 & 0 & 0 & \frac{1}{G_{23}} & 0 & 0 \\ 0 & 0 & 0 & 0 & \frac{1}{G_{31}} & 0 \\ 0 & 0 & 0 & 0 & 0 & \frac{1}{G_{12}} \end{bmatrix} \qquad (6)$$

remember that for certain ply lay-ups, normal stresses may be significant and therefore can not be neglected. For a lamina oriented as shown in Figure 2-4, a state of plane stress is defined by the following relations.

$$\sigma_3 = 0 \qquad \tau_{23} = 0 \qquad \tau_{31} = 0$$

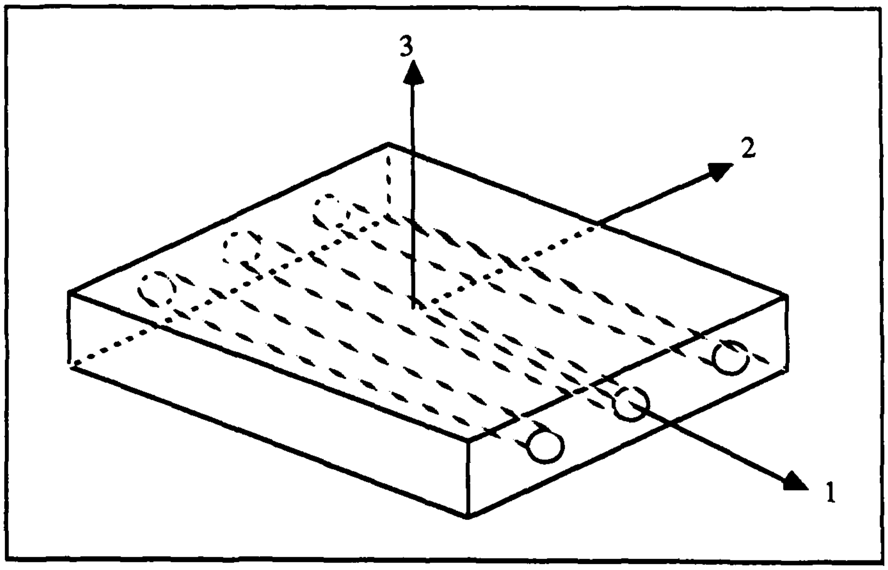

Figure 2-4. Unidirectional Lamina

Therefore, equation (5) can be further simplified as shown in equation (7).

$$\begin{Bmatrix} \varepsilon_1 \\ \varepsilon_2 \\ \gamma_{12} \end{Bmatrix} = \begin{bmatrix} S_{11} & S_{12} & 0 \\ S_{12} & S_{22} & 0 \\ 0 & 0 & S_{66} \end{bmatrix} \begin{Bmatrix} \sigma_1 \\ \sigma_2 \\ \tau_{12} \end{Bmatrix} \tag{7}$$

To obtain the stress-strain relations from equation (7), one need only invert the compliance matrix (S_{ij}), which results in the reduced stiffness matrix (Q_{ij}) as shown in equation (8).

$$\begin{Bmatrix} \sigma_1 \\ \sigma_2 \\ \tau_{12} \end{Bmatrix} = \begin{bmatrix} Q_{11} & Q_{12} & 0 \\ Q_{12} & Q_{22} & 0 \\ 0 & 0 & Q_{66} \end{bmatrix} \begin{Bmatrix} \varepsilon_1 \\ \varepsilon_2 \\ \gamma_{12} \end{Bmatrix} \tag{8}$$

The components of the reduced stiffness matrix (Q_{ij}) may be defined in terms of the components of the compliance matrix (S_{ij}) or in terms of engineering constants as [12]:

$$Q_{11} = \frac{S_{22}}{S_{11}S_{22}-S^2_{12}} = \frac{E_1}{1-\nu_{12}\nu_{21}}$$

$$Q_{12} = -\frac{S_{12}}{S_{11}S_{22}-S^2_{12}} = \frac{\nu_{12}E_2}{1-\nu_{12}\nu_{21}} = \frac{\nu_{21}E_1}{1-\nu_{12}\nu_{21}} \tag{9}$$

$$Q_{22} = \frac{S_{11}}{S_{11}S_{22}-S^2_{12}} = \frac{E_2}{1-\nu_{12}\nu_{21}}$$

$$Q_{66} = \frac{\nu_{12}}{E_1} = \frac{\nu_{21}}{E_2} = \frac{1}{S_{66}} = G_{12}$$

For an orthotropic lamina subjected to in-plane forces, equations (7) thru (9) form the foundation for stiffness and stress calculations.

Typically, in most applications, the principal directions of orthotropy do not coincide with the coordinate axes (see Figure 2-5). In these instances, we must use a transformation relationship between stresses and strains in the principal material directions and those in the coordinate directions.

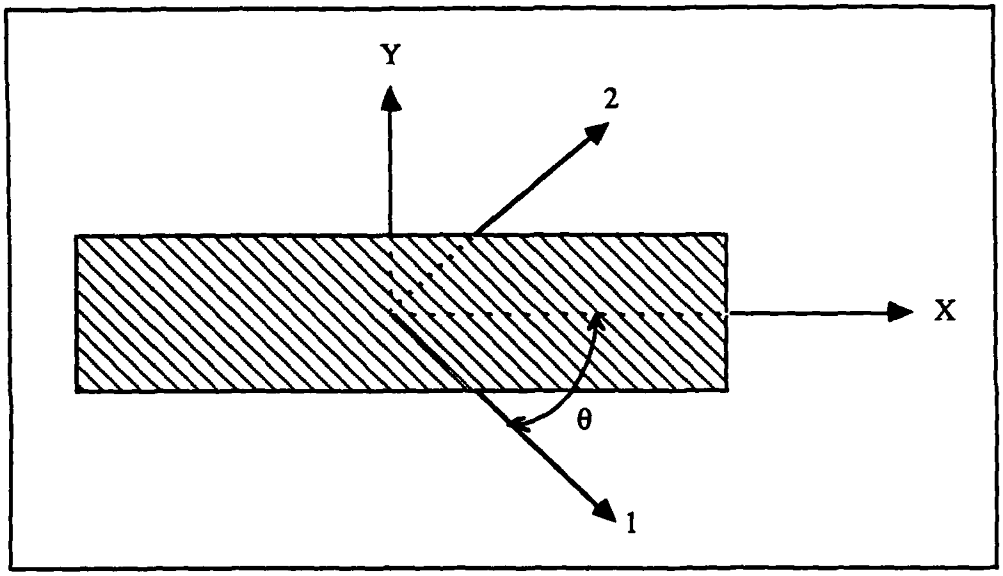

Figure 2-5. Coordinate & Principal Material Axes

From simple geometric considerations, a transformation equation can easily be written to express stresses in an X-Y coordinate system in terms of stresses in the principal material directions. This transformation can be expressed as follows:

$$\begin{Bmatrix} \sigma_x \\ \sigma_y \\ \tau_{xy} \end{Bmatrix} = \begin{bmatrix} m^2 & n^2 & -2nm \\ n^2 & m^2 & 2nm \\ nm & -nm & m^2 - n^2 \end{bmatrix} \begin{Bmatrix} \sigma_1 \\ \sigma_2 \\ \tau_{12} \end{Bmatrix} \qquad (10)$$

where:

$m = \cos\theta$
$n = \sin\theta$

If we implement the transformations, we can generalize equation (8) to account for a lamina in which the fibers are not aligned with the coordinate axes. The stress-strain expression can then be written as shown in equation (11).

$$\begin{Bmatrix} \sigma_x \\ \sigma_y \\ \tau_{xy} \end{Bmatrix} = \begin{bmatrix} \bar{Q}_{11} & \bar{Q}_{12} & \bar{Q}_{16} \\ \bar{Q}_{12} & \bar{Q}_{22} & \bar{Q}_{26} \\ \bar{Q}_{16} & \bar{Q}_{26} & \bar{Q}_{66} \end{bmatrix} \begin{Bmatrix} \varepsilon_x \\ \varepsilon_y \\ \gamma_{xy} \end{Bmatrix} \tag{11}$$

The matrix ($\bar{Q}_{ij}$) is referred to as the transformed reduced stiffness matrix. The components of the transformed reduced stiffness matrix are defined as follows:

$$\begin{aligned}
\bar{Q}_{11} &= Q_{11}m^4 + 2(Q_{12} + 2Q_{66})n^2m^2 + Q_{22}n^4 \\
\bar{Q}_{12} &= (Q_{11} + Q_{22} - 4Q_{66})n^2m^2 + Q_{12}(n^4 + m^4) \\
\bar{Q}_{22} &= Q_{11}n^4 + 2(Q_{12} + 2Q_{66})n^2m^2 + Q_{22}m^4 \\
\bar{Q}_{16} &= (Q_{11} - Q_{12} - 2Q_{66})nm^3 + (Q_{12} - Q_{22} + 2Q_{66})n^3m \\
\bar{Q}_{26} &= (Q_{11} - Q_{12} - 2Q_{66})n^3m + (Q_{12} - Q_{22} + 2Q_{66})nm^3 \\
\bar{Q}_{66} &= (Q_{11} + Q_{22} - 2Q_{12} - 2Q_{66})n^2m^2 + Q_{66}(n^4 + m^4)
\end{aligned} \tag{12}$$

where: $m = \cos\theta$

$n = \sin\theta$

In the general form of the stress-strain relations, as shown in equation (11), it is important to note that there is coupling between shear strain and normal stresses and also between shear stress and normal strains. The mechanical behavior of a lamina can be described by equation (11). With this information, we can now proceed to study the behavior of a laminated fiber-reinforced composite laminate.

As previously discussed, interlaminar shear stresses develop in composite laminates due to the tendency of each ply to deform according to its respective material properties. These interlaminar shear stresses often result in the complicated phenomenon of delamination. Typically interlaminar normal stress (σ_z, Figure 2-6) is the most predominant stress affecting delamination. Although the stress analysis used in this study does not take into account the stacking sequence of a laminate, work has been done by Sandhu [19,24] in formulating "Delamination Moment Coefficients" which describe the tendency of a composite to delaminate.

If we generalize equation (11) for each ply in a laminate, we can rewrite the expression as shown in equation (13). The behavior of a given laminate can be determined by summing the individual behavior of each lamina. This approach essentially ignores delamination effects, and an equivalent stiffness matrix is generated by the finite element program discussed in Section II B.

$$\begin{Bmatrix} \sigma_x \\ \sigma_y \\ \tau_{xy} \end{Bmatrix}_k = \begin{bmatrix} \bar{Q}_{11} & \bar{Q}_{12} & \bar{Q}_{16} \\ \bar{Q}_{12} & \bar{Q}_{22} & \bar{Q}_{26} \\ \bar{Q}_{16} & \bar{Q}_{26} & \bar{Q}_{66} \end{bmatrix} \begin{Bmatrix} \varepsilon_x \\ \varepsilon_y \\ \gamma_{xy} \end{Bmatrix}_k \qquad (13)$$

where: k = the k^{th} ply

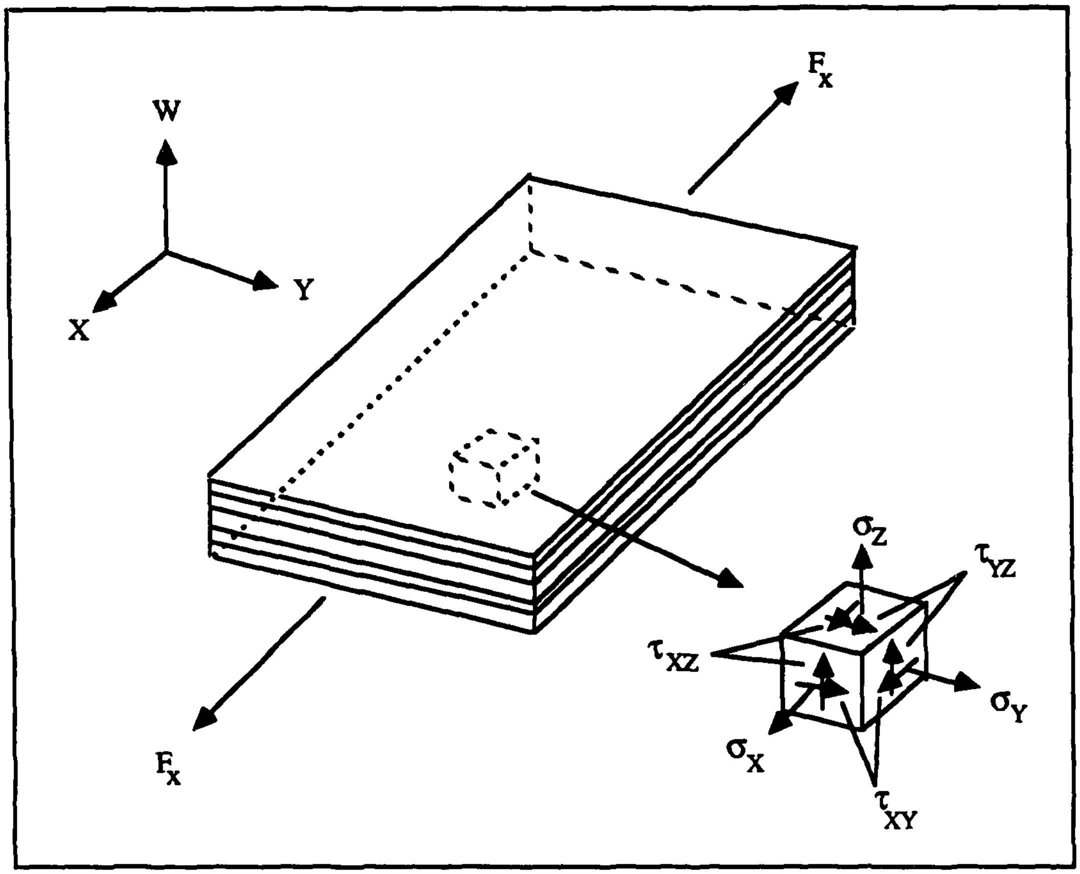

Figure 2-6. Interlaminar Stresses

B. Linear Finite Element Theory.

The finite element method is a numerical scheme used for solving problems in continuum mechanics. As such, its success depends totally upon the reliability of the computer program used. To minimize computer time, a linear finite element program (PLSTR) was used for several important aspects of this thesis. This program was written by Dr. R.S. Sandhu, and was used for modeling, convergence studies, and contour plotting. The program uses a ply-by-ply analysis technique and also takes into account the number and orientation of orthotropic plies of a given laminate. Since PLSTR makes use of constant strain triangle elements, the theory of finite elements as it applies to this element will be briefly discussed.

The constant strain triangle has six degrees of freedom as shown in Figure 2-7. This element is one of the earliest finite elements and is easy to formulate [6,14]. For the constant strain triangle, the assumed displacement field is linear in the x and y coordinates. Using the convention of [6], the displacement fields may be written as:

$$u = [X]\{a_1 \quad a_2 \quad a_3\} \quad \text{and} \quad v = [X]\{a_4 \quad a_5 \quad a_6\} \tag{14}$$

where:

$$[X] = [1 \quad x \quad y]$$

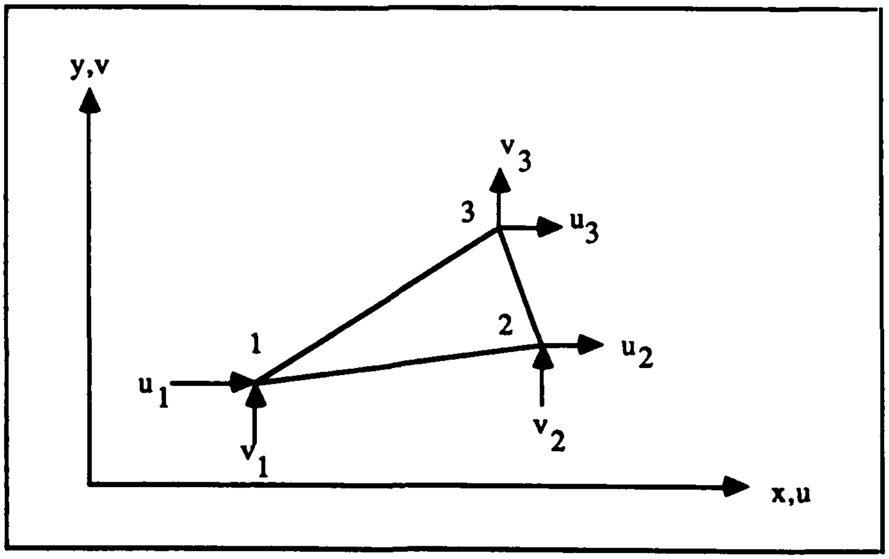

Figure 2-7. Constant Strain Triangle

If we consider equation (14) at the three nodes of Figure 2-7, we can write, for the u displacement field, the following equation.

$$\begin{Bmatrix} u_1 \\ u_2 \\ u_3 \end{Bmatrix} = [A] \begin{Bmatrix} a_1 \\ a_2 \\ a_3 \end{Bmatrix} \qquad (15)$$

where:

$$[A] = \begin{bmatrix} 1 & x_1 & y_1 \\ 1 & x_2 & y_2 \\ 1 & x_3 & y_3 \end{bmatrix}$$

If we invert matrix [A] we obtain the following:

$$[A]^{-1} = \frac{1}{2A} \begin{bmatrix} x_2y_3 - x_3y_2 & x_3y_1 - x_1y_3 & x_1y_2 - x_2y_1 \\ y_2 - y_3 & y_3 - y_1 & y_1 - y_2 \\ x_3 - x_2 & x_1 - x_3 & x_2 - x_1 \end{bmatrix} \qquad (16)$$

where:

A = the area of the constant strain triangle

In terms of nodal degrees of freedom, equation (14) can be written as:

$$u = [\, N_1 \;\; N_2 \;\; N_3 \,] \{\, u_1 \;\; u_2 \;\; u_3 \,\} \qquad (17)$$

where:

$$[\, N_1 \;\; N_2 \;\; N_3 \,] = [\, 1 \;\; x \;\; y \,][A]^{-1}$$

If the displacement functions are differentiated, we obtain the strains for the element (small strain assumption) as follows:

$$\varepsilon_x = \frac{\partial u}{\partial x} \qquad \varepsilon_y = \frac{\partial v}{\partial y} \qquad \gamma_{xy} = \frac{\partial u}{\partial y} + \frac{\partial v}{\partial x} \qquad (18)$$

The strain-displacement matrix [B] operates on the displacement matrix {d} to give us strains as follows:

$$\begin{Bmatrix} \varepsilon_x \\ \varepsilon_y \\ \gamma_{xy} \end{Bmatrix} = [B] \begin{Bmatrix} u_1 \\ u_2 \\ u_3 \\ v_1 \\ v_2 \\ v_3 \end{Bmatrix} \tag{19}$$

where:

$$[B] = \begin{bmatrix} 0 & 1 & 0 & 0 & 0 & 0 \\ 0 & 0 & 0 & 0 & 0 & 1 \\ 0 & 0 & 1 & 0 & 1 & 0 \end{bmatrix} [A]^{-1}$$

The element stiffness matrix for an isotropic material may now be formulated as shown in equation (20).

$$[k] = \int_A [B]^T [E] [B] \, t \, da = [B]^T [E] [B] \, t A \tag{20}$$

where:

t = the element thickness

$$[E] = \frac{E}{1-\nu^2} \begin{bmatrix} 1 & \nu & 0 \\ \nu & 1 & 0 \\ 0 & 0 & \frac{1-\nu}{2} \end{bmatrix} \text{(plane stress assumption)}$$

Since we have already developed an expression for the stress-strain relation for an orthotropic material (see equation (13)), we can say that $[\bar{Q}_{ij}]$ is analogous to [E]. Therefore, we can rewrite equation (20) as follows:

$$[k] = \int_A [B]^T\ [\bar{Q}]\ [B]\ t\, dA = [B]^T\ [\bar{Q}]\ [B]\ t\ A \qquad (21)$$

where:

$$[\bar{Q}] = \begin{bmatrix} \bar{Q}_{11} & \bar{Q}_{12} & \bar{Q}_{16} \\ \bar{Q}_{12} & \bar{Q}_{22} & \bar{Q}_{26} \\ \bar{Q}_{16} & \bar{Q}_{26} & \bar{Q}_{66} \end{bmatrix}$$

The program PLSTR makes use of four constant strain triangles to produce the quadrilateral elements which were used in this study (see Figure 2-8). Since there are two degrees of freedom per node, the resulting stiffness matrix is a 10 x 10. However, two of the rows and columns of this matrix are based on the fictitious node "M" as shown in Figure 2-8. Therefore, the stiffness matrix can be reduced to an 8 x 8 by assuming that there are no applied loads at "M". The [B] matrix may be reduced from a 3 x 10 to a 3 x 8 by assuming that displacements at node "M" are given by:

$$u_M = \frac{u_I + u_J + u_K + u_L}{4}$$

$$v_M = \frac{v_I + v_J + v_K + v_L}{4}$$

In order to account for through the thickness ply orientations, an equivalent stiffness matrix was formulated. The program PLSTR makes use of the assumption that displacements through the thickness of the laminate are constant. Therefore, the equivalent stiffness matrix is formulated by summing up the individual stiffness matrices for each ply as shown in equation (22).

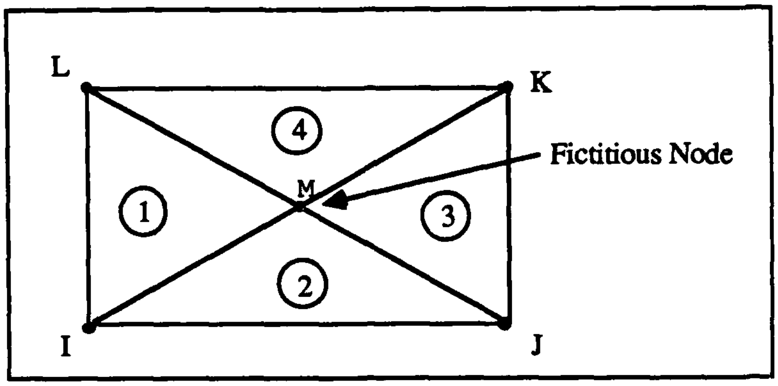

Figure 2-8. Quadrilateral Element

$$[k_{eq}] = A \sum_{i=1}^{n} [B]^T [\bar{Q}_i] [B] t_i \qquad (22)$$

where:

i = the i^{th} lamina
n = the total number of plies
t_i = the thickness of the i^{th} ply

Since elements of different plies, through the thickness of the laminate, share common nodes (see Section III B (3)), they will therefore all deform by the same amount for a given load. "Whether or not an element fails depends on its own material properties and on its orientation to the given load [13]."

C. Nonlinear Constitutive Relationships.

The nonlinear material finite element program used for this thesis (PLSTREN) was written by Dr. R.S. Sandhu. This progressive-ply-failure program predicts both damage initiation and propagation in composite laminates. The program is modular by design and allows for the use of various finite elements, ply failure criteria, and post-failure element unloading options [21]. Although this program is well documented [23,25], the pertinent theory, as it applies to this thesis, will be discussed.

As previously mentioned in Section I, Gr/PEEK exhibits nonlinear behavior (also see Appendix A). Therefore, it is appropriate to use an incremental form of the constitutive law. To define this incremental form of the constitutive law, two assumptions are made [25].

(1) increments of strain depend upon the strain state and the increment of stress

(2) the increment of strain is proportional to the increment of stress

Therefore, the incremental constitutive law for an anisotropic material (plane stress assumption) is written as:

$$d\varepsilon_i = S_{ij}(\varepsilon_i)d\sigma_j \qquad (i,j = 1,2,6) \tag{23}$$

Equation (23) can be written in matrix form as follows:

$$\begin{Bmatrix} d\varepsilon_1 \\ d\varepsilon_2 \\ d\varepsilon_6 \end{Bmatrix} = \begin{bmatrix} S_{11} & S_{12} & S_{16} \\ S_{21} & S_{22} & S_{26} \\ S_{16} & S_{26} & S_{66} \end{bmatrix} \begin{Bmatrix} d\sigma_1 \\ d\sigma_2 \\ d\sigma_6 \end{Bmatrix} \tag{24}$$

Equation (24) can be written more simply as:

$$[d\varepsilon] = [S]\,[d\sigma] \tag{25}$$

where:

$d\sigma_1$ = normal stress increment in the fiber direction
$d\varepsilon_1$ = normal strain increment in the fiber direction
$d\sigma_2$ = normal stress increment in the transverse direction
$d\varepsilon_2$ = normal strain increment in the transverse direction
$d\sigma_6$ = shear stress increment
$d\varepsilon_6$ = shear strain increment
S_{ij} = compliance matrix components which represent the average values during the increment of stresses

For an orthotropic lamina (see Section II A), we can simplify equation (24) by setting

$$S_{16} = S_{26} = 0 \tag{26}$$

This assumption requires that the lamina remain orthotropic at any given level of load. Furthermore, we can define the remaining components of the compliance matrix in terms of engineering constants as follows:

$$S_{11} = \frac{1}{E_{11}} \qquad S_{22} = \frac{1}{E_{22}} \qquad S_{66} = \frac{1}{G_{12}}$$

$$S_{12} = S_{21} = -\frac{\nu_{12}}{E_{11}} = -\frac{\nu_{21}}{E_{22}} \tag{27}$$

If we combine equations (24), (26), and (27), we obtain the incremental stress-strain relations for a given lamina.

$$d\varepsilon_1 = \frac{d\sigma_1}{E_{11}} (1-\nu_{12}R) \tag{28}$$

$$d\varepsilon_2 = \frac{d\sigma_2}{E_{22}} \left(1-\frac{\nu_{21}}{R} \right) \tag{29}$$

$$d\varepsilon_6 = \frac{d\sigma_6}{G_{12}} \tag{30}$$

where:

$$R = \frac{d\sigma_2}{d\sigma_1} \qquad (d\sigma_1 \neq 0)$$

Inspection of equations (28) and (29) reveal that errors would result from using $d\varepsilon_1$ or $d\varepsilon_2$ to determine the incremental elastic constants (E_{11} or E_{22}) from stress-strain curves obtained under simple load conditions. For the simple case of uniaxial loading of an anisotropic material, the resulting stress state is not the same as that obtained under biaxial loading conditions. This can be explained more clearly in pictorial form where it is clear that simple loading conditions do not accurately represent a state of biaxial stress.

> For example, $d\varepsilon_2$ of equation (29) corresponds to curve ON (Figure 2-9) on the plane OEHG, while simple stress strain curve OM lies on the plane OEDC [25].

Since no experimental data is available for the biaxial state of stress, we must somehow take into account the effect of a biaxial stress state. Sandhu accomplishes this by assuming that simple equivalent strain increments can be computed as follows.

$$d\varepsilon 1_{eq} = \frac{d\varepsilon_1}{1-\nu_{12}R} \qquad (31)$$

$$d\varepsilon 1_{eq} = \frac{d\varepsilon_2}{1-\frac{\nu_{21}}{R}} \qquad (32)$$

If we invert equation (23) and write an equivalent expression for the kth ply we obtain equation (33).

$$[d\sigma]_k = [C]_k\ [d\varepsilon]_k \qquad (33)$$

where:

$[C]_k$ = stiffness matrix of the kth ply
$[d\sigma]_k$ = stress increment in the kth ply relative to the material axes 1,2
$[d\varepsilon]_k$ = strain increment in the kth ply relative to the material axes 1,2

As discussed in Section II A. and shown graphically in Figure 2-5, the coordinate axes (X & Y) do not in general coincide with the principal material axes. Therefore, the stress and strain increments in the two coordinate systems must be related by an appropriate

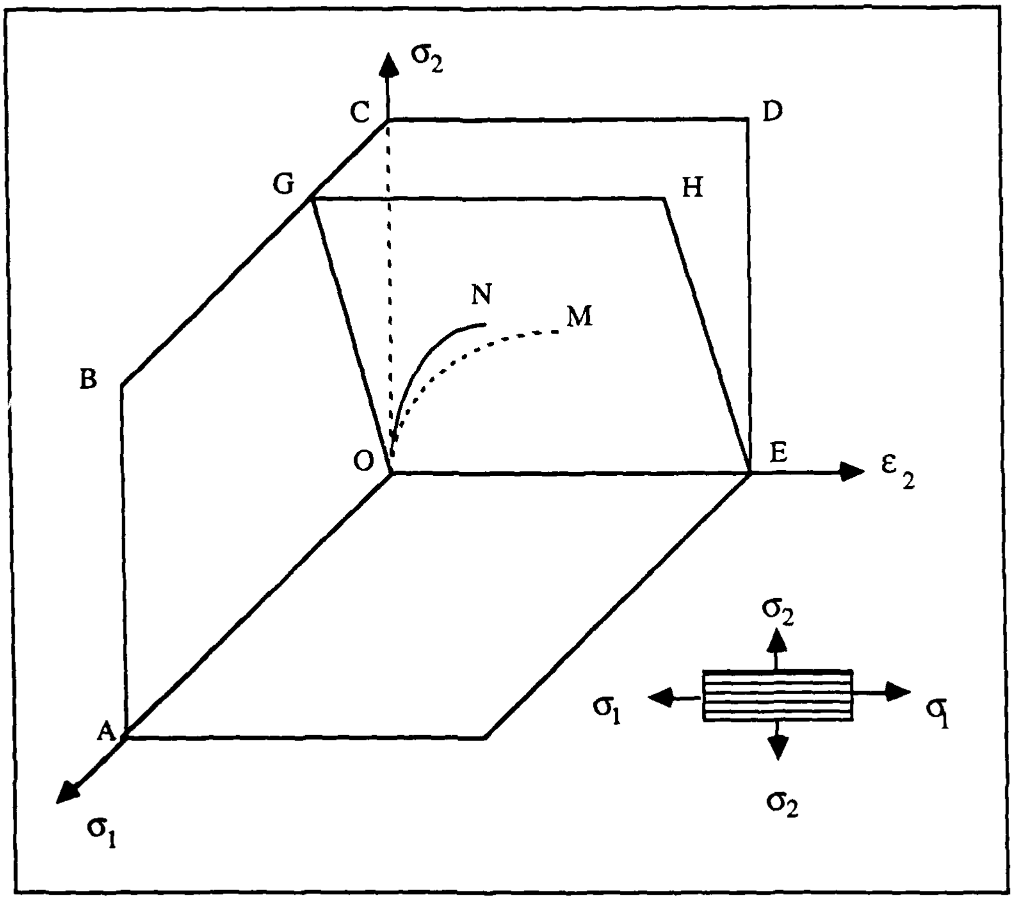

Figure 2-9. ε_2 Under a Biaxial State of Stress [23,25]

transformation matrix. Following the convention used by [23,25], we can relate the stress and strain increments in the two coordinate systems by the transformation matrix $[T]_k$.

$$[d\sigma]_k = [T]_k\,[d\bar{\sigma}]_k \qquad (34)$$

$$[d\varepsilon]_k = [T]_k\,[d\bar{\varepsilon}]_k$$

where:

$[d\bar{\sigma}]_k$ = stress increment in x,y coordinate system

$[d\bar{\varepsilon}]_k$ = strain increment in x,y coordinate system

Substituting equation (34) into equation (33) yields:

$$[T]_k\,[d\bar{\sigma}]_k = [\bar{C}]_k\,[d\bar{\varepsilon}]_k \tag{35}$$

where:

$$[\bar{C}]_k = [T]^{-1}\,[C]_k\,[T]_k$$

Since the assumption is made that stresses are uniformly distributed through the thickness of <u>each</u> ply, we can define the stress resultant increments [dN] (in the x,y coordinate system) as follows:

$$[dN] = \sum_{k=1}^{P} [d\bar{\sigma}]_k\, t_k \tag{36}$$

where:

t_k = thickness of the k^{th} ply
P = total number of plies in the laminate

Making use of our transformations (equation 35), the stress resultant increments may be written as:

$$[dN] = \sum_{k=1}^{P} t_k\; [\bar{C}]_k\, [d\bar{\varepsilon}]_k \tag{37}$$

Since the strain increments $[d\bar{\varepsilon}]_k$ are the same for all plies through the thickness of the laminate, we can write the following:

$$[d\bar{\varepsilon}]_k = [d\varepsilon]$$

Therefore equation (37) becomes:

$$[dN] = [F]\,[d\varepsilon] \tag{38}$$

where:

$$[F] = \sum_{k=1}^{P} t_k \, [\bar{C}]_k$$

If equation (38) is inverted, $[F]^{-1}$ represents the average compliance properties of the given laminate during the (n)th load increment [25].

$$[d\varepsilon] = [F]^{-1} [dN] \qquad (39)$$

The problem in evaluating equation (39) is that the properties (values) of $[F]^{-1}$ are not known at the start of the (n)th load increment. Therefore, the properties of $[F]^{-1}$ at the end of the (n-1)th load increment are used. This method is often referred to as the "predictor corrector" method.

$$[d\varepsilon]_n = [F]^{-1}_{n-1} [dN]_n \qquad (40)$$

These equations set up the incremental scheme under which PLSTREN operates. Once the strain increments have been calculated from equation (40), $[d\sigma]_k$, $[d\varepsilon]_k$, and $d\varepsilon l_{eq}$ are calculated. These stress and strain increments are added to the nth load increment stresses and strains to yield the current stress and strain states in all plies. These "current" stresses and strains are used to calculate the average elastic properties of the plies and a new $[F]^{-1}$ is calculated. The incremental scheme is continued until the values of $[d\varepsilon]_{n+1}$ and $[d\varepsilon]_n$ have converged (see equation 41).

$$\frac{[d\varepsilon]_{n+1} - [d\varepsilon]_n}{[d\varepsilon]_n} < 0.001 \qquad (41)$$

PLSTREN requires that the mechanical properties of the laminate be entered in the form of tabular data. These properties were determined by [13] through simple tests (uniaxial tension and compression along and transverse to the material axes and shear). Once this basic stress-strain data has been read by the program, piecewise cubic spline interpolation functions [2] are used to represent the data. The advantage of the cubic spline functions is that they yield smooth stress-strain curves from which accurate moduli of elasticity over the entire range of the curves can be determined [23].

For clarity, the basic property tests, resulting curves, and corresponding basic properties are shown in Table 2-1. In addition, the material property curves are shown in Appendix A. As might be expected, a laminate can not continue to be loaded without failing. Therefore, the failure criterion used by PLSTREN is discussed in Section II D.

Table 2-1. Property Tests/Resulting Curves/Corresponding Basic Properties

TEST	*CURVE*	*PROPERTY OBTAINED*
0° Tension	σ_1 vs ε_1 → ν_{12} vs ε_1 →	E_1^T ν_{12}^T
0° Compression	σ_1 vs ε_1 → ν_{12} vs ε_1 →	E_1^C ν_{12}^C
90° Tension	σ_2 vs ε_2	E_2^T
90° Compression	σ_2 vs ε_2	E_2^C
$\pm 45^{\circ}$ Tension	τ_{12} vs γ_{12}	G_{12}

D. Strain Energy Failure Theory.

As expected, continued loading of a laminate will cause failure. This failure condition, under general states of stress, is determined by a total strain energy failure criterion developed by Sandhu [21,22,23,25]. For nonlinear materials, the failure state is assumed to be a function of both stresses and strains. Therefore, a scalar function, f, is defined which accounts for the failure condition of a given material as:

$$f(\sigma,\varepsilon,K) = 1 \tag{42}$$

where:

σ = stress state
ε = strain state
K = material characteristics

If equation (42) is written in an explicit form, whereby the scalar strain energy is used as a measure to determine the effects of both stress and strain states of the material, equation (42) can be expressed (for an orthotropic material) as:

$$K_{ij}\left[\int_{\varepsilon_{ij}}\sigma_{ij}\,d\varepsilon_{ij}\right]^{m} = 1 \qquad (i,j = 1,2,3) \tag{43}$$

where:

ε_{ij} = current strain components
m = parameter defining the shape of the failure surface in the strain-energy space

The failure criterion is based upon the total strain energies. For our special case of plane stress, equation (43) can be written as:

$$K_1\left[\int_{\varepsilon_1}\sigma_1 d\varepsilon_1\right]^{m_1} + K_2\left[\int_{\varepsilon_2}\sigma_2 d\varepsilon_2\right]^{m_2} + K_6\left[\int_{\varepsilon_6}\sigma_6 d\varepsilon_6\right]^{m_6} = 1 \tag{44}$$

One will notice from equation (44) that the failure criterion is based upon the concept that strain energies under longitudinal, transverse, and shear loadings are independent parameters. Therefore, the ratios of current energy levels (due to longitudinal, transverse, and shear loading) to the maximum energy levels that are available for each, must be considered. The shape of the failure surface in strain-energy space is governed by the shape factor, m_i [20,21]. For $m_1=m_2=m_6=2$, the failure surface is spherical, and for $m_1=m_2=m_6=1$, the failure surface is pyramidal. This failure criterion is compared (for varying m_i's) with several other theories in Figure 2-10 [23]. It should be pointed out that this comparison was confined to the first quadrant of stress space, and used boron-epoxy material systems. For purposes of this thesis, and for lack of reliable experimental data for Gr/PEEK laminas under biaxial stress states, m_i was taken to be unity. Therefore, when the sum of the three ratios of equation (44) equals unity, the lamina degrades completely. The next question which must now be addressed is; does the fiber fail or does the matrix fail, and how do we unload failed elements?

Since equation (44) indicates when lamina failure occurs, we now need only determine the failure mode. At present, two failure modes are possible. These include either matrix or fiber failure. The matrix failure mode can occur without causing fiber failure. When matrix failure occurs, the failed lamina continues to carry loads parallel to the fibers but is unloaded in transverse tension and shear. If fiber failure occurs, the lamina is considered unable to carry any load, and loads are transferred to the adjacent lamina. To determine which of the two failure modes are appropriate, Sandhu developed a criterion given by:

$$\frac{K_1\left[\int_{\varepsilon_1}\sigma_1 d\varepsilon_1\right]}{\sum\limits_{i=(1,2,3)} K_i\left[\int_{\varepsilon_i}\sigma_i d\varepsilon_i\right]} = \text{Check} \qquad (45)$$

If Check ≥ 0.1 then *Fiber Failure*
If Check < 0.1 then *Matrix Failure*

Simply stated, this criterion predicts fiber failure when the ratio of longitudinal strain energy to total strain energy equals or exceeds 10%. This value (10%) was developed through fracture testing experience with several different composite materials, and has been found to yield good analytical results [10,13].

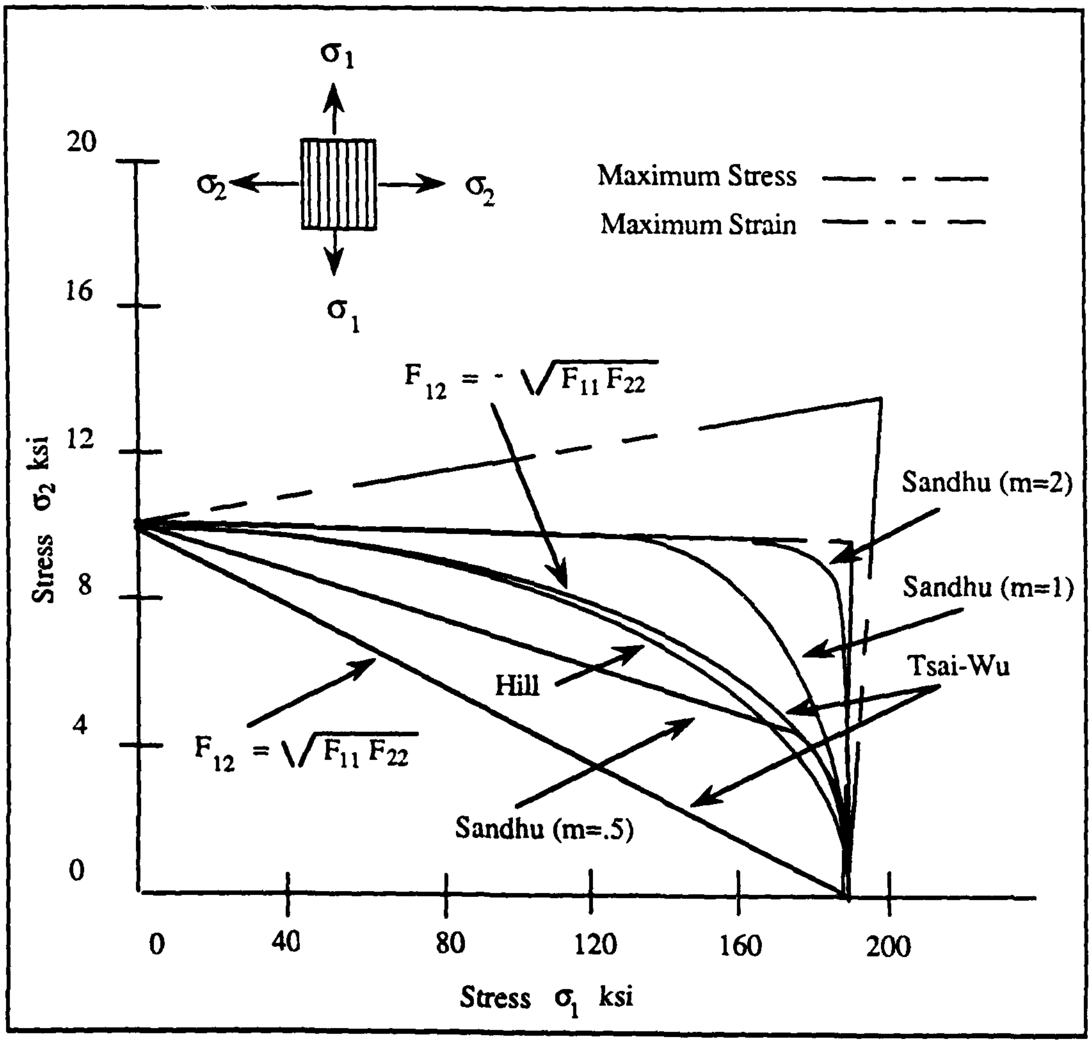

Figure 2-10. Comparison of Strength Theories [20]

Once ply failure has occured in a given element, the failed element can no longer sustain loads. Therefore, the load which was sustained by the failed element must be redistributed to other adjacent elements of the laminate. This study made use of a gradual unloading scheme (option 1).

Option 1. (Gradual Unloading) - With this option it is assumed that as elements fail, adjacent elements are able to carry the load previously carried by the failed elements. This unloading scheme is accomplished by assigning negative values to the affected moduli while continuing the incremental loading (see Figure 2-11). When the stresses in the failed elements are reduced to zero, the moduli are set to nominally small values (100 psi).

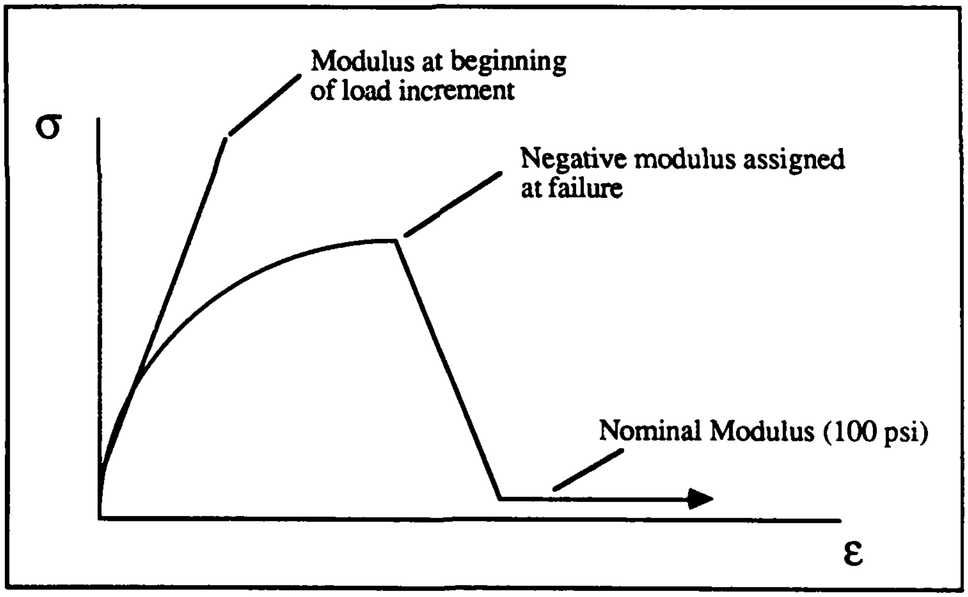

Figure 2-11. Gradual Unloading Scheme

III. Analysis

As previously discussed in Section II, this study made use of both linear and nonlinear finite element programs. The primary purpose of the linear finite element analysis was to develop a finite element model for use with the nonlinear finite element program. In addition, the linear finite element analysis was conducted to:

(1) verify the "convergence" (i.e. accuracy) of analytical data obtained by using the finite element model.

(2) study the effects of the eccentric circular discontinuity on the overall stress state of the Gr/PEEK laminates.

(3) study boundary condition and gage length effects on the overall stress state of the Gr/PEEK laminates.

The nonlinear finite element analysis made use of the finite element model developed from the linear analysis. The purpose of the nonlinear finite element analysis was to determine the initiation, progression of failure, and failure loads of the Gr/PEEK laminates studied.

As outlined below, this section discusses the analytical portion of this study.

(A) Specimen Geometry
(B) Finite Element Model Development
(C) Convergence Study
(D) Boundary Conditions
(E) Eccentricity/Boundary Condition/Gage Length - - Effects (Linear Analysis)
(F) Nonlinear Analysis

A. Specimen Geometry.

Before discussing the development of the finite element model, a brief description of the specimens used during the experimental portion of this study is presented. As previously mentioned in Section I, Gr/PEEK (16 ply) composite laminates were tested. The four ply lay-ups studied were $[0^o{}_{16}]$, $[90^o{}_{16}]$, $[\pm 45^o]_{4s}$, and $[0^o/\pm 45^o/90^o]_{2s}$.

Since this study involved eccentricity effects, several of the specimens were not geometrically symmetric (Figure 3-1). Therefore, the finite element models developed were "whole models." This term, "whole model," implies that geometric symmetry could not be used to simplify the model used in the analysis. In some instances (where the specimens are geometrically symmetric), it is possible to represent the specimens by finite element models in which only one-half or one-fourth of the specimen is modeled. This simplification (not appropriate in this study) leads to finite element models, with fewer elements, which require less computer time to analyze.

B. Finite Element Model Development.

When constructing a finite element model, it is imperitive that the actual dimensions of the specimen, applied loading, and the physical boundary conditions be modeled as accurately as possible. As discussed in Section IIIA, whole models were required in this study. Therefore, three separate finite element models were required to represent the three different size specimens shown in Figure 3-1. In addition to this requirement, glass epoxy tabs as well as through the thickness ply orientations were incorporated into the finite element models. Finally, the finite element mesh required refinement in areas where high gradients of stress were expected [6]. This refinement was required so that large jumps in stress were avoided as boundaries between finite elements were crossed. This was particularly important in this study, since the quadrilateral elements used for modeling were constructed from constant strain triangle elements (see Section II B).

The last complication to the development of the finite element model was the use of a mounting fixture. The mounting fixture (see Section IV D) allowed in-plane rotation of the specimen.

(1) Modeling of Specimen Widths.

After a considerable amount of work, a method was proposed by Dr. Sandhu to develop one model which could be used to represent the three different width specimens (Figure 3-1). This method involved the development of a finite element model (Figure 3-2)

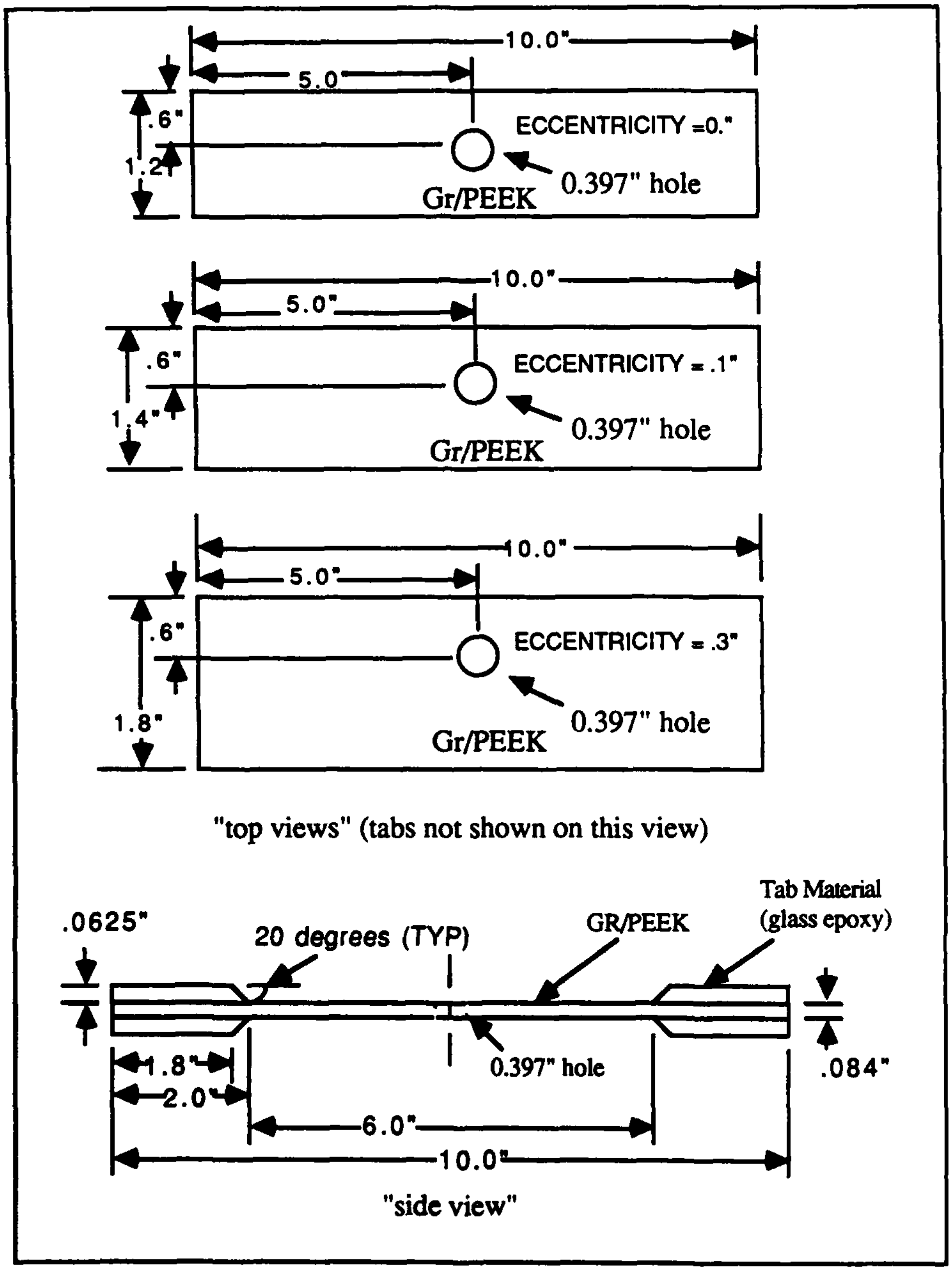

Figure 3-1. Specimen Geometry

which represented the widest specimen shown in Figure 3-1.

To represent the other two (more narrow) specimens shown in Figure 3-1, the finite element model (Figure 3-2) was modified. This modification involved the mathematical elimination of the rows of finite elements at the bottom of the model (Figure 3-2). This was accomplished by "zeroing out" the elements below rows AA or BB (Figure 3-2). The term "zeroing out" an element implies that a nominally low modulus of 1000 psi (compared to the actual modulus of 19,200,000 psi) was assigned to that particular element. Therefore, the zeroed out elements contributed an insignificant amount to the overall stiffness of the model. By reducing the model shown in Figure 3-2, it was possible (by zeroing out rows of elements) to develop the finite element models shown in Figure 3-3. The significance of this reduction was that one finite element model was used to represent three different width specimens.

(2) Modeling of Glass Epoxy Tabs.

As previously mentioned, it was necessary to incorporate glass epoxy tabs (Figure 3-1) in the finite element model. This was accomplished by further modifications to the finite element models shown in Figure 3-3. The addition of tabs to the model was accomplished by adding an additional finite element (through the thickness) to each element contained within the tab area (see Figures 3-4 B and 3-4 C). Since out-of-plane bending was not allowed (analytically), the total thickness of the upper and lower tabs (Figure 3-4 A) were modeled as one element with a thickness equal to the sum of the upper and lower tab thicknesses (Figure 3-4 C). Also, note that the finite element mesh is refined as you move into the tab area (A to B, Figure 3-4 B). This refinement was incorporated due to an expected stress gradient arising from the geometric discontinuity caused by the tab material. The tabs were tapered to minimize this geometric discontinuity (Figure 3-4 A).

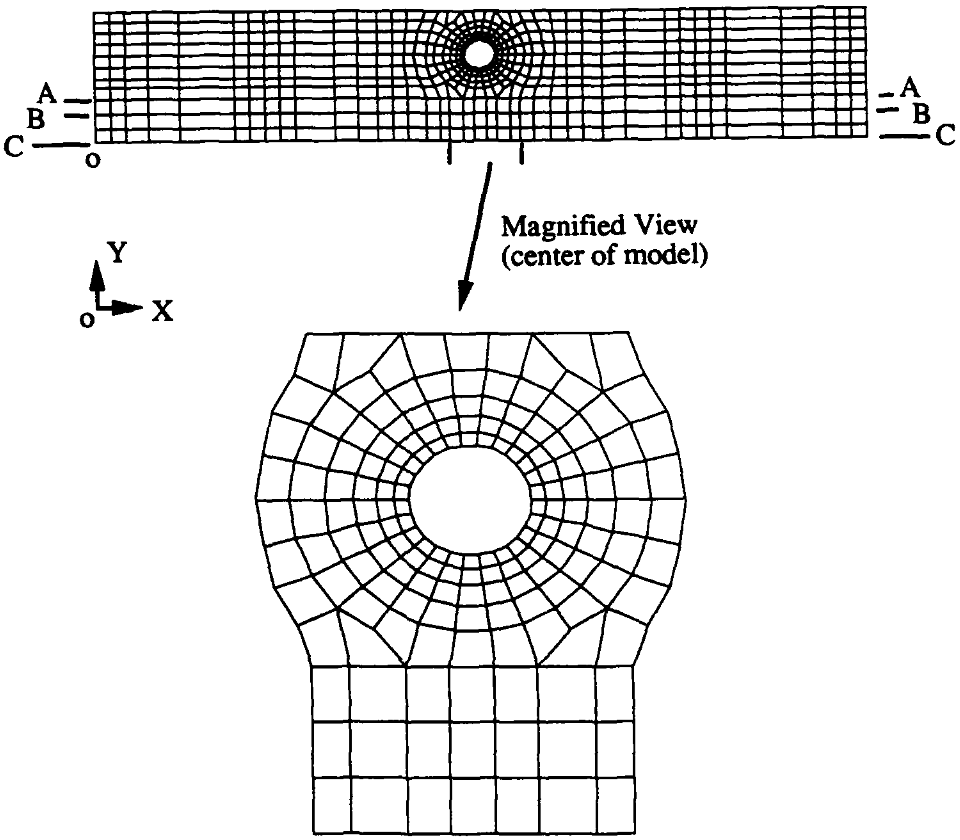

Note the mesh refinement adjacent to the discontinuity, this is an area of high stress gradients.

Line CC is located at Y=0.0"
Line BB is located at Y=0.4"
Line AA is located at Y=0.6"

Point o is the origin of the coordinate system

Figure 3-2. Finite Element Model

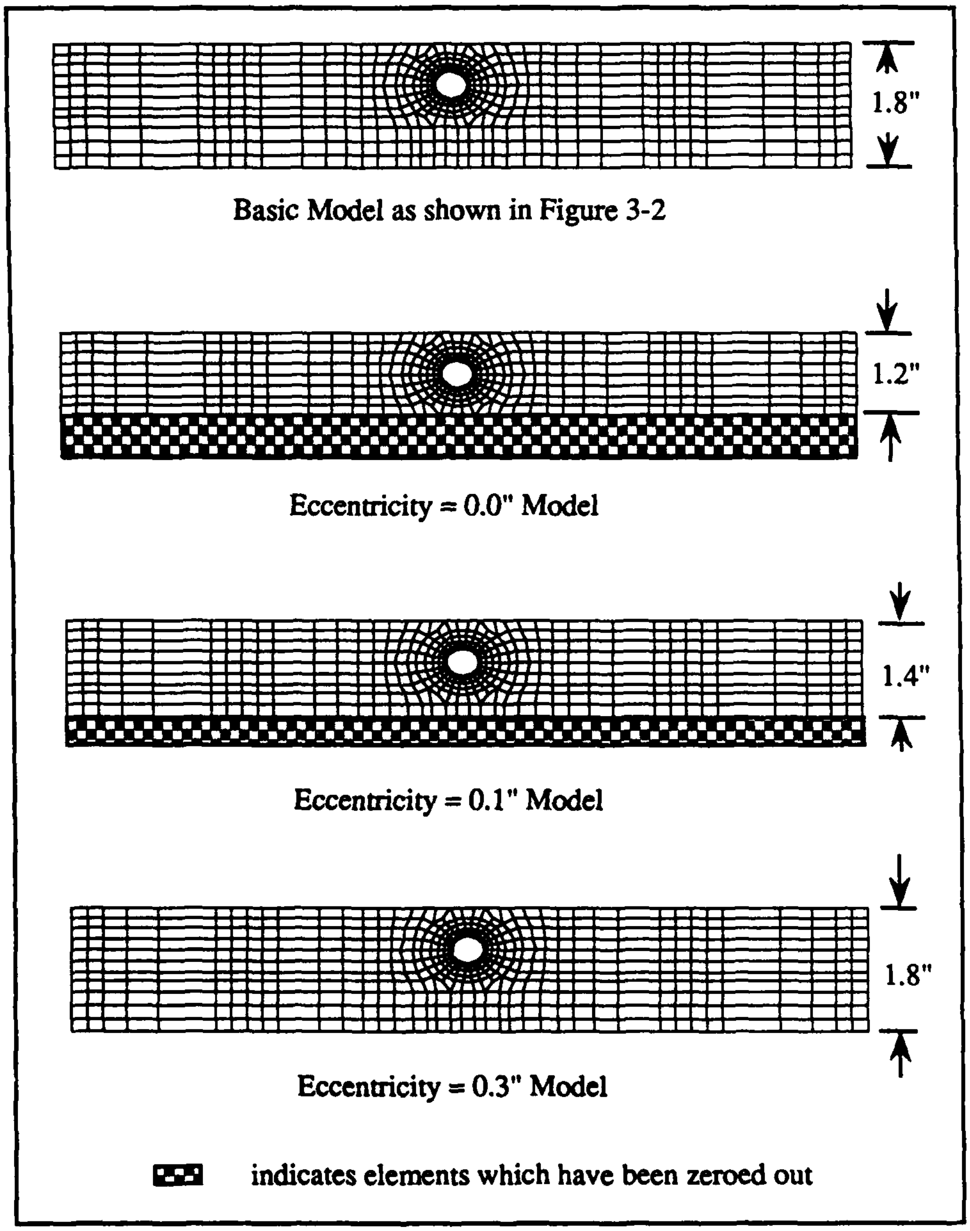

Figure 3-3. Finite Element Models (no tabs)

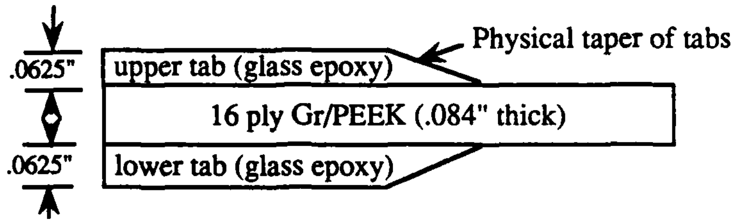

Figure 3-4 A. Cross-Sectional View of Specimen (left end)

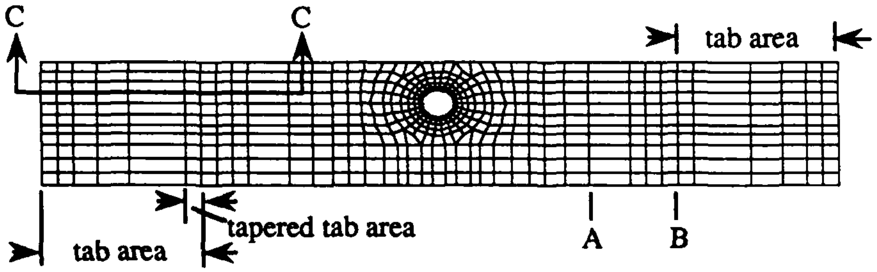

Figure 3-4 B. Finite Element Model

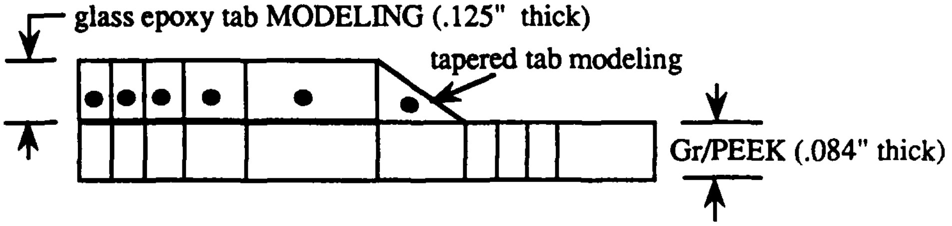

Figure 3-4 C. Section CC

● indicates elements added to finite element model to account for the glass epoxy tabs; the thickness of these elements is the sum of the upper and lower tab thicknesses.

Figure 3-4. Tab Area Modeling

(3) Modeling of Through the Thickness Ply Orientations.

Since four different ply lay-ups (stacking sequences) were considered in this study, it was necessary to model the various ply orientations through the thickness of the laminates. This was a simple task for both the $[0^o{}_{16}]$ and $[90^o{}_{16}]$ laminates. As shown in Figure 3-5, both of these laminates were modeled as one through the thickness element. For the $[\pm45^o]_{4S}$ laminates, the laminate was modeled as two through the thickness elements as shown in Figure 3-5. Finally, the $[0^o/\pm45^o/90^o]_{2S}$ laminates (quasi isotropic) were modeled as four through the thickness elements as shown in Figure 3-5.

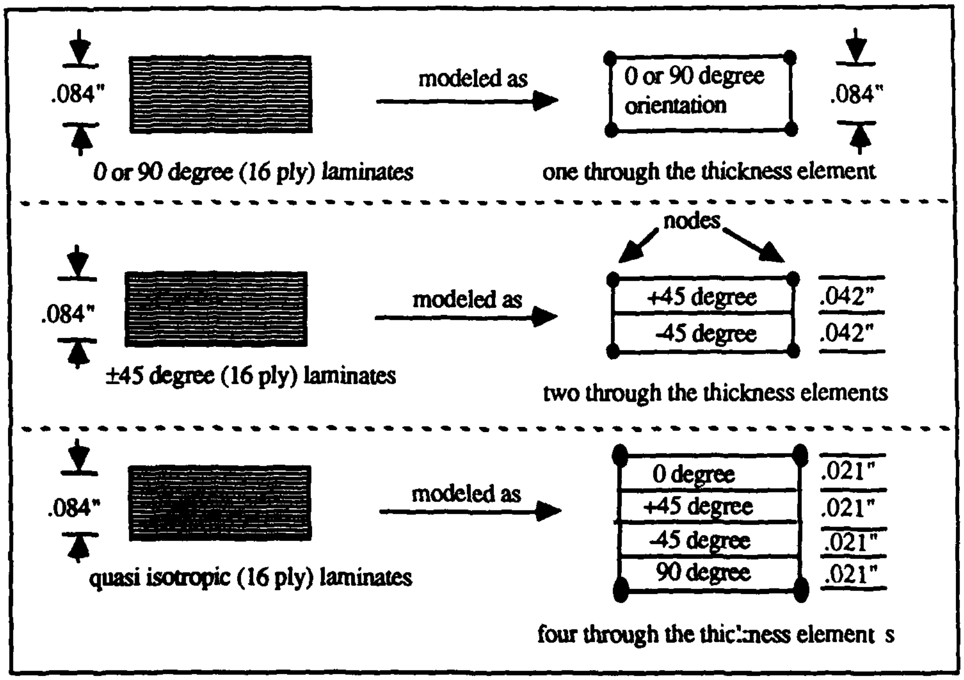

Figure 3-5. Through the Thickness Finite Element Modeling

Since through the thickness finite elements share the same four nodes (see Section II B, also Figure 3-5), the finite element models for the four stacking sequences each contained 682 nodes. However, since the four stacking sequences required a different number of elements through the thickness of the laminate (Figure 3-5), the total number of elements for the four stacking sequences were as follows:

$[0^{o}{}_{16}]$ ----------- 831 elements
$[90^{o}{}_{16}]$ ----------- 831 elements
$[\pm 45^{o}]_{4s}$ ----------- 1142 elements
$[0^{o}/\pm 45^{o}/90^{o}]_{2s}$ ---------- 2664 elements

In order to facilitate the entry of required input data, a FORTRAN program was written to take the finite element model developed for the $[0^{o}{}_{16}]$ laminates and make the modifications necessary to develop the models for the $[\pm 45^{o}]_{4s}$ and $[0^{o}/\pm 45^{o}/90^{o}]_{2s}$ laminates.

(4) Modeling of the Mounting Fixture.

The last complication to the finite element model was the use of a mounting fixture. Photographs of this fixture as well as a detailed explanation of the fixture are provided in Section IV D. As shown in Figure 3-6 (also in more detail in Figure 4-8), the fixture utilized steel blocks to rigidly secure the specimens during testing. These steel blocks were allowed to rotate (in-plane) through the use of bearings (see Figures 3-6 and 4-8).

Since the steel blocks shown in Figure 3-6 were allowed to rotate (in-plane) with the specimen, the tab area of the finite element model was modified to include the steel blocks. This was accomplished by using the equivalent material properties for a combination of the glass epoxy tabs and the steel blocks (see Figure 3-7). These equivalent material properties were obtained by using the Program SQ5 [18].

Therefore as shown in Figure 3-7, the steel blocks of the mounting fixture and the glass epoxy tabs (non-tapered portion) were combined to form one through the thickness finite element with the equivalent material properties of steel and glass epoxy.

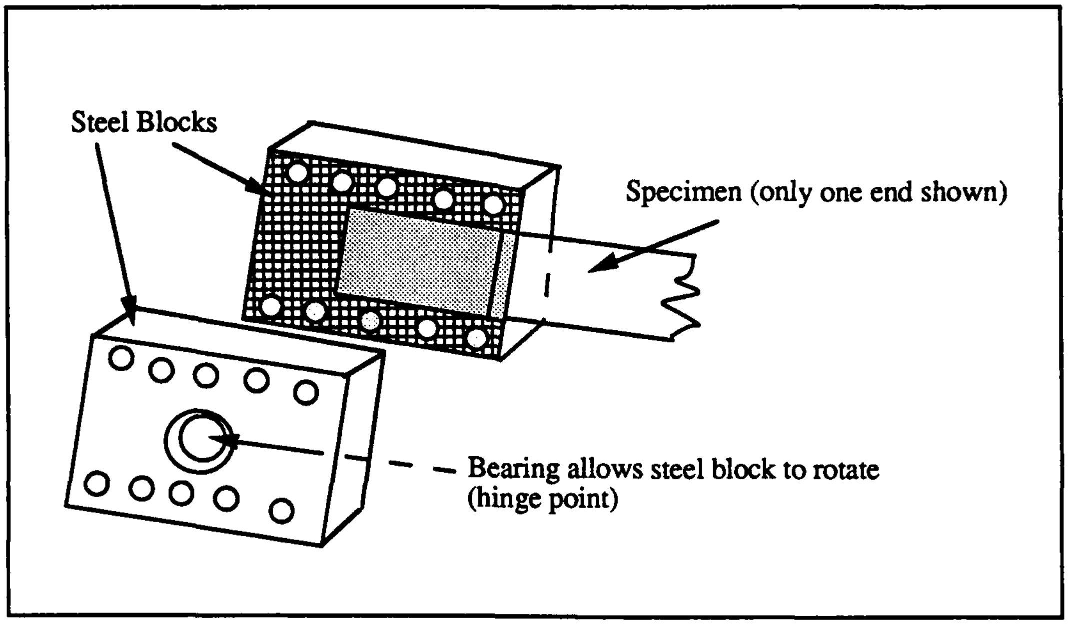

Figure 3-6. Specimen Mounting (Fixture)

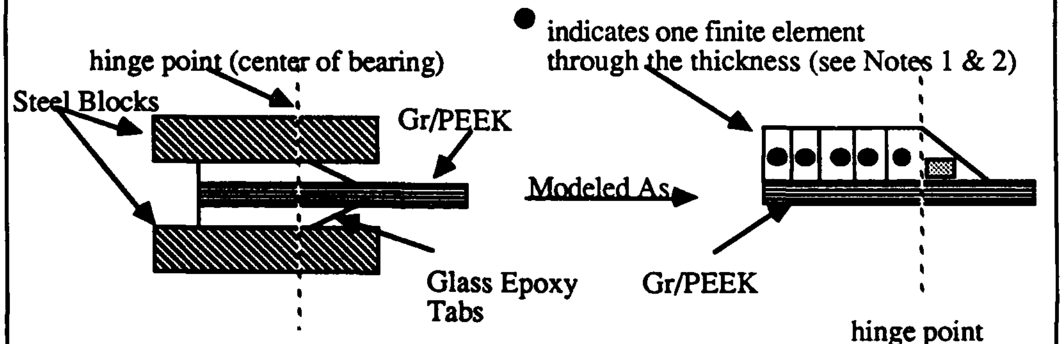

Top View of Figure 3-6

1. This element has a thickness equal to the combined thicknesses of the steel blocks AND the glass epoxy tabs.
2. The equivalent material properties for this element were obtained through the use of the Program SQ5 [18].

▨ indicates tapered element (glass epoxy properties)

Figure 3-7. Mounting Fixture Modeling

The next question which must be addressed is; does the model accurately represent the specimens used during experimentation?

C. Convergence Study.

In order to verify the suitability of the finite element model, the zero eccentricity model (Figure 3-3) was used in a convergence study. The zero eccentricity model was used because a detailed convergence study was completed by [10] on a very similar model, and in addition, abundant stress intensity factor information is available for symmetric isotropic plates containing circular discontinuities [15]. Therefore, the zero eccentricity model was given isotropic properties as follows:

$$E_{11} = E_{22} = 19{,}200{,}000 \text{ psi}$$

$$\nu = .3$$

$$G_{12} = \frac{E_{11}}{2(1+\nu)} = 7{,}384{,}615 \text{ psi}$$

The isotropic model was then run using the linear finite element program (see Section II B), and the stress intensity factor (SIF) at the edge of the hole (point A, Figure 3-8 A) was found to be 3.29. Peterson [15] reports the SIF as 3.45, and Fisher [10] found the SIF to be 3.28. The goal of this convergence study was to insure that the finite element model would give a SIF within 5% of published values for the theoretical value of the SIF. A comparison of the SIF obtained from this model and the SIF reported by Peterson [15], showed a percent error of 4.6%. From this comparison of SIFs, and from the mesh refinement studies completed by [10], the mesh refinement of the finite element model was found to be satisfactory.

D. Boundary Conditions.

Once the finite element models had been developed (Section III B), the appropriate boundary conditions were required to complete the modeling process. Since a mounting fixture (Section III B(4)) was used in this study, two sets of boundary conditions were required. First, boundary conditions were developed for models which did not allow in-plane rotation. And secondly, a set of boundary conditions were developed for the models which allowed in-plane rotation.

(1) Boundary Conditions (No Mounting Fixture).

As shown in Figure 3-8 A, boundary conditions were developed for the models which did not allow in-plane rotation. These boundary conditions were as follows:

a). Nodes located along the line x=3.8" were given prescribed displacements of zero in both the x and y-directions.

b). Nodes located along the line x=10.2" were given a prescribed displacement in the x-direction, and a zero displacement in the y-direction.

c). All other nodes in the model were free to displace in both the x and y-directions.

These boundary conditions were developed to simulate the actual boundary conditions present during experimentation without the mounting fixture. These boundary conditions resulted from specimen mounting in the grips of the Instron Test Machine (Section IV C, Figure 4-6). It is important to note that prescribed displacements were not given to nodes which surrounded "zeroed out" elements (see Section III B(1)).

(2) Boundary Conditions (Mounting Fixture).

As shown in Figure 3-8 B, boundary conditions were developed for models which allowed in-plane rotation. These boundary conditions were as follows:

a). The node (node I) located at the geometric centerline of the model, and at x=3.8", was given prescribed displacements of zero in both the x and y-directions.

b). The node (node J) located at the geometric centerline of the model, and at x= 10.2", was given a prescribed displacement in the x-direction, and a zero displacement in the y-direction.

c). All other nodes in the model were free to displace in both the x and y-directions.

These boundary conditions were developed to simulate the actual boundary conditions present during experimentation with the mounting fixture. Since in-plane rotation of the

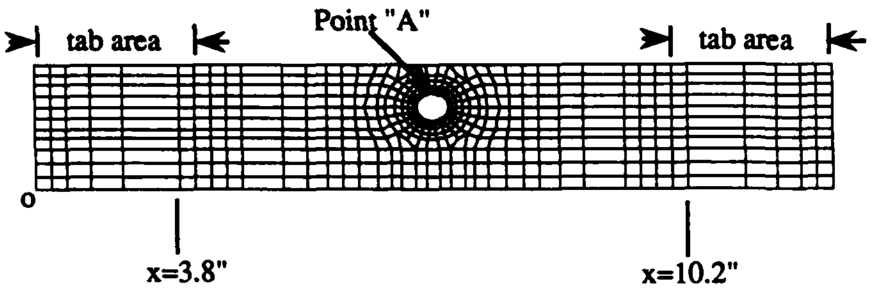

Figure 3-8 A. Boundary Conditions (no mounting fixture)

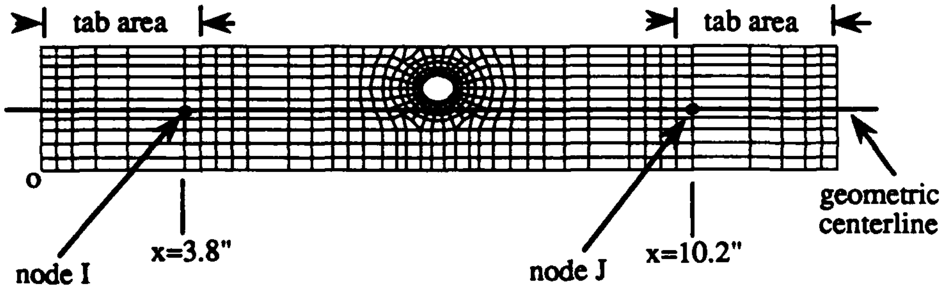

Figure 3-8 B. Boundary Conditions (mounting fixture)

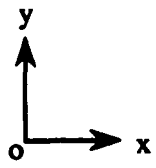

Point "o" is the origin of the coordinate system.

Figure 3-8. Boundary Conditions (Modeling) specimen was allowed, only two nodes (nodes I and J, Figure 3-8 B) were given prescribed displacements. Therefore, in-plane rotation was allowed about axes (normal to the plane of Figure 3-8 B) through nodes I and J. For a detailed explanation of the mounting fixture, as well as photographs, refer to Section IV D. It is important to note that as the specimen widths changed (Figure 3-1), the y-location of the geometric centerline also changed.

E. Eccentricity/Boundary Condition/Gage Length - - Effects (Linear Analysis).

As previously discussed, the linear analysis involved more than just the development of a suitable finite element model. An extensive linear study was completed before starting the nonlinear finite element analysis (Section III F). This study was undertaken to gain insight into eccentricity, boundary condition, and gage length effects. As outlined below, this section discusses the results from the linear analysis.

(1) Contour Plotting
(2) Graphs (Stress States)
    a) Near Field/Far Field Stress States
    b) Uniformity of Far Field Axial Stress (gage length effects)

(1) Contour Plotting.

To study the effects of both the eccentric circular discontinuity and the mounting fixture on the overall stress states of the Gr/PEEK laminates, contours were plotted. The output strain data obtained from the linear finite element program was used to plot contours for the specimens tested experimentally (see Tables 4-1 through 4-4). These contour plots (Appendix B) are grouped according to the stacking sequence of the laminate, and also by the boundary conditions used with the finite element models (see Section III D). In order to discuss the results from this study, the contour plots for the $[90^{o}_{16}]$ laminates have been taken from Appendix B and are shown in Figures 3-9 and 3-10. The terms "hinge" and "no hinge" in these figures indicates that in-plane rotation (analytically) was or was not allowed, respectively (see Section III D).

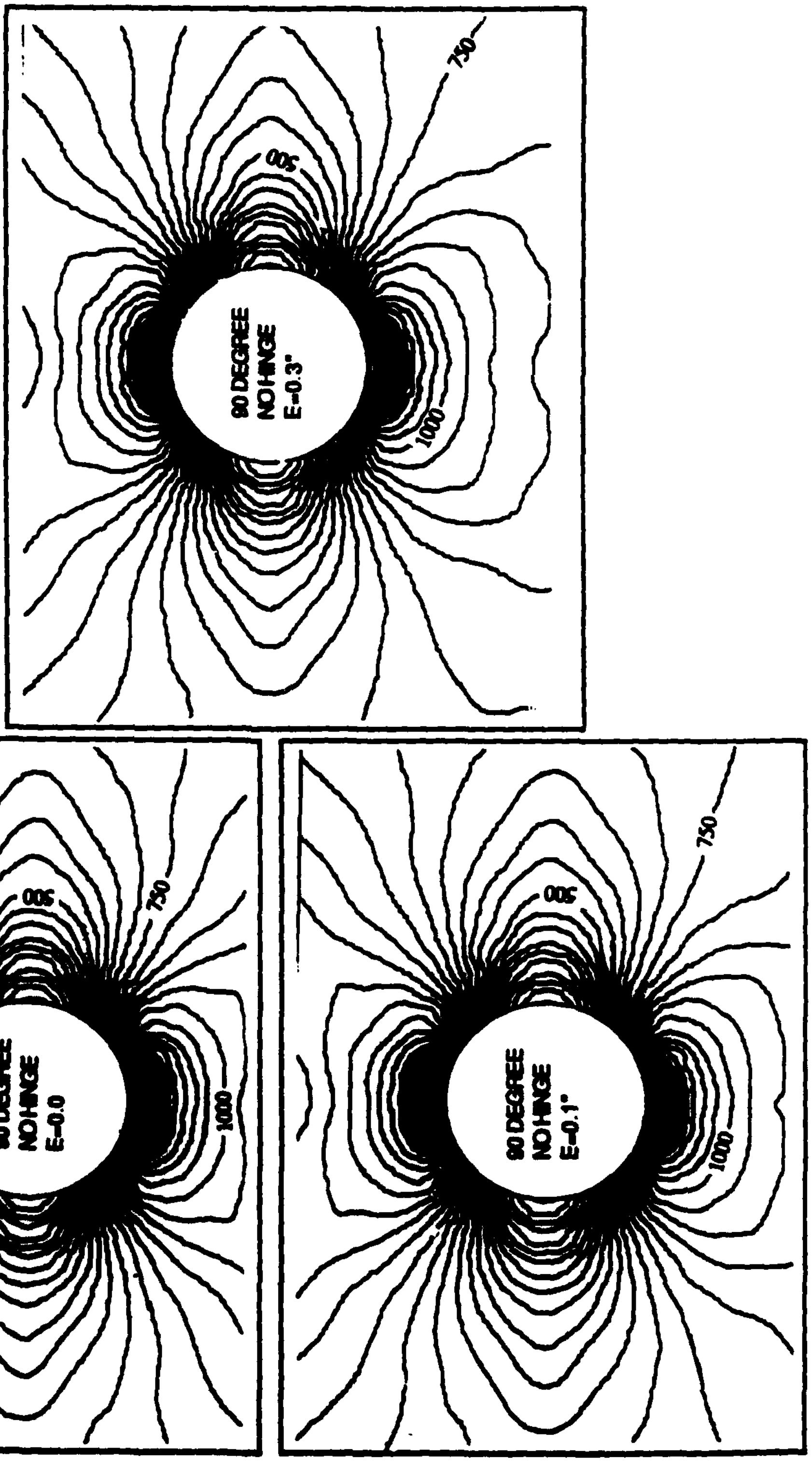

Figure 3-9. Contour Plots (90 degree lay-up / no mounting fixture)

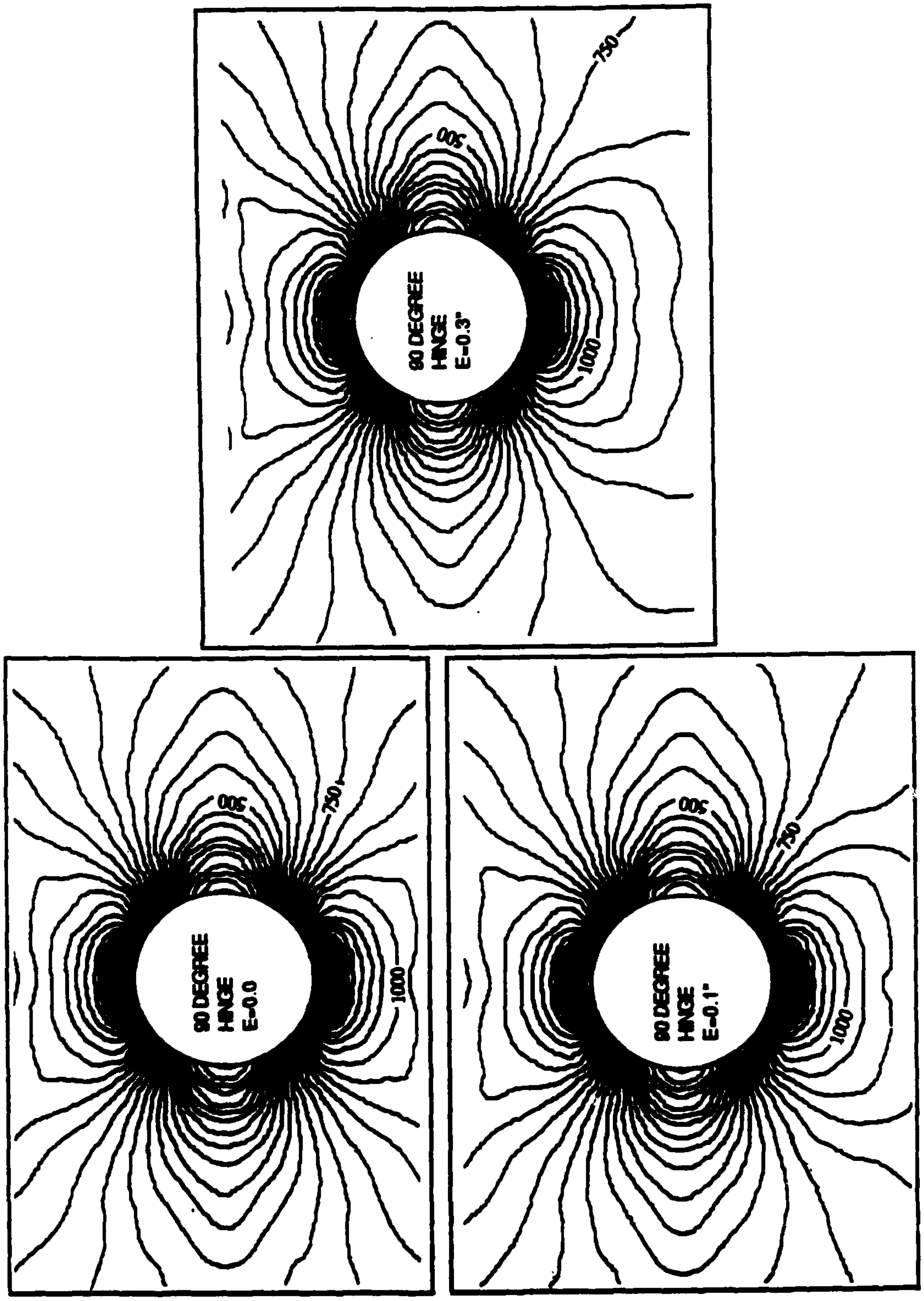

Figure 3-10. Contour Plots (90 degree lay-up / mounting fixture)

Close inspection of Figures 3-9 and 3-10 provide important information. First, note that the contours are not symmetric for the nonsymmetric models (eccentricity ≠ 0.0"). The contours show higher levels of strain above the discontinuity compared with the levels of strain (at an equal distance) below the discontinuity. This verified an early assumption that the eccentric circular discontinuity would create a centroid (area) shift, and therefore the tensile loading (from the Instron) would produce a bending moment (see Figure 3-11). This bending moment (Figure 3-11), produced a positive (tensile) stress above the discontinuity and a negative (compressive) stress below the discontinuity. The stresses from the bending moment, combined with the tensile loading from the Instron, produced higher strains (for the nonsymmetric models) above the discontinuity. Secondly, no apparent differences were noted between Figures 3-9 and 3-10. Even if Figures 3-9 and 3-10 were placed on top of each other (overlaid), only very slight differences between the contours were noted. This is significant because Figure 3-9 shows contours for finite element models which do not allow in-plane rotation; while Figure 3-10 shows contours

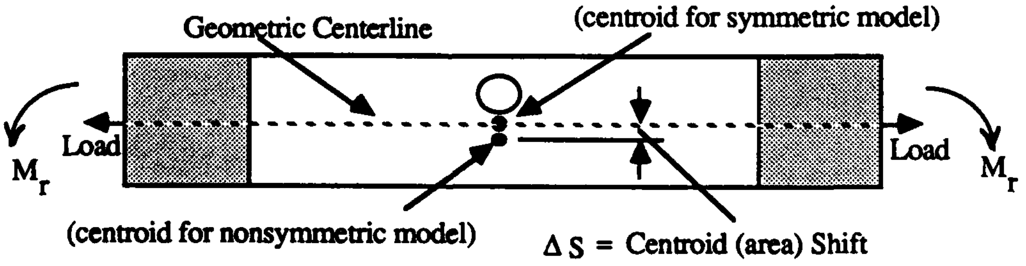

The eccentric circular discontinuity causes a centroid (area) shift. Therefore, the applied load (from the Instron) creates a bending moment (M_r).

$$\boxed{M_r = \Delta S \text{ X } \text{Load}}$$

Figure 3-11. Centroid Shift and Resulting Bending Moment for finite element models in which in-plane rotation is allowed (see Section III D). Therefore, the use of the mounting fixture (see Section IV D), which allowed in-plane rotation, did not appreciably affect the stress state near the discontinuity.

Finally, contours were also plotted to verify the validity of the output data obtained from the linear finite element program. These contours are compared to experimentally obtained photographs of the photoelastic stress states of the Gr/PEEK laminates tested (see Section V A). Since experimentation was conducted for this comparison, a discussion of the results of this study are discussed in Section V A.

(2) Graphs (Stress States).

a) Near Field/Far Field Stress States.

In addition to contour plots, graphs of both near field (Figure 3-12) and far field (Figure 3-13) stress states were constructed from the output strain data. These graphs were constructed to study boundary condition and eccentricity effects on both the near field and far field stress states. Strains were used for these graphs instead of stresses because strains were continuous through the thickness of the laminates (see Section II B). These graphs (Appendix C) are grouped according to the stacking sequence of the laminate, and also by the boundary conditions used with the finite element models (see Section III D). In order to discuss the results from this study, the graphs for the $[90^{o}_{16}]$ laminates have been taken from Appendix C, and are shown in Figures 3-14 and 3-15.

Inspection of Figures 3-14 and 3-15 provide important information. First, Figure 3-14 shows the near field axial strains for the $[90^{o}_{16}]$ laminates. Note that the strains (for the nonsymmetric models) are not symmetric, with the strain above the discontinuity being higher than the strain (at an equal distance) below the discontinuity. This can be attributed to the bending moment (Figure 3-11) discussed in Section III E (1). Also, note that there is

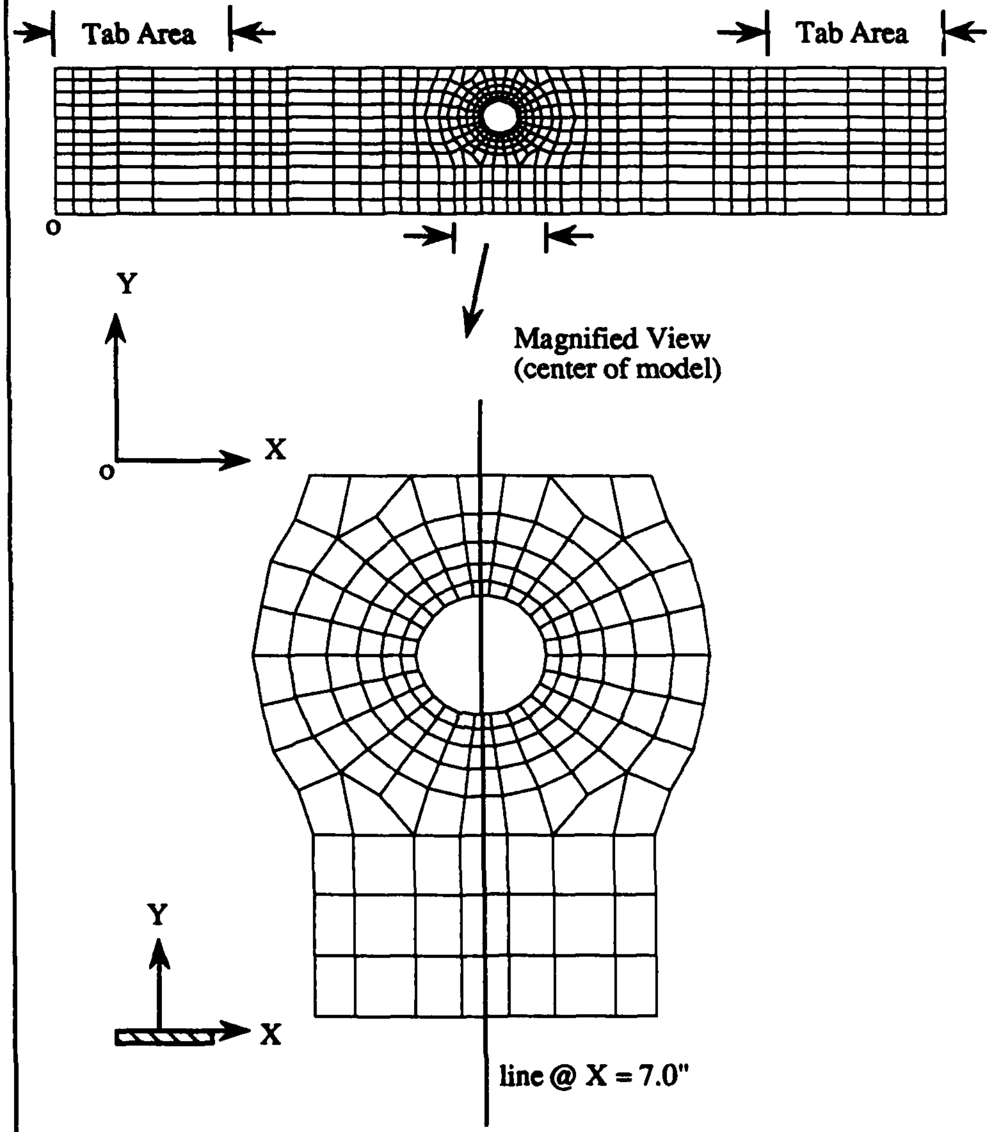

Figure 3-14 was plotted from data obtained along the line X=7.0".

Figure 3-12. Near Field Location for Figure 3-14

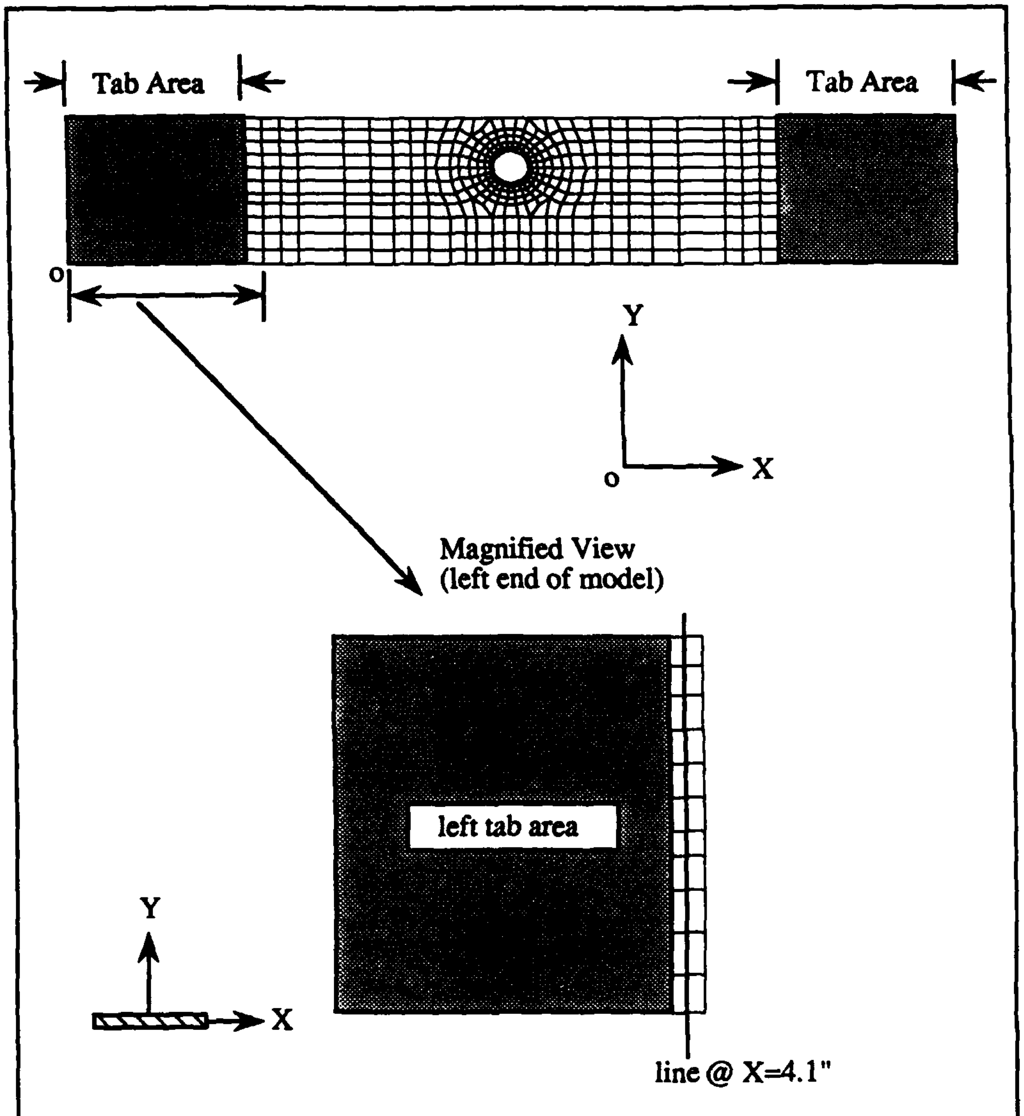

Figure 3-15 was plotted from data obtained along the line X=4.1"

Figure 3-13. Far Field Location for Figure 3-15

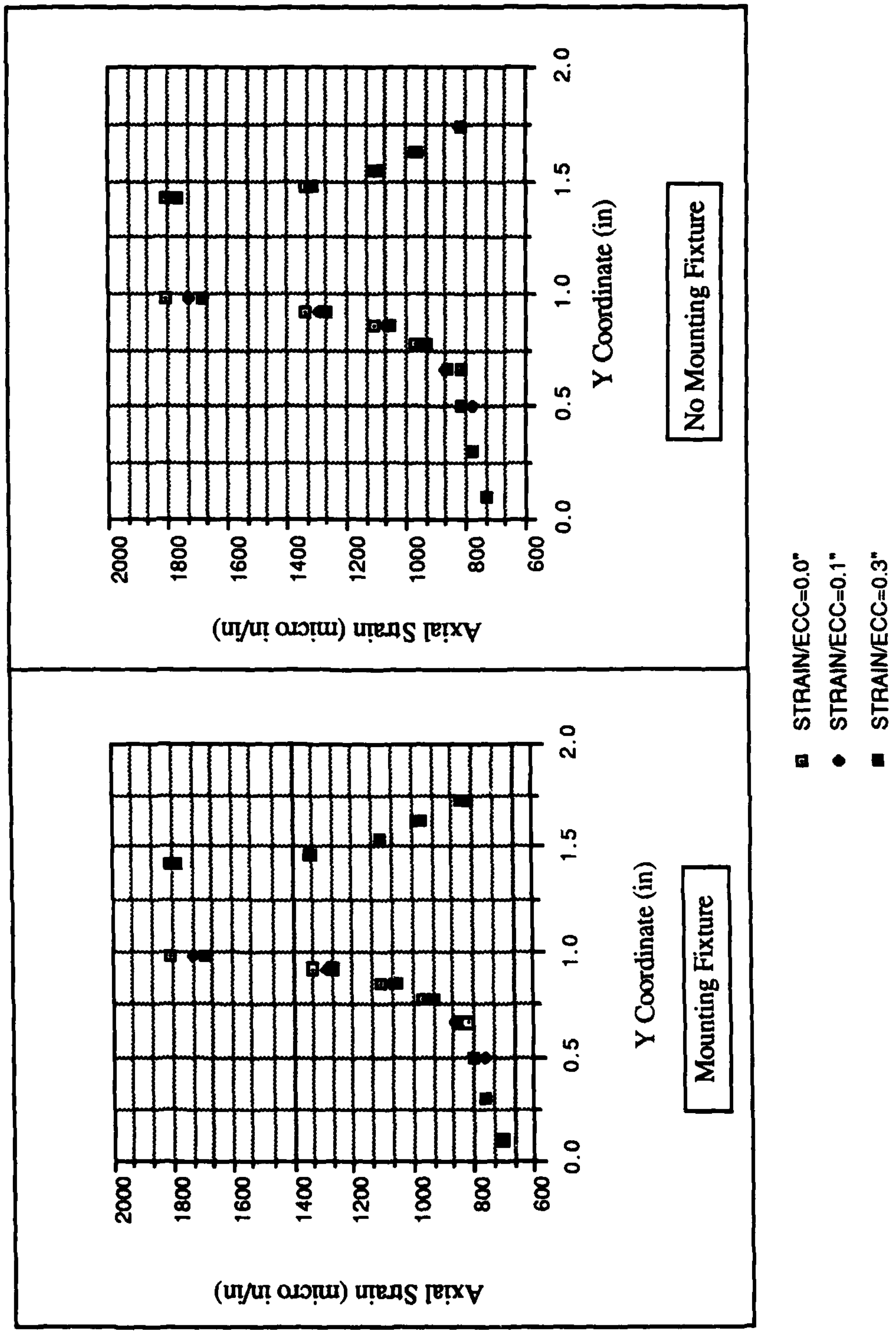

Figure 3-14. Near Field Axial Strain Plots (90 degree lay-up)

no apparent difference between the graphs (Figure 3-14) showing data with and without the mounting fixture. This again suggests that the use of the mounting fixture (Section IV D) did not affect the stress state near the discontinuity. Finally, Figure 3-15 shows the far field axial strains for the [90°_{16}] laminates. These graphs (Figure 3-15) show that the variations in far field axial strains were reduced by the use of mounting fixture. However, as already noted in Figure 3-14, *this reduction in the variations of the far field axial strains did not affect the state of stress near the discontinuity*. Therefore, although the use of the mounting fixture caused a more uniform state of far field stress, the linear analysis predicted that the near field stress state would not be affected by the use of the mounting fixture.

b) Uniformity of Far Field Axial Stress (gage length effects).

References [10,13] had assumed, in their studies of Gr/PEEK, that a uniform state of stress existed far field (see Figure 3-13). Therefore, a study was conducted to determine if in fact a uniform state of stress existed far field. Since the effects of the discontinuity would be reduced at the far field location as the gage length (length between the tabs) of the specimens was increased, a model with a 12" gage length was developed (Figure 3-16). With this model, the variation in axial stress (for a constant value of x) was studied (see Figure 3-16).

Figure 3-17 shows the results from this study. Note that the far field axial stress is uniform at x=0" (see Figure 3-17). This corresponds to a gage length of 12" as shown in Figure 3-16. As the discontinuity was approached (x increased, Figure 3-16) the variations of axial stress became larger (Figure 3-17). Therefore, a 12" gage length would be required to insure that a uniform state of far field stress exists. This was a problem because the Gr/PEEK panels available for this thesis were only large enough to fabricate specimens with 6" gage lengths (same size as used by [10,13]). Therefore, since failure

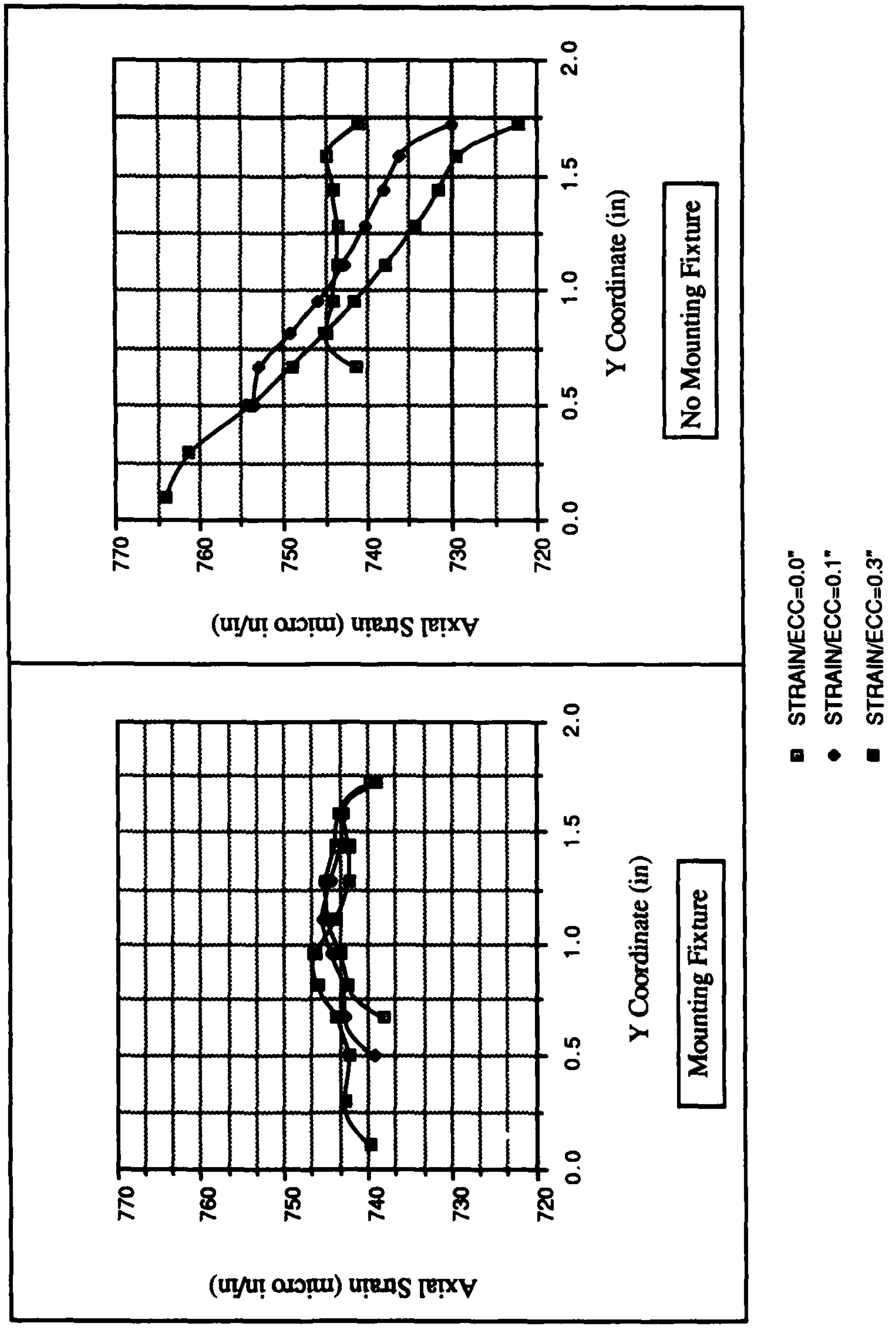

Figure 3-15. Far Field Axial Strain Plots (90 degree lay-up)

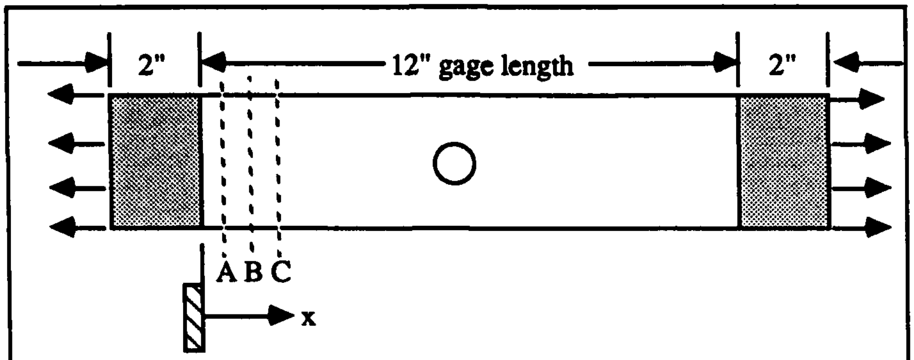

Note. This model was used to generate the data shown in Figure 3-17. The variations in axial stress along x=constant lines (such as A, B, and C) are plotted in Figure 3-17.

Figure 3-16. 12" Gage Length Model

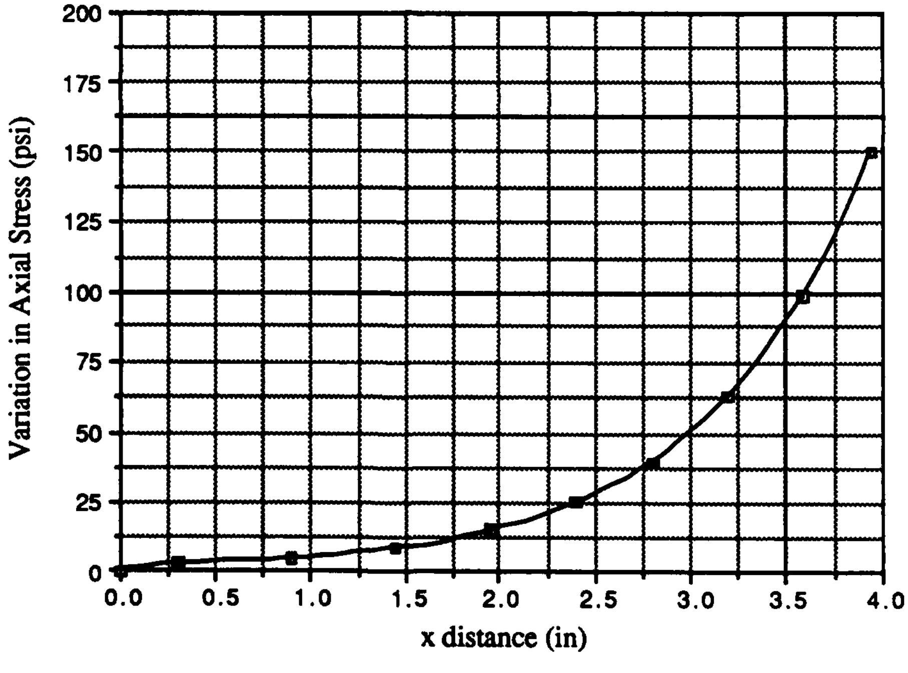

See Figure 3-16 for the meaning of "x distance"

Figure 3-17. Variation of Axial Stress versus Distance would initiate at the discontinuity, a study was conducted to see if gage length effects would affect the stress intensity factor (SIF) at the discontinuity.

To see if the SIF at the discontinuity would be affected by the gage length, three different models were constructed (see Figure 3-18). These models had gage lengths of 12", 10", and 6". Linear computer runs were made for these models, and the SIFs at the discontinuity (point A, Figure 3-18) were calculated. For all three models, the SIFs (at point A) were found to be equal to three significant digits (SIF=3.29). Therefore, the gage lengths did not affect the state of stress near the discontinuity. As a result, a 6" gage length was also used for this thesis.

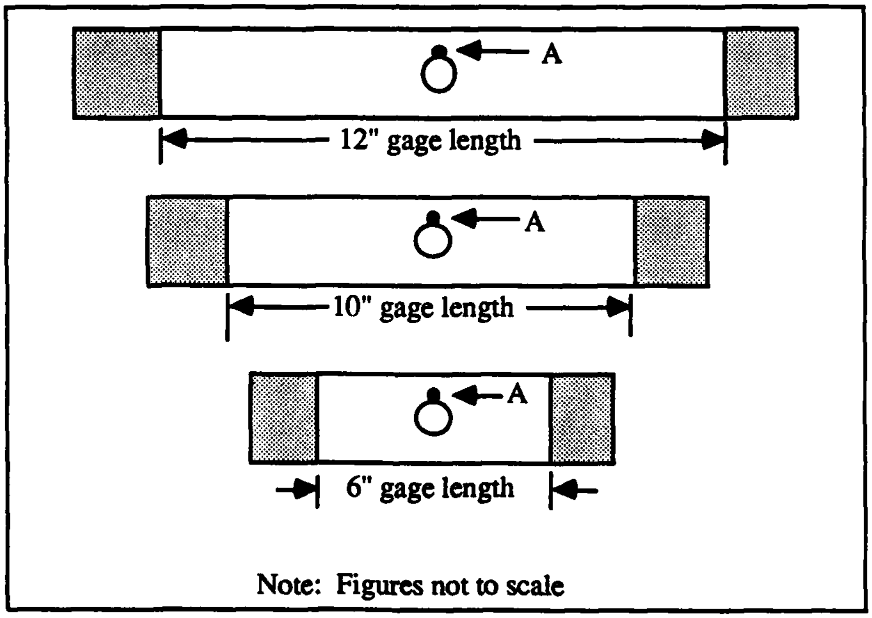

Figure 3-18. Three Different Gage Length Models

F. Nonlinear Analysis.

As previously mentioned, Gr/PEEK exhibits nonlinear stress-strain behavior (see Appendix A). Therefore, to accurately study Gr/PEEK laminates, a nonlinear analysis was required. The nonlinear material finite element program used for this thesis (discussed in Section II C) requires the use of efficient computer resources.

To make a nonlinear run, a batch file was used to route the program, and the required input files, from a CYBER mainframe computer to a CRAY mainframe computer. The program was then executed on the CRAY. Past experience with this nonlinear program [10,13] has shown that it is actually less expensive to execute the program on the CRAY than it is on the CYBER. Although the CRAY performed the executions at a higher expense per second than the CYBER, the execution time was significantly faster, thus saving on the overall expense of the analysis [13].

Once a nonlinear run had been completed by the CRAY, the batch file then routed the output files back to the CYBER. These output files are discussed in Appendix D.

In order to verify the nonlinear finite element analysis, experimentation was conducted. The following Section (Section IV) outlines the details of the experimental portion of this study.

IV. Experimentation

The purpose of the experimental portion of this study was to determine the ultimate strength, failure modes, and stress-strain response of Gr/PEEK laminates containing an eccentrically located, 0.4 in diameter circular discontinuity. Two sets of experiments were conducted. In one set, the purpose was to verify the predictions of the nonlinear finite element analysis. The other set of experiments was conducted to verify the validity of the analytic stress state predictions of the linear finite element program. The laminates tested experimentally consisted of four different ply lay-ups as follows: $[0^{\circ}{}_{16}]$, $[90^{\circ}{}_{16}]$, $[\pm 45^{\circ}]_{4s}$, and $[0^{\circ}/\pm 45^{\circ}/90^{\circ}]_{2s}$.

Experimentation was conducted at the Structures Division of the Flight Dynamics Laboratory (Wright-Patterson AFB, Ohio). A total of fifty-two specimens were fabricated. Forty-eight of these specimens were instrumented with strain gages while the remaining four were used for photoelastic testing. All testing was accomplished at room temperature using a 20-kip Instron Universal Test Machine (referred to as an "Instron").

The specific objectives, of the experimental portion of this study, were as follows:

(1) Determine the ultimate strength, the "gross" failure modes, stress-strain response, and the boundary condition effects of Gr/PEEK laminates containing a 0.4 in diameter (eccentrically located) circular discontinuity.

(2) Determine the overall stress state of Gr/PEEK laminates, containing a 0.4 in diameter circular discontinuity, through photoelastic techniques.

A. Specimen Description.

The specimens used in this study were fabricated from panels of Gr/PEEK supplied by the Fiberite Corporation of Great Britain. These panels consisted of four different ply lay-ups (previously mentioned) of APC-2 with Hercules AS4 graphite fibers contained in a Victrex® PEEK matrix. Fiber content was guaranteed by the manufacturer to be 61% by volume and 68% by weight.

All panels were subjected to a C-scan evaluation by [10] to insure that they were free of significant defects. The C-scan testing was conducted by the Non-Destructive Branch of the Materials Laboratory (Wright-Patterson AFB, Ohio).

From the panels of Gr/PEEK, fifty-two specimens were fabricated. Tabs were bonded to these specimens as shown in Figure 4-1. The tabs were constructed from G-10 glass epoxy [$0^o/90^o$], and allowed for a uniform transfer of load from the Instron to the Gr/PEEK specimens. In addition, the tabs provided a contact area, for the knurled mounting grips of the Instron, to secure the specimens; this contact area prevented damage to the specimens.

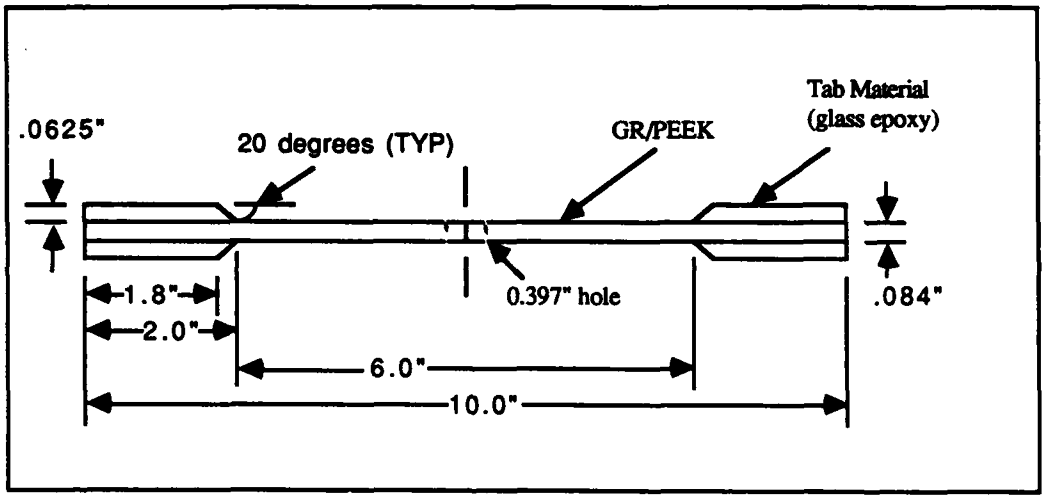

Figure 4-1. Specimen Dimensions

The values of eccentricity used for this study (see Figure 4-2), were chosen for two different reasons. First, it was imperitive that the ultimate strength of the specimens did not exceed the load capacity of the Instron. And secondly, the grips utilized by the Instron required specimens with widths less than two inches. From Figure 4-2, it is obvious that three different width specimens were tested, with the width of the specimen determining the value of eccentricity.

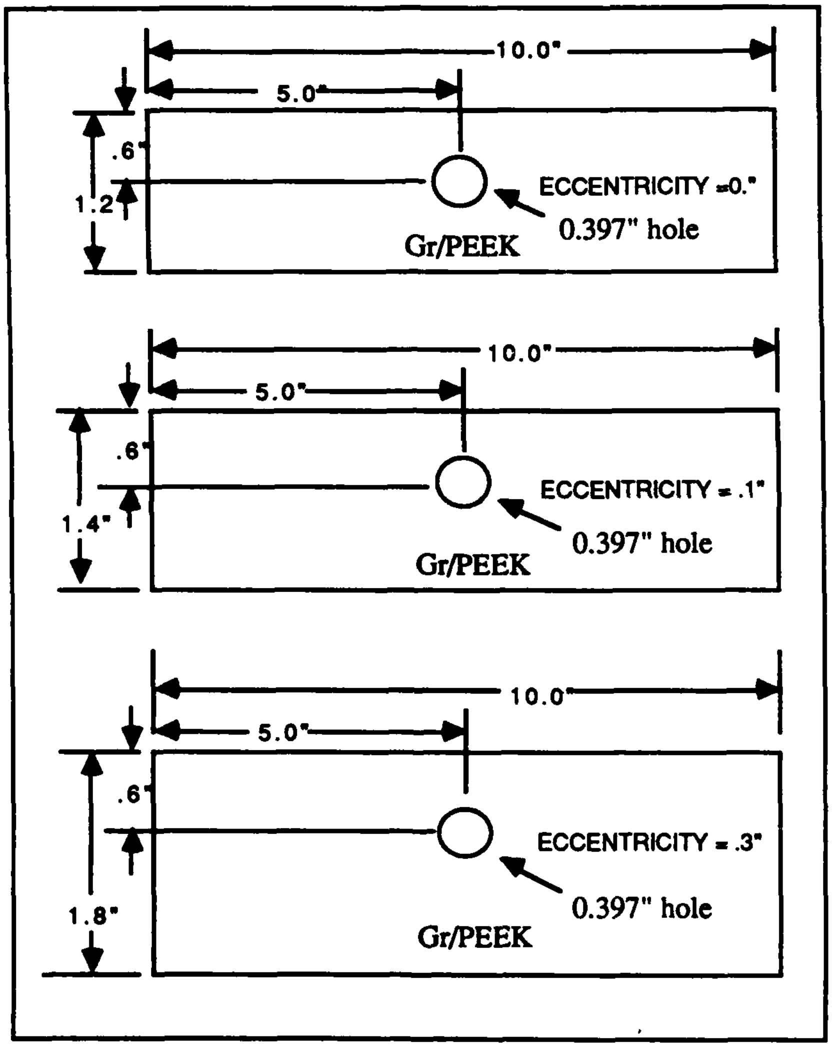

Figure 4-2. Specimen Widths (eccentricity)

B. Specimen Instrumentation.

As previously mentioned, forty-eight specimens were instrumented with strain gages. These gages were bonded to the specimens as shown in Figure 4-3.

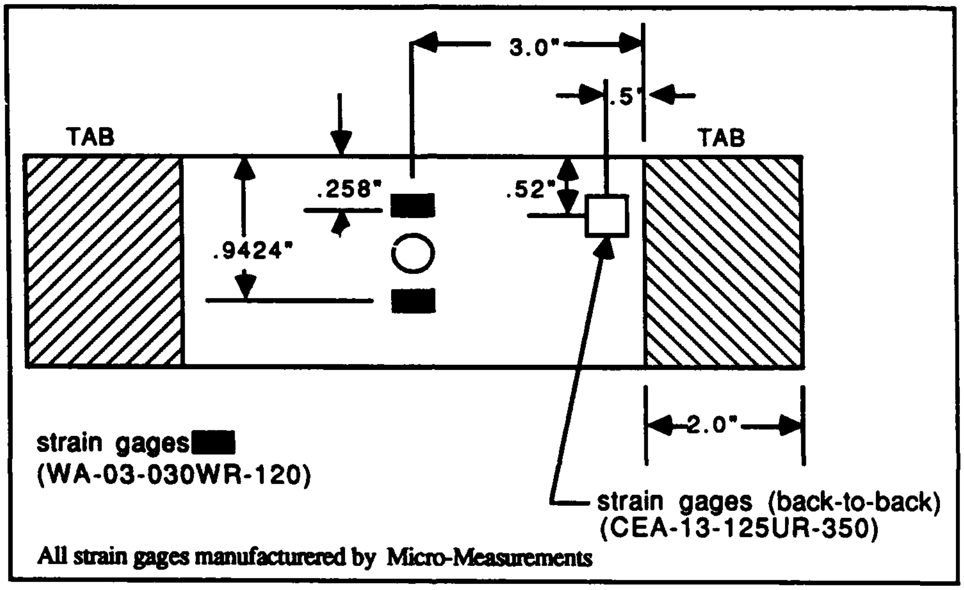

All strain gages manufacturered by Micro-Measurements

Figure 4-3. Strain Gage Locations

The two gages located adjacent to the discontinuity were referred to as "near field" gages, while the two gages located near the tab area were referred to as "far field" gages. The location of the four strain gages with respect to the finite element model are shown in Figure 4-4. As shown in Figure 4-4, the strain gages were positioned with the center of each gage located on the centroid of a single finite element. This placement was used because both the linear and nonlinear finite element programs give stress and strain output at the centroid of the finite elements. Therefore, no interpolation was required to compare experimental and analytical results. The far field gages were used to determine

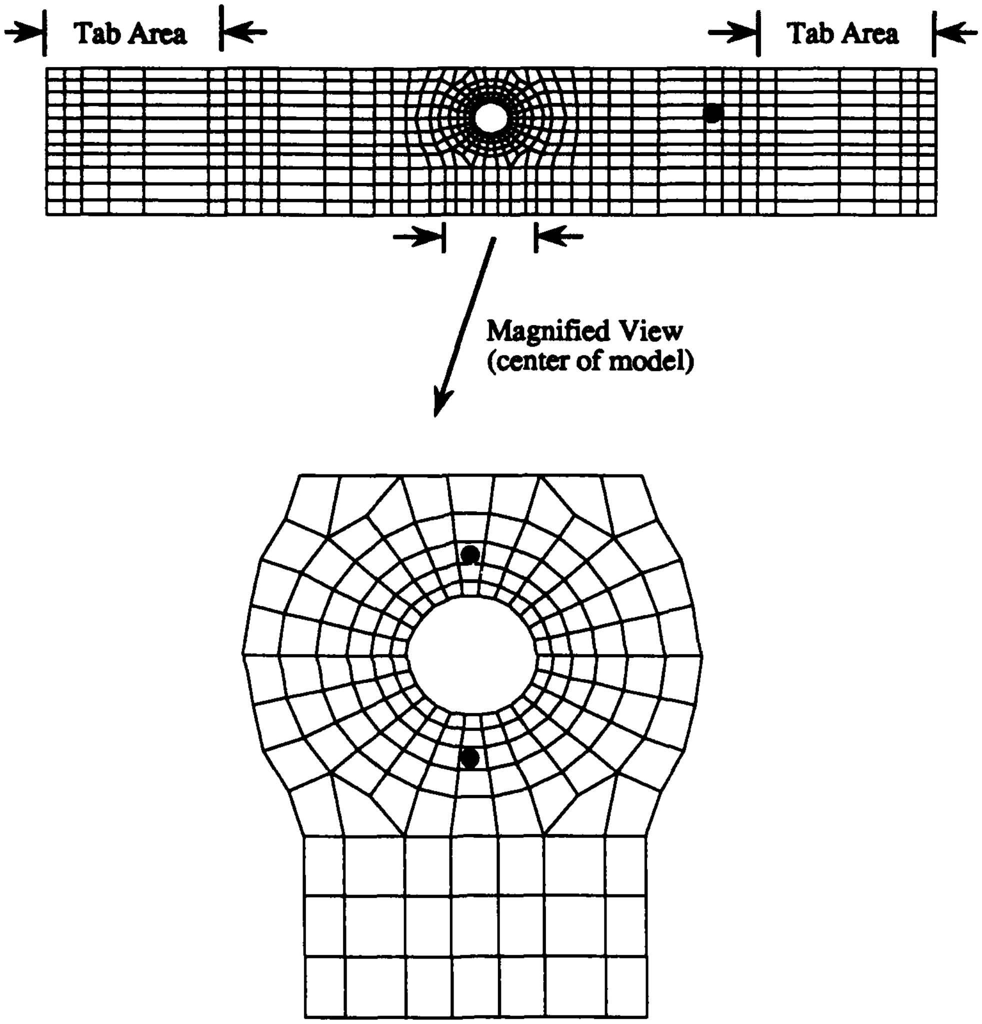

● indicates strain gage locations

NOTE: The gage near the tab area is mirrored by another strain gage on the reverse side of the specimen (see Figure 4-3).

Figure 4-4. Strain Gage Locations (Finite Element Model) the failure strain for each laminate. These far field gages were placed where the stresses in the laminate were considered uniform. The analytical study (Section III E (2)b) showed that a far field "uniform stress" state was never obtained with the six inch gage length specimens used during testing. However, the variation of far field axial stresses was found to be small (see Figure 3-17). The near field gages were placed as close to the discontinuity as physically possible, while still insuring that the center of the gages were located on the centroid of a single finite element.

All four of the strain gages were strain gage rosettes (see Figure 4-5) which have the capability to measure longitudinal, shear, and transverse strains.

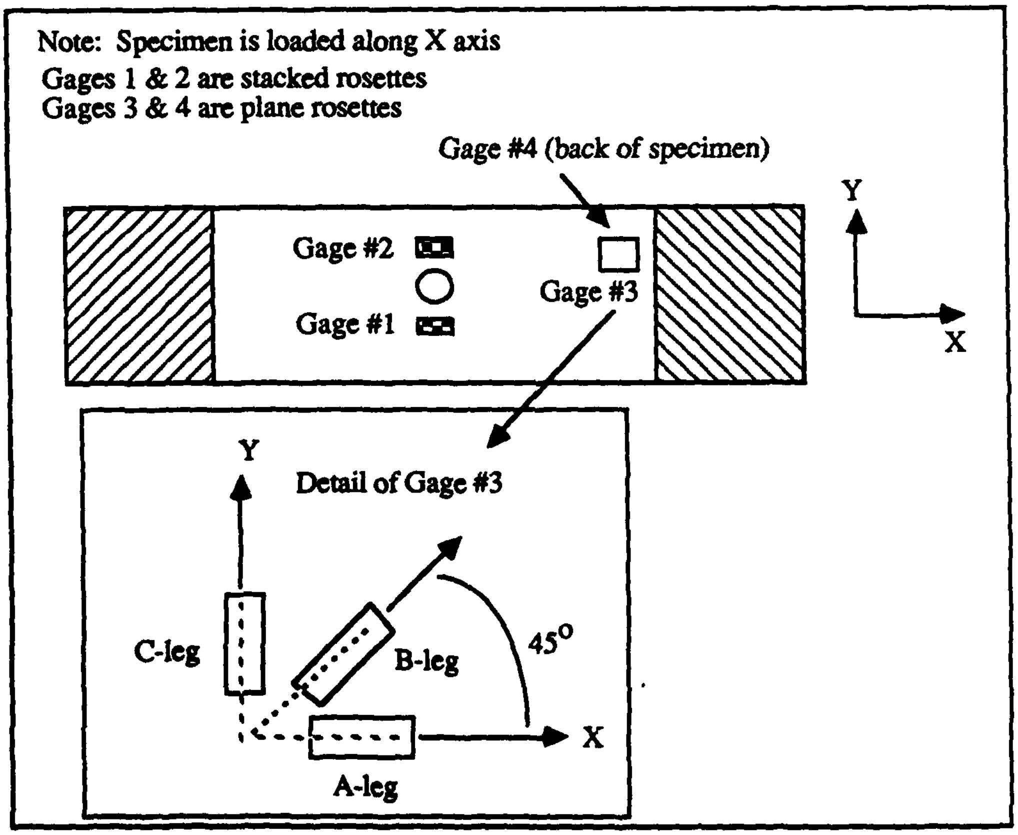

Figure 4-5. Orientation and Numbering of Strain Gage Rosettes

The far field gages were placed back-to-back (i.e. the back gage mirrored the front gage). This configuration insured that if one of the gages failed, one gage would still gather test data at the far field location. In addition, if both gages functioned properly, the far field strain could be taken as the average values obtained from both of the far field gages. This allowed for the detection of a misplaced gage or specimen misalignment in the Instron. The near field gages were not located back-to-back due to nonavailability of the strain gages during testing.

The strain gage rosettes were located so that the A-legs (see Figure 4-5) were parallel to the loading axis of the specimens. Therefore, the A-legs measured longitudinal strain, the B-legs (in conjunction with data obtained from the A and C legs) provided shear strain data, and the C-legs measured transverse strains. Each strain gage was numbered as shown in Figure 4-5. This numbering scheme was used for all of the specimens so that no confusion would result when connecting the gages to the data acquisition system.

C. Instrumented Specimen Testing.

All forty-eight instrumented specimens were tested (in tension) to their ultimate strength. The Instron (see Figure 4-6) was used to apply this tensile loading under room temperature conditions. The loading rate for all testing was a constant crosshead (see Figure 4-6) velocity of 0.05 inches per minute. The crosshead is the component of the Instron which provides the displacement loading [13]. The loading rate of 0.05 inches per minute was chosen primarily for the reason that previous testing of Gr/PEEK indicated that this rate was a "median speed between a faster impact type loading and a slower creep type loading [13]."

During testing, the load as a function of time was obtained by two methods as follows:

(1) The Instron provided strip chart information (see Figure 4-6) of load versus time through the use of permanently mounted strain gages which measured the crosshead displacement.

(2) A voltmeter (see Figure 4-6) was used to measure resistance across the load cell of the Instron. This resistance was a function of both the load setting of the Instron and the applied load. Therefore, the load at any time could be determined based upon the reading from the voltmeter.

Since all testing was recorded on video tape (see Figure 4-6), the voltmeter gave a visual indication of the applied load at any time. As shown in Figure 4-6, the voltmeter was located adjacent to the specimen. This setup was ideal for post-failure analysis since specimen failure could be easily correlated with the failure load.

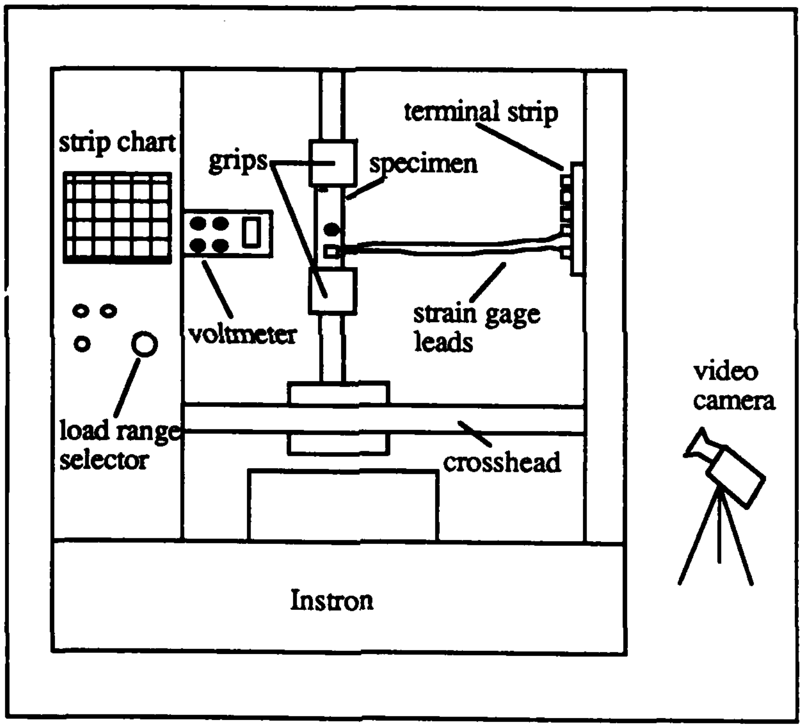

Figure 4-6. 20-kip Instron Universal Test Machine

A data acquisition system (see Figure 4-7) was required to record test data. This test data included both the applied load and the strain from each leg of the four strain gages. The load was determined by measuring the resistance across the load cell during testing.

For each leg of the strain gages, one pair of leads (wires) was connected to a terminal strip (see Figure 4-6). From the terminal strip, signals were sent to the data acquisition system. The data acquisition system consisted of a strain gage conditioner, amplifier, multiplexer, and VAX computer. The data acquisition system was controlled by a Zenith personal computer.

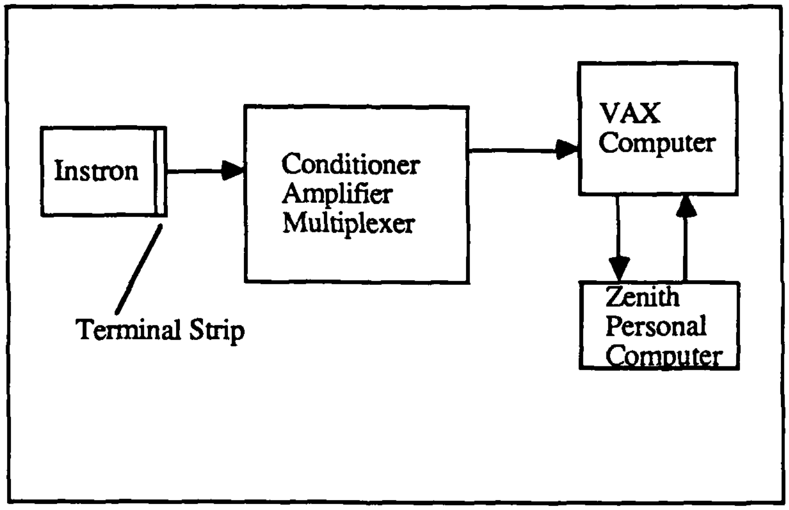

Figure 4-7. Data Acquisition System

Test data could be recorded up to three times per second. This rate was referred to as the "sampling rate." Based upon past studies of Gr/PEEK [13], a sampling rate of 2 samples per second was used for $[0^{o}_{16}]$, $[\pm 45^{o}]_{4s}$, and $[0^{o}/\pm 45^{o}/90^{o}]_{2s}$ laminates. For $[90^{o}_{16}]$ laminates, a sampling rate of 3 samples per second was used since these laminates failed at relatively low loads. By increasing the sampling rate for the $[90^{o}_{16}]$ laminates, more data was collected, and the strain at failure was more accurate.

D. Mounting Fixture.

As previously stated, one objective of the experimental portion of this study was to determine the boundary condition effects on the failure modes and ultimate strength of the Gr/PEEK specimens. Since the specimens tested in this study were not all geometrically symmetric (see Figure 4-2), in-plane bending was anticipated due to a centroid (area) shift created by the eccentrically located circular discontinuity (see Figure 3-11). To study this in-plane bending, a mounting fixture (see Figure 4-8) was fabricated. This fixture was fabricated from 4340 steel and was heat treated to 160 ksi after fabrication. The fixture design was based on a previous design by Sandhu which was used in 1985 by Cron [7].

Figure 4-8. Mounting Fixture

The mounting fixture allowed the specimens to rotate (in-plane). This rotation was possible because the specimen was mounted in steel blocks which contained bearings (Figure 4-9). The bearings were "seated" on steel pins which extended through the outer steel plates of the fixture (Figure 4-8).

The procedure used to mount test coupons in the mounting fixture was as follows:

(1) Place inner (knurled) mounting blocks in the recess of the aluminum setup template (Figure 4-9).

(2) Place specimen between the inner (knurled) mounting blocks and torque bolts to 30 ft-lbs (Figure 4-9).

(3) Place the specimen and inner mount blocks within the outer steel plates of the mounting fixture and secure the outer plates with bolts (Figure 4-8).

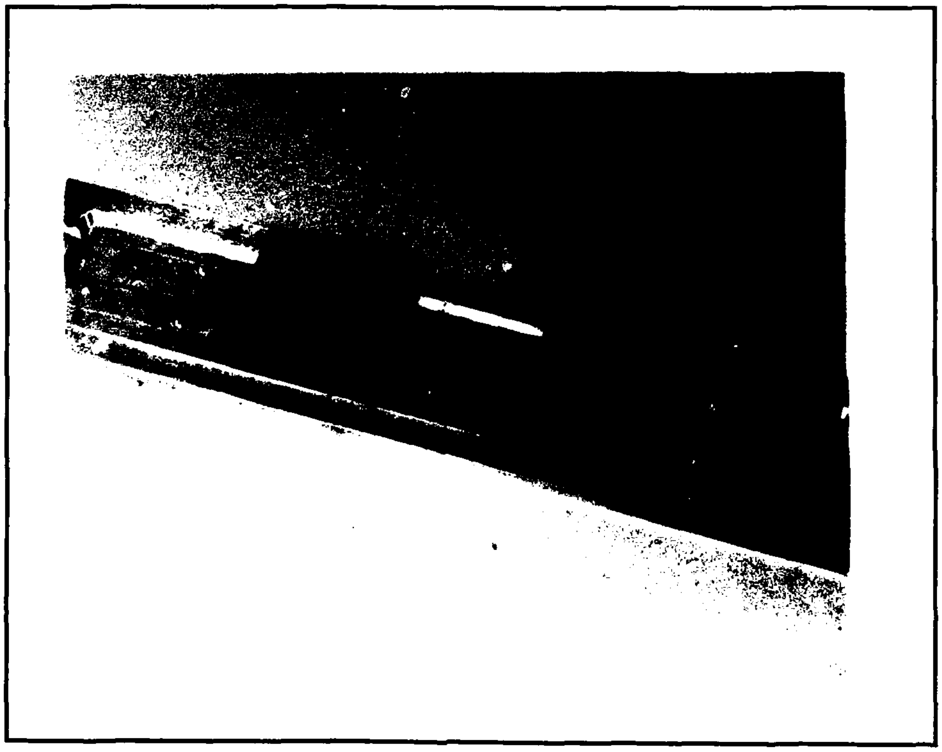

Figure 4-9. Specimen Mounting in Fixture

Once the fixture had been assembled, it was installed in the Instron by removing the grips (see Figure 4-6) and securing the fixture by two steel pins. As one might expect, the assembled fixture was heavy and cumbersome. Therefore, extreme care had to be taken to insure the specimens were not damaged when mounting the fixture in the Instron.

Due to the very time consuming procedure required for testing specimens with the mounting fixture, the only values of eccentricity tested with the mounting fixture were eccentricities of 0.3 inches.

E. Photoelastic Testing.

In order to verify the contour plotting, which was used to study the effects of eccentricity (see Section III E), photoelastic testing was conducted. Therefore, photoelasticity was utilized to verify "gross" stress states predicted by the analytical study. For completeness, a brief theory of photoelasticity is presented in Appendix E.

Since the analytical study (Section III E) indicated that the use of the mounting fixture would not appreciably affect the stress state adjacent to the discontinuity, the mounting fixture was not used during photoelastic testing. Furthermore, since a limited number of Gr/PEEK panels were available for testing, only four specimens were tested using photoelasticity. These specimens had an eccentricity of zero (see Figure 4-2), and one specimen from each of the four ply lay-ups was tested. The zero eccentricity specimens were used because these specimens were available as project residue from testing completed by [10].

A photoelastic coating was bonded to each test specimen as shown in Figure 4-10. The specimens were then mounted in the Instron and loaded at a constant crosshead velocity of 0.05 inches per minute. This loading was continued until the specimen failed.

The photoelastic testing was recorded on video tape, and photographs were later obtained from this tape (see Section V A). The voltmeter was also used to obtain the magnitude of the applied loading at any time. The voltmeter was an essential part of the test setup since a visible indication of the applied load was required to correlate the level of loading with the photographs obtained from the video tape (see Section V A). The voltmeter is shown to the left of the specimen (Figure 4-11).

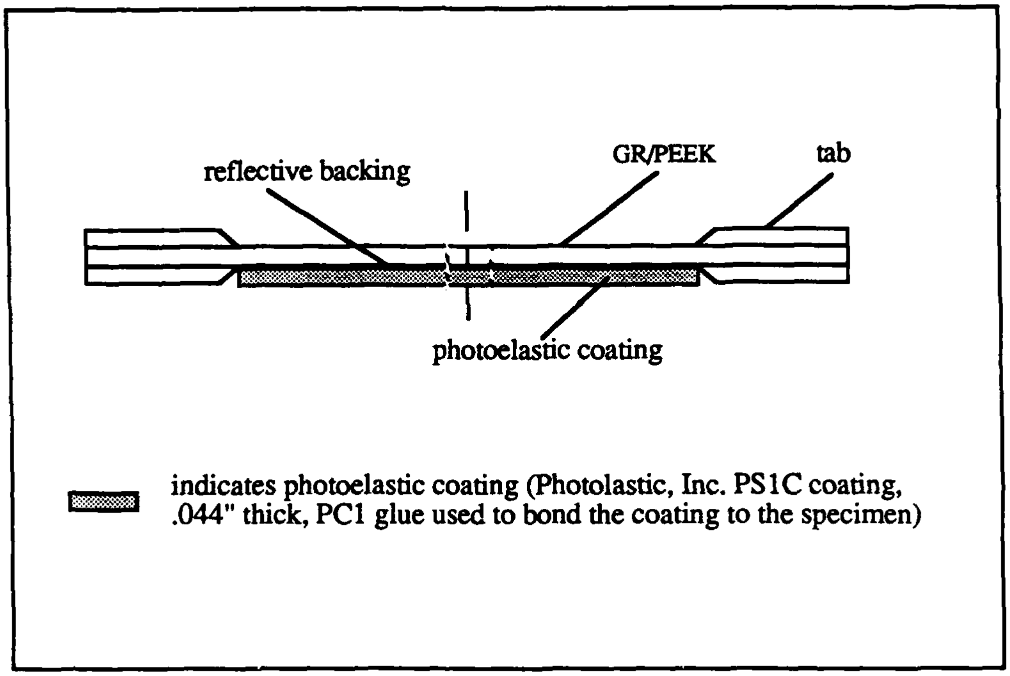

Figure 4-10. Application of Photoelastic Coating

In addition to the Instron, video camera, and voltmeter, a polariscope [16] was used during testing. Simply stated, the polariscope (for purposes of this study) was used to polarize the light source used during testing. Figure 4-11 shows a view (looking through the video camera) of the test setup. This figure shows the light source on the far right side of the photograph. This light source was passed through a polarizer and then entered the photoelastic coating (center of Figure 4-11). The light then reflected off the reflective backing of the photoelastic coating (see Figure 4-10), and passed through another polarizer (left side of Figure 4-11). The visible fringes which resulted from this process were then recorded by the video camera.

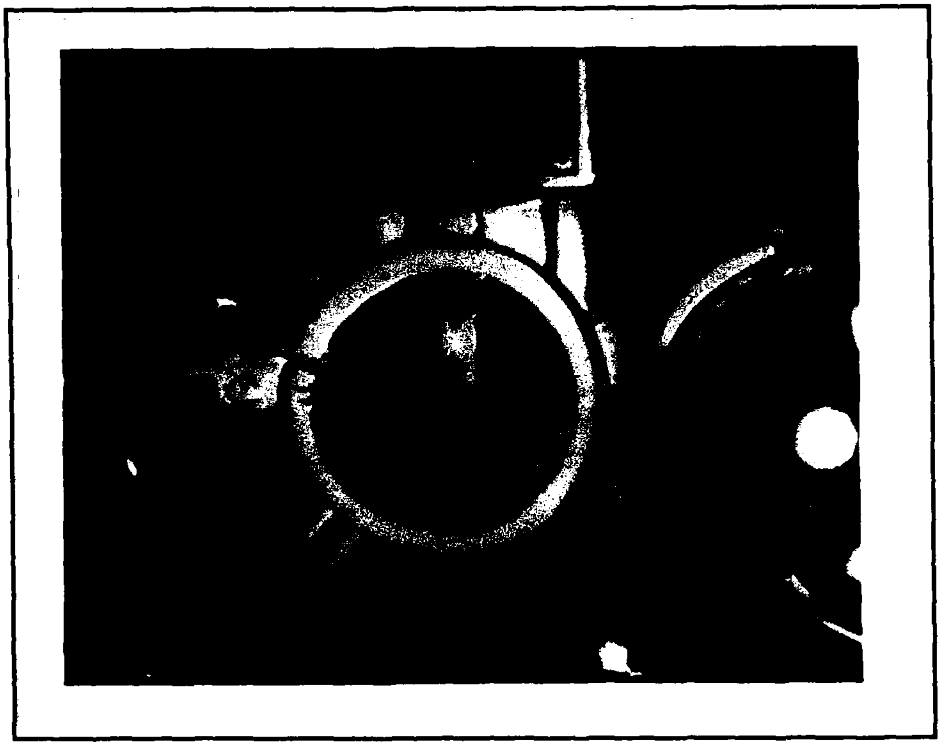

Figure 4-11. Photoelastic Test Setup

A simple schematic is shown in Figure 4-12. This figure shows pictorially the photoelastic technique used in this study.

F. Test Summary.

A total of fifty-two specimens were tested experimentally. A test summary is shown in Tables 4-1 through 4-4. These tables are grouped according to the ply lay-up of the laminates, and specify whether the particular test specimen was instrumented with strain gages or was used for photoelastic testing. Finally, the tables show the value of eccentricity of the particular specimen and whether or not the mounting fixture was utilized.

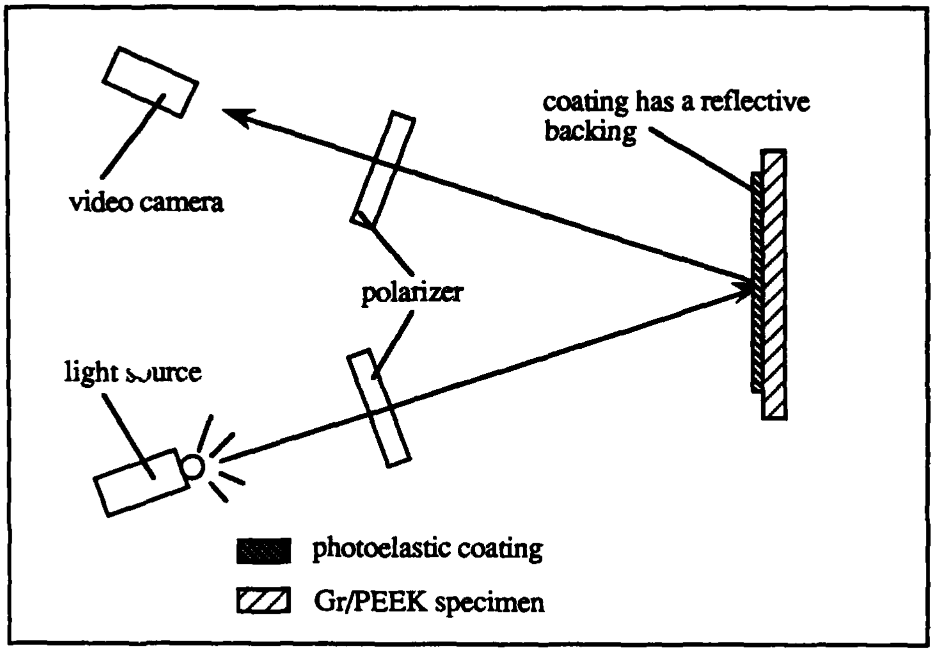

Figure 4-12. Photoelastic Technique

Coupon Number	Serial Number	Eccentricity	Strain Gages	Photoelasticity	Fixture
A5-0T-00-01-H	001	0.0"		√	
A5-0T-00-02-H	002	0.0"	√		
A5-0T-00-03-H	003	0.0"	√		
A5-0T-00-04-H	004	0.0"	√		
B8-0T-01-02-H	005	0.1"	√		
B8-0T-01-03-H	006	0.1"	√		
B8-0T-01-04-H	007	0.1"	√		
B9-0T-03-02-NH	008	0.3"	√		
B9-0T-03-03-NH	009	0.3"	√		
B9-0T-03-04-NH	010	0.3"	√		
B8-0T-03-02-H	011	0.3"	√		√
B8-0T-03-03-H	012	0.3"	√		√
B8-0T-03-04-H	013	0.3"	√		√

Table 4-1. Test Summary for $[0^o_{16}]$ Laminates.

Coupon Number	Serial Number	Eccentricity	Strain Gages	Photoelasticity	Fixture
B5-90T-00-01-H	014	0.0"		√	
B6-90T-00-02-H	015	0.0"	√		
B6-90T-00-03-H	016	0.0"	√		
B6-90T-00-04-H	017	0.0"	√		
A6-90T-01-02-H	018	0.1"	√		
A6-90T-01-03-H	019	0.1"	√		
A6-90T-01-04-H	020	0.1"	√		
A8-90T-03-02-NH	021	0.3"	√		
A8-90T-03-03-NH	022	0.3"	√		
A8-90T-03-04-NH	023	0.3"	√		
A6-90T-03-02-H	024	0.3"	√		√
A6-90T-03-03-H	025	0.3"	√		√
A6-90T-03-04-H	026	0.3"	√		√

Table 4-2. Test Summary for $[90^{o}_{16}]$ Laminates.

Coupon Number	Serial Number	Eccentricity	Strain Gages	Photoelasticity	Fixture
C3-45T-00-01-H	027	0.0"		√	
C3-45T-00-02-H	028	0.0"	√		
C4-45T-00-03-H	029	0.0"	√		
C4-45T-00-04-H	030	0.0"	√		
C5-45T-01-02-H	031	0.1"	√		
C5-45T-01-03-H	032	0.1"	√		
C5-45-01-04-H	033	0.1"	√		
C5-45T-03-02-NH	034	0.3"	√		
C5-45T-03-03-NH	035	0.3"	√		
C5-45T-03-04-NH	036	0.3"	√		
C5-45T-03-02-H	037	0.3"	√		√
C5-45T-03-03-H	038	0.3"	√		√
C5-45T-03-04-H	039	0.3"	√		√

Table 4-3. Test Summary for $[\pm 45^{o}]_{4s}$ Laminates.

Coupon Number	Serial Number	Eccentricity	Strain Gages	Photoelasticity	Fixture
E2-QT-00-01-H	040	0.0"		√	
E2-QT-00-02-H	041	0.0"	√		
E3-QT-00-03-H	042	0.0"	√		
E3-QT-00-04-H	043	0.0"	√		
E3-QT-01-02-H	044	0.1"	√		
E3-QT-01-03-H	045	0.1"	√		
E3-QT-01-04-H	046	0.1"	√		
E4-QT-03-02-NH	047	0.3"	√		
E4-QT-03-03-NH	048	0.3"	√		
E4-QT-03-04-NH	049	0.3"	√		
E3-QT-03-02-H	050	0.3"	√		√
E3-QT-03-03-H	051	0.3"	√		√
E3-QT-03-04-H	052	0.3"	√		√

Table 4-4. Test Summary for $[0^{0}/\pm45^{0}/90^{0}]_{2s}$ Laminates.

V. Results and Discussion

This section discusses the results from both the analytical (Section III) and the experimental (Section IV) portions of this study. As previously mentioned in Section IV, experimentation was conducted for two reasons. First, to verify the validity of the analytic stress state predictions of the linear finite element program. And secondly, to verify the nonlinear finite element predictions of ultimate strength, failure modes, and stress-strain response of the Gr/PEEK laminates studied.

Specifically, this section discusses the results of both the analytical and experimental studies to include:

(A) Stress States
(B) Failure loads/Failure Modes/Stress-Strain Response
(C) Eccentricity/Mounting Fixture - - Effects

(A) Stress States.

The validity of the analytic stress state predictions obtained from the linear finite element program, were verified through the use of photoelastic techniques (Section IV E). Contour plots were generated from data obtained from the linear finite element program (Section III E (1)). These contour plots, as well as photographs taken during photoelastic testing, are shown in Figures 5-1 through 5-4. Each of these figures corresponds to a particular stacking sequence and also to a specific level of loading. As already noted in Section IV E, photoelasticity was used only to verify "gross" stress state predictions of the linear finite element program.

Close inspection of Figures 5-1 through 5-4 reveal that the photoelastic fringes are not geometrically symmetric. Since the specimens tested using photoelasticity were zero eccentricity specimens (see Figure 4-2), nonsymmetry of the fringes was not expected. However, this nonsymmetry can be attributed to several different factors. First, photoelasticity (adjacent to a discontinuity) does not provide an accurate measure of the state of

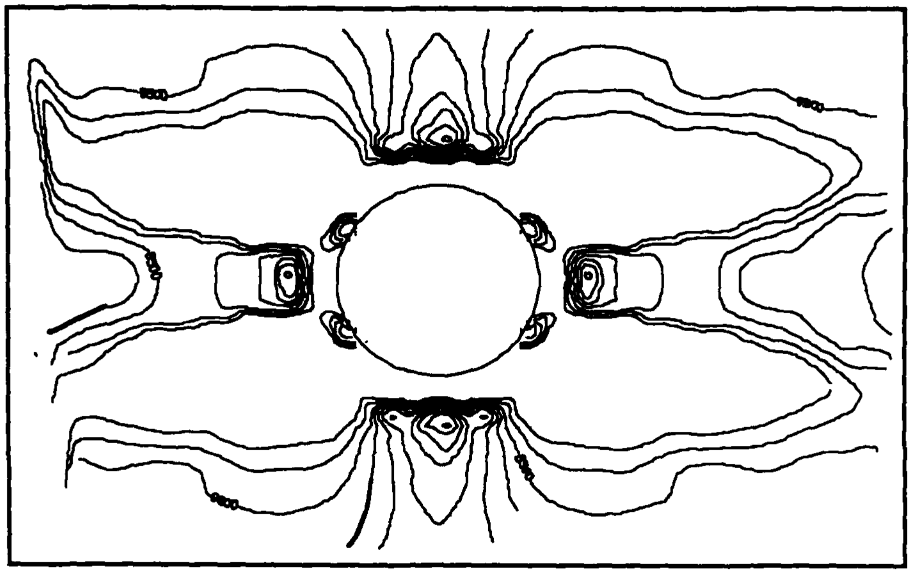

applied loading=5508 lbs / contour plot

applied loading=5508 lbs /photoelastic fringes

Figure 5-1. Analytical versus Experimental Contours ($[0^{o}_{16}]$ laminate)

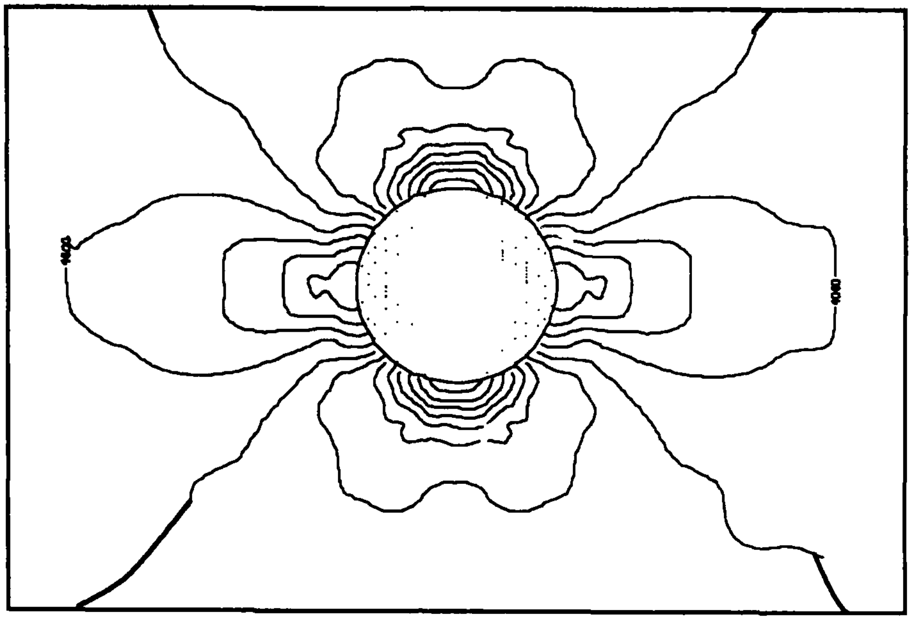

applied loading=530.4 lbs / contour plot

applied loading=530.4 lbs / photoelastic fringes

Figure 5-2. Analytical versus Experimental Contours ($[90^{\circ}_{16}]$ laminate)

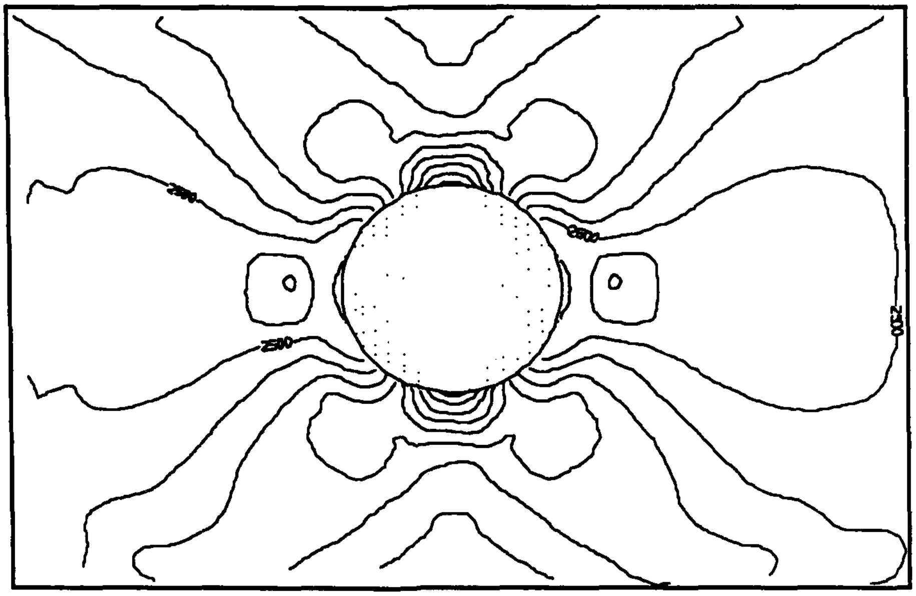

applied loading=367.2 lbs / contour plot

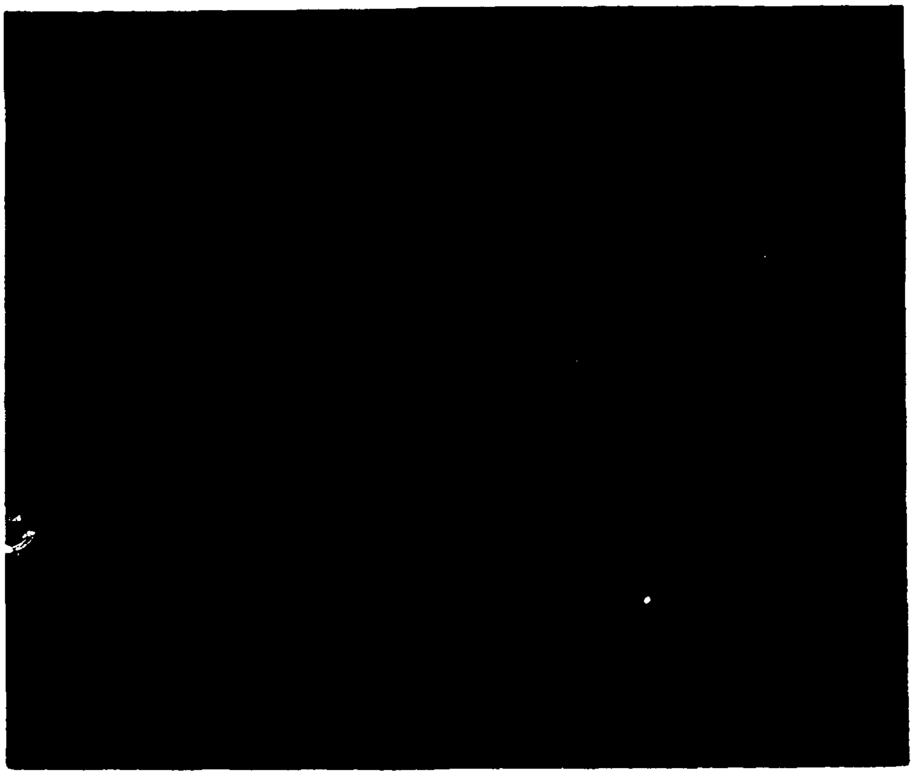

applied loading=367.2 lbs / photoelastic fringes

Figure 5-3. Analytical versus Experimental Contours ($[\pm45^{0}]_{4s}$ laminate)

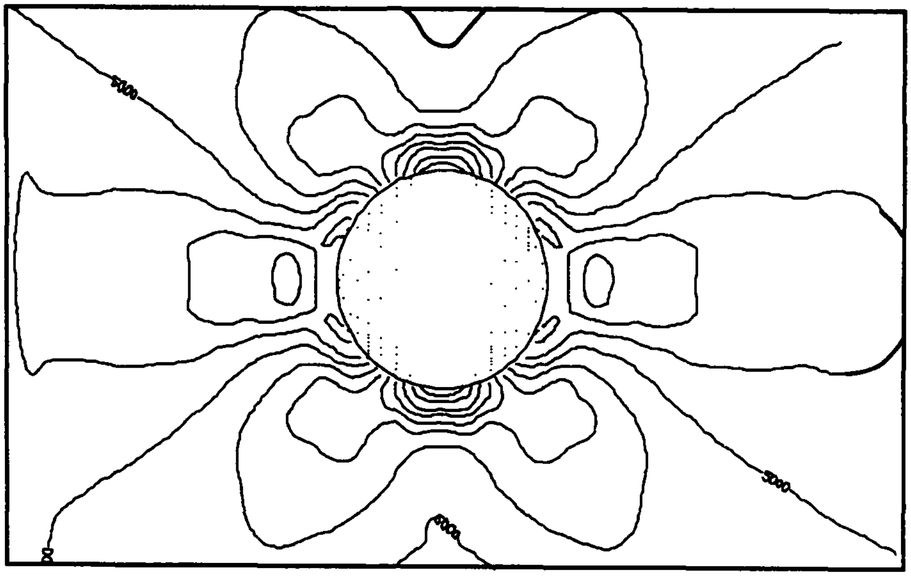

applied loading=1978.8 lbs / contour plot

applied loading=1978.8 lbs / photoelastic fringes

Figure 5-4. Analytical versus Experimental Contours ($[0^\circ/\pm45^\circ/90^\circ]_{2s}$ laminate) stress [16]. This is due primarily to edge effects present where the photoelastic coating meets the edge of the discontinuity. Secondly, it is impossible to obtain a "perfect" adhesive bond (i.e. no voids, uniform glue thickness, etc.) between the Gr/PEEK specimens and the photoelastic coatings (see Figure 4-10). Therefore, the stress state of the Gr/PEEK specimens could not be exactly duplicated by the photoelastic coating (see Appendix E for a brief theory of photoelasticity). Finally, it is impossible to locate a circular discontinuity in the exact geometric center of a specimen. Even the slightest offset of the discontinuity will cause nonsymmetry of the fringes.

Figures 5-1 through 5-4 show good correlation between the analytical predictions of the "gross" stress states and the actual stress states present during experimentation. *This correlation (for all four stacking sequences) is significant.* As previously discussed in Section II A(2), an analytical attempt was made to study the Gr/PEEK laminates with a two-dimensional model. With this assumption, one assumes that through the thickness normal stresses (as well as other interlaminar stresses) may be neglected. Therefore, since the analytical predictions of the "gross" stress states correlated well with the experimental stress states, it appears that the two-dimensional model adequately predicts the "gross" stress states observed from the photoelastic testing. This was important since the linear finite element program was used to develop the finite element model used for this study (see Section III).

(B) Failure Loads/Failure Modes/Stress-Strain Response.

In this section, the experimental and analytical (nonlinear) predictions of the failure characteristics of the Gr/PEEK laminates are discussed. First, the experimental failure loads, experimental scatter, and the analytical predictions of failure loads are presented. Secondly, the eccentricity effects on the analytical predictions of the nominal (far field) failure stress are discussed. And finally, the experimental and analytical predictions of the failure modes and stress-strain responses are discussed. This discussion is presented according to the stacking sequence of the laminates as follows:

(1) $[0^{\circ}{}_{16}]$ laminates
(2) $[90^{\circ}{}_{16}]$ laminates
(3) $[\pm 45^{\circ}]_{4s}$ laminates
(4) $[0^{\circ}/\pm 45^{\circ}/90^{\circ}]_{2s}$ laminates

Since eccentricity and boundary condition effects were observed to cause similar analytical results for all four of the stacking sequences, Section V C presents a general discussion on eccentricity and boundary condition effects for all four stacking sequences.

(1) $[0^{\circ}{}_{16}]$ laminates.

Table 5-1 shows the experimental results of the ultimate strength tests for the $[0^{\circ}{}_{16}]$ laminates. The scatter of the experimental data (Table 5-1) is shown graphically in Figure 5-5. This figure also lists the standard deviation for each hole location (value of eccentricity) tested experimentally. The standard deviation was calculated as:

$$s = \left[\frac{\sum_{i=1}^{N} (y_i - \bar{y})}{N} \right]^{\frac{1}{2}} \qquad (1)$$

where:

s = standard deviation
y_i = i^{th} data point
N = total number of data points
$\bar{y}$ = mean value of all data points

Table 5-1. Experimental Results for $[0^{o}_{16}]$ Laminates.

Serial Number	Eccentricity	Mounting Fixture	Failure Load (lbs)
002	0.0"		4918.12
003	0.0"		5174.97
004	0.0"		5376.14
005	0.1"		6987.95
006	0.1"		6675.78
007	0.1"		7090.03
008	0.3"		9545.49
009	0.3"		9421.02
010	0.3"		9468.81
011	0.3"	✓*	6986.00
012	0.3"	✓	9085.47
013	0.3"	✓	8345.11

* (✓indicates that the mounting fixture was used)

Figure 5-5 shows that for the eccentricity=0.3" testing (with the mounting fixture), there was an unacceptable amount of experimental scatter. This scatter may have been a result of initial damage to the specimens (note the relatively low failure load for specimen 011, Table 5-1). As noted in Section IV D, testing with the mounting fixture was difficult due to the weight of the assembled fixture. Therefore, it would have been very easy to damage a specimen while installing the mounting fixture in the Instron Test Machine.

A summary of the average experimental failure loads (calculated from Table 5-1), as well as the analytical predictions of failure loads, are given in Table 5-2. In addition, Table 5-2 shows the percent difference between the average experimental failure loads and the

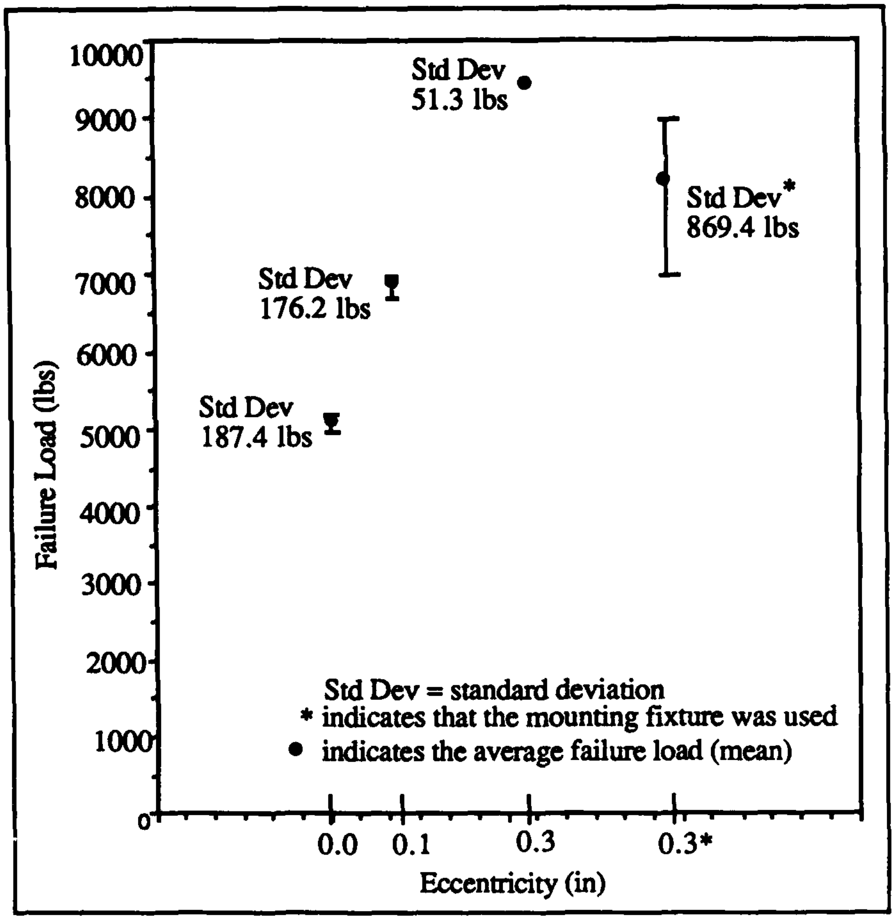

Figure 5-5. Experimental Scatter for $[0^{o}_{16}]$ laminates

analytical predictions of failure loads. This percent difference was calculated as:

$$\frac{\text{avg experimental failure load (lbs) - analytical failure load (lbs)}}{\text{avg experimental failure load (lbs)}} \times 100 \qquad (2)$$

If the analytical predictions of the nominal (far field) failure stresses are examined, the effects of eccentricity on the nominal failure stress can be determined. Table 5-3 lists both the analytical failure loads and the nominal (far field) failure stresses.

Table 5-2. Summary of Average Experimental Failure Loads and Analytical Failure Loads for $[0^{o}_{16}]$ Laminates.

Eccentricity	Average Experimental Failure Load (lbs)	Analytical Failure Load (lbs)	% diff. (Ex. vs Anal.)
0.0" (no fixture)	5156.41	5935.36	-15.1%
0.1" (no fixture)	6917.92	7041.71	-1.8%
0.3" (no fixture)	9478.44	9241.27	+2.5%
0.3" (with fixture)	8138.86	8952.14	-9.1%

Table 5-3. Summary of Analytical Failure Loads and Nominal (far field) Failure Stresses for $[0^{o}_{16}]$ Laminates.

Eccentricity	Analytical Failure Load (lbs)	Nominal Failure (far field) Stress (psi)
0.0" (no fixture)	5935.36	58,882.54
0.1" (no fixture)	7041.71	59,878.49
0.3" (no fixture)	9241.27	61,119.51
0.3" (with fixture)	8952.14	59,207.27

The initial attempt in this thesis was to remove the edge effects created by locating the discontinuity adjacent to the edge of the specimen. Therefore, for all the specimens considered in this study, the distance from the edge of the discontinuity, to the edge of the specimen (see Figure 4-2), was always greater than or equal to the diameter of the discontinuity (0.4"). This distance was maintained (for all specimens) so that edge effects would not vary for the different values of eccentricity considered in this study. From Table 5-3, note that the analytical predictions of nominal failure stresses do not appreciably differ for the different values of eccentricity; therefore, since edge effects were effectively controlled by main-taining at least 0.4 inches between the edge of the discontinuity and the edge of the specimen, it appears that the values of eccentricity considered in this study did not appreciably affect the nominal failure stress for the $[0^{o}{}_{16}]$ laminates.

The "knock down" (reduction) of the nominal failure stress, due to the discontinuity, was significant. The nominal failure stress for $[0^{o}{}_{16}]$ laminates (without a discontinuity) is 298,300 psi [13]. Therefore, for this laminate, the nominal failure stress (due to the 0.4" discontinuity) was reduced by a factor of approximately 5 (from Table 5-3). This is significantly *higher* than the knockdown for an isotropic material of the same geometry. Peterson [15] reports that for an isotropic material (of the same geometry), the nominal failure stress would be reduced by a factor of 3.46. Since the $[0^{o}{}_{16}]$ laminates failed along the fiber direction, the magnitude of the knockdown of nominal failure stress is not unreasonable. This is because once the ultimate stress of the laminate was reached (at the edge of the discontinuity), the laminate split along the fiber direction. This failure mode occurred at a relatively low nominal stress. Once the zero degree fibers adjacent to the discontinuity failed, the matrix (which is relatively weak) failed very rapidly (split).

For all of the $[0^{o}{}_{16}]$ specimens, the failure mode was characterized by splitting at the edge of the discontinuity (parallel to the fibers). Figures 5-6 and 5-7 show photographs of the failed specimens. The splitting of the specimens (cracks) has been highlighted by silver lines (Figures 5-6 and 5-7). The terms "hinge" and "no hinge" shown on these figures, refers to testing with or without the mounting fixture, respectively. For purposes of this study, failure (both experimental and analytical) was assumed to occur at the load which

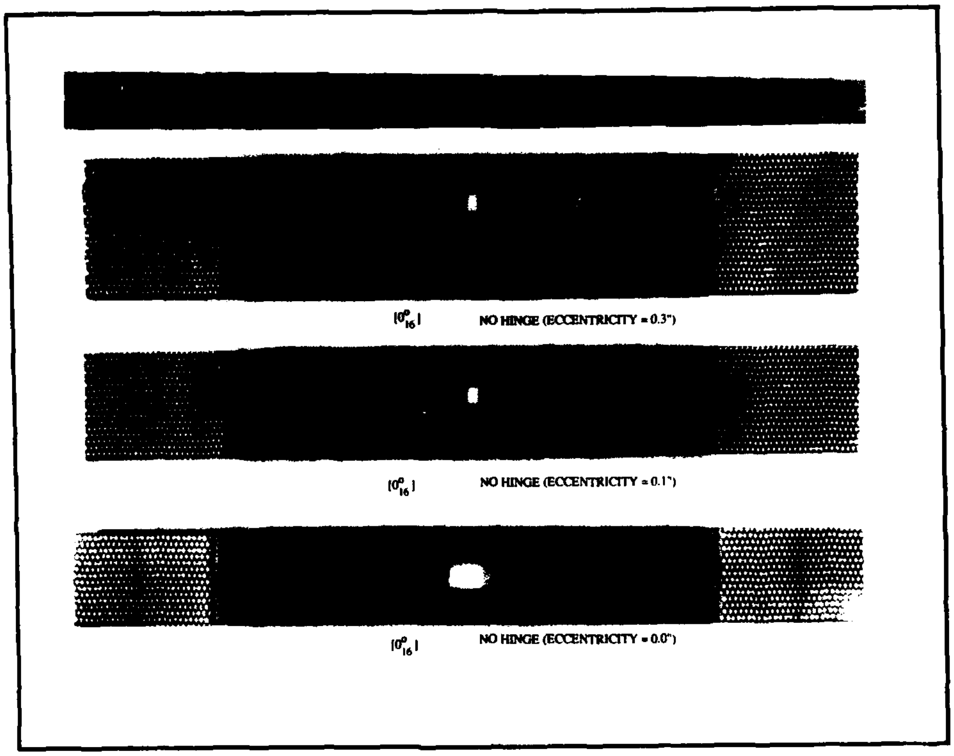

Figure 5-6. Failed [0^{o}_{16}] Specimens (no mounting fixture)

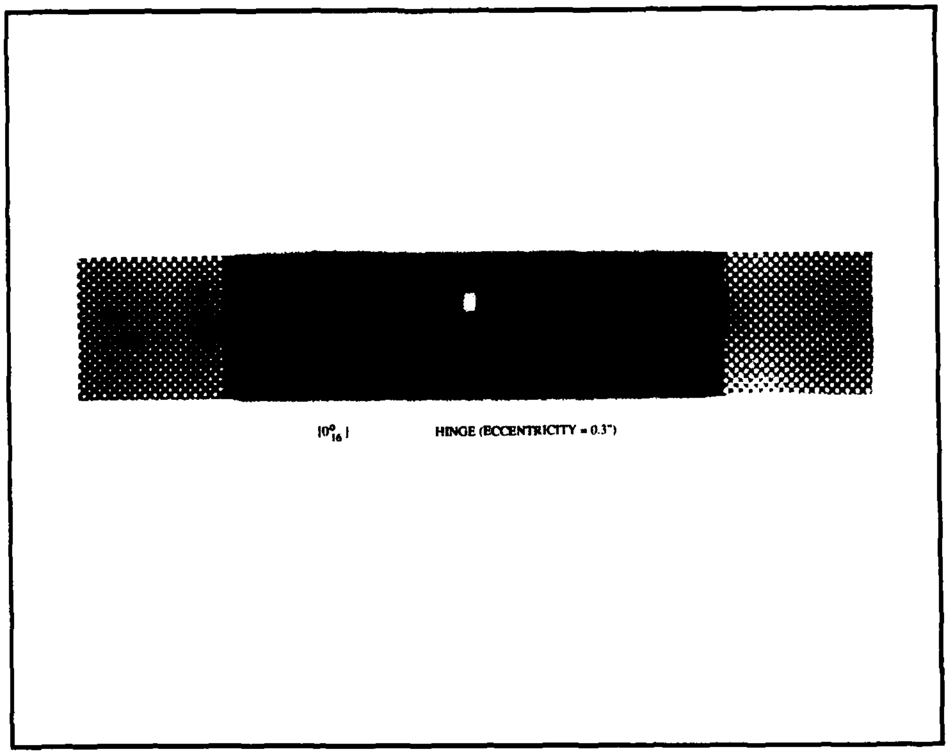

Figure 5-7. Failed [0^{o}_{16}] Specimen (mounting fixture)

produced splitting. This assumption was made because once the specimens split, the geometry of the problem was entirely changed. Instead of a specimen with a circular discontinuity, the specimen was now comprised of three different sections (see Figure 5-6). These three sections could be described as two rectangular sections above and below the discontinuity, and a center section (left and right of the discontinuity) which was unloaded. Therefore, the original finite element models (Figure 3-3) could not be expected to provide accurate data beyond the "splitting" load. This is due to the fact that the geometry of the finite element model no longer matched the geometry of the "split" specimens.

The determination of the experimental failure load was an easy task. When splitting occurred, an instantaneous drop in the applied load was observed on the Instron strip chart (see Figure 4-6). Also, the output strain gage data (Section IV C) showed discontinuous jumps in strain at the instant of splitting. Therefore, an accurate value of the experimental failure load was easily obtained.

Once the experimental failure mode had been observed, the determination of the analytical failure load was also straightforward. Since splitting was initiated at the edge of the discontinuity (point A, Figure 5-8), the stress at the edge of the discontinuity was obtained (from the nonlinear output) for each increment of loading. Since the nonlinear finite element program provided stress and strain data only at the centroid of the finite elements, Lagrange extrapolation [5] was used to calculate the value of stress at the edge of the discontinuity. Once the stress level at the edge of the discontinuity reached the ultimate stress of the Gr/PEEK, splitting was assumed to occur, and the failure load from the nonlinear output was recorded.

One interesting point regarding the splitting of these laminates becomes apparent if the values of transverse stress (σ_y) along the split (points B,C,and D; Figure 5-8) are examined. It was observed that these transverse stresses (less than 200 psi) were too small to cause splitting. Therefore, the splitting could be caused by a dynamic process, such as a relax-

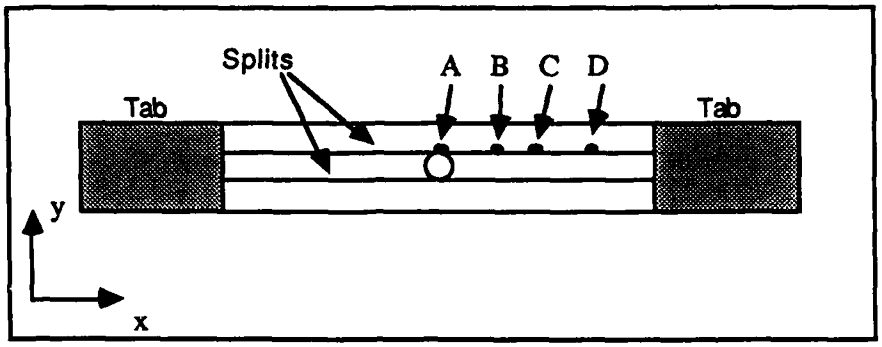

Figure 5-8. $[0^o_{16}]$ Laminate Splitting

ation stress wave generated by splitting of the fibers at the hole. Therefore, if splitting was caused by a dynamic phenomenon (such as a stress wave), the finite element solution (a static solution) can not be expected to predict splitting. Other possibilities for splitting might include edge effects or some other three-dimensional effect at the edge of the discontinuity.

Stress-strain response plots were constructed by [13] for symmetric models (eccentricity = 0.0"). Therefore, in an effort to bound the ranges of eccentricities considered in this study, only the stress-strain response plots for the eccentricity = 0.3" models were constructed (Figures 5-9 through 5-11). Figure 5-9 shows the experimental and analytical near field response at strain gage #1. The experimental and analytical near field response at strain gage #2 is shown in Figure 5-10. Finally, the experimental and analytical far field response is shown in Figure 5-11 as the average strains from strain gages #3 and #4. From these three figures, note that there is excellent (within 5%) correlation between the analytical predictions of axial stress-strain response, and the experimental axial stress-strain response (for a constant value of stress). This correlation was noted at both the near field (Figures 5-9 and 5-10) and the far field (Figure 5-11) locations. Also, from these three figures, note that there is good (within 10%) correlation between the analytical predictions of transverse stress-strain response (for levels of stress up to the point of the splitting of the laminate) and the experimental transverse stress-strain response (for a constant value of stress).

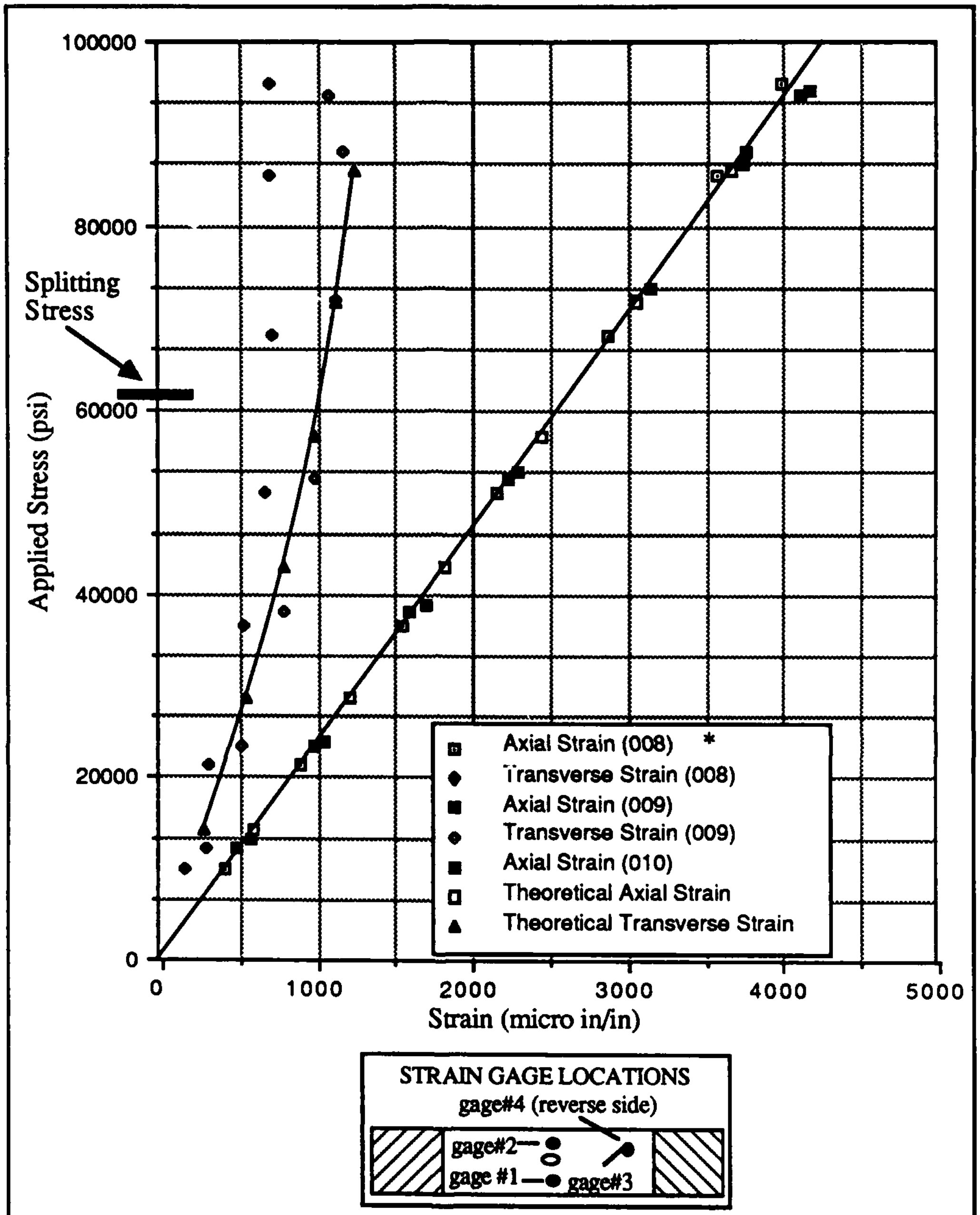

NOTES:

1. * indicates serial number of test specimen
2. transverse strain for specimen #010 not available (bad gage)
3. 0 degree lay-up / eccentricity=0.3" / no mounting fixture

Figure 5-9. Near Field (gage #1) Stress-Strain Response

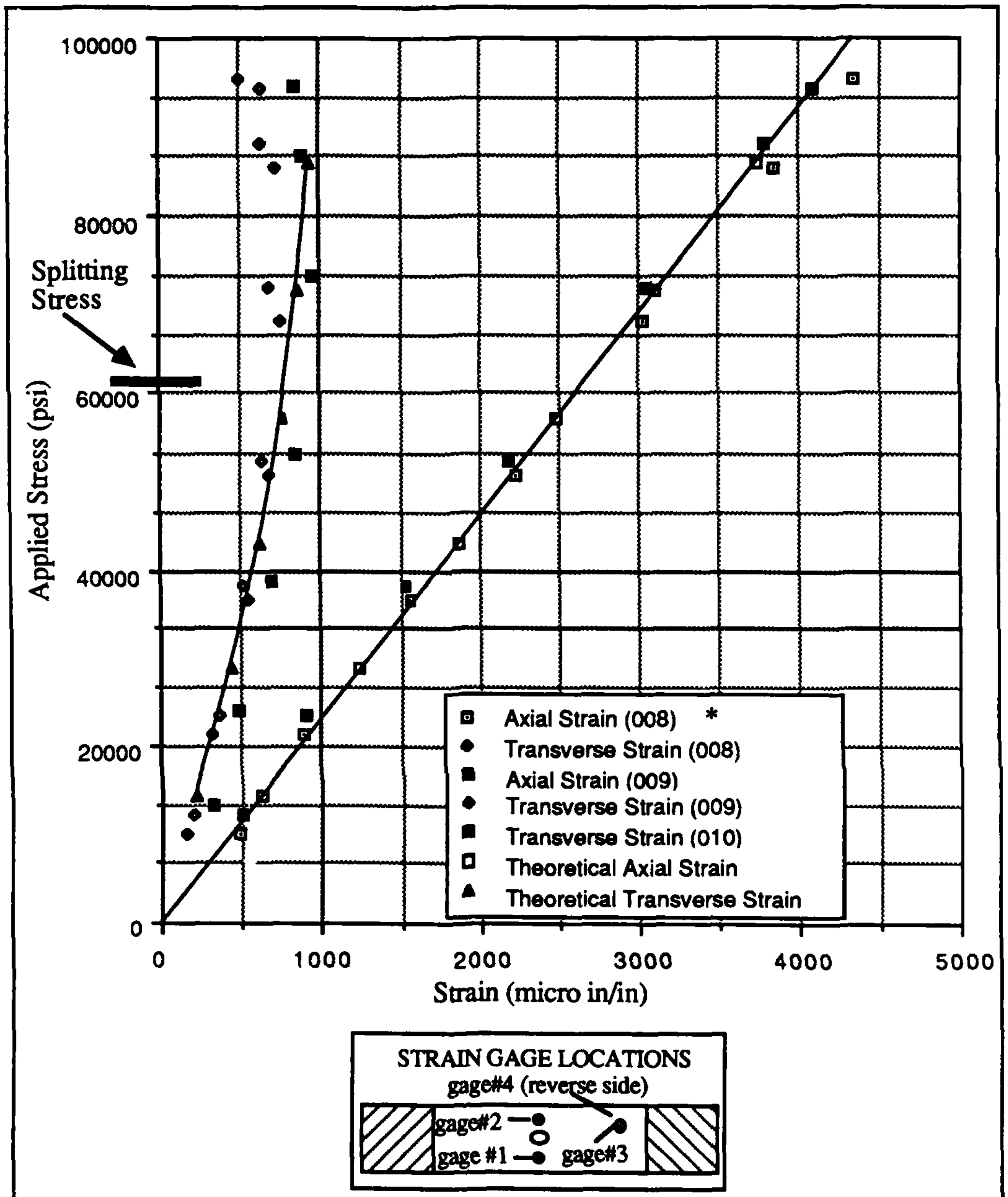

NOTES:

1. * indicates serial number of test specimen
2. axial strain for specimen #010 not available (bad gage)
3. 0 degree lay-up / eccentricity=0.3" / no mounting fixture

Figure 5-10. Near Field (gage #2) Stress Strain Response

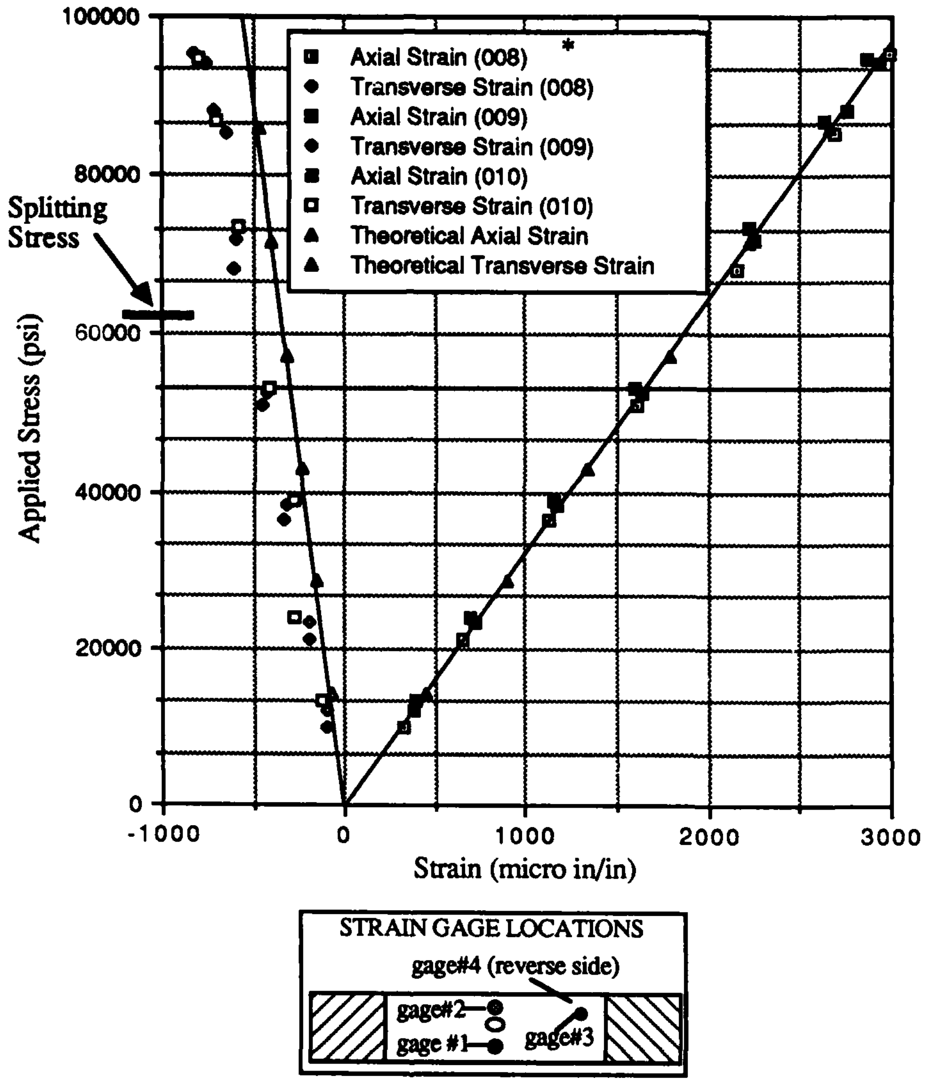

NOTES:

1. * indicates serial number of test specimen
2. 0 degree lay-up / eccentricity=0.3" / no mounting fixture

Figure 5-11. Far Field (gage #3) Stress Strain Response

In summary, the analytical solution did a good job of predicting the splitting (failure) load of the $[0^o{}_{16}]$ laminates. Also, the analytical stress-strain response predictions correlated well with the experimental stress-strain response. Finally, the analytical solution did not predict the failure progression (splitting) of these laminates. As already mentioned, this splitting may be caused by a dynamic phenomenon (such as a stress wave), or some other three-dimensional phenomenon (such as edge effects). Therefore, the two-dimensional finite element solution (a static solution) was not able to predict splitting.

(2) $[90^o{}_{16}]$ laminates.

Table 5-4 shows the experimental results of the ultimate strength tests for the $[90^o{}_{16}]$ laminates. The scatter of the experimental data (Table 5-4) is shown graphically in Figure 5-12. This figure also lists the standard deviation for each hole location (value of eccentricity) tested experimentally. The standard deviation was calculated from equation (1), Section V B(1). Figure 5-12 shows that experimental scatter was not significant during the testing of these laminates.

A summary of the average experimental failure loads (calculated from Table 5-4) as well as the analytical predictions of failure loads are given in Table 5-5. In addition, Table 5-5 shows the percent difference between the average experimental failure loads and the analytical predictions of failure loads. This percent difference was calculated from equation 2, Section V B(1).

If the analytical predictions of the nominal (far field) failure stresses are examined, the effects of eccentricity on the nominal failure stress can be determined. Table 5-6 lists both the analytical failure loads and the nominal (far field) failure stresses. As previously discussed (Section V B(1)), the distance from the edge of the discontinuity to the edge of the specimen (Figure 4-2) was always greater than or equal to the diameter of the discontinuity (0.4"). This distance was maintained so that edge effects would not vary for the

Table 5-4. Experimental Results for $[90^{o}_{16}]$ Laminates.

Serial Number	Eccentricity	Mounting Fixture	Failure Load (lbs)
015	0.0"		704.40
016	0.0"		742.29
017	0.0"		799.78
018	0.1"		845.85
019	0.1"		828.64
020	0.1"		956.03
021	0.3"		1085.12
022	0.3"		1198.66
023	0.3"		1247.73
024	0.3"	✓*	1213.36
025	0.3"	✓	1301.00
026	0.3"	✓	1150.74
* (✓ indicates that the mounting fixture was used)			

different values of eccentricity considered in this study. From Table 5-6, note that the analytical predictions of nominal failure stresses do not appreciably differ for the different values of eccentricity; therefore, since edge effects were controlled by maintaining at least 0.4 inches between the edge of the discontinuity and the edge of the specimen, it appears that the values of eccentricity considered in this study did not appreciably affect the nominal failure stress for this stacking sequence.

The knock down (reduction) of the nominal failure stress (due to the 0.4" discontinuity) was significantly lower than that obtained for the $[0^{o}_{16}]$ laminates. The nominal failure stress for $[90^{o}_{16}]$ laminates (without a discontinuity) is 14,110 psi [13]. Therefore, for

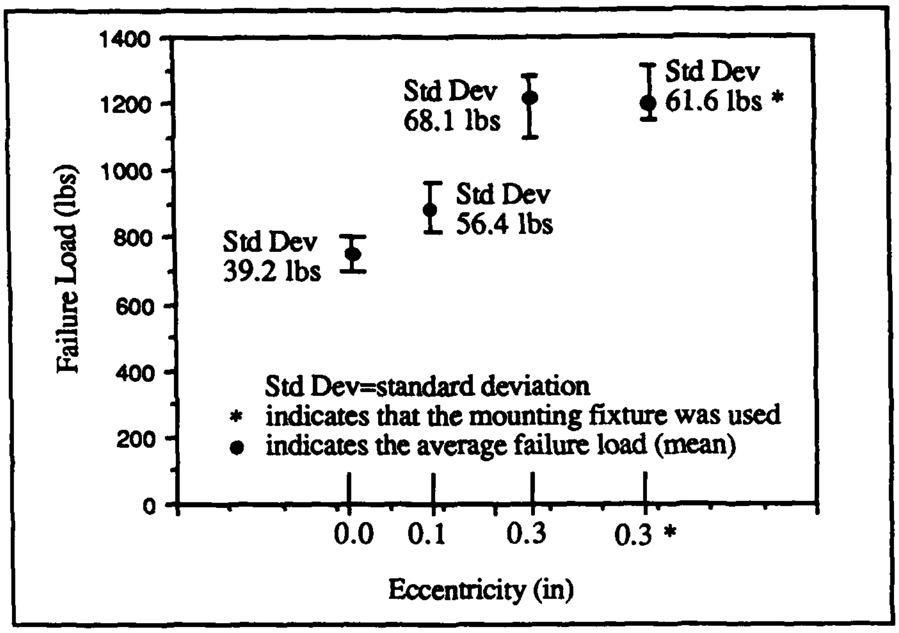

Figure 5-12. Experimental Scatter for $[90^{o}_{16}]$ Laminates

Table 5-5. Summary of Average Experimental Failure Loads and Analytical Failure Loads for $[90^{o}_{16}]$ Laminates.

Eccentricity	Average Experimental Failure Load (lbs)	Analytical Failure Load (lbs)	% diff. (Ex. vs Anal.)
0.0" (no fixture)	748.82	729.05	+2.6%
0.1" (no fixture)	876.84	894.89	-2.1%
0.3" (no fixture)	1177.17	1217.37	-3.4%
0.3" (with fixture)	1221.70	1172.56	+4.0%

Table 5-6. Summary of Analytical Failure Loads and Nominal (far field) Failure Stresses for $[90^{o}_{16}]$ Laminates.

Eccentricity	Analytical Failure Load (lbs)	Nominal Failure (far field) Stress (psi)
0.0" (no fixture)	729.05	7,232.64
0.1" (no fixture)	894.89	7,609.61
0.3" (no fixture)	1217.37	8,051.39
0.3" (with fixture)	1172.56	7,755.03

this laminate, the nominal failure stress (due to the 0.4" discontinuity) was reduced by a factor of approximately 1.8 (see nominal failure stresses, Table 5-6). This is significantly *lower* than the knock down of nominal failure stress (due to a circular discontinuity) for an isotropic material of the same geometry, reported as 3.46 by [15].

For all of these specimens, experimental failure occurred parallel to the fibers and was initiated at the discontinuity. Figures 5-13 and 5-14 show photographs of the failed specimens. This mode of failure was expected since the $[90^{o}_{16}]$ laminates are characterized by matrix failure (parallel to the fibers) at the narrowest part of the cross-sectional area [13]. Failure of these laminates was very rapid, therefore, it was impossible to determine if failure was initiated above or below the discontinuity.

Figures 5-15 through 5-18 show the analytical predictions of failure progression and failure loads for the $[90^{o}_{16}]$ laminates. These figures show that failure of these laminates was initiated at the discontinuity. These figures also show that "free-floating" nodes occurred at the analytical failure load. The term "free-floating" node indicates an instability of the displacements of a node. This instability occures due to the large displacement of a node, which causes the rotation of a line connecting two nodes (i.e. one side of a finite

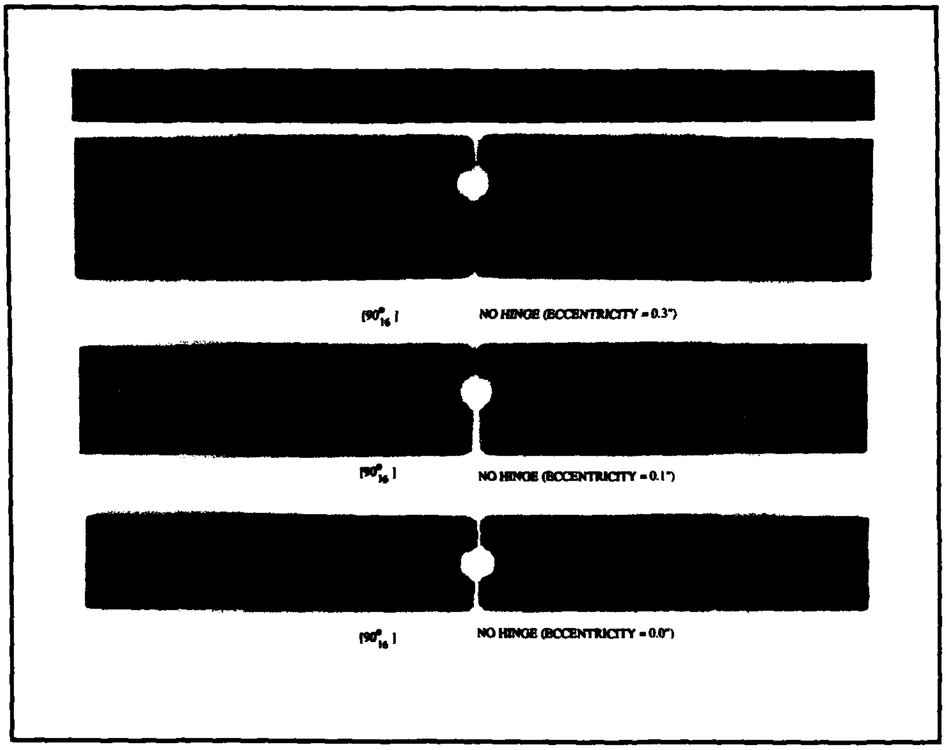

Figure 5-13. Failed $[90^{o}_{16}]$ Specimens (no mounting fixture)

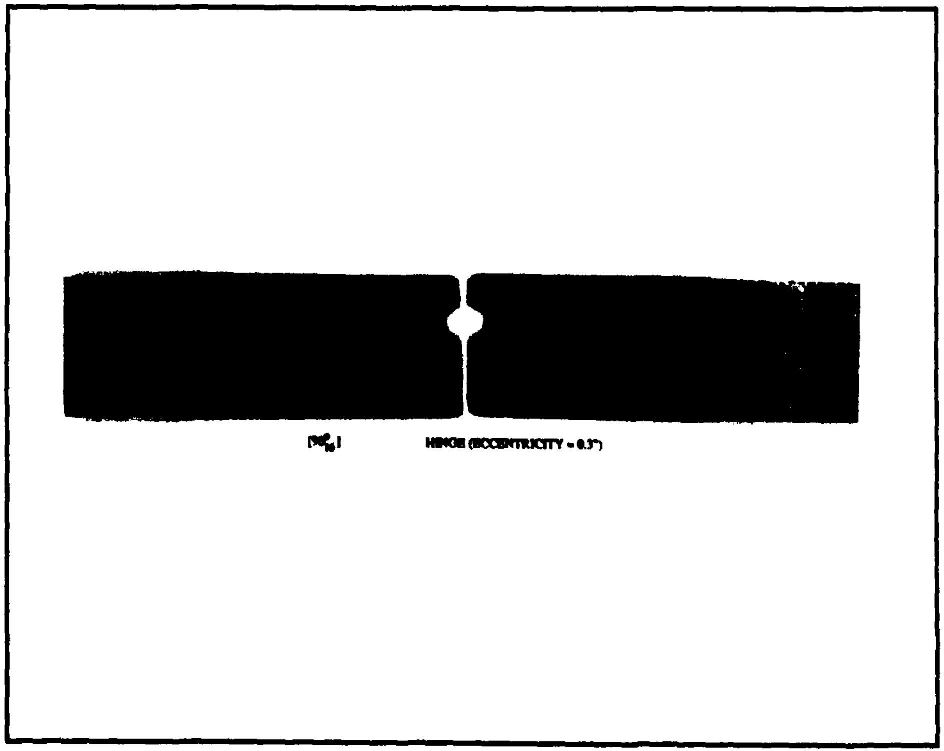

Figure 5-14. Failed $[90^{o}_{16}]$ Specimen (mounting fixture)

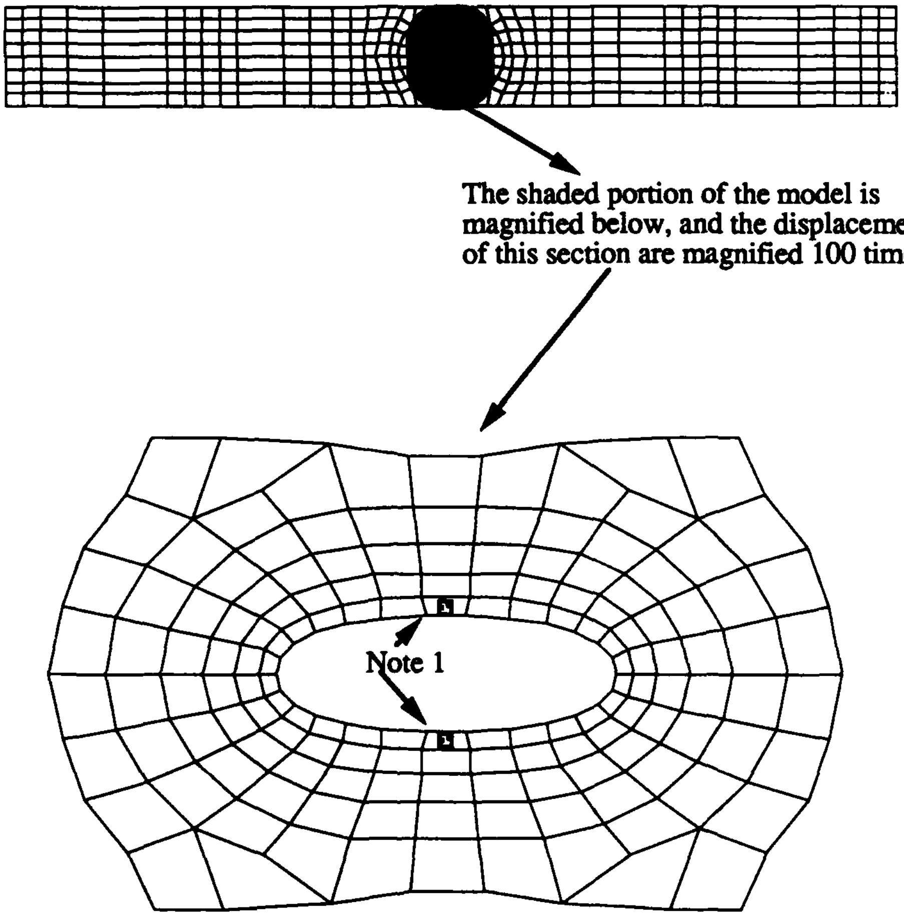

The shaded portion of the model is magnified below, and the displacements of this section are magnified 100 times.

▣ indicates element failure at 688.4 lbs

1. Free-floating nodes occurred (instability) @ 729.05 lbs; in addition, the load increments converged at the FAILURE LOAD (729.05 lbs)

Figure 5-15. Failure Progression (90 degree / e=0.0" / no mounting fixture)

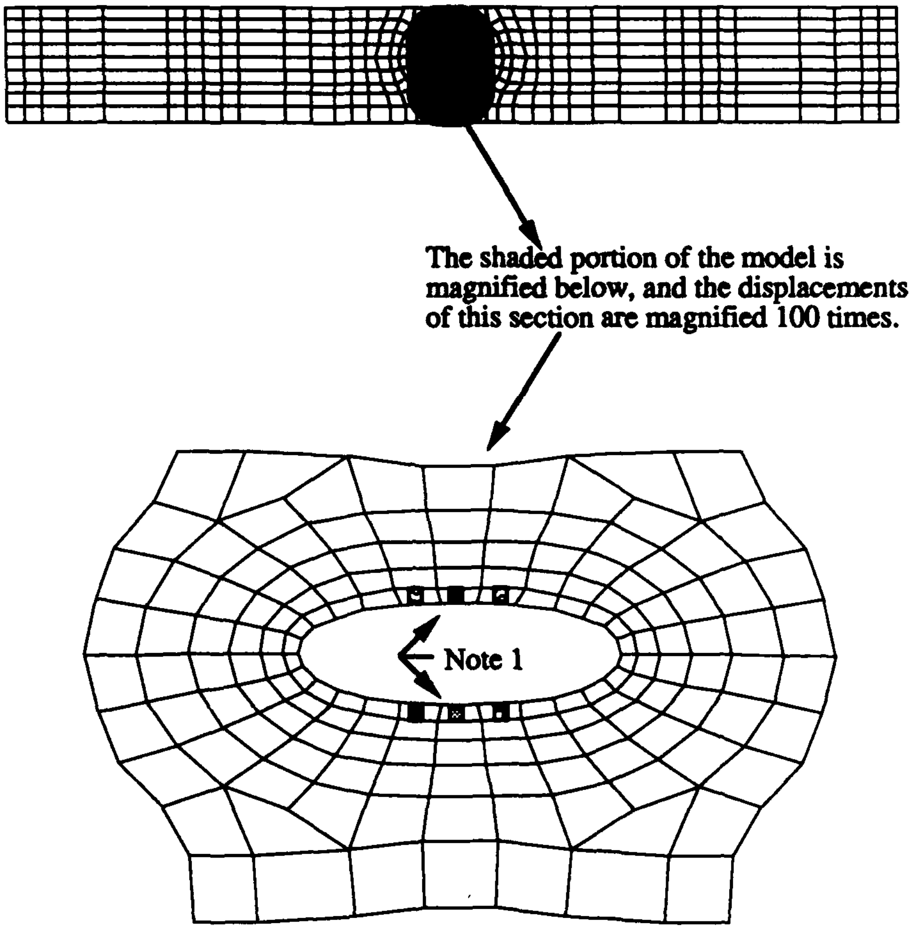

■ indicates element failure at 814.73 lbs

▩ indicates element failure at 854.02 lbs

▨ indicates element failure at 865.09 lbs

■ indicates element failure at 894.89 lbs (FAILURE LOAD)

1. Free-floating nodes occurred (instability) @ 894.89 lbs; in addition, the load increments converged at the FAILURE LOAD (894.89 lbs).

Figure 5-16. Failure Progression (90 degree / e=0.1" / no mounting fixture)

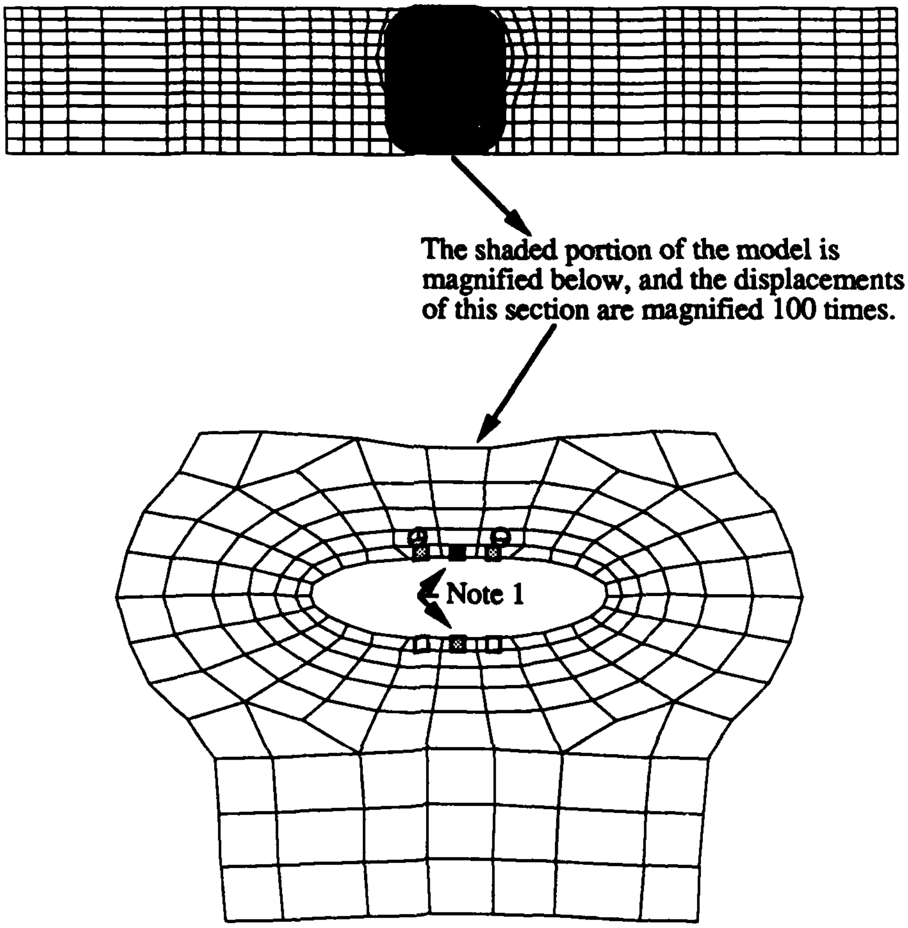

The shaded portion of the model is magnified below, and the displacements of this section are magnified 100 times.

■ indicates element failure at 1062.09 lbs

▨ indicates element failure at 1129.33 lbs

□ indicates element failure at 1179.75 lbs

⊖ indicates element failure at 1217.37 lbs

1. Free-floating nodes occurred (instability) @ 1179.75 lbs; in addition, the load increments converged at the FAILURE LOAD (1217.37 lbs).

Figure 5-17. Failure Progression (90 degree / e=0.3" / no mounting fixture)

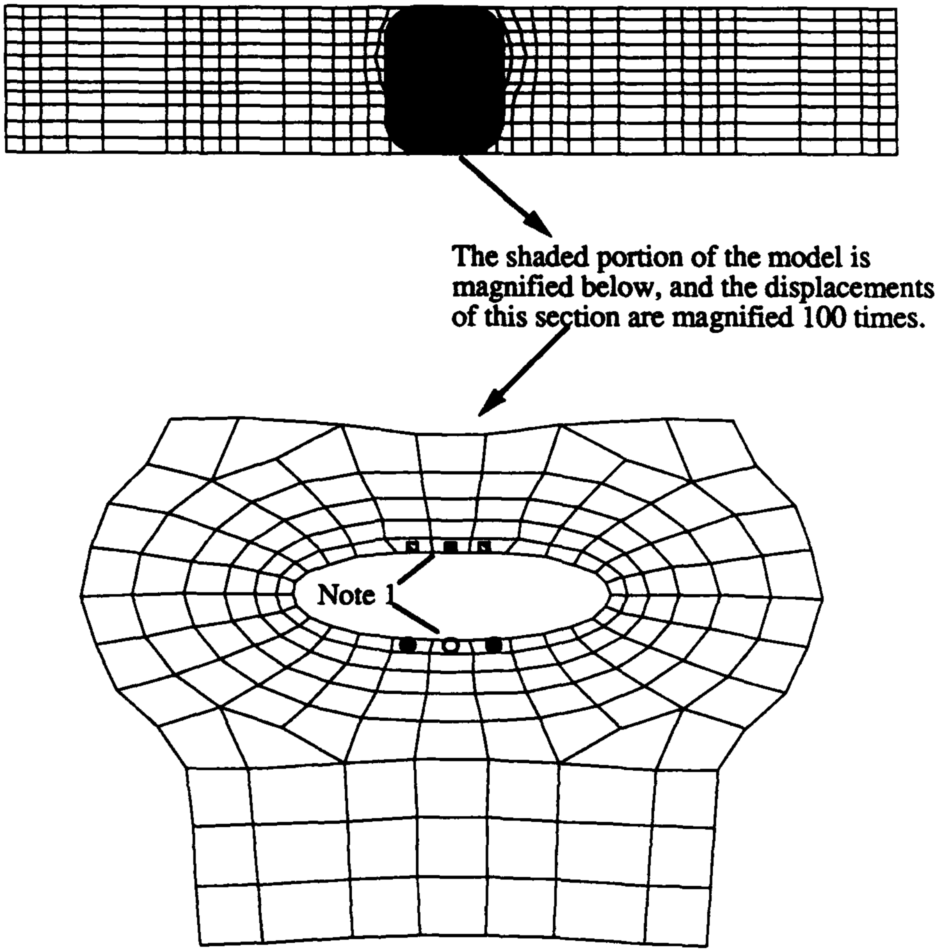

The shaded portion of the model is magnified below, and the displacements of this section are magnified 100 times.

■ indicates element failure at 1042.59 lbs

▣ indicates element failure at 1110.76 lbs

○ indicates element failure at 1120.92 lbs

● indicates element failure at 1172.56 lbs

1. Free-floating nodes occurred (instability) @ 1172.56 lbs; in addition, the load increments converged at the FAILURE LOAD (1172.56 lbs).

Figure 5-18. Failure Progression (90 degree / e=0.3" / mounting fixture) element). This rotation of a line, connecting two nodes, is visible in Figures 5-15 through 5-18.

Stress-strain response plots for the eccentricity = 0.3" model were constructed (Figures 5-19 through 5-21). Figure 5-19 shows the experimental and analytical near field response at strain gage #1. The experimental and analytical near field response at strain gage #2 is shown in Figure 5-20. And finally, the experimental and analytical far field response is shown in Figure 5-21 as the average strains from strain gages #3 and #4. From these three figures, note that there is good, within 10%, correlation between the analytical predictions of axial stress-strain response, and the experimental axial stress-strain response (for a constant value of stress). Also, from these figures, note that there is excellent correlation between the analytical predictions of transverse stress-strain response and the experimental transverse stress-strain response (for a constant value of stress).

In summary, the analytical solution did an excellent job of predicting both the failure loads and failure modes for the $[90^{o}{}_{16}]$ laminates. In addition, the analytical stress-strain response predictions correlated very well with the experimental stress-strain response.

(3) $[\pm45^{o}]_{4s}$ laminates.

Table 5-7 shows the experimental results of the ultimate strength tests for the $[\pm45^{o}]_{4s}$ laminates. The scatter of the experimental data (Table 5-7) is shown graphically in Figure 5-22. This figure also lists the standard deviation for each hole location (value of eccentricity) tested experimentally. The standard deviation was calculated from equation (1), Section V B(1). Figure 5-22 shows that experimental scatter was not significant during the testing of these laminates.

A summary of the average experimental failure loads (calculated from Table 5-7), as well as the analytical predictions of failure loads, are given in Table 5-8. In addition, Table 5-8

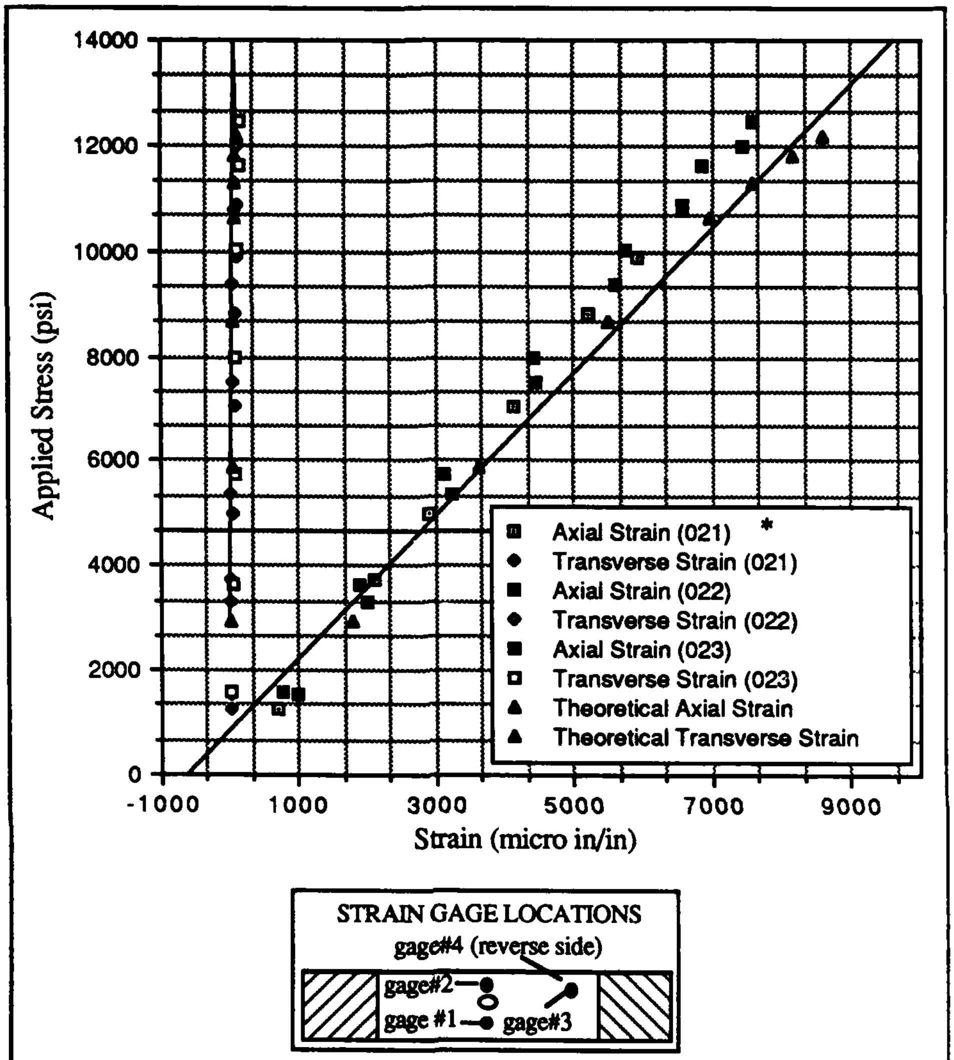

NOTES:

1. * indicates serial number of test specimen
2. 90 degree lay-up / eccentricity=0.3" / no mounting fixture

Figure 5-19. Near Field (gage #1) Stress Strain Response

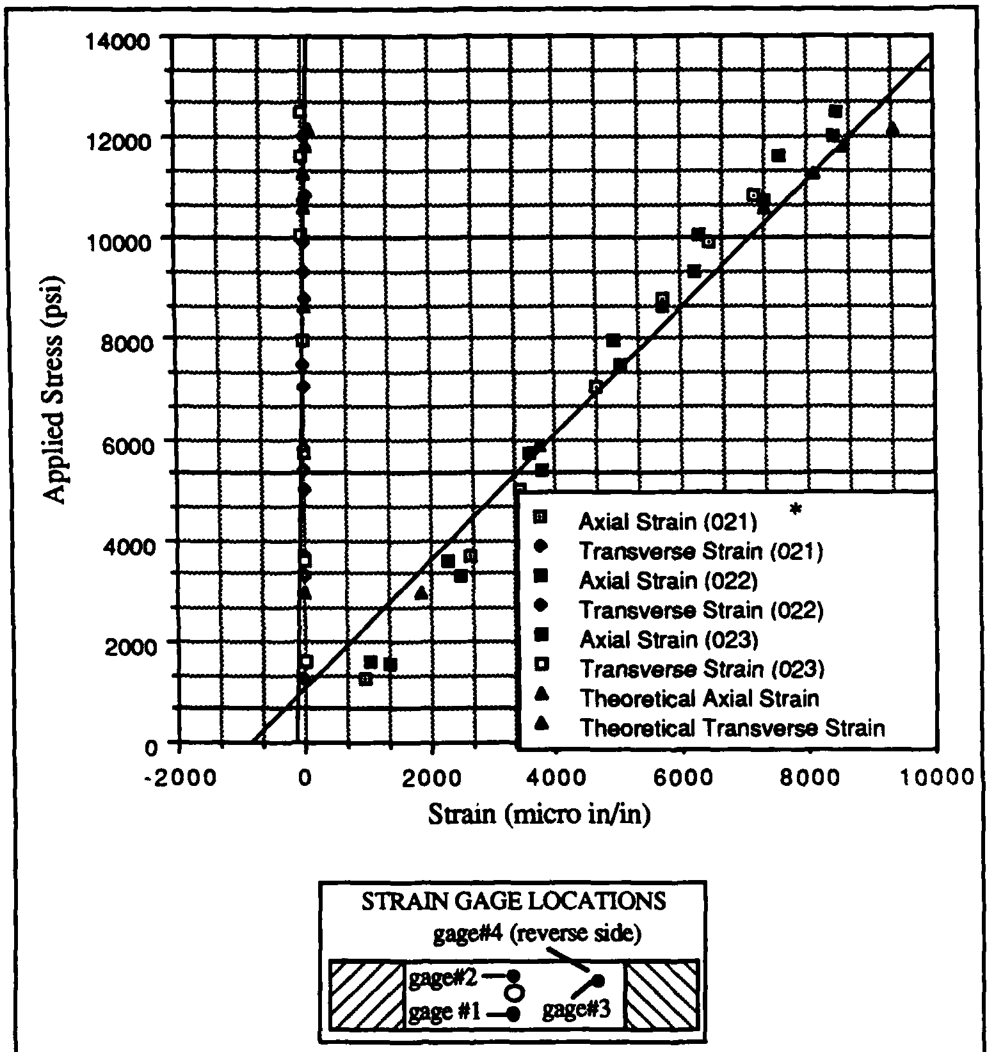

NOTES:

1. * indicates serial number of test specimen
2. 90 degree lay-up / eccentricity=0.3" / no mounting fixture

Figure 5-20. Near Field (gage #2) Stress Strain Response

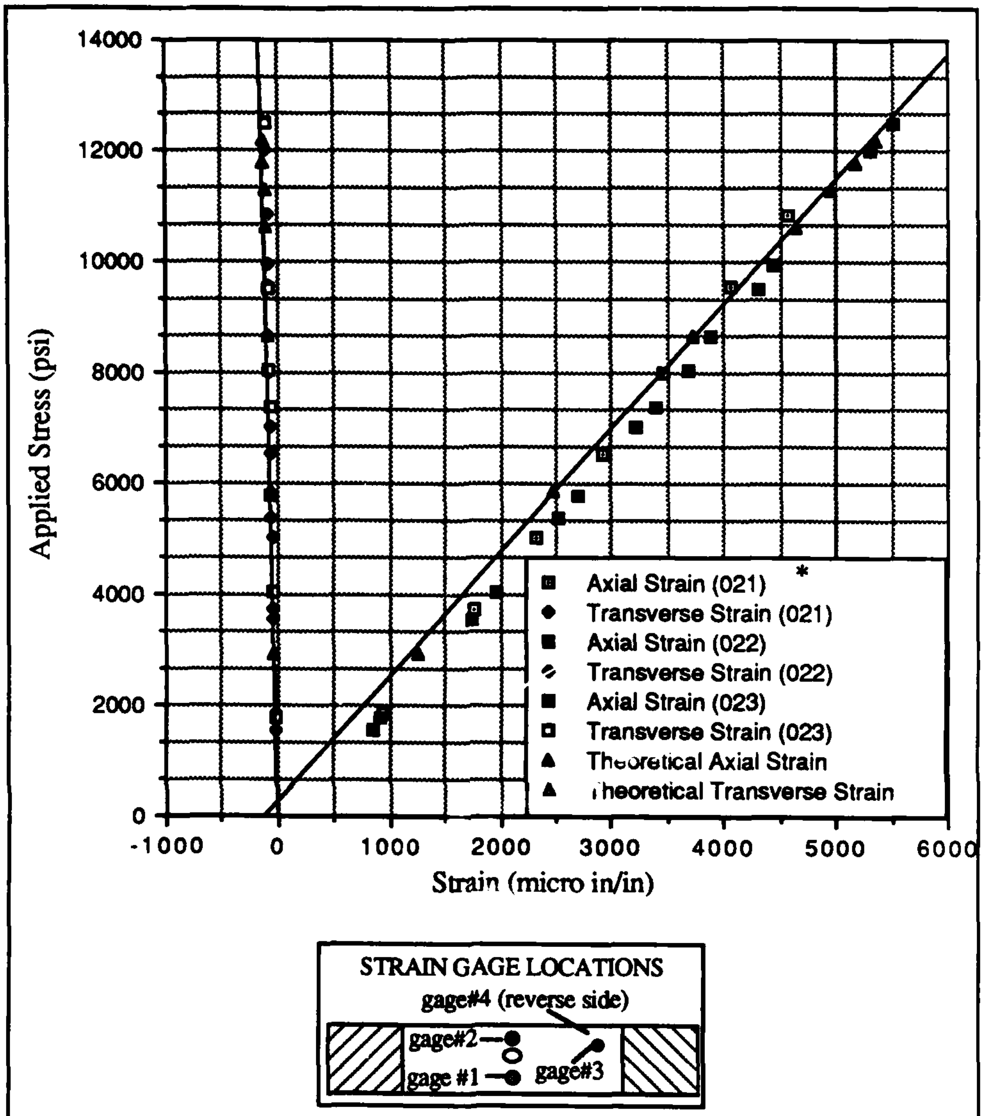

NOTES:

1. * indicates serial number of test specimen
2. 90 degree lay-up / eccentricity=0.3" / no mounting fixture

Figure 5-21. Far Field (gage #3) Stress Strain Response

Table 5-7. Experimental Results for $[\pm 45^{\circ}]_{4s}$ Laminates.

Serial Number	Eccentricity	Mounting Fixture	Failure Load (lbs)
028	0.0"		2434.54
029	0.0"		2289.37
030	0.0"		2290.32
031	0.1"		2807.02
032	0.1"		3044.05
033	0.1"		3261.84
034	0.3"		4122.58
035	0.3"		4030.70
036	0.3"		3813.52
037	0.3"	✓*	4537.12
038	0.3"	✓	4421.36
039	0.3"	✓	4105.35

* (✓ indicates that the mounting fixture was used)

shows the percent difference between the average experimental failure loads and the analytical predictions of failure loads. This percent difference was calculated from equation (2), Section V B(1).

The failure loads predicted analytically were significantly lower than the experimental failure loads (see Table 5-8). This difference may be caused by a phenomenon known as scissoring. This phenomenon can best be described as a tendency of the ±45 degree fibers to align themselves with the load. This phenomenon was noted by [10,13] and is shown in Figure 5-23. The result of scissoring is that the laminate is able to sustain higher loads. This is due to the fact that scissoring causes the fibers, the principle load carriers, to become more aligned with the load (see Figure 5-23). Therefore, the laminate is able to

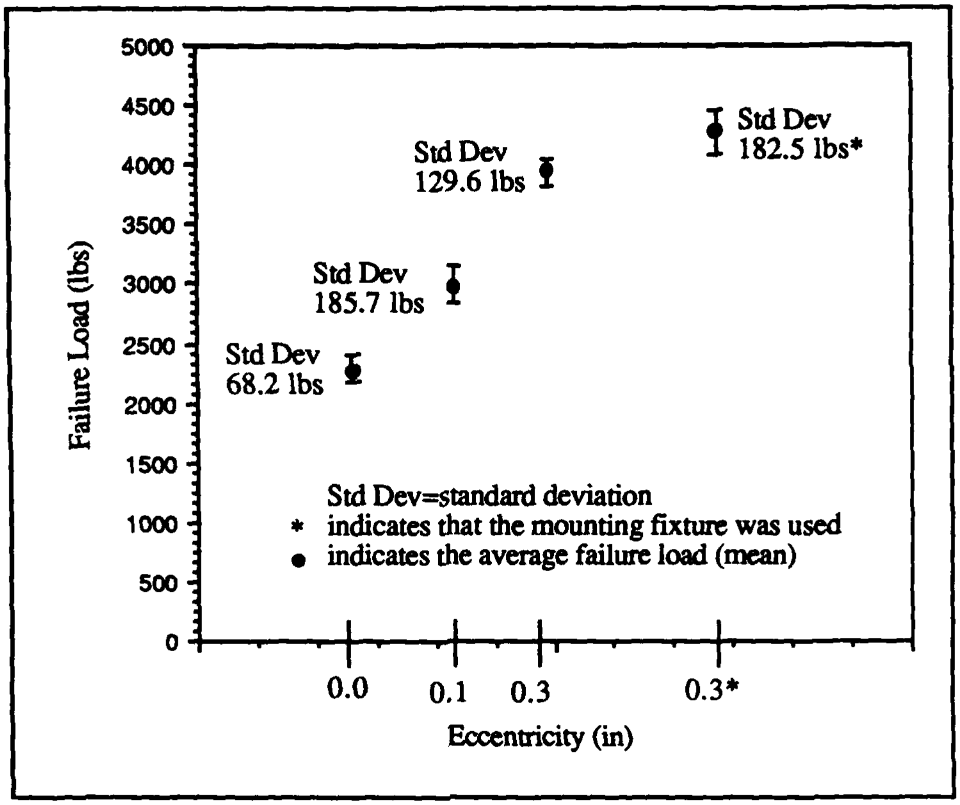

Figure 5-22. Experimental Scatter for $[\pm45^{\circ}]_{4s}$ Laminates

Table 5-8. Summary of Average Experimental Failure Loads and Analytical Failure Loads for $[\pm45^{\circ}]_{4s}$ Laminates.

Eccentricity	Average Experimental Failure Load (lbs)	Analytical Failure Load (lbs)	% diff. (Ex. vs Anal.)
0.0" (no fixture)	2338.08	1949.26	+16.6%
0.1" (no fixture)	3037.64	2133.70	+29.8%
0.3" (no fixture)	3988.93	2931.39	+26.5%
0.3" (with fixture)	4354.61	2590.33	+40.5%

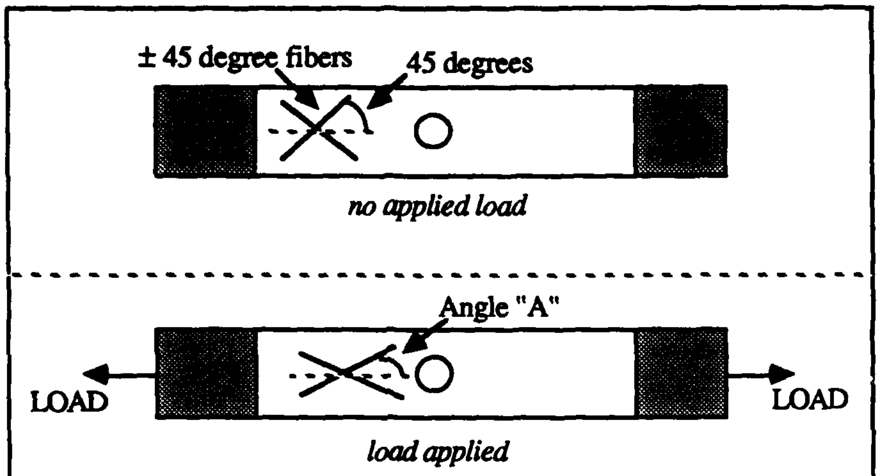

Note: Angle "A" is less than 45 degrees. This decrease (from the original 45 degrees) is caused by scissoring. Also note that the fibers are tending to align themselves with the loading.

Figure 5-23. Scissoring of ±45 Degree Fibers

sustain higher loading. Since the ply orientations (±45 degree is this case) are fixed as inputs to the nonlinear material finite element program, the nonlinear analysis did not account for scissoring. It should be pointed out that scissoring is a nonlinear strain-displacement phenomenon; therefore, it is a geometric nonlinearity as opposed to a material nonlinearity (such as stress-strain). As a result, the nonlinear predictions of failure loads are lower than those obtained experimentally (Table 5-8). Another possibility for the difference in experimental and analytical failure loads, is the fact that the two-dimensional approach used in this study did not take into account any of the interlaminar stresses, or other three-dimensional effects, that may alter the failure loads for this stacking sequence.

If the analytical predictions of the nominal (far field) failure stresses are examined, the effects of eccentricity on the nominal failure stress can be determined. Table 5-9 lists both the analytical failure loads and the nominal (far field) failure stresses. As previously discussed (Section V B(1)), the distance from the edge of the discontinuity to the edge of the

Table 5-9. Summary of Analytical Failure Loads and Nominal (far field) Failure Stresses for $[\pm 45^{\circ}]_{4s}$ Laminates.

Eccentricity	Analytical Failure Load (lbs)	Nominal Failure (far field) Stress (psi)
0.0" (no fixture)	1949.26	19,337.90
0.1" (no fixture)	2133.70	18,143.71
0.3" (no fixture)	2931.39	19,387.50
0.3" (with fixture)	2590.33	17,131.81

specimen (Figure 4-2) was always greater than or equal to the diameter of the discontinuity (0.4"). This distance was maintained so that edge effects would not vary for the different values of eccentricity considered in this study. From Table 5-9, note that the analytical predictions of nominal failure stresses do not appreciably differ for the different values of eccentricity; therefore, since edge effects were controlled by maintaining at least 0.4 inches between the edge of the discontinuity and the edge of the specimen, it appears that the values of eccentricity considered in this study did not appreciably affect the nominal failure stress for this stacking sequence.

The knock down (reduction) of the nominal failure stress, due to the 0.4" discontinuity, was calculated from Table 5-9. The nominal failure stress for these laminates, without a discontinuity, is equal to 56,170 psi [13]. Therefore, the nominal failure stress was reduced by a factor of approximately 3. The reduction of nominal failure stress, due to a circular discontinuity, for an isotropic material of the same geometry, is reported as 3.46 [15].

The failure mode of these specimens was visible as a shear dominated failure surface (i.e. mode II dominated the failure). This shear dominated failure surface and the high strains (visible as necking) near the discontinuity, are shown in Figures 5-24 and 5-25.

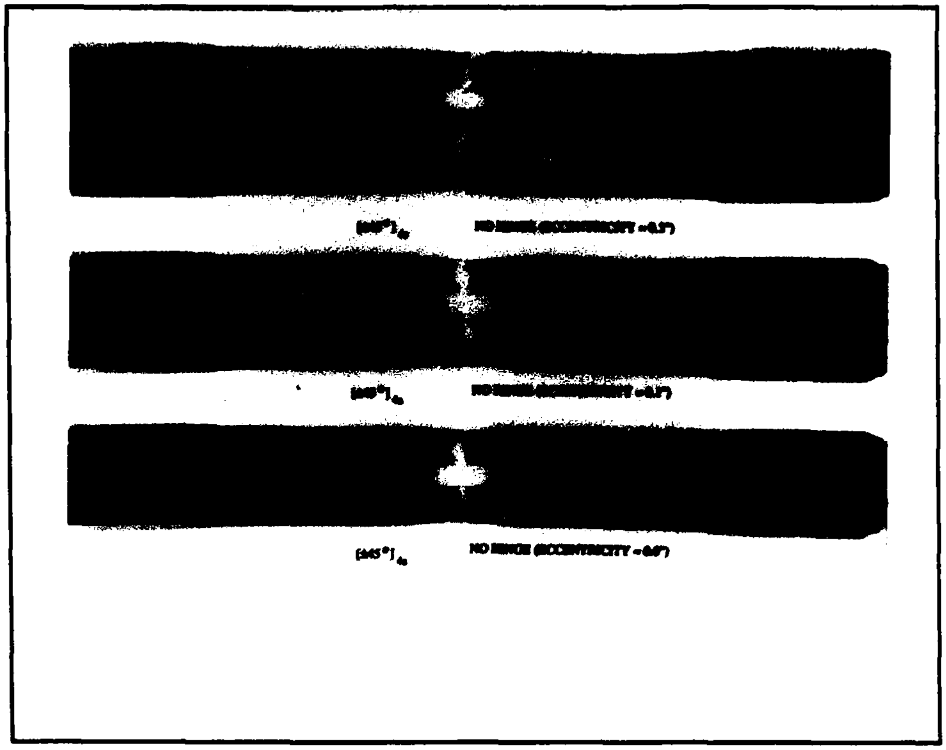

Figure 5-24. Failed $[\pm 45^{\circ}]_{4s}$ Specimens (no mounting fixture)

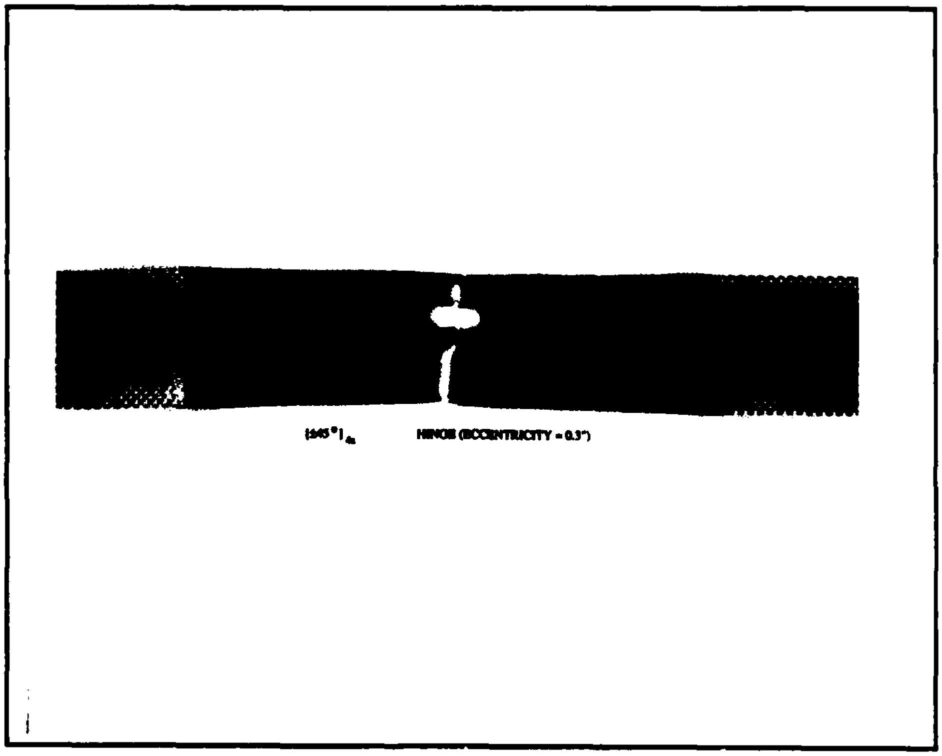

Figure 5-25. Failed $[\pm 45^{\circ}]_{4s}$ Specimen (mounting fixture)

Figures 5-26 through 5-29 show the analytical predictions of failure progression and failure loads for the $[\pm 45^{o}]_{4s}$ laminates. From these figures, note that the damage zones (failed finite elements) appear to be failing in ±45 degree directions. Therefore, it appears that the analytical solution is predicting a shear (mode II) type failure. However, previous research by [13] examined Gr/PEEK laminates, for zero eccentricity, which had been tested to a percentage of their failure load. Through the use of stereo x-rays, the failure zones appeared as triangular areas above and below the discontinuity [13]. These damaged zones, at 95% of failure load [13], are reproduced in Figure 5-30. The difference in failure zones between those predicted analytically (this study) and those shown in Figure 5-30 [13], might be due to the fact that interlaminar stresses, and other three-dimensional effects, were not considered in this study.

Stress-strain response plots for the eccentricity = 0.3" model were constructed (Figures 5-31 through 5-33). Figure 5-31 shows the experimental and analytical near field response at strain gage #1. The experimental and analytical near field response at strain gage #2 is shown in Figure 5-32. And finally, the experimental and analytical far field response is shown in Figure 5-33 as the average strains from strain gages #3 and #4. From these three figures, note that very little experimental data was available. This is due to the fact that two of the three specimens tested experimentally did not provide strain information. The strain gages on these two specimens "saturated" at a very low level of load. This saturation resulted from improperly adjusted instrumentation equipment, and was not the result of strains above the operating limits of the gages (gages used were good up to 5% strain). The strain gages on the specimen, which did provide strain information, saturated at approximately 4% far field strain (Figure 5-33), and between 1% and 2% near field strain (Figures 5-31 and 5-32). The ±45 degree laminates are difficult (experimentally) to obtain strain data for; this is due to high strains present at the failure loads [10.13]. In addition,

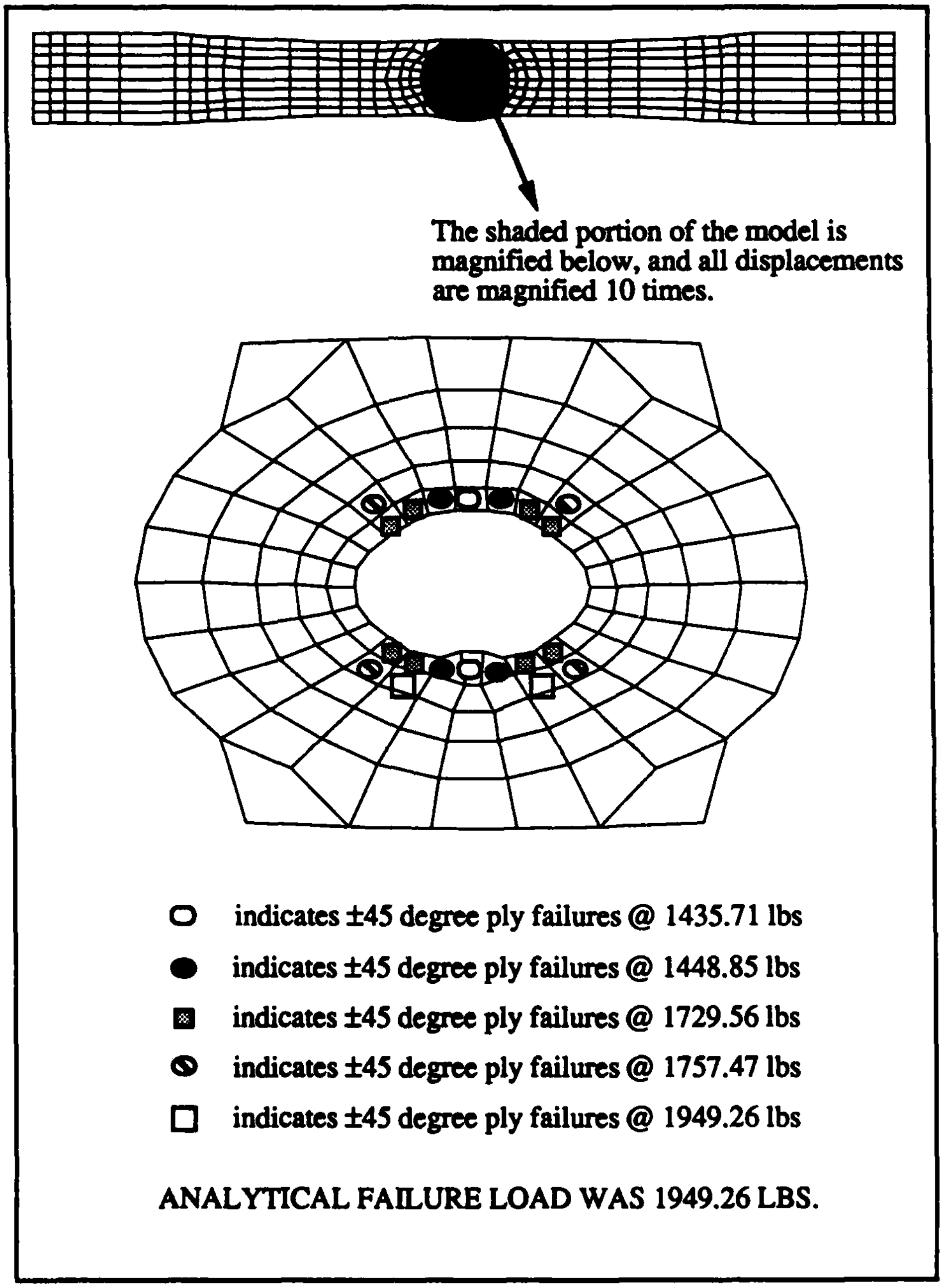

○ indicates ±45 degree ply failures @ 1435.71 lbs

● indicates ±45 degree ply failures @ 1448.85 lbs

▨ indicates ±45 degree ply failures @ 1729.56 lbs

⊘ indicates ±45 degree ply failures @ 1757.47 lbs

☐ indicates ±45 degree ply failures @ 1949.26 lbs

ANALYTICAL FAILURE LOAD WAS 1949.26 LBS.

Figure 5-26. Failure Progression (±45 degree / e=0.0" / no mounting fixture)

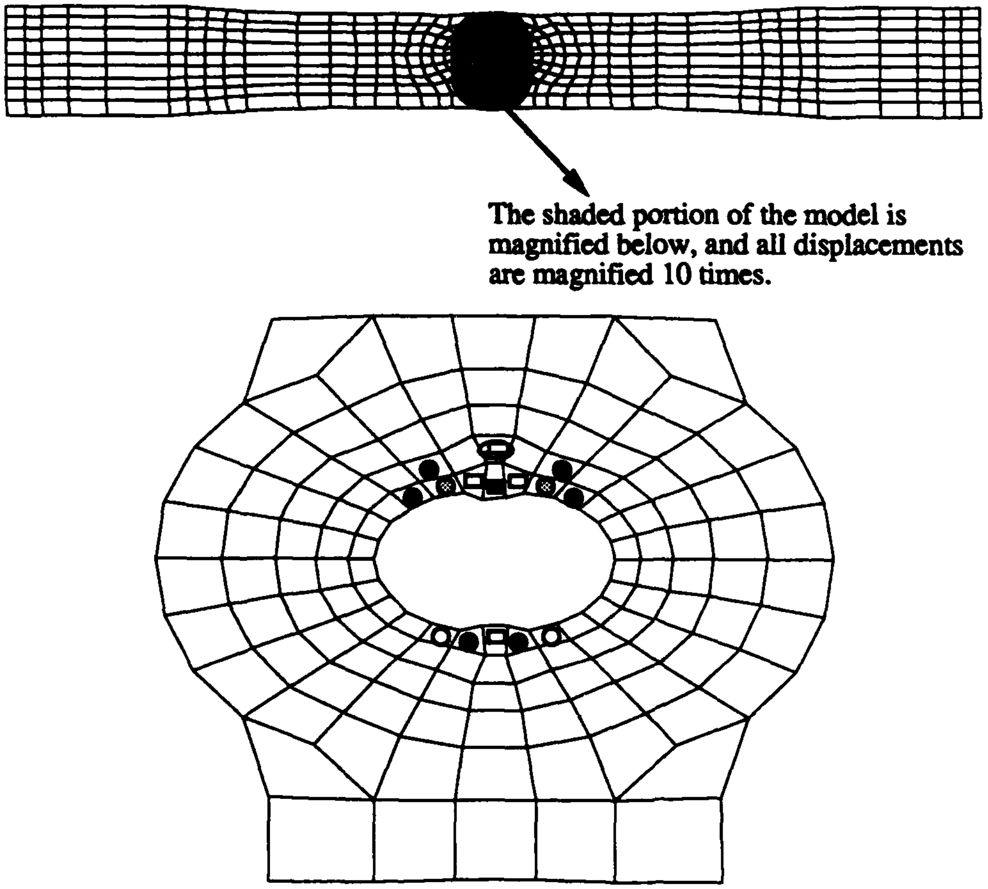

The shaded portion of the model is magnified below, and all displacements are magnified 10 times.

■ indicates ±45 degree ply failures @ 1710.67 lbs

□ indicates ±45 degree ply failures @ 1736.16 lbs

◉ indicates ±45 degree ply failures @ 1920.35 lbs

● indicates ±45 degree ply failures @ 1927.32 lbs

○ indicates ±45 degree ply failures @ 2117.58 lbs

⊖ indicates ±45 degree ply failures @ 2132.19 lbs

ANALYTICAL FAILURE LOAD WAS 2132.19 LBS.

Figure 5-27. Failure Progression (±45 degree / e=0.1" / no mounting fixture)

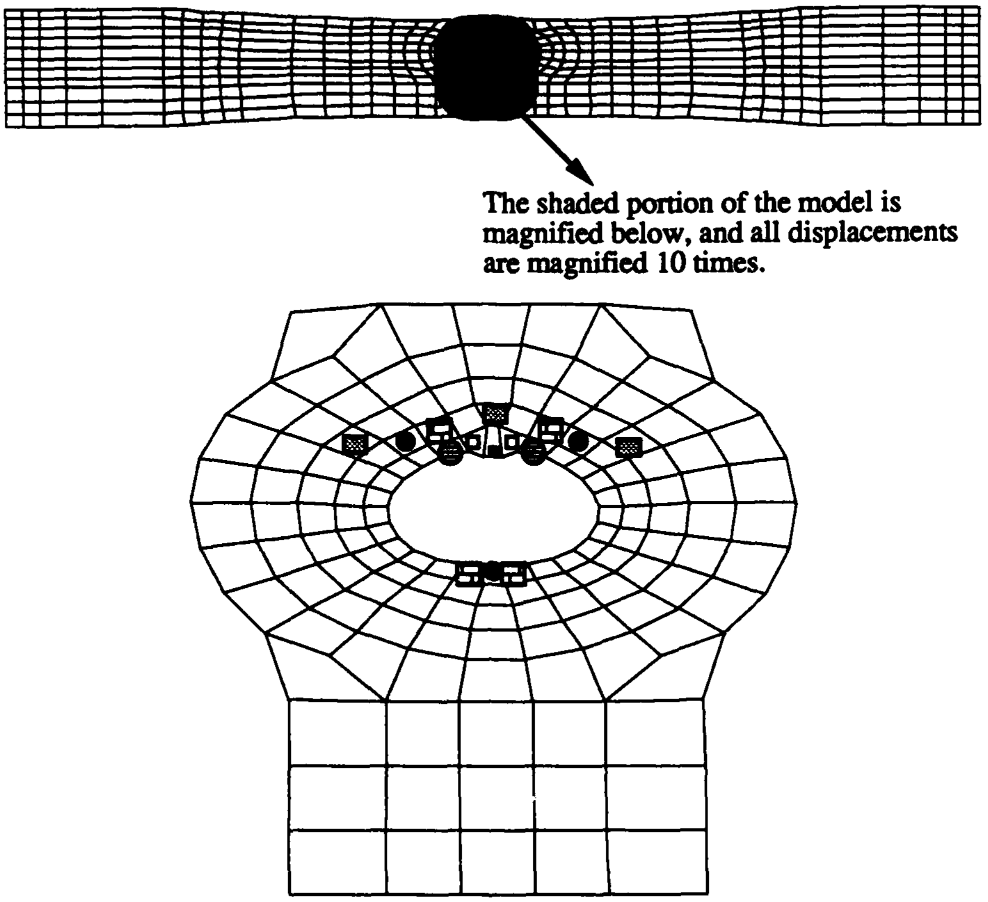

The shaded portion of the model is magnified below, and all displacements are magnified 10 times.

- ▪ indicates ±45 degree ply failures @ 2403.13 lbs
- □ indicates ±45 degree ply failures @ 2438.23 lbs
- ● indicates ±45 degree ply failures @ 2652.16 lbs
- • indicates ±45 degree ply failures @ 2672.68 lbs
- ⊟ indicates ±45 degree ply failures @ 2733.16 lbs
- ▨ indicates ±45 degree ply failures @ 2929.94 lbs

ANALYTICAL FAILURE LOAD WAS 2929.94 LBS.

Figure 5-28. Failure Progression (±45 degree / e=0.3" / no mounting fixture)

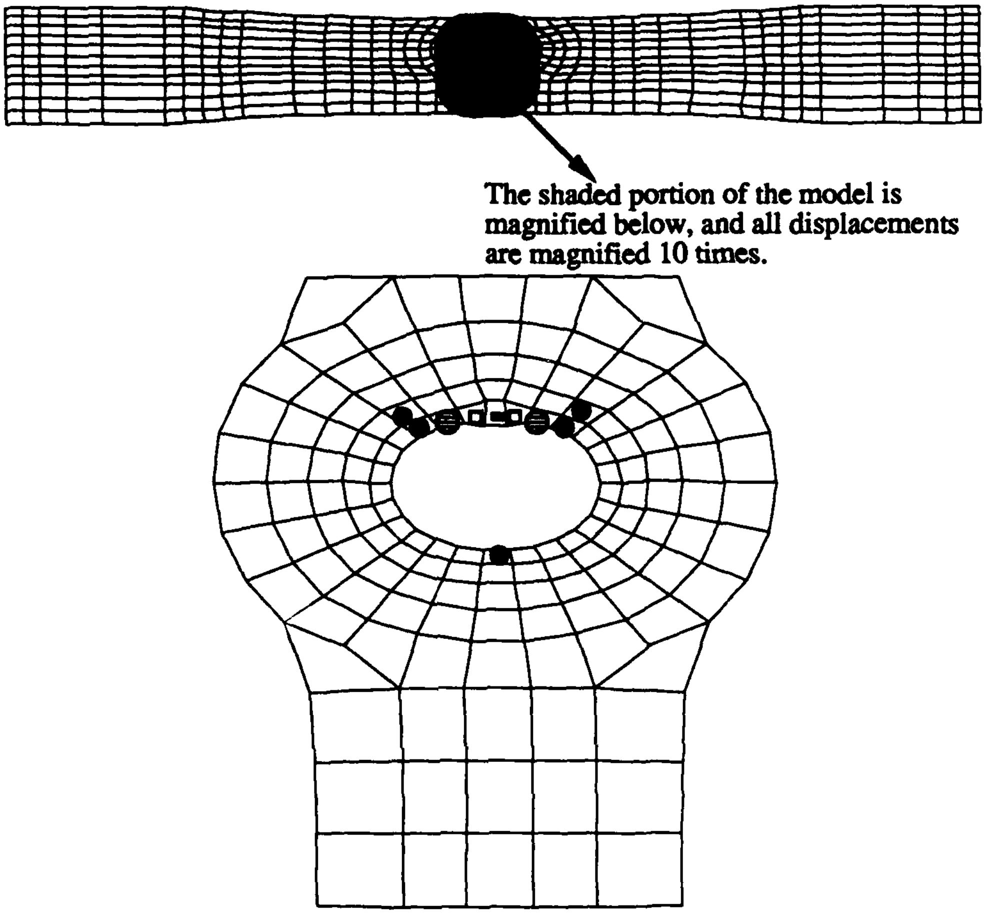

The shaded portion of the model is magnified below, and all displacements are magnified 10 times.

- ■ indicates ±45 degree ply failures @ 2287.55 lbs
- □ indicates ±45 degree ply failures @ 2321.40 lbs
- ⊖ indicates ±45 degree ply failures @ 2549.89 lbs
- ● indicates ±45 degree ply failures @ 2587.96 lbs

ANALYTICAL FAILURE LOAD WAS 2587.96 LBS.

Figure 5-29. Failure Progression (±45 degree / e=0.3" / mounting fixture)

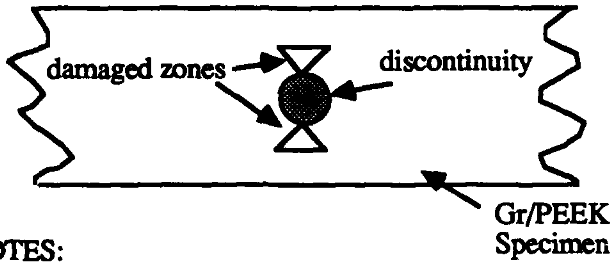

NOTES:

1. Figure shows center section of laminate only.
2. This drawing was created from Figure 77 [13].
3. Intent is ONLY to show experimentally obtained damaged areas.

Figure 5-30. Damaged Zones $[\pm 45^{\circ}]_{4s}$ Laminate [13]

scissoring has also been found to contribute to the premature failure of strain gages on these laminates [10,13]. The analytical stress-strain response predictions do not appear to correlate well with the experimental stress-strain response (except for very low levels of load). However, since only one specimen provided strain information, the analytical predictions of stress-strain response could not be adequately compared with the experimental stress-strain response.

Even though the stress-strain response plots (Figures 5-31 through 5-33) did not provide as much insight into the stress-strain behavior of this laminate as desired, a "numerical instability" in the analysis is obvious in Figure 5-32. This numerical instability is apparent as a scattering of the data at high levels of loading (Figure 5-32). These load levels resulted in the failure of the finite elements shown in Figure 5-28. This numerical instability caused the program to stop execution due to the nonconvergence of incremental strains resulting from an addition increment of load (equation (41), Section II C). Therefore, for this laminate, the load at which the program stopped execution was considered to be the analytical failure load.

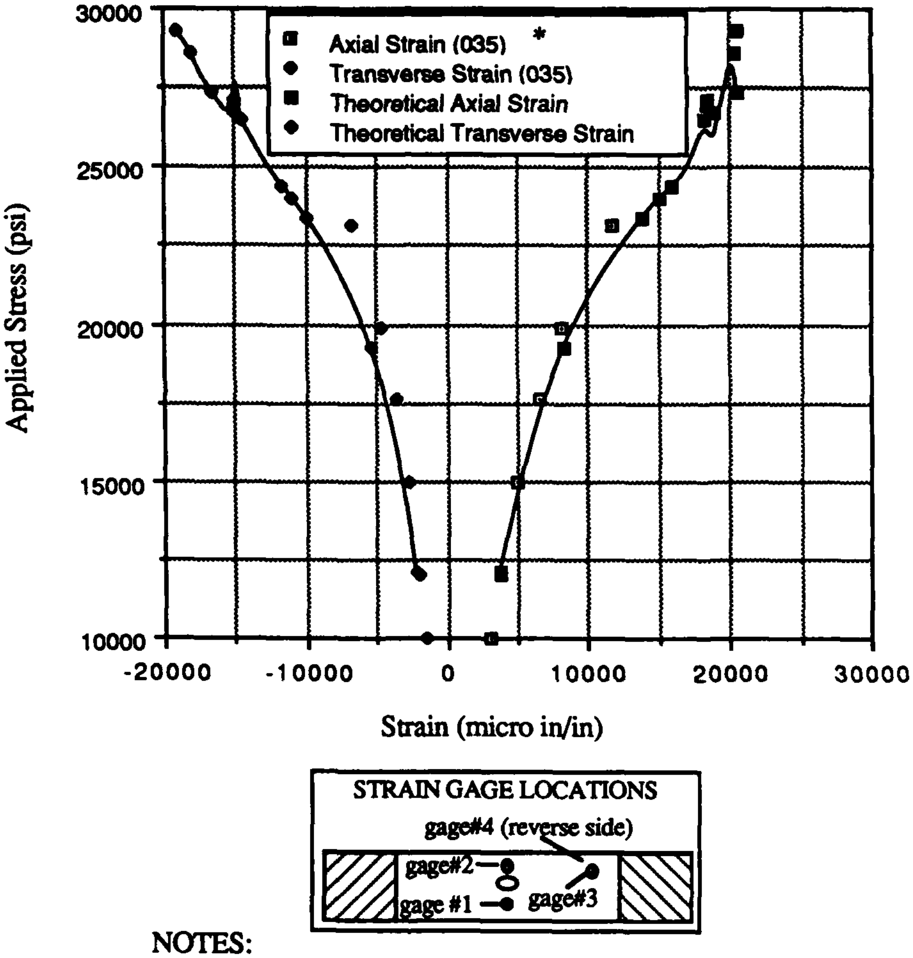

NOTES:

1. * indicates serial number of test specimen
2. ±45 degree lay-up / eccentricity=0.3" / no mounting fixture
3. no data available from specimens 034 & 036 (gages saturated)

Figure 5-31. Near Field (gage #1) Stress Strain Response

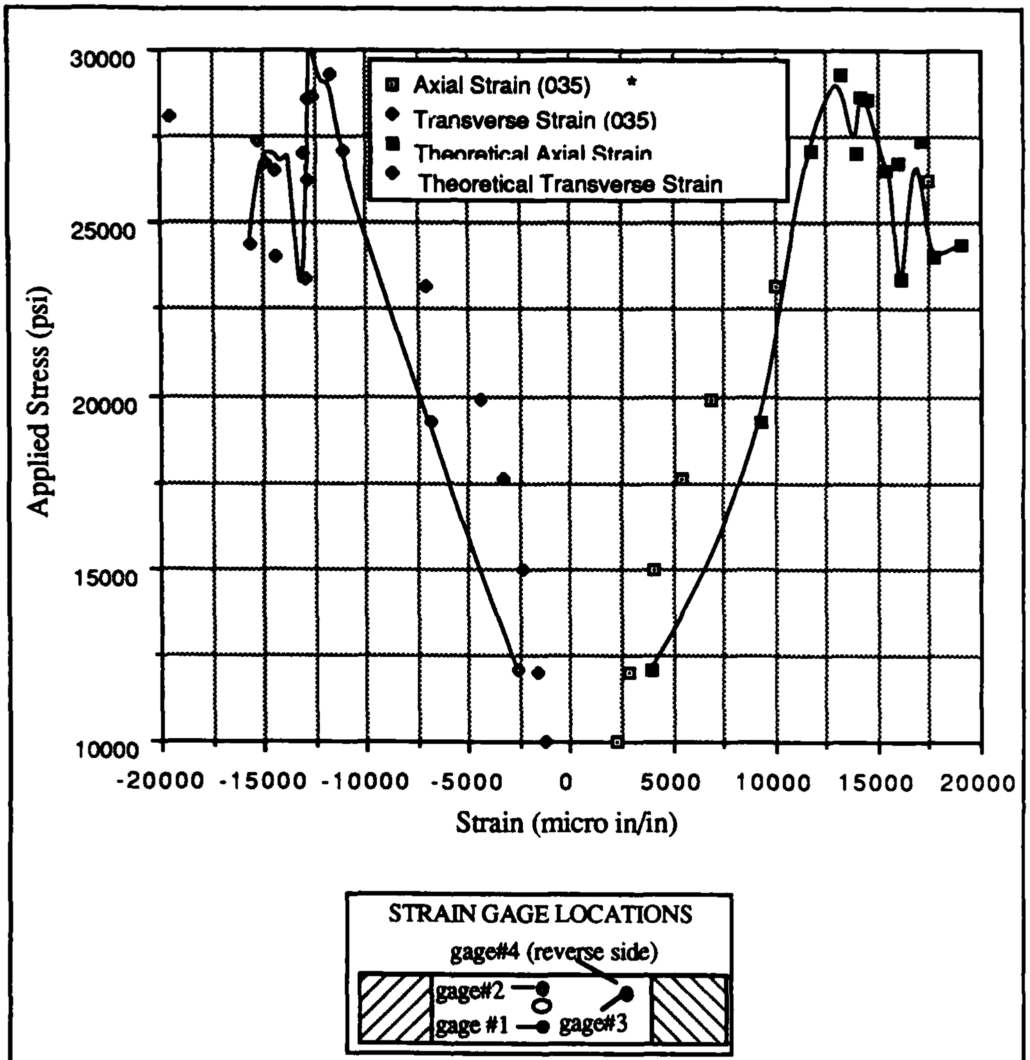

NOTES:

1. * indicates serial number of test specimen
2. ±45 degree lay-up / eccentricity=0.3" / no mounting fixture
3. no data available from specimens 034 & 036 (gages saturated)

Figure 5-32. Near Field (gage #2) Stress Strain Response

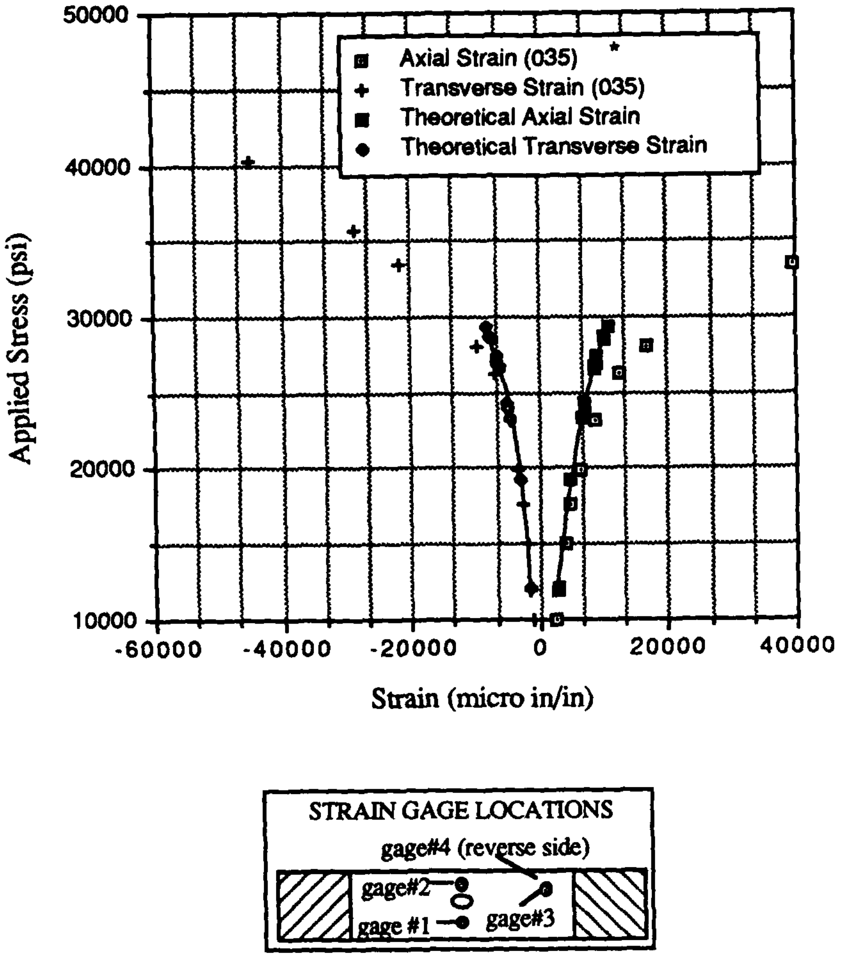

NOTES:

1. * indicates serial number of test specimen
2. ±45 degree lay-up / eccentricity=0.3" / no mounting fixture
3. no data available from specimens 034 & 036 (gages saturated)

Figure 5-33. Far Field (gage #3) Stress Strain Response

In summary, the analytical solution underestimated the failure loads (from 16.6% to 40.5%) for the $[\pm45^{o}]_{4s}$ laminates. This underestimation may be due to scissoring of the ±45 degree fibers, or may be a result of ignoring the interlaminar stresses (since this was a 2-D study). It appears that the analytical solution predicts a shear (mode II) failure for this stacking sequence, and the high strains at failure (necking) were also predicted analytically. Finally, although it appears that the analytical stress-strain response correlated (for low levels of load) with the experimental stress-strain response, the experimentation did not provide enough useful data to verify the analytical predictions of stress-strain response.

(4) $[0^{o}/\pm45^{o}/90^{o}]_{2s}$ laminates.

Table 5-10 shows the experimental results of the ultimate strength tests for the $[0^{o}/\pm45^{o}/90^{o}]_{2s}$ laminates. The scatter of the experimental data (Table 5-10) is shown graphically in Figure 5-34. This figure also lists the standard deviation for each hole location (value of eccentricity) tested experimentally. The standard deviation was calculated from equation (1), Section V B(1). Figure 5-34 shows that experimental scatter was not significant during the testing of these laminates.

A summary of the average experimental failure loads (calculated from Table 5-10), as well as the analytical predictions of failure loads, are given in Table 5-11. In addition, Table 5-11 shows the percent difference between the average experimental failure loads and the analytical predictions of failure loads. This percent difference was calculated from equation (2), Section V B(1).

If the analytical predictions of the nominal (far field) failure stresses are examined, the effects of eccentricity on the nominal failure stress can be determined. Table 5-12 lists both the analytical failure loads and the nominal (far field) failure stresses. As previously discussed (Section V B(1)), the distance from the edge of the discontinuity, to the edge of

Table 5-10. Experimental Results for $[0^\circ/\pm45^\circ/90^\circ]_{2s}$ Laminates.

Serial Number	Eccentricity	Mounting Fixture	Failure Load (lbs)
041	0.0"		4250.97
042	0.0"		3944.13
043	0.0"		4008.59
044	0.1"		4832.06
045	0.1"		4846.99
046	0.1"		5445.63
047	0.3"		6683.89
048	0.3"		6617.70
049	0.3"		6750.09
050	0.3"	✓*	6222.60
051	0.3"	✓	6413.33
052	0.3"	✓	6719.92

* (✓ indicates that the mounting fixture was used)

the specimen (Figure 4-2), was always greater than or equal to the diameter of the discontinuity (0.4"). This distance was maintained so that edge effects would not vary for the different values of eccentricity considered in this study. From Table 5-12, note that the analytical predictions of nominal failure stresses do not appreciably differ for the different values of eccentricity; therefore, since edge effects were controlled by maintaining at least 0.4 inches between the edge of the discontinuity and the edge of the specimen, it appears that the values of eccentricity considered in this study did not appreciably affect the nominal failure stress for this stacking sequence.

The nominal failure stress for $[0^\circ/\pm45^\circ/90^\circ]_{2s}$ laminates, without a discontinuity, is

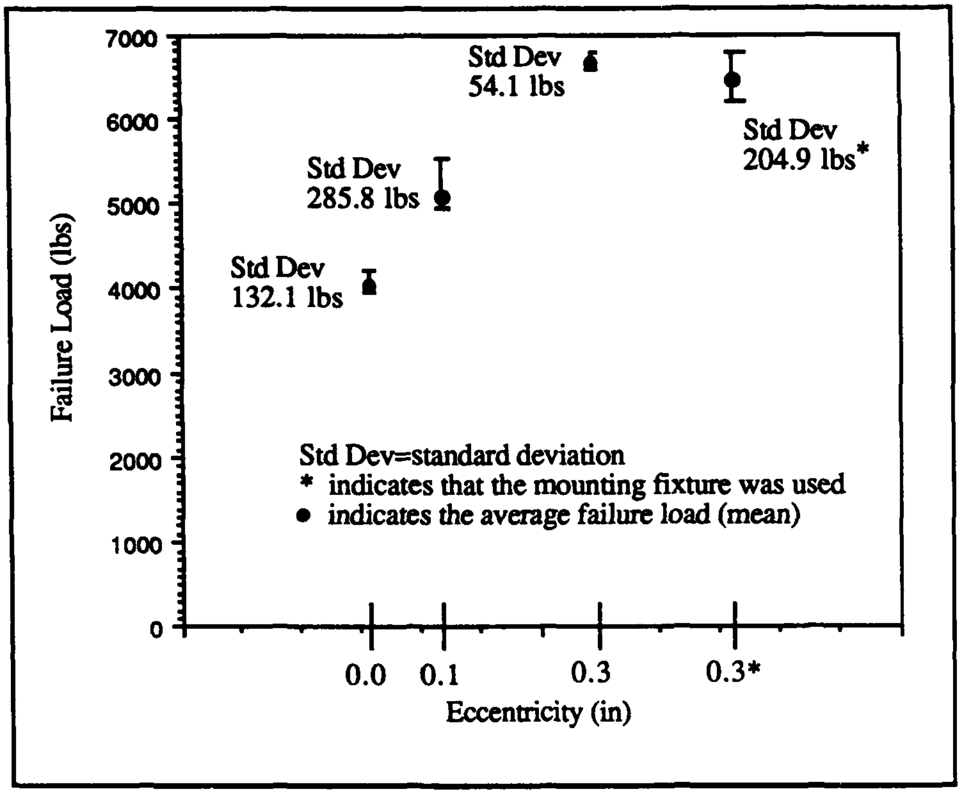

Figure 5-34. Experimental Scatter for $[0^\circ/\pm45^\circ/90^\circ]_{2s}$ Laminates

Table 5-11. Summary of Average Experimental Failure Loads and Analytical Failure Loads for $[0^\circ/\pm45^\circ/90^\circ]_{2s}$ Laminates.

Eccentricity	Average Experimental Failure Load (lbs)	Analytical Failure Load (lbs)	% diff. (Ex. vs Anal.)
0.0" (no fixture)	4067.90	3920.27	+3.6%
0.1" (no fixture)	5041.56	4810.02	+4.6%
0.3" (no fixture)	6683.89	6388.39	+4.4%
0.3" (with fixture)	6451.95	6323.25	+2.0%

Table 5-12. Summary of Analytical Failure Loads and Nominal (far field) Failure Stresses for $[0^o/\pm45^o/90^o]_{2s}$ Laminates.

Eccentricity	Analytical Failure Load (lbs)	Nominal Failure (far field) Stress (psi)
0.0" (no fixture)	3920.27	38,891.57
0.1" (no fixture)	4810.02	40,901.53
0.3" (no fixture)	6388.39	42,251.26
0.3" (with fixture)	6323.25	41,820.44

equal to 98,400 psi [17]. Therefore, for this laminate, the nominal failure stress, due to the 0.4" discontinuity, was reduced by a factor of approximately 2.4 (see nominal failure stresses, Table 5-12). This is *lower* than the reduction of nominal failure stress (due to a circular discontinuity) for an isotropic material of the same geometry; reported as 3.46 by [15].

The failure mode of these specimens was visible as a shear (mode II) failure surface (Figures 5-35 and 5-36). However, the shear failure, mode II, for these laminates (Figures 5-35 and 5-36) does not appear to be as shear dominated as was noted for the $[\pm45^o]_{4s}$ laminates (Figures 5-24 and 5-25). Therefore, it appears that the failure surface (region) is a combination of the failure modes noted for the $[0^o{}_{16}]$, $[90^o{}_{16}]$, and the $[\pm45^o]_{4s}$ laminates.

Figures 5-37 through 5-40 show the analytical predictions of failure progression and failure loads for the $[0^o/\pm45^o/90^o]_{2s}$ laminates. Note, from these figures, that the shear (mode II) failure is not predicted analytically. This could be due to several reasons. First, recall (Section V B(3)) that the ±45° plies require large strains before failure; but, the 0° plies in the $[0^o/\pm45^o/90^o]_{2s}$ laminates prevent large strains. Therefore, once the level of

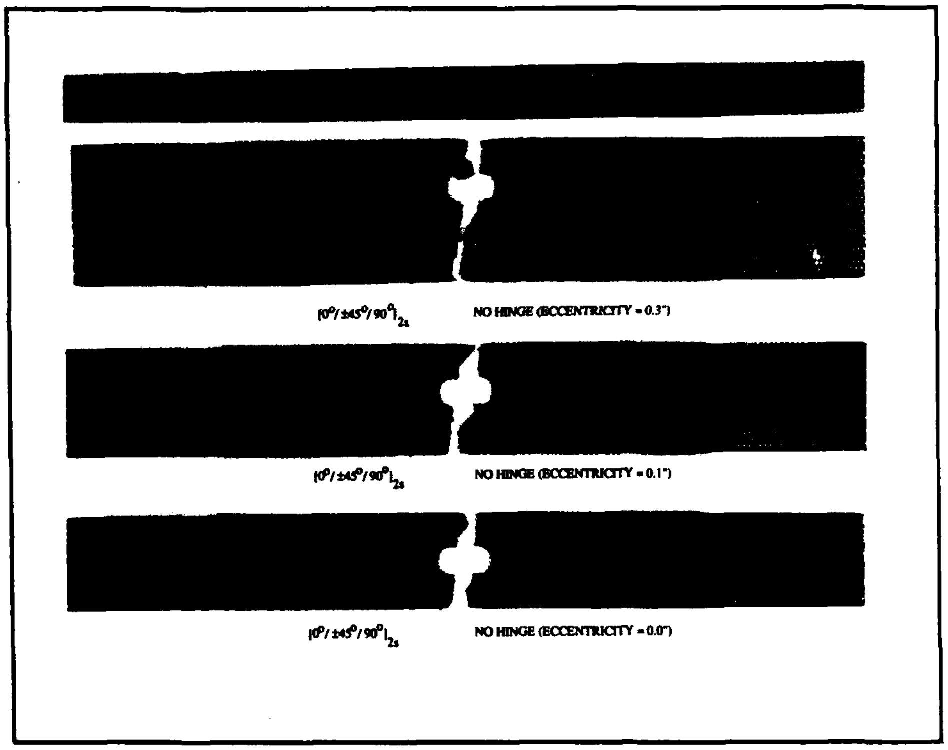

Figure 5-35. Failed $[0^\circ/\pm45^\circ/90^\circ]_{2s}$ Specimens (no mounting fixture)

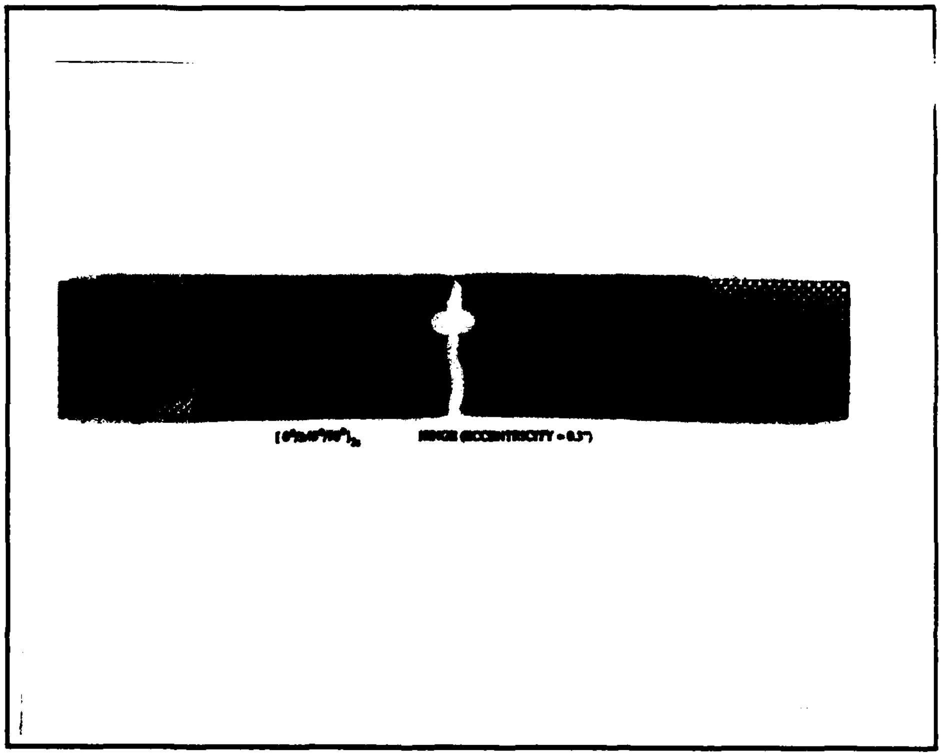

Figure 5-36. Failed $[0^\circ/\pm45^\circ/90^\circ]_{2s}$ Specimen (mounting fixture)

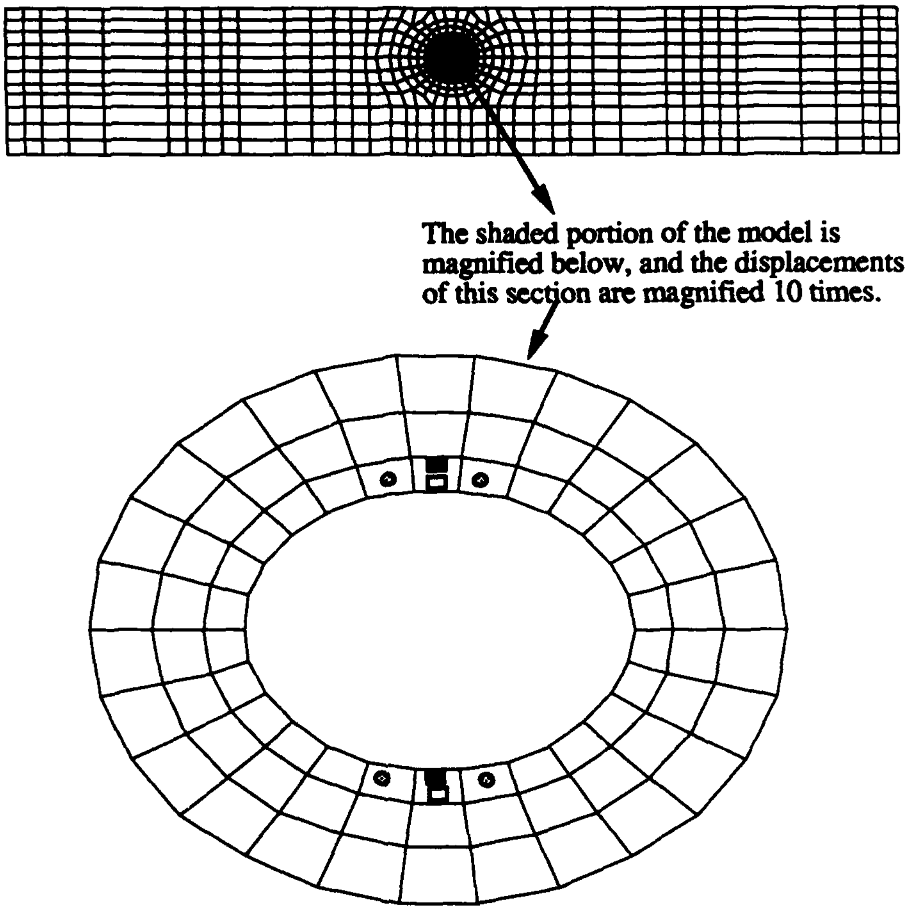

The shaded portion of the model is magnified below, and the displacements of this section are magnified 10 times.

■ indicates 90 degree ply failure at 3680.20 lbs

● indicates 90 degree ply failure at 3920.27 lbs

☐ indicates 0 degree ply failure at 3920.27 lbs

NOTE: Only the area around the hole shown for clarity.

ANALYTICAL FAILURE LOAD WAS 3920.27 LBS.

Figure 5-37. Failure Progression (quasi / e=0.0" / no mounting fixture)

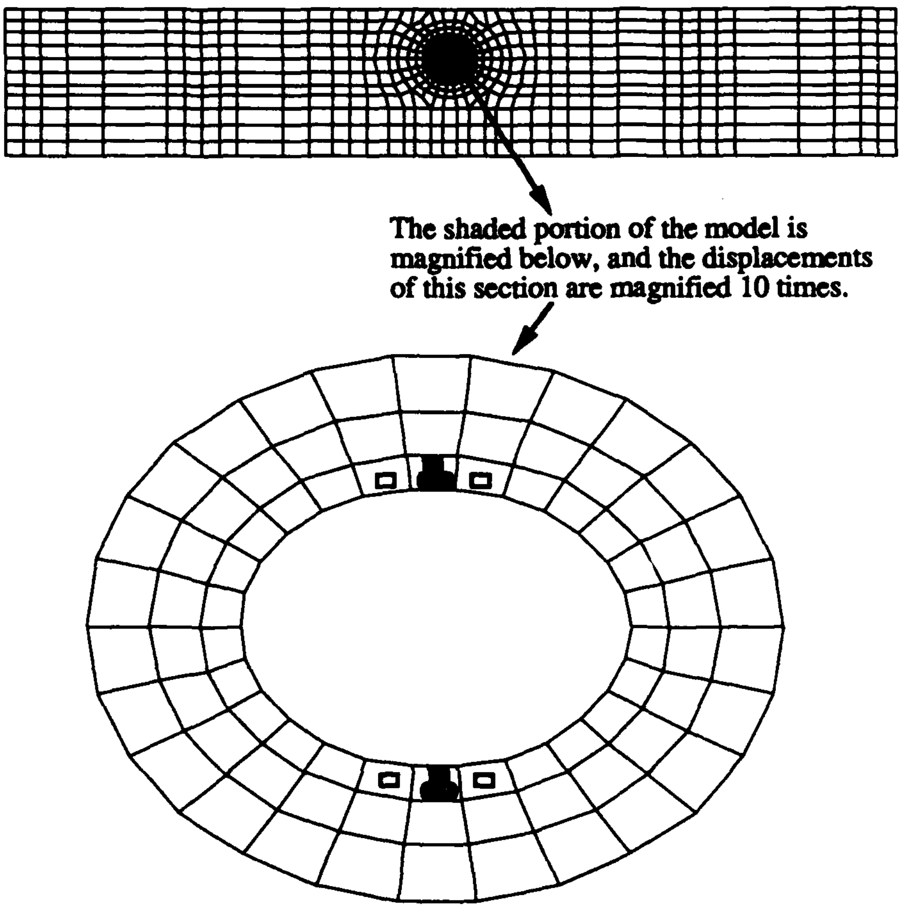

The shaded portion of the model is magnified below, and the displacements of this section are magnified 10 times.

■ indicates 90 degree ply failure at 4335.02 lbs

□ indicates 90 degree ply failure at 4810.02 lbs

● indicates 0 degree ply failure at 4810.02 lbs

NOTE: Only the area around the hole shown for clarity.

ANALYTICAL FAILURE LOAD WAS 4810.02 LBS.

Figure 5-38. Failure Progression (quasi / e=0.1" / no mounting fixture)

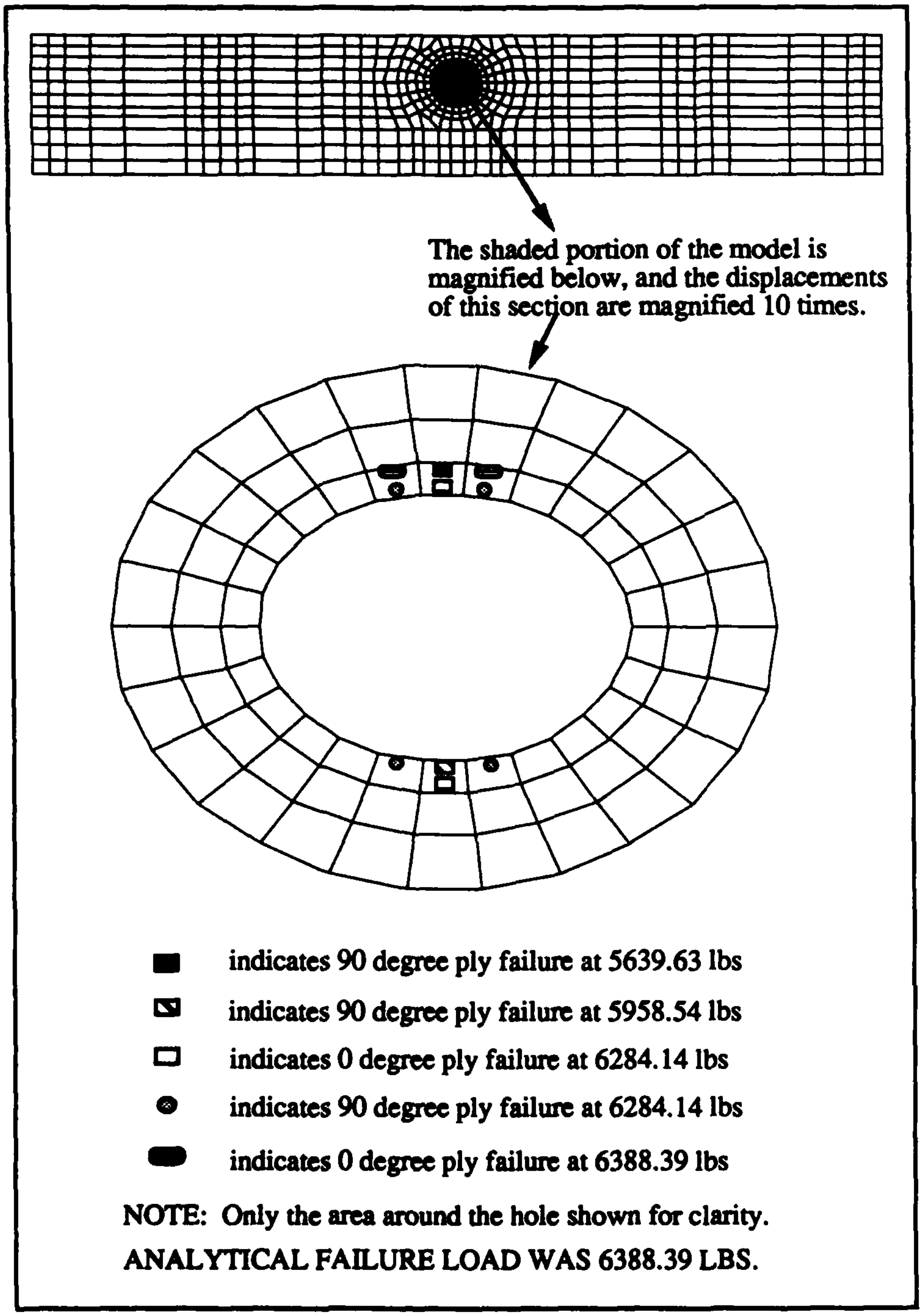

The shaded portion of the model is magnified below, and the displacements of this section are magnified 10 times.

■ indicates 90 degree ply failure at 5639.63 lbs

▧ indicates 90 degree ply failure at 5958.54 lbs

□ indicates 0 degree ply failure at 6284.14 lbs

⊗ indicates 90 degree ply failure at 6284.14 lbs

⬬ indicates 0 degree ply failure at 6388.39 lbs

NOTE: Only the area around the hole shown for clarity.

ANALYTICAL FAILURE LOAD WAS 6388.39 LBS.

Figure 5-39. Failure Progression (quasi / e=0.3" / no mounting fixture)

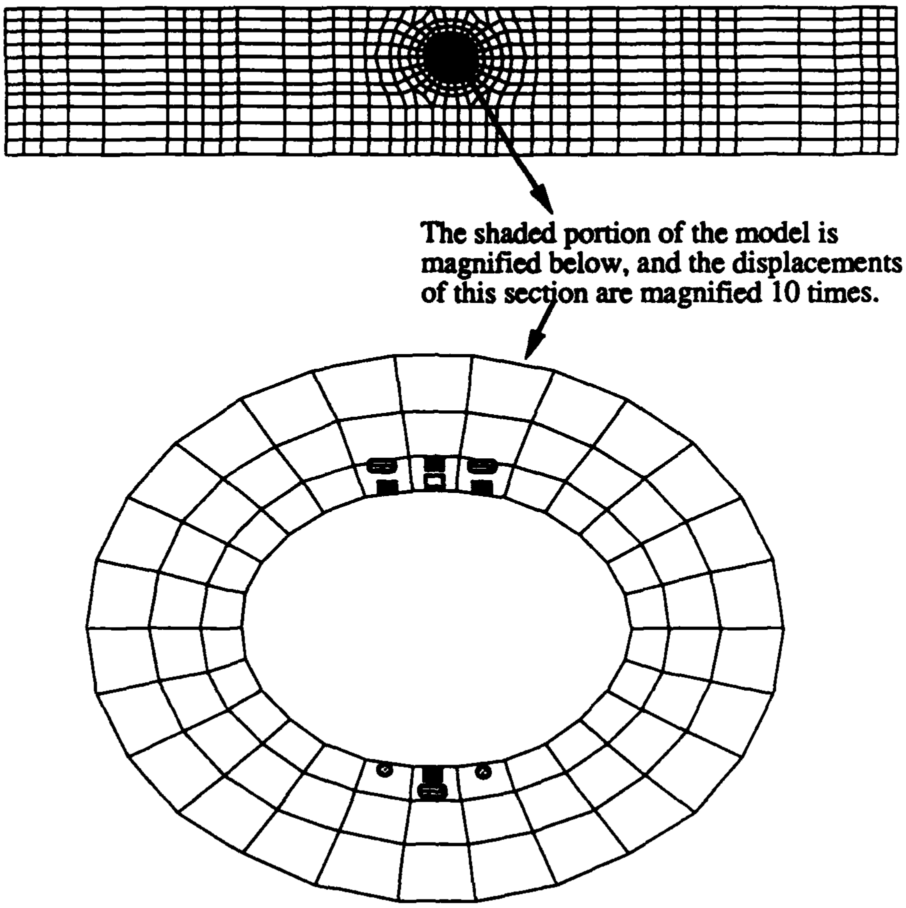

The shaded portion of the model is magnified below, and the displacements of this section are magnified 10 times.

■ indicates 90 degree ply failure at 6183.87 lbs

□ indicates 0 degree ply failure at 6183.87 lbs

◉ indicates 90 degree ply failure at 6323.25 lbs

⬬ indicates 0 degree ply failure at 6323.25 lbs

NOTE: Only the area around the hole shown for clarity.

ANALYTICAL FAILURE LOAD WAS 6323.25 LBS.

Figure 5-40. Failure Progression (quasi / e=0.3" / mounting fixture) loading is high enough to cause failure of the zero degree plies adjacent (above and below) to the discontinuity, the level of loading is much higher than the neighboring ±45° plies (or 90° plies) can sustain. As a result, Figures 5-37 through 5-40 show that the analytical solution predicted catastrophic failure of these laminates once the 0° plies adjacent (above and below) to the discontinuity failed. Another possibility which might have affected the analytical predictions of damage progression (Figures 5-37 through 5-40) is the fact that the two-dimensional study did not account for interlaminar stresses, which for this stacking sequence, may alter the failure mode.

Stress-strain response plots for the eccentricity = 0.3" model were constructed (Figures 5-41 through 5-43). Figure 5-41 shows the experimental and analytical near field response at strain gage #1. The experimental and analytical near field response at strain gage #2 is shown in Figure 5-42. And finally, the experimental and analytical far field response is shown in Figure 5-43 as the average strains from strain gages #3 and #4. From these three figures, note that there is good, within 10%, correlation (up to the level of loading which caused failure of the 0° plies) between the analytical predictions of axial stress-strain response, and the experimental axial stress-strain response. The analytical predictions of near field axial stress-strain response were found to deviate from the experimental stress-strain response at the level of loading which corresponded to the analytical failure of the zero degree plies adjacent, above and below, to the discontinuity (0° ply failures are shown in Figure 5-39). This deviation is shown in Figures 5-41 and 5-42. Finally, there was excellent correlation between the analytical predictions of transverse stress-strain response and the experimental stress-strain response.

In summary, the analytical solution did a good job of predicting the failure loads for the $[0^\circ/\pm45^\circ/90^\circ]_{2s}$ laminates. The analytical stress-strain response predictions correlated well with the experimental stress-strain response up to the point of 0° ply failures, adjacent to the discontinuity.

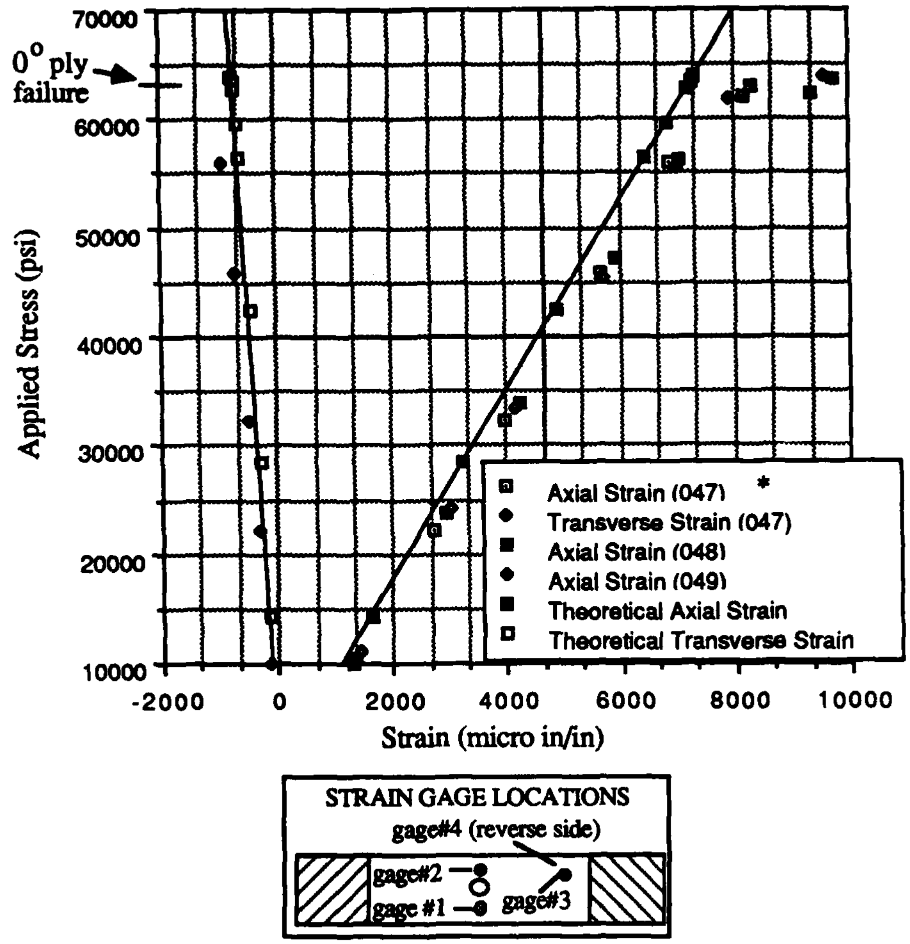

NOTES:

1. * indicates serial number of test specimen
2. quasi lay-up / eccentricity=0.3" / no mounting fixture
3. transverse strain data not available (specimens 048 or 049)

Figure 5-41. Near Field (gage #1) Stress Strain Response

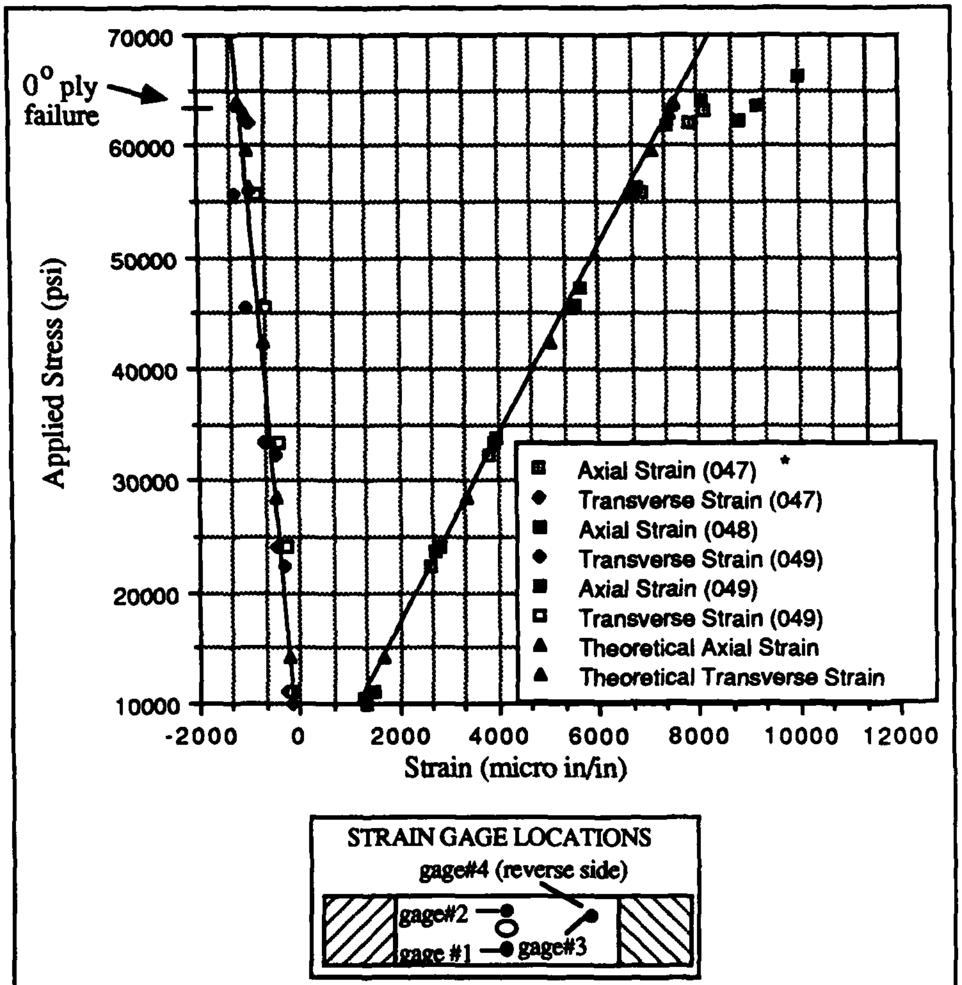

NOTES:

1. * indicates serial number of test specimen
2. quasi lay-up / eccentricity=0.3" / no mounting fixture

Figure 5-42. Near Field (gage #2) Stress Strain Response

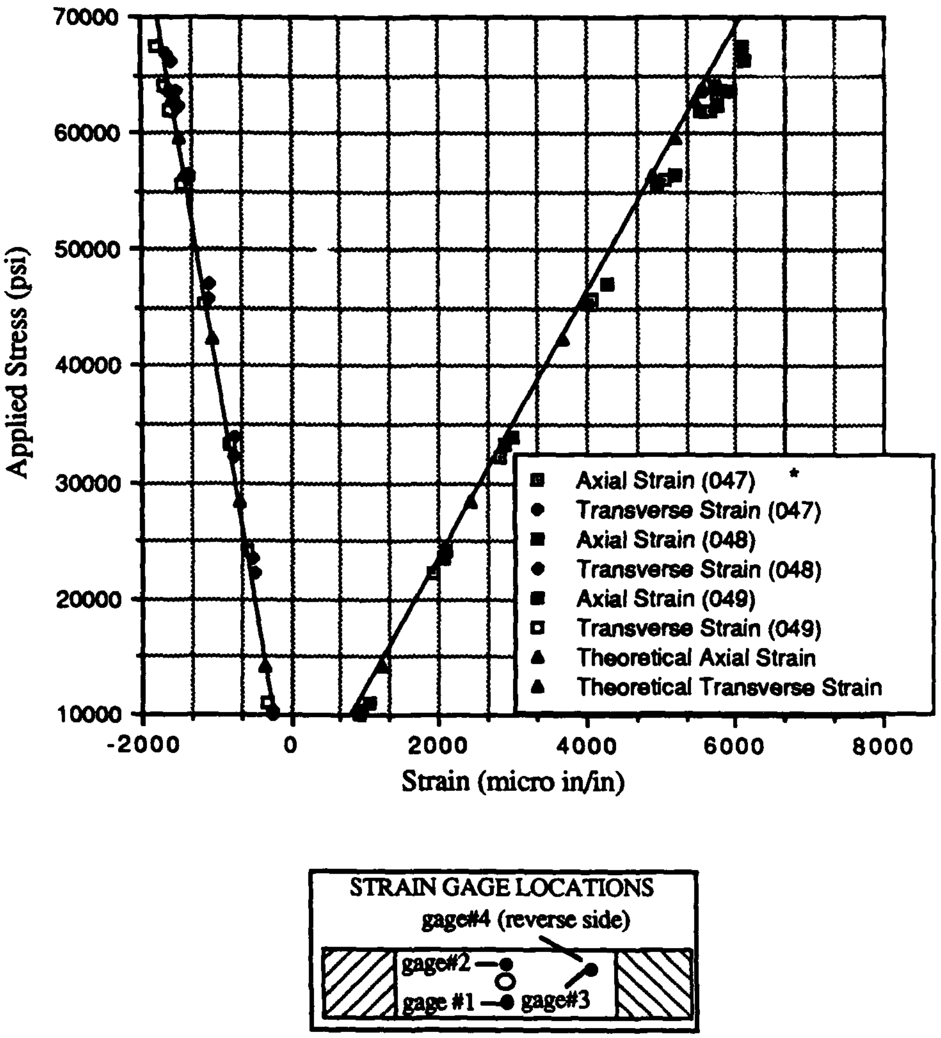

NOTES:

1. * indicates serial number of test specimen
2. quasi lay-up / eccentricity=0.3" / no mounting fixture

Figure 5-43. Far Field (gage #3) Stress Strain Response

(C) Eccentricity/Mounting Fixture - - Effects.

(1) Eccentricity Effects.

As discussed in detail in Section III E (1), the eccentric circular discontinuity creates a centroid (area) shift. This shift in centroid is shown in Figure 3-11.

The eccentricity effects and resulting bending moment (Figure 3-11), created higher tensile stresses above the discontinuity. Therefore, elements above the discontinuity tended to fail more quickly than corresponding elements below the discontinuity. These effects are quite obvious from the failure progression plots (Figures 5-16, 5-17, 5-18, 5-27, 5-28, 5-29, 5-39, 5-40).

From the experimentation, the eccentricity effects (in terms of failure progression) were not observed. This was due to the fact that failure was too rapid to determine if (by viewing the video tape frame by frame) failure initiated above or below the discontinuity. Only a limited quantity of Gr/PEEK panels were available for testing. Therefore, all specimens were tested to their ultimate failure load. If more Gr/PEEK panels had been available during this study, the experimental verification of the analytical predictions of eccentricity effects on failure progression may have been possible. This could have been achieved by testing specimens to a percentage of their ultimate failure load. These specimens could have then been examined for damaged areas through the use of stereo x-ray techniques [10,13], and failure initiation, as well as failure progression, could have been determined.

(2) Mounting Fixture Effects.

The linear study, Section III E, predicted that the use of the mounting fixture would not appreciably affect the stress state near the discontinuity. However, the nonlinear analysis predicted slightly lower failure loads for models which utilized the boundary conditions (Section III D) associated with the mounting fixture. These analytical failure loads are summarized (from Tables 5-2, 5-5, 5-8, and 5-11) in Table 5-13. These lower failure load

Table 5-13. Summary of Analytical Predictions of Failure Loads with and without the Mounting Fixture.		
Stacking Sequence	Analytical Failure Load (lbs) for eccentricity of 0.3" (mounting fixture)	Analytical Failure Load (lbs) for eccentricity of 0.3" (no mounting fixture)
$[0^{o}_{16}]$	8952.14	9241.27
$[90^{o}_{16}]$	1172.56	1217.37
$[\pm 45^{o}]_{4s}$	2590.33	2931.39
$[0^{o}/\pm 45^{o}/90^{o}]_{2s}$	6323.25	6388.39

predictions (for models which used the mounting fixture boundary conditions) can be explained in terms of the in-plane rotation which was permitted by the mounting fixture. The output data (for all four stacking sequences) was examined, and depending on the boundary conditions used (i.e. in-plane rotation was/was not permitted) a difference in near field axial stresses was noted. These differences in axial stresses can be explained by considering Figure 5-44. This figure shows two $[\pm 45^{o}]_{4s}$ models (at the same level of load). One of these models (Figure 5-44 A) uses the boundary conditions associated with the mounting fixture, while the other model (Figure 5-44 B) uses the boundary conditions associated with no mounting fixture. In Figure 5-44 A, note that in-plane rotation is very apparent, while Figure 5-44 B shows that with the no mounting fixture boundary conditions, no in-plane rotation is allowed. In addition, after examining the stress levels, for both models, above and below the discontinuity (Figure 5-44 C), the axial stresses for the model which allowed in-plane rotation were found to be higher, above the discon-

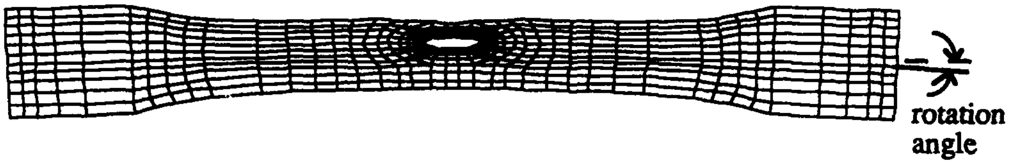

Figure 5-44 A. $[\pm 45^{\circ}]_{4s}$ Model (eccentricity=0.3"/mounting fixture)

initial displ = .002866"/displacements magnified 1000 times/NOTE ROTATION

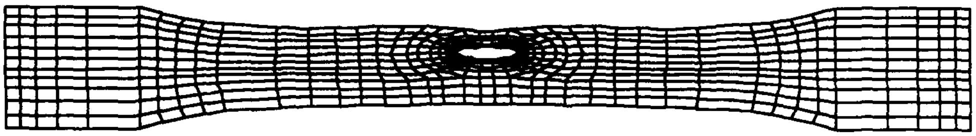

Figure 5-44 B. $[\pm 45^{\circ}]_{4s}$ Model (eccentricity=0.3"/no mounting fixture)

initial displ = .002866"/displacements magnified 1000 times/NO ROTATION

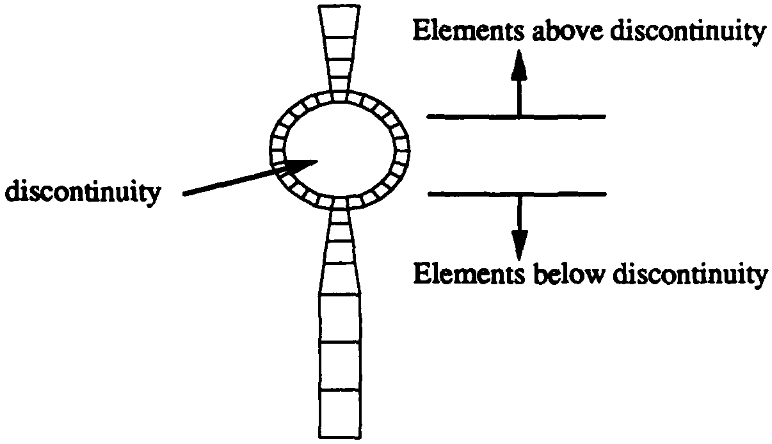

Figure 5-44 C. Elements Adjacent to Discontinuity (undistorted)

Figure 5-44. Mounting Fixture Effects

tinuity, than for the model which did not allow in-plane rotation . Furthermore, the axial stresses for the model which allowed in-plane rotation were found to be lower, below the discontinuity, than for the model which did not allow in-plane rotation. Therefore, the in-plane rotation creates higher axial stresses above the discontinuity and consequently, leads to failure at lower levels of load than for the models which do not allow in-plane rotation (see Table 5-13). As noted in Figure 5-44, the displacements for Figures 5-44 A and 5-44 B were magnified 1000 times. If the displacements were not significantly magnified (over 100 times), the in-plane rotation was not visible.

Experimentally, the use of the mounting fixture did not always lower the failure loads for the laminates (see Tables 5-2, 5-5, 5-8, and 5-11). This is most likey due to the fact that only three specimens were tested experimentally for each of the stacking sequences (see Tables 5-1, 5-4, 5-7, 5-10). Therefore, since the analytical solution predicted only *slightly* lower failure loads (with the use of the mounting fixture), even small scattering of the experimental data (see Figures 5-5, 5-12, 5-22, and 5-34) could account for not always noting the trend of lower failure loads with the use of the mounting fixture. Also, as noted in the previous paragraph, the in-plane rotations were very small, and therefore, it was impossible to observe if in-plane rotations actually occurred during the experimentation.

VI. Conclusions

This section summarizes the conclusions relating to the objectives listed in Section I A. First, the conclusions from a comparison of analytical and experimental results are presented. Secondly, conclusions relating to both boundary condition effects (i.e. mounting fixture effects) and eccentricity effects on the failure characteristics of the Gr/PEEK laminates are discussed. And finally, general conclusions relating to the suitability of the numerical tools (linear and nonlinear finite element programs), used in this study, are discussed.

A. Experimental versus Analytical Failure Predictions.

(1) $[0^o{}_{16}]$ laminates.

The finite element (FE) solution did a good job of predicting the splitting (failure) loads for these laminates. In addition, the FE stress-strain response predictions correlated well with the experimental stress-strain response. However, the FE solution did not predict the failure progression (i.e. splitting) in terms of damage accumulation. The splitting of these laminates may be caused by a dynamic phenomenon, such as a stress wave, or may be caused due to some other three-dimensional effect, such as edge effects. Therefore, the two-dimensional FE solution was not able to predict failure progression.

(2) $[90^o{}_{16}]$ laminates.

For these laminates, the FE solution did a good job of predicting both the experimental failure loads and the experimental stress-strain response. In addition, the numerical predictions of damage accumulation (failure progression) showed that damage initiation would occur above and below the discontinuity, and that failure would occur rapidly once the damage initiation occurred. These predictions (of failure progression) matched the results obtained from experimentation, where is was observed that these laminates failed suddenly, and damage initiation occurred above and below the discontinuity.

(3) [±45°]$_{4s}$ laminates.

For these laminates, the FE solution was found to significantly underestimate the experimental failure loads. This underestimation may be due to scissoring of the ±45 degree fibers, or may be a result of ignoring the interlaminar stresses (since this was a two-dimensional study). Since the scissoring phenomenon causes the fibers to become more aligned with the axial loading, one would expect that the experimental failure loads would be higher than the analytical predictions (since the program utilized did not account for scissoring). The experimental scattering of test data was not significant enough to account for the numerical underestimation of the failure loads.

The FE solution predicted a shear (mode II) failure for these laminates, and also predicted the high strains (necking) at failure. Finally, although the FE predictions of stress-strain response correlated, for low levels of load, with the experimental stress-strain response, the experimentation did not provide enough useful data to verify the analytical predictions of stress-strain response.

(4) [0°/±45°/90°]$_{2s}$ laminates.

The FE solution did a good job of predicting the experimental failure loads for these laminates. In addition, the FE stress-strain response predictions, up to the point of failure, correlated well with the experimental stress-strain response.

The failure of these laminates was characterized by a shear (mode II) failure. However, the failure regions of these laminates did not appear to be as shear dominated as was noted for the [±45°]$_{4s}$ laminates. Therefore, it appears that the failure mode for these laminates is some combination of the failure modes noted for the [0°$_{16}$], [90°$_{16}$], and [±45°]$_{4s}$ laminates.

The FE solution did not predict the shear (mode II) failure. This may be due to several reasons. First, the ±45 degree plies require large strains before failure; but, the zero degree plies in the $[0^{\circ}/\pm45^{\circ}/90^{\circ}]_{2s}$ laminate prevent large strains. Therefore, once the level of loading was high enough to cause failure of the zero degree plies, adjacent (above and below) to the discontinuity, the level of load was much higher than the neighboring ±45 degree plies (or 90 degree plies) could sustain. As a result, the FE solution predicted catastrophic failure of these laminates once the zero degree plies, adjacent (above and below) to the discontinuity, failed. Another possibility which might have affected the FE predictions of damage progression, is the fact that the two-dimensional FE solution did not account for interlaminar stresses, which for this stacking sequence, may alter the failure mode.

During the experimentation, audible "popping" of the fibers could be heard for several minutes before the laminates failed. Therefore, one would think that the damage zone (at the failure load) would not be as small as the damage zone predicted by the FE solution. One possibility for the prediction of a small damage zone, is the fact that interlaminar stresses were ignored in this study, and as mentioned previously, these stresses may have an effect on the failure characteristics of this stacking sequence.

B. Boundary Condition/Eccentricity Effects.

(1) Boundary Condition Effects.

The linear FE study predicted that the use of the mounting fixture would not appreciably affect the stress states (near the discontinuity) for the Gr/PEEK laminates considered in this study. The nonlinear FE study predicted that *slightly* lower failure loads would result from the use of the mounting fixture. These lower failure loads appear to result from the in-plane rotation allowed by the mounting fixture. This in-plane rotation results in a higher axial stress region above the discontinuity, and consequently led to failure at lower levels of load.

The experimental verification of the FE predictions of boundary condition effects, was inconclusive. Since only three specimens (for each stacking sequence and value of eccentricity) were tested experimentally, experimental scattering of test data could account for not always observing a lowering of the experimental failure loads through the use of the mounting fixture. It should be noted that the experimentation did verify lower failure loads for the $[0^{\circ}_{16}]$ and $[0^{\circ}/\pm45^{\circ}/90^{\circ}]_{2s}$ laminates when the mounting fixture was used.

(2) Eccentricity Effects.

The eccentric circular discontinuity created a centroid (area) shift. This centroid shift, and resulting bending moment, created higher tensile stresses above the discontinuity. This phenomenon was predicted by the FE study, and it was observed that elements above the discontinuity tended to fail more quickly than corresponding elements below the discontinuity. Therefore, *eccentricity effects* led to a higher axial stress region above the discontinuity. However, the nominal (far field) failure stresses, for all four stacking sequences, did not appreciably differ for the different values of eccentricity considered.

Eccentricity effects (in terms of failure progression) were not observed experimentally. This was due to the fact that failure was too rapid to determine if (by viewing a video tape of the testing frame-by-frame) failure initiated above or below the discontinuity. If more panels of Gr/PEEK had been available for this study, stereo x-ray techniques [10,13] could have been used to study specimens which had been tested to a percentage of their ultimate load. This may have provided insight into the eccentricity effects on the initiation and progression of failure.

C. General Conclusions.

(1) Linear Finite Element Program (PLSTR).

The linear finite element program was very useful in providing a numerical tool which was used to develop the finite element models and predict states of stress for this study. In addition, the program was used to generate data for contour plotting and deformed model plots (models under loading). Since inexpensive computer resources (such as VAX mainframes) can quickly, under 60 real time seconds, handle the computations required by this program, the program is very useful for preliminary work leading into a nonlinear study (where more expensive computer resources such as the CRAY are required). Finally, the linear finite element program closely approximated the experimentally obtained stress states of the Gr/PEEK laminates.

(2) Nonlinear Material Finite Element Program (PLSTREN).

The nonlinear material finite element program is a progressive-ply-failure program which predicts both damage initiation and progression. This program was found to give good results for predicting the failure characteristics (due to an eccentric circular discontinuity) for $[0^{o}_{16}]$, $[90^{o}_{16}]$, and $[0^{o}/\pm45^{o}/90^{o}]_{2s}$ Gr/PEEK laminates. Since this program requires efficient computer resources, a detailed linear study (using PLSTR) should be conducted before using PLSTREN. By accomplishing this preliminary linear work, the lengthy modeling process, and inevitable errors, can be completed on low cost computer resources. Finally, the total strain energy failure criterion and the unloading option utilized by PLSTREN produced relatively good results.

(3) Closing.

This thesis has taken a detailed "look" at the objectives stated in Section I A. It has shown that the nonlinear material finite element program (PLSTREN) is able to predict the eccentricity effects on the failure characteristics of Gr/PEEK laminates. It is hoped that this study will contribute, in some small way, to other research projects involving thermoplastic composite laminates, such as Gr/PEEK.

Appendix A. Material Property Curves

Basic property tests were conducted by [13] to obtain the material properties for Gr/PEEK (at room temperature). This data is shown graphically (Figures A1 through A7) to demonstrate the nonlinear relationships between stress and strain for Gr/PEEK.

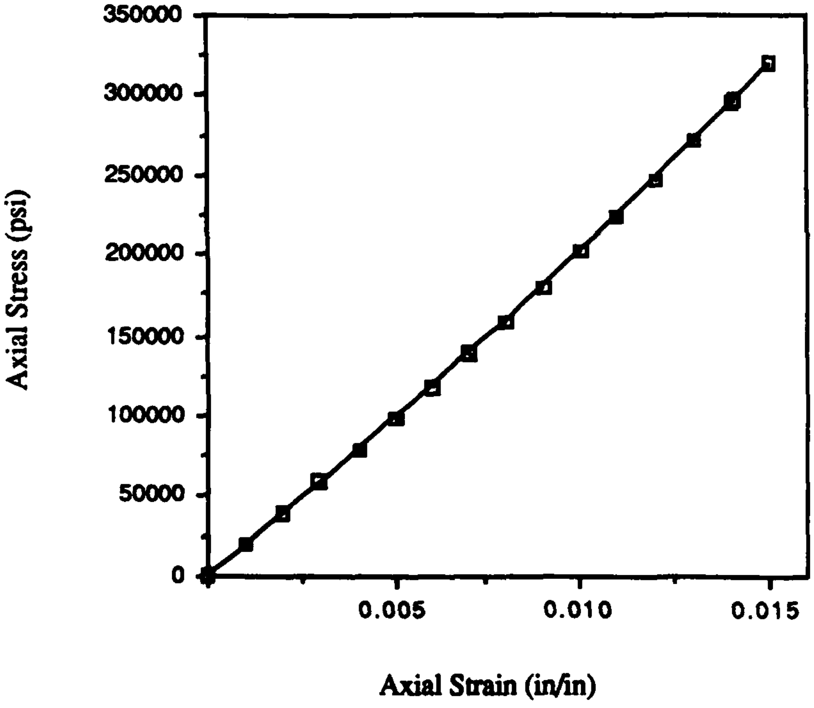

Figure A-1. σ_1 vs ε_1 (0° tension)

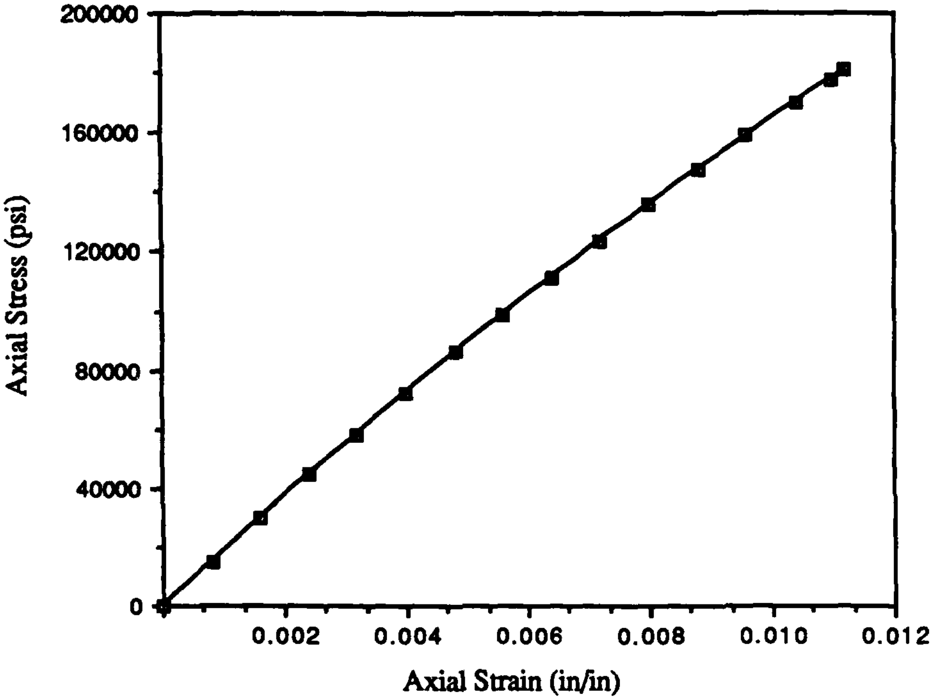

Figure A-2. σ_1 vs ε_1 (0° compression)

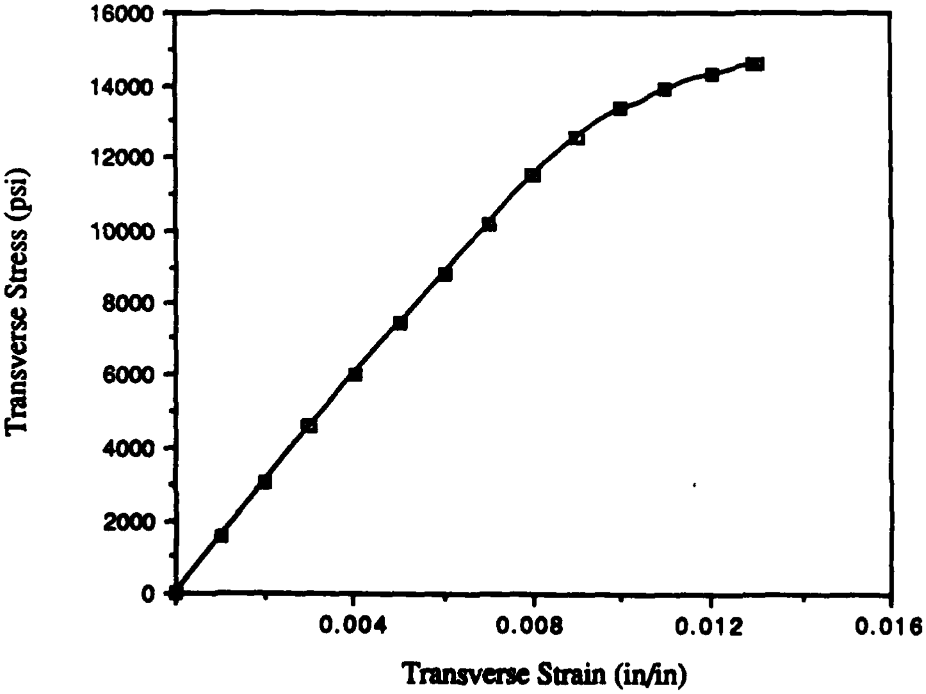

Figure A-3. σ_2 vs ε_2 (90° tension)

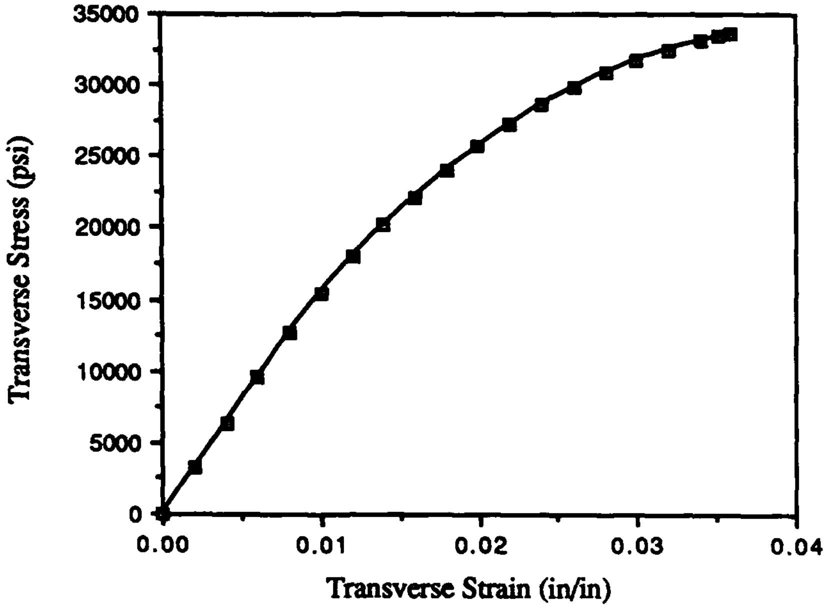

Figure A-4. σ_2 vs ε_2 (90° compression)

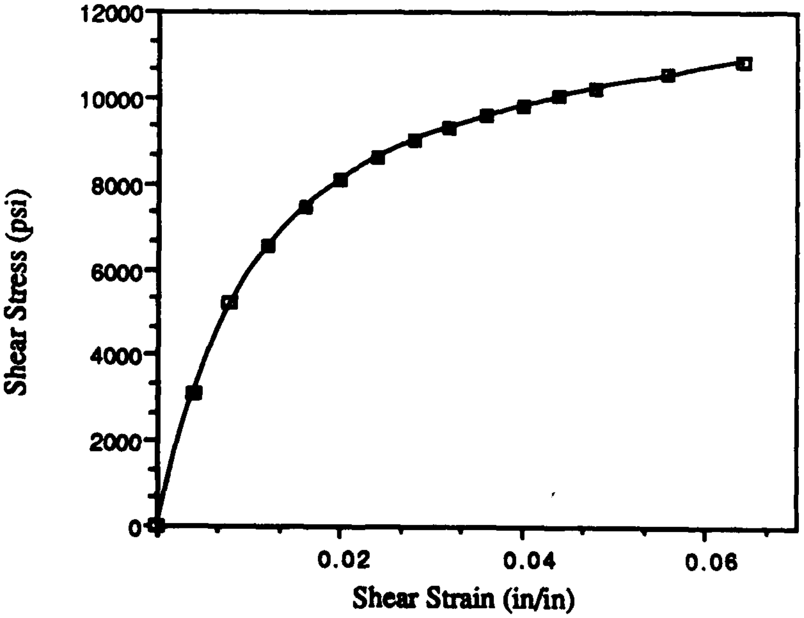

Figure A-5. τ_{12} vs γ_{12} (±45 tension)

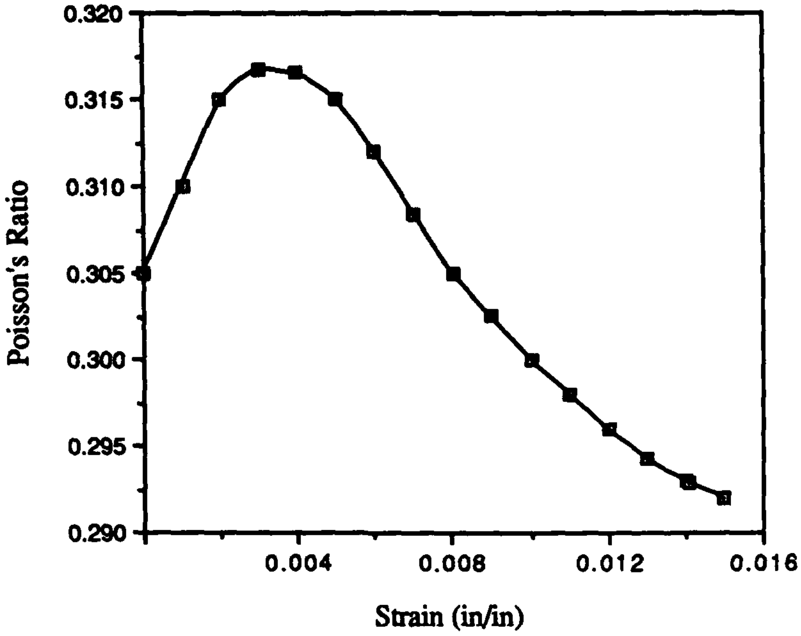

Figure A-6. ν_{12} vs ε_1 (0^{o} tension)

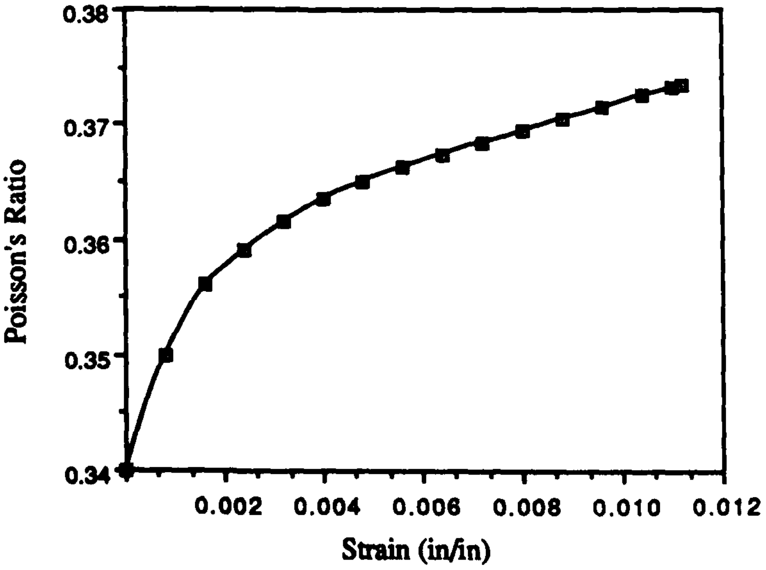

Figure A-7. ν_{12} vs ε_1 (0^{o} compression)

Appendix B. Contour Plots (Linear Analysis)

As mentioned in Section III E (1), contour plots were generated for all of the specimens tested experimentally (see Tables 4-1 through 4-4). These contour plots were generated to study the effects of both the eccentric circular discontinuity and the mounting fixture on the overall stress state of the Gr/PEEK laminates. Since the highest concentration of stress was located adjacent to the discontinuity, a window (see Figure B-1) surrounding the discontinuity was selected for the contour plots. The contour plots (see Figures B-2 through B-11) are grouped according to the stacking sequence of the laminate and also by the boundary conditions used with the finite element models. These boundary conditions simulated the use of either the mounting fixture or the Instron Test Machine grips (see Section III D). The term "no hinge" on the contour plots shown in this section indicates that no in-plane rotation (analytically) was permitted. The term "hinge" on the contour plots indicates that in-plane rotation (analytically) was permitted. Finally, the value of eccentricity is also given on each contour plot.

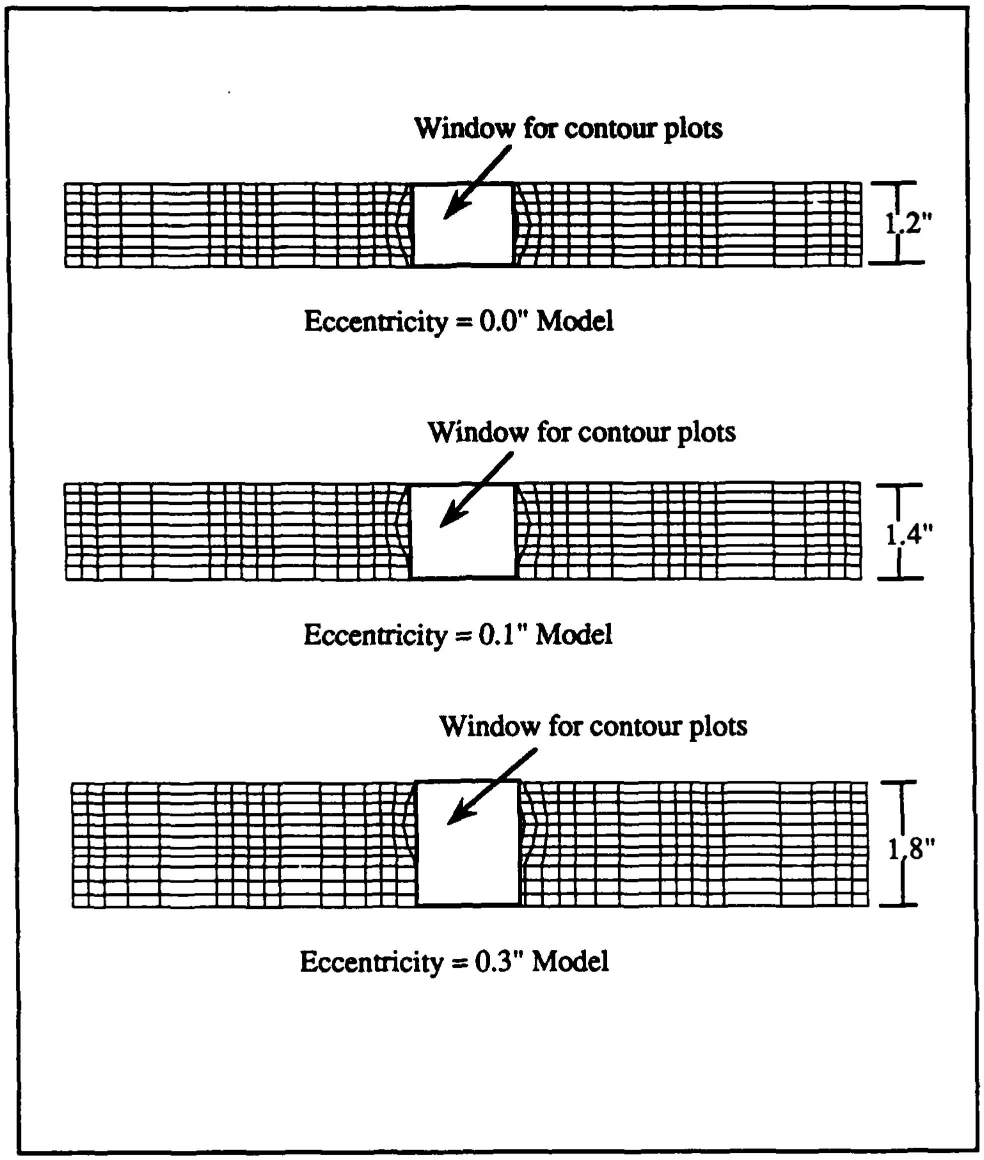

Figure B-1. Windows for Contour Plots

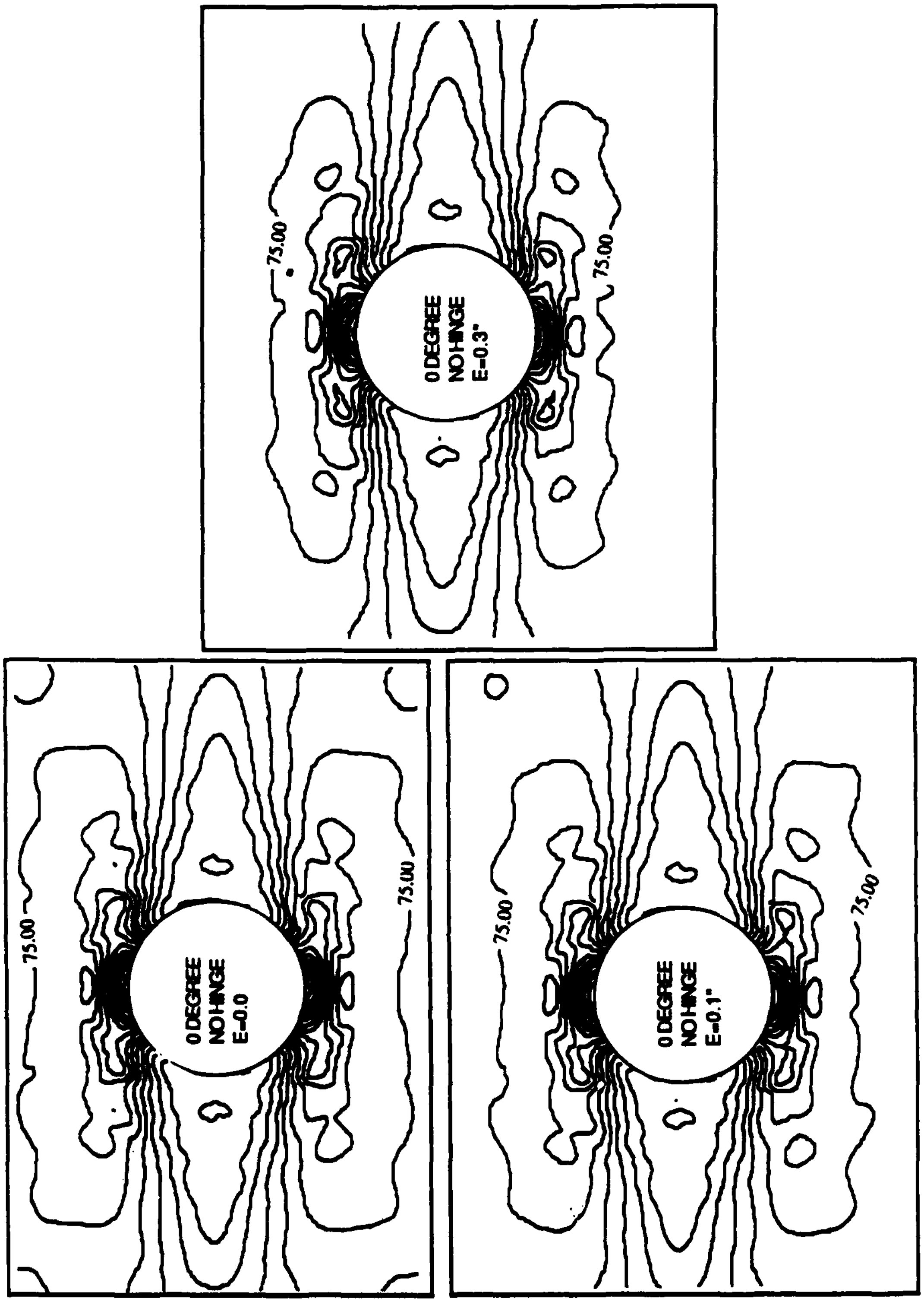

Figure B-2. Contour Plots (0 degree lay-up / no mounting fixture)

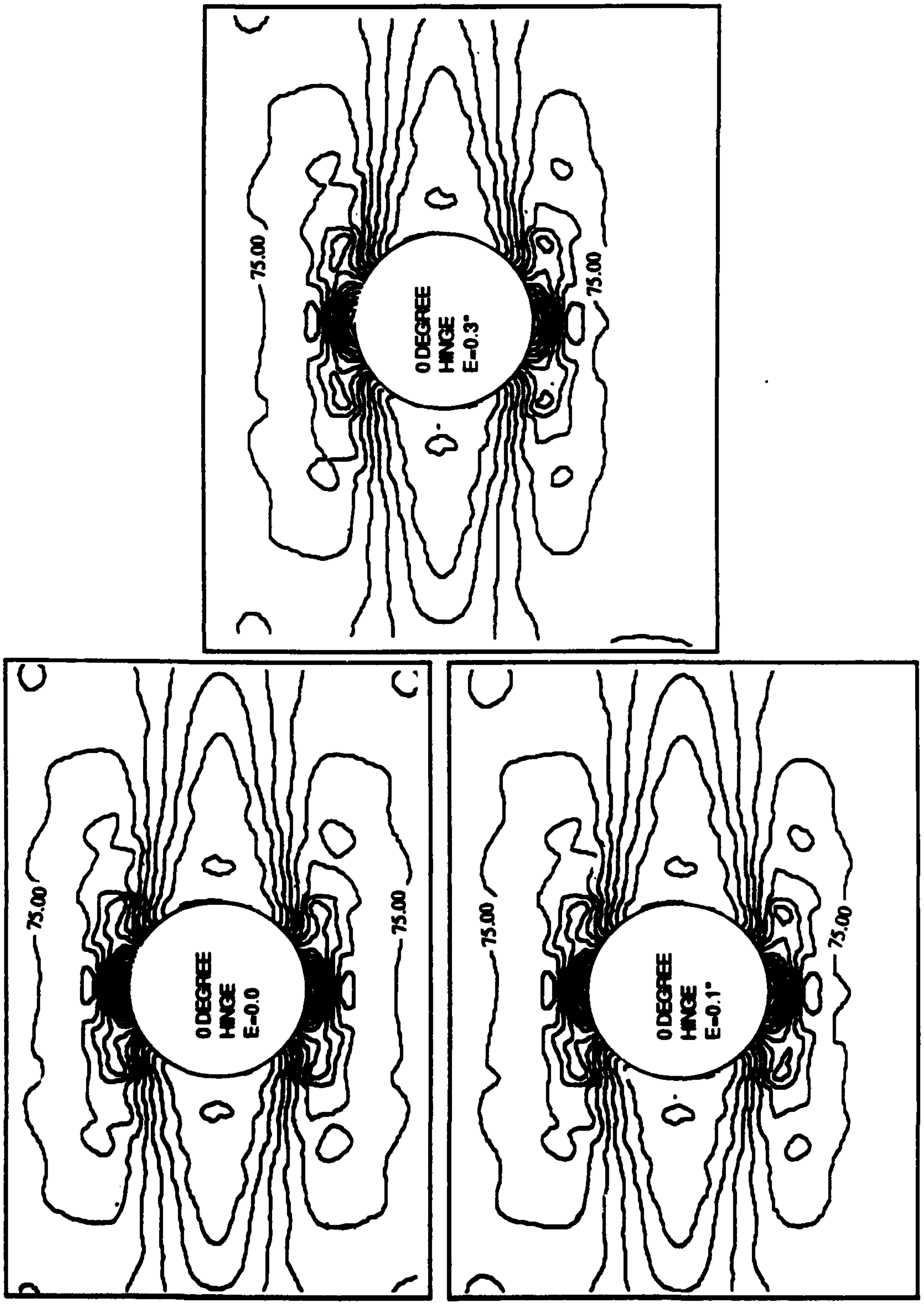

Figure B-3. Contour Plots (0 degree lay-up / mounting fixture)

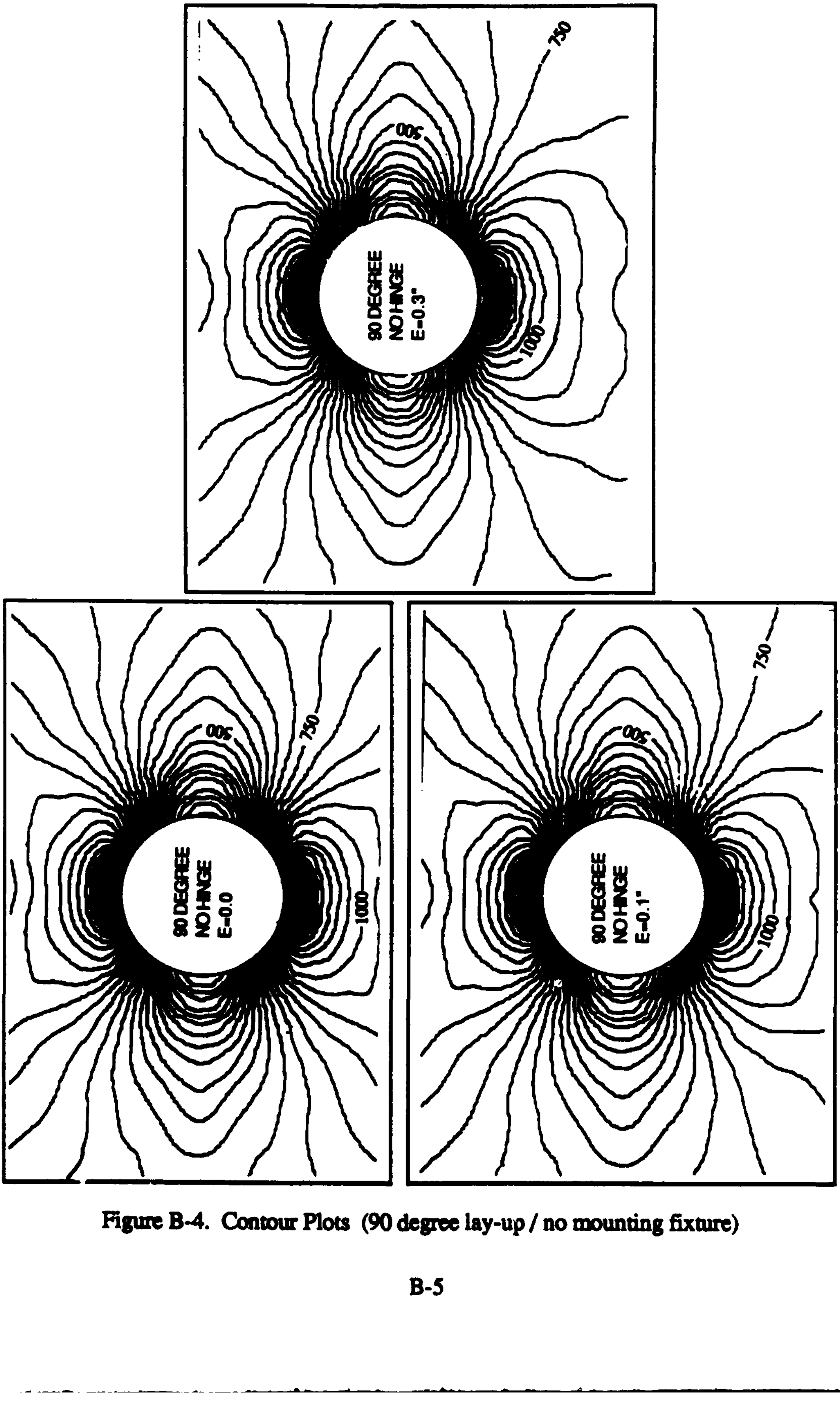

Figure B-4. Contour Plots (90 degree lay-up / no mounting fixture)

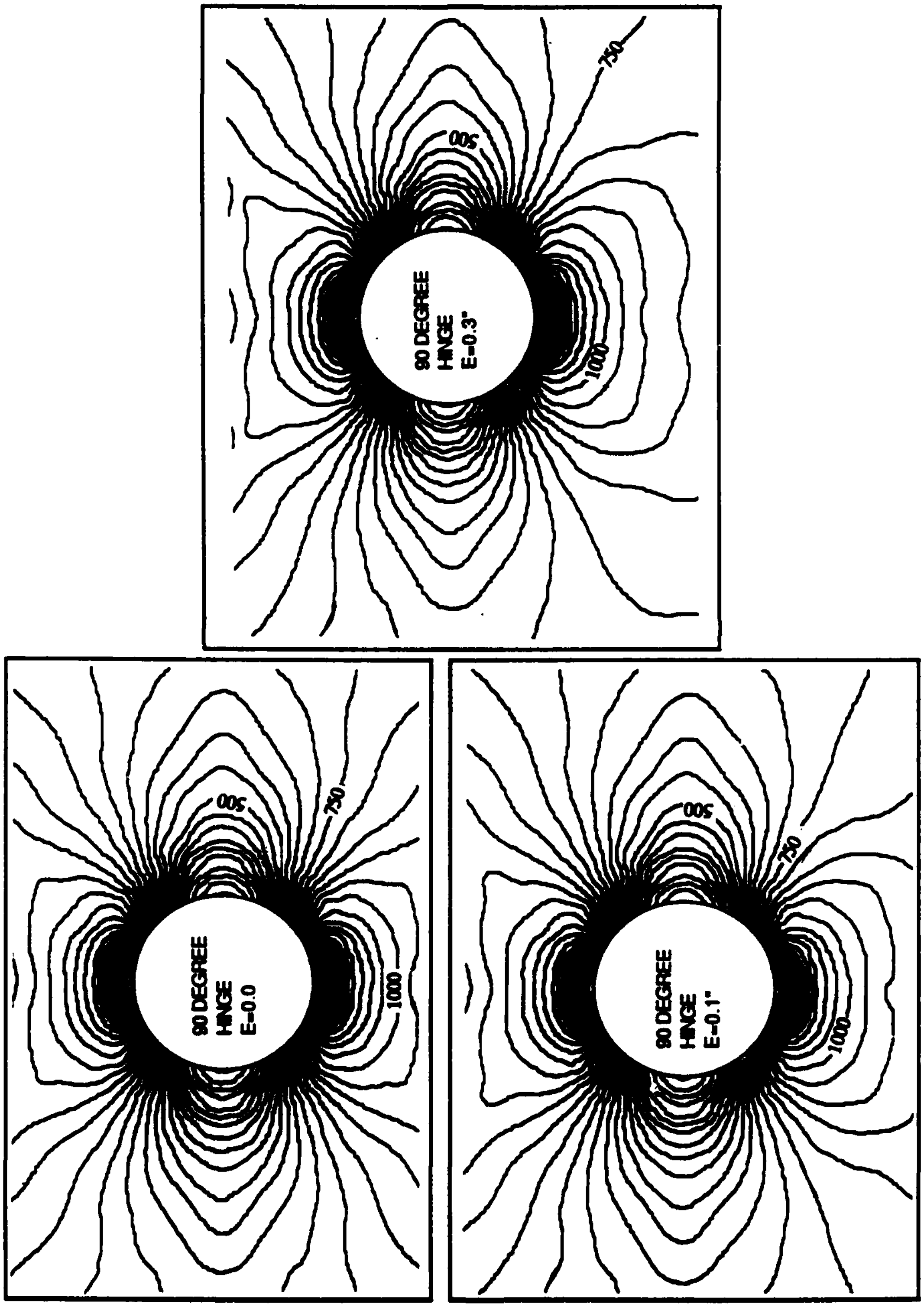

Figure B-5. Contour Plots (90 degree lay-up / mounting fixture)

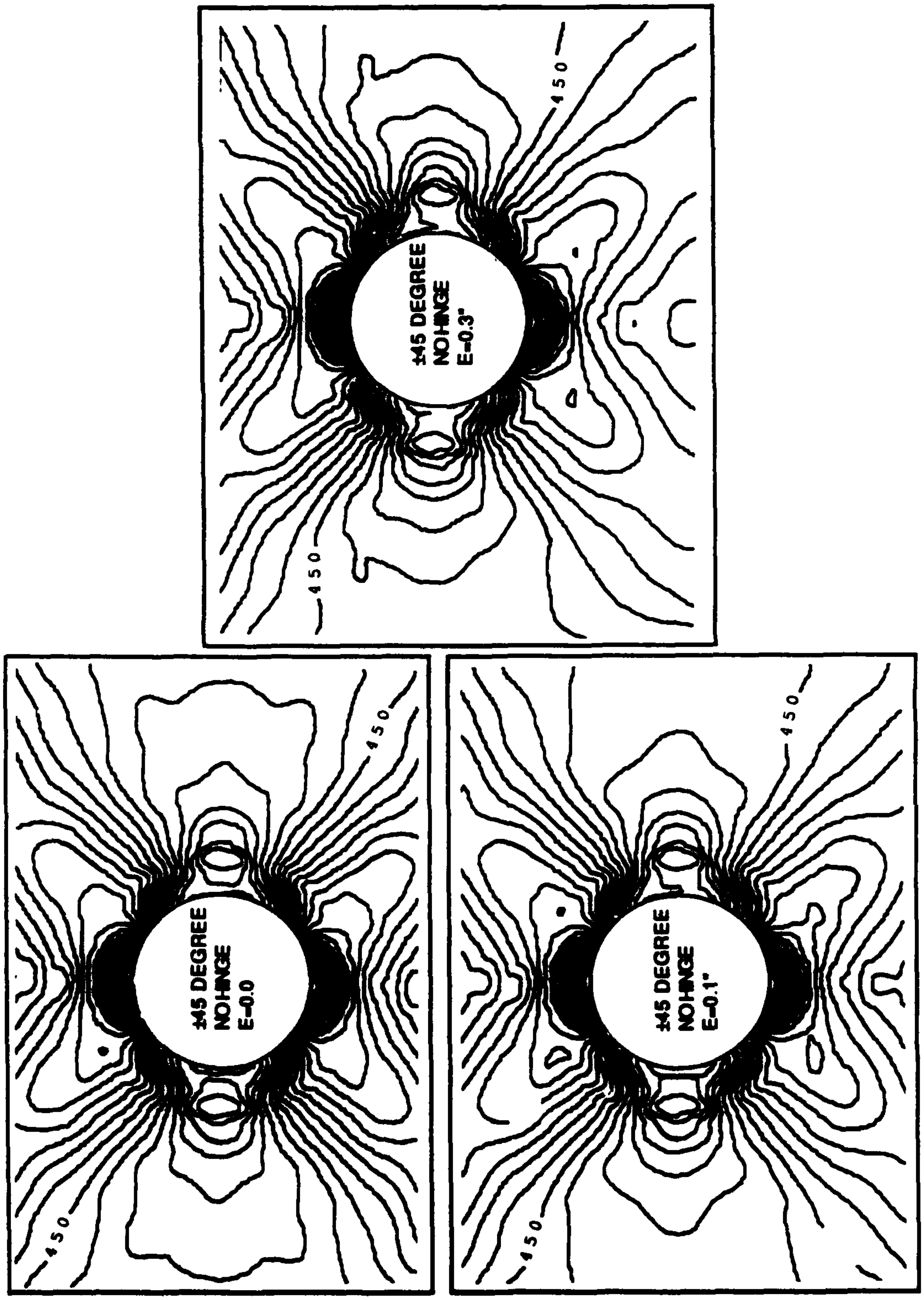

Figure B-6. Contour Plots (±45 degree lay-up / no mounting fixture)

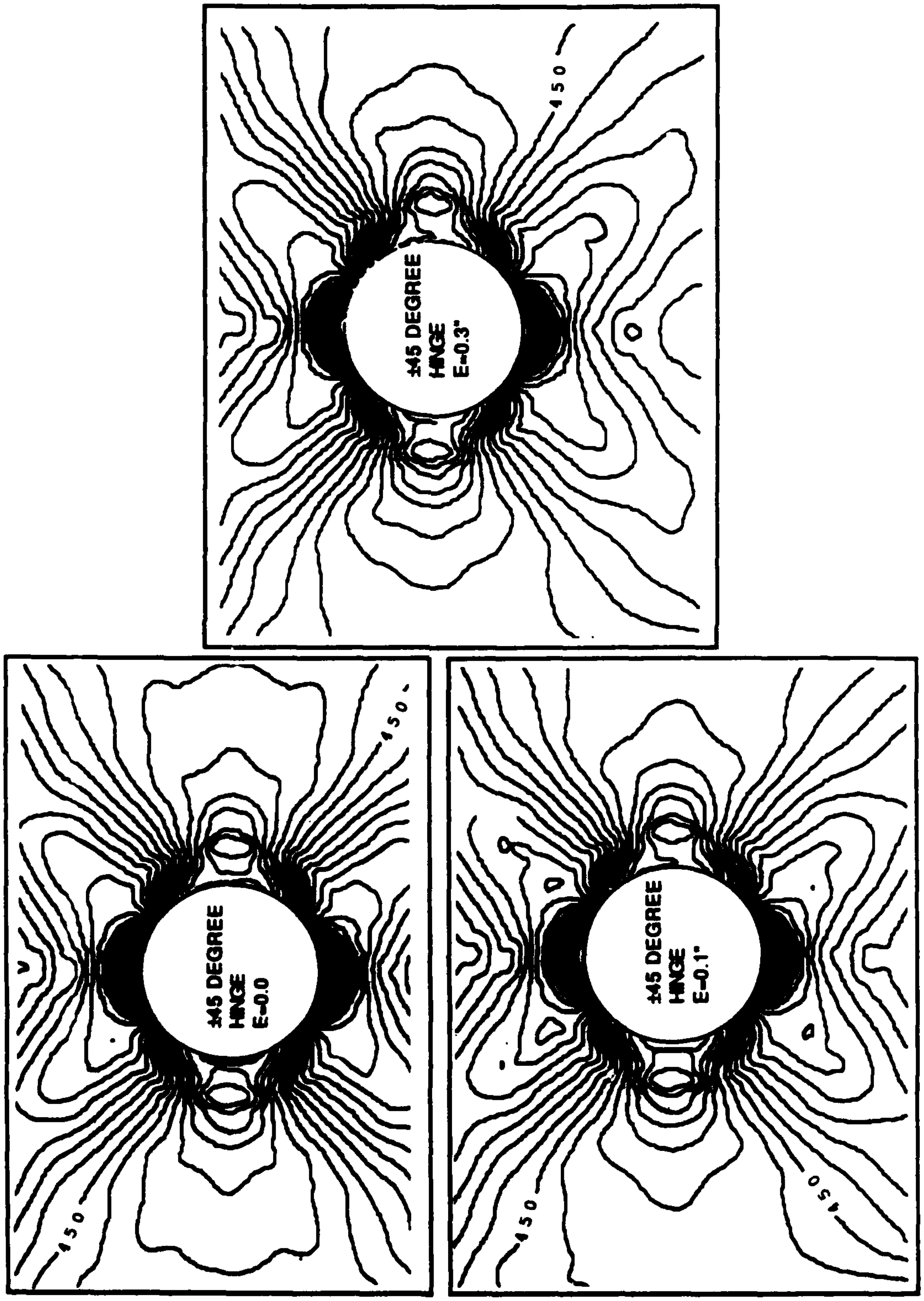

Figure B-7. Contour Plots (±45 degree lay-up / mounting fixture)

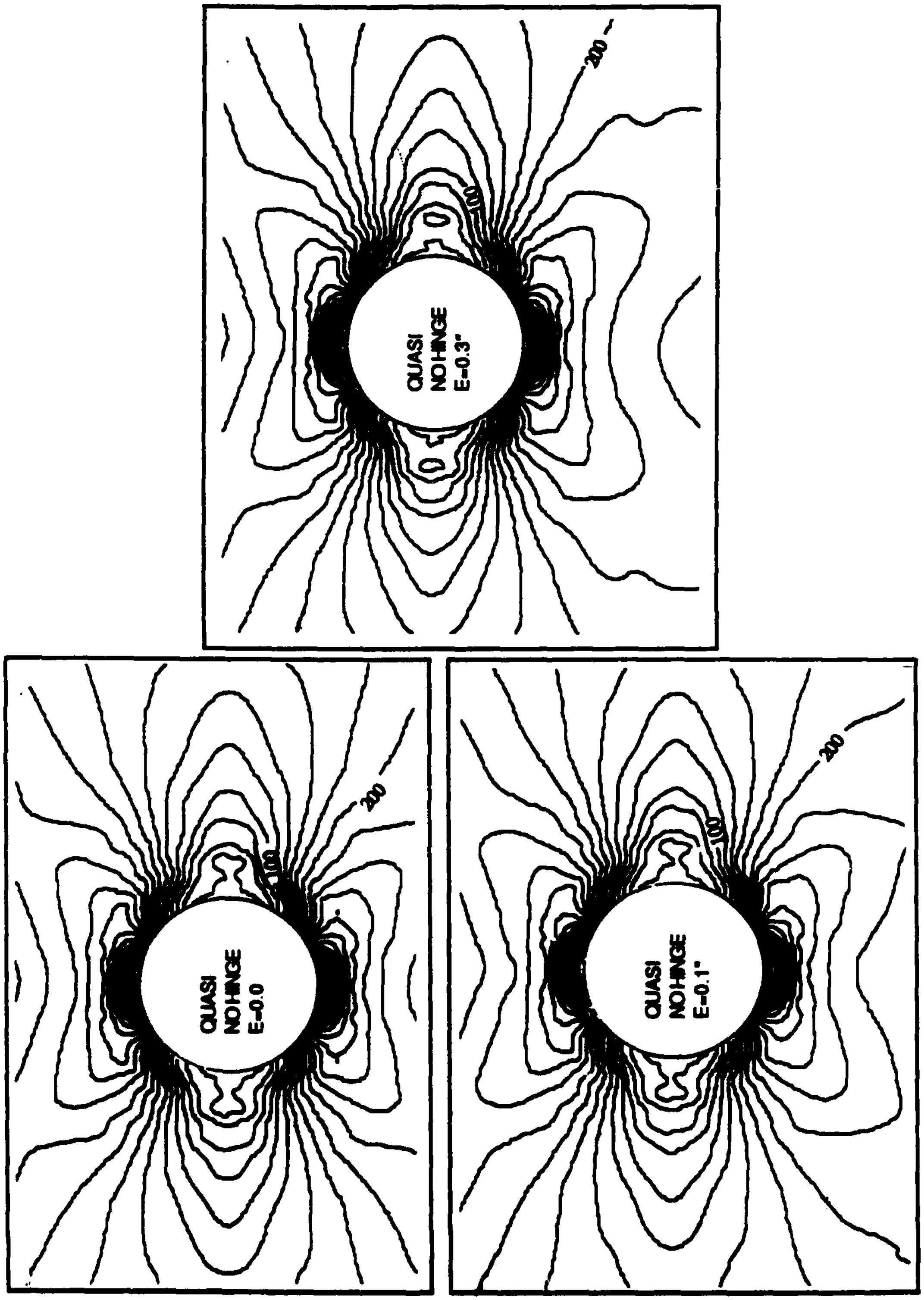

Figure B-8. Contour Plots (quasi lay-up / no mounting fixture)

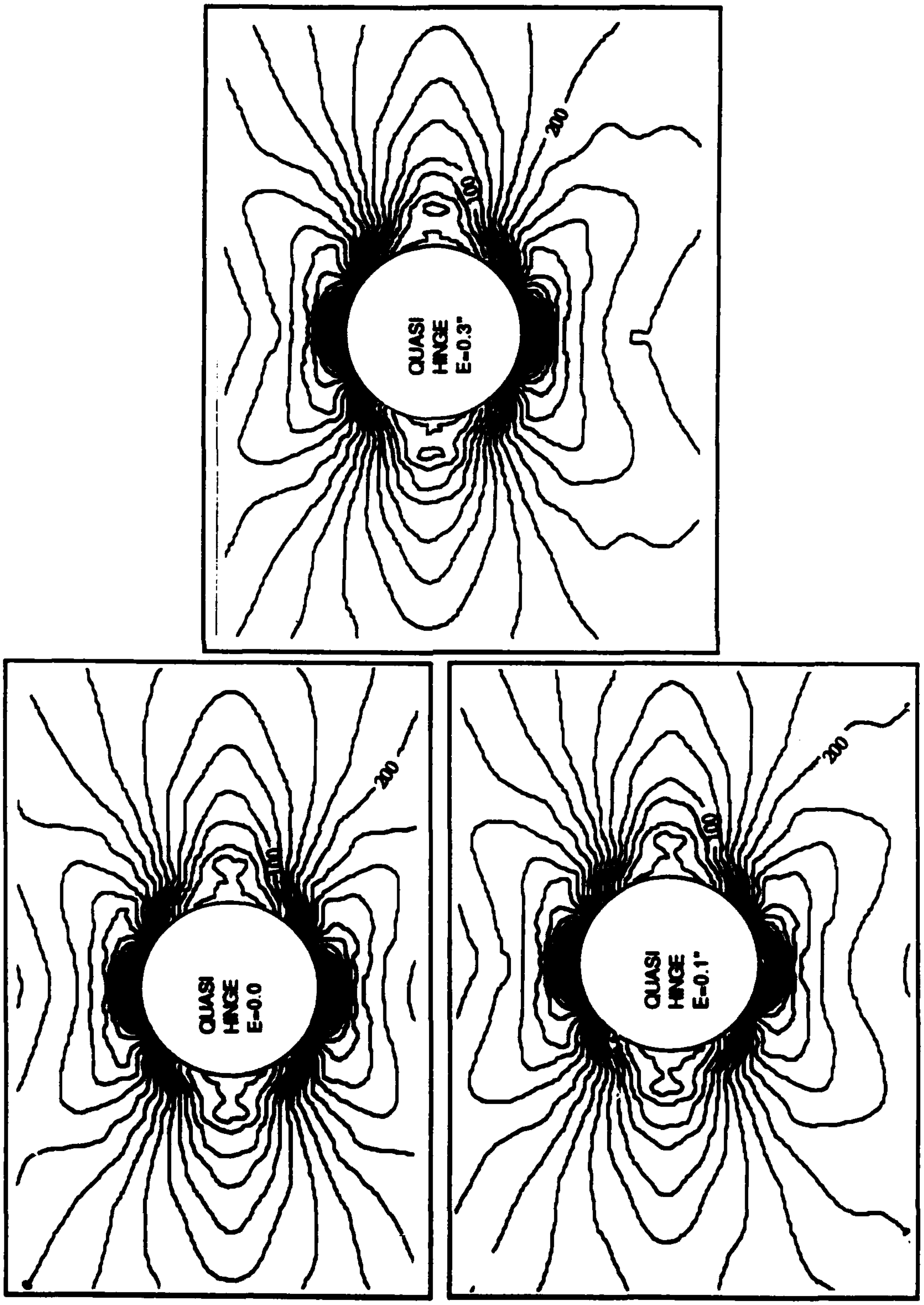

Figure B-9. Contour Plots (quasi lay-up / mounting fixture)

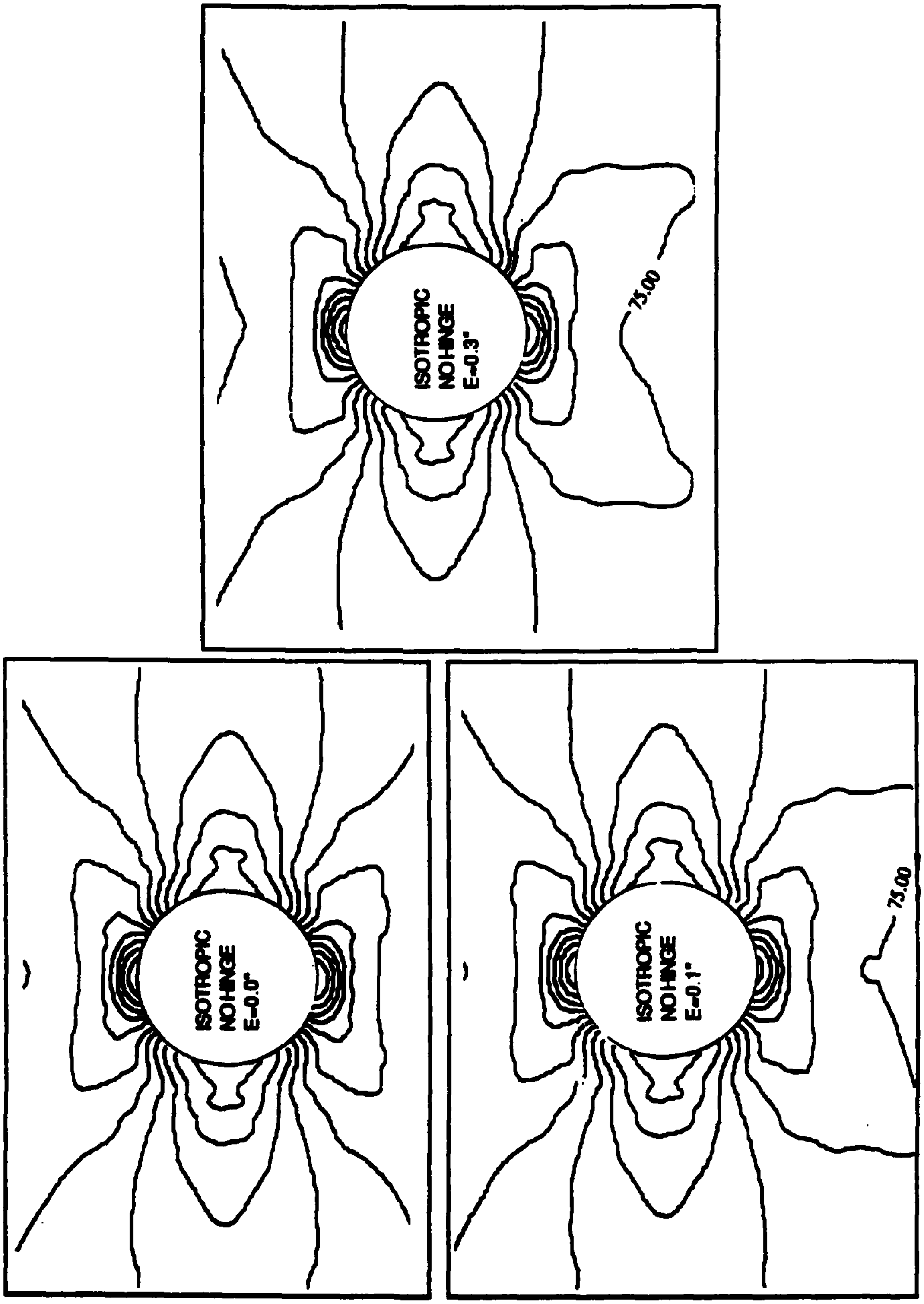

Figure B-10. Contour Plots (isotropic model / no mounting fixture)

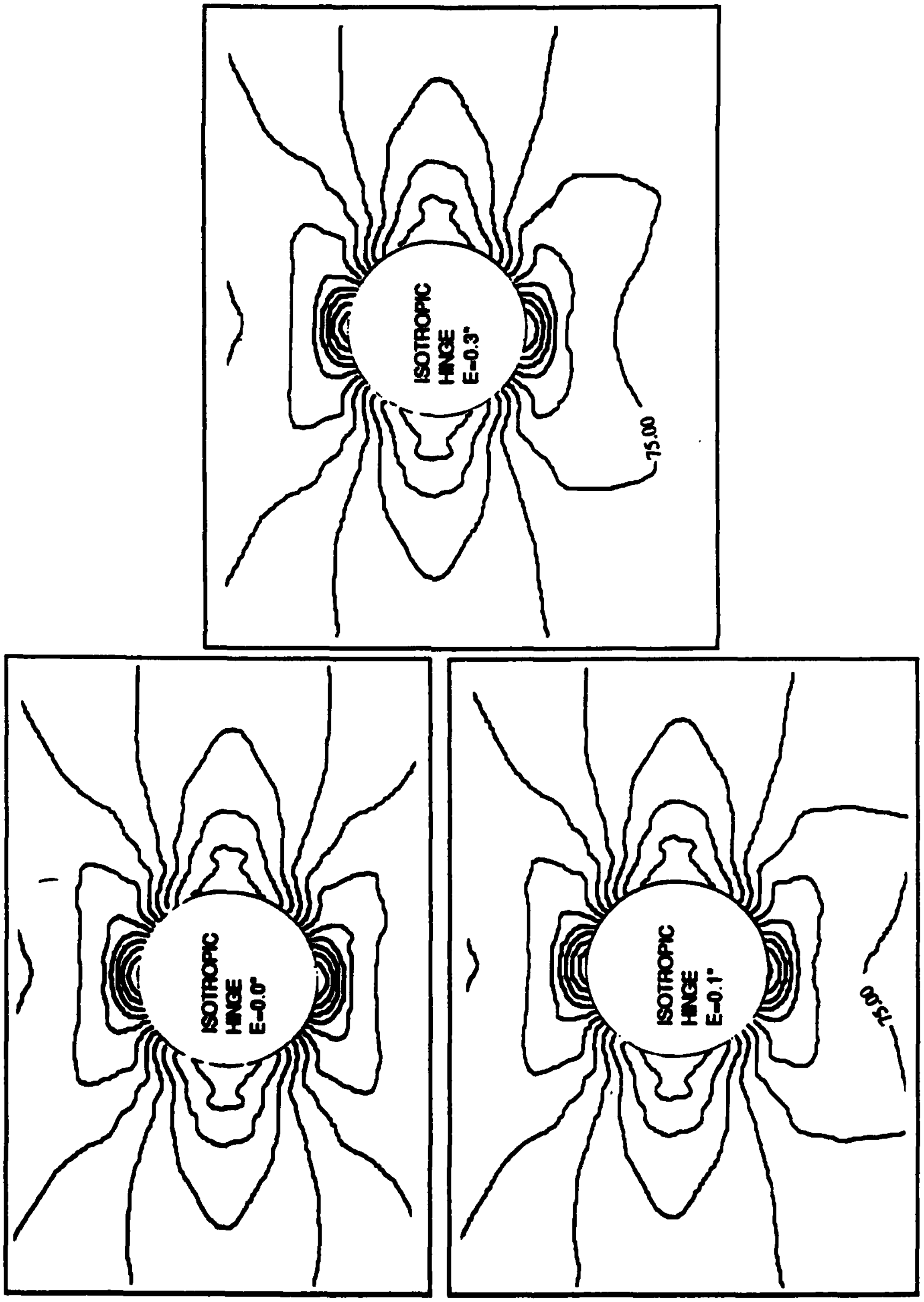

Figure B-11. Contour Plots (isotropic model / mounting fixture)

Appendix C. Stress State Plots (Linear Analysis)

As mentioned in Section III E (2)a, plots were generated for both near field and far field stress states. These plots were made in order to study boundary condition and eccentricity effects near the discontinuity (near field) as well as near the tab area (far field). Figure C-1 shows the near field location. Figures C-3 through C-6 were plotted at the near field location shown in Figure C-1. Figure C-2 shows the far field location. Figures C-7 through C-10 were plotted at the far field location shown in Figure C-2. The data used to generate Figures C-3 through C-10, was obtained from output data from linear finite element runs.

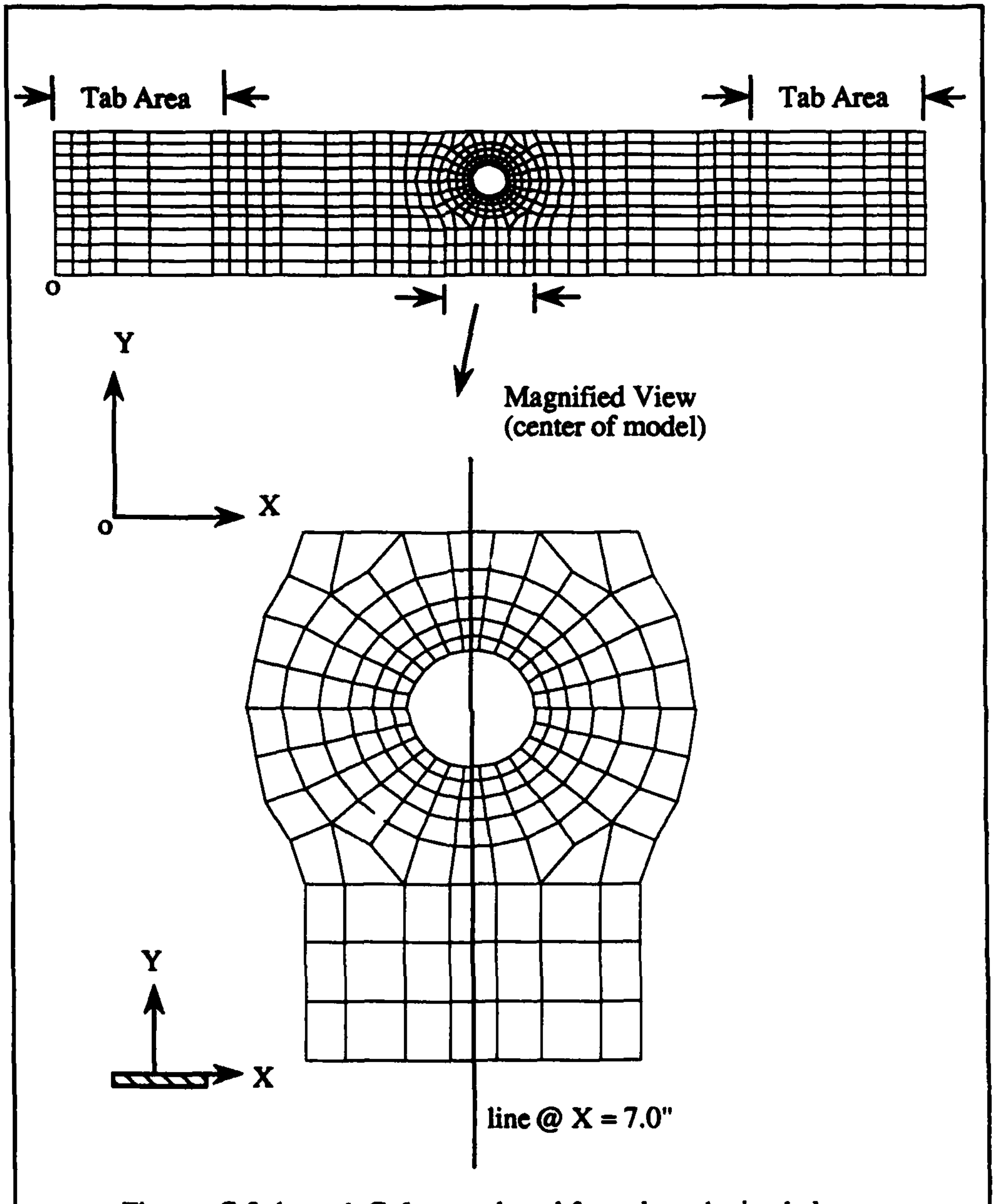

Figures C-3 through C-6 were plotted from data obtained along the line X=7.0".

Figure C-1. Near Field Locations for Plots

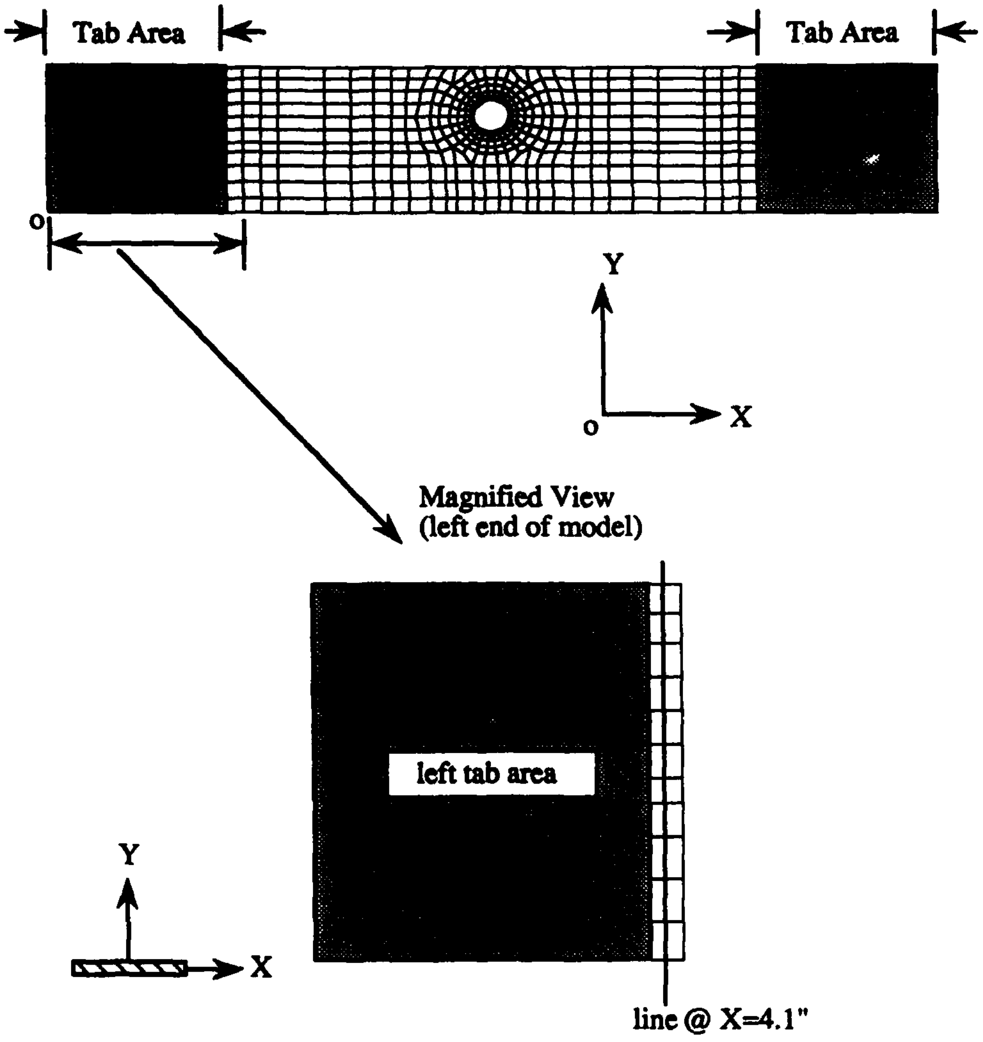

Figures C-7 through C-10 were plotted from data obtained along the line X=4.1".

Figure C-2. Far Field Locations for Plots

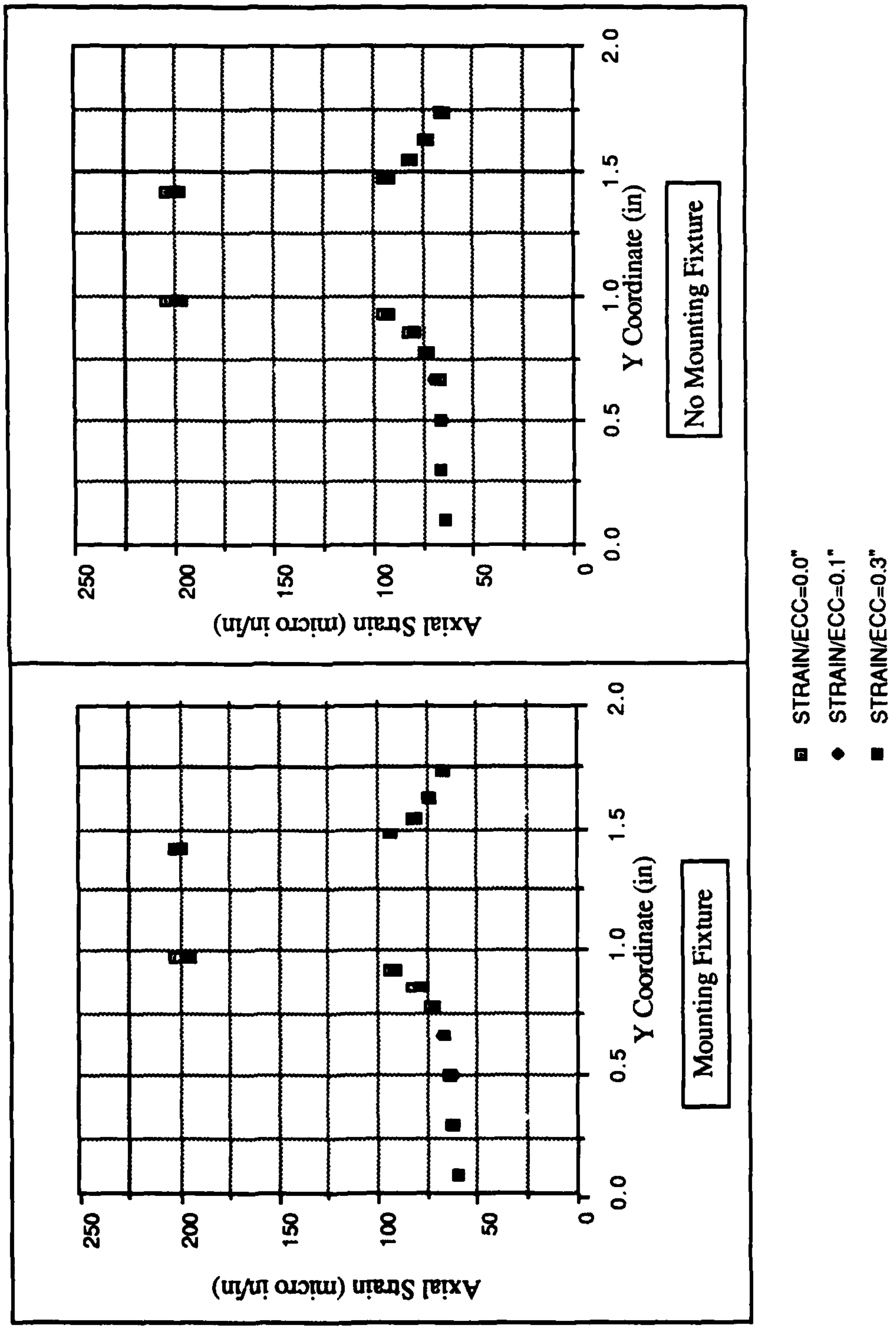

Figure C-3. Near Field Axial Strain Plots (0 degree lay-up)

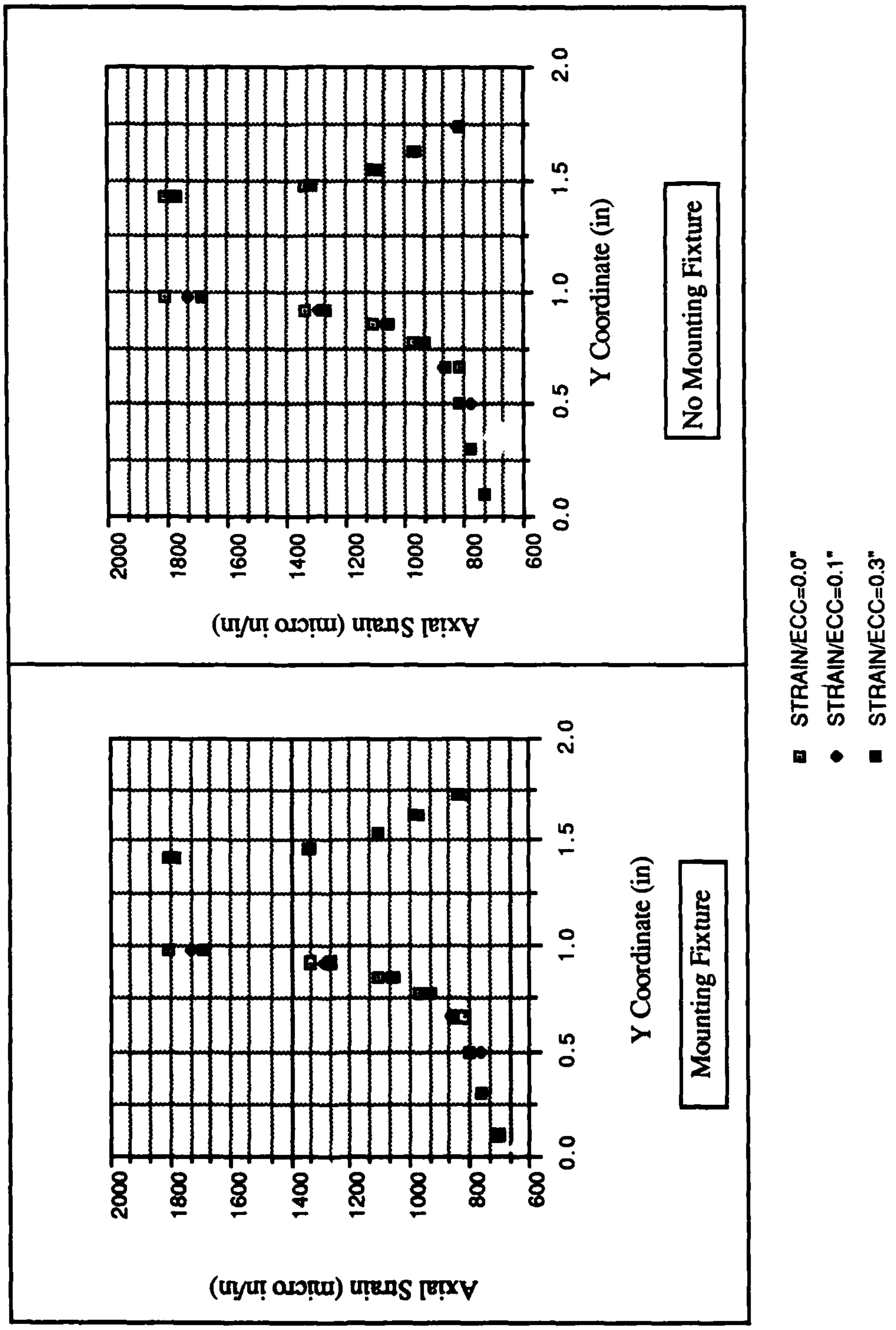

Figure C-4. Near Field Axial Strain Plots (90 degree lay-up)

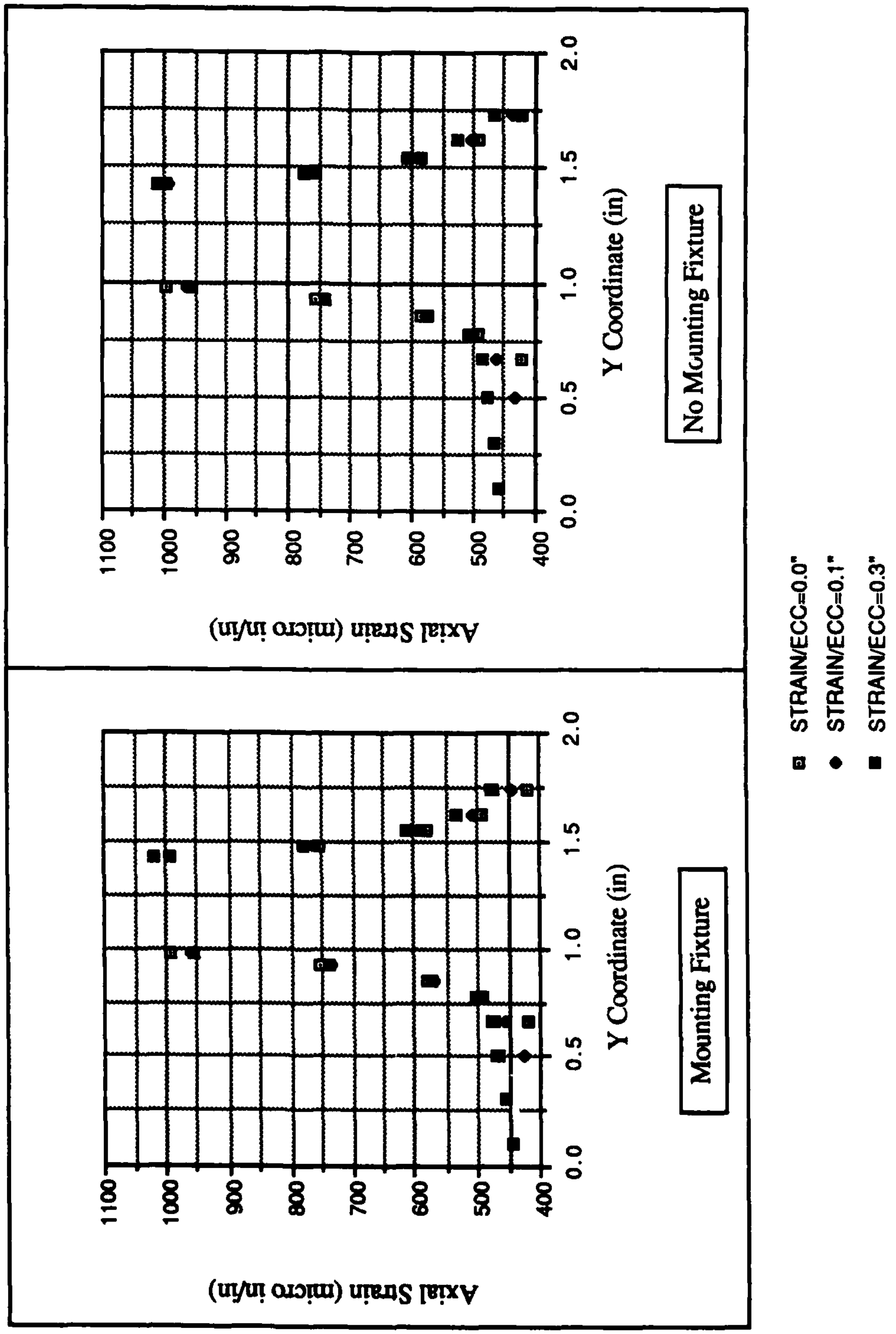

Figure C-5. Near Field Axial Strain Plots (±45 degree lay-up)

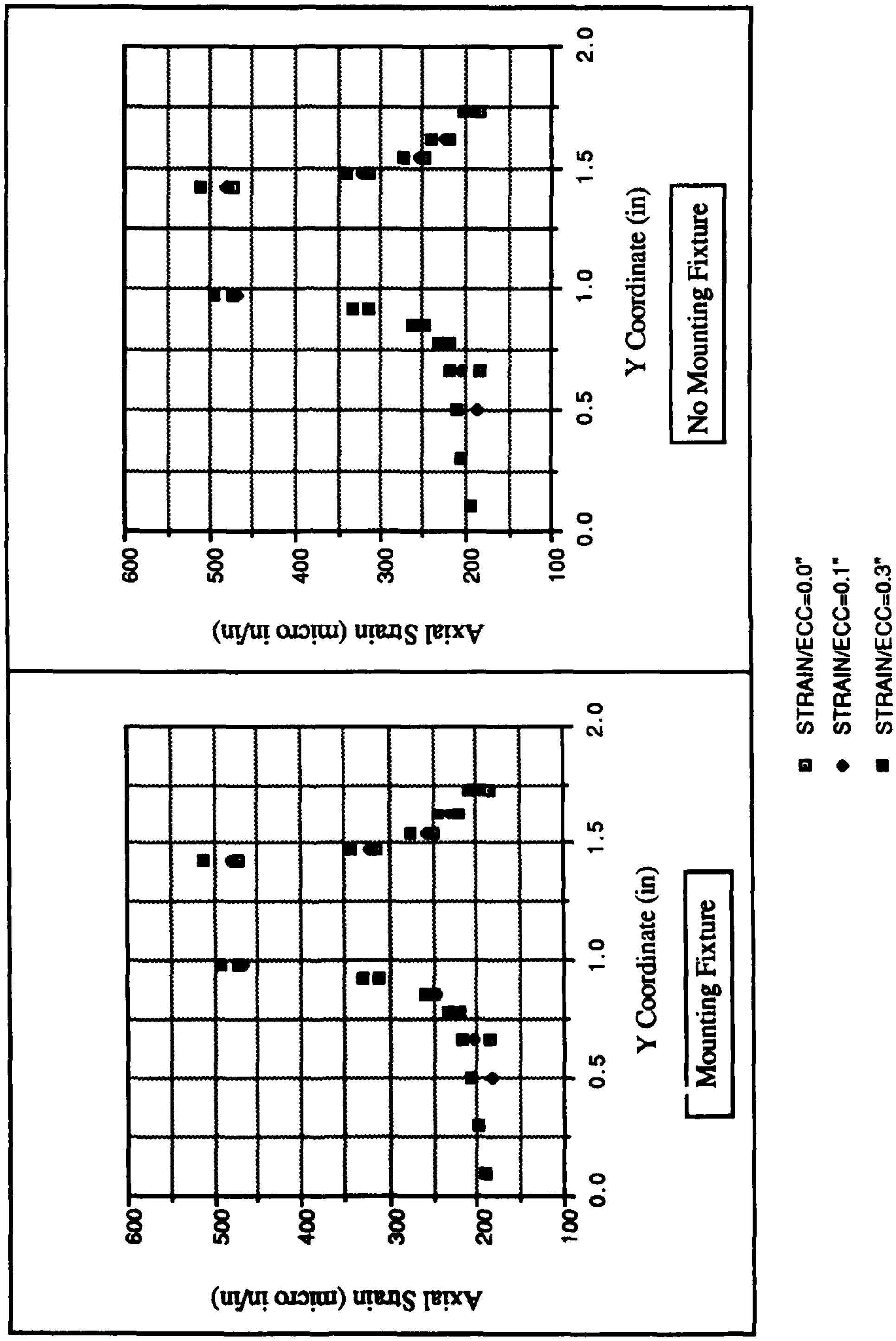

Figure C-6. Near Field Axial Strain Plots (quasi lay-up)

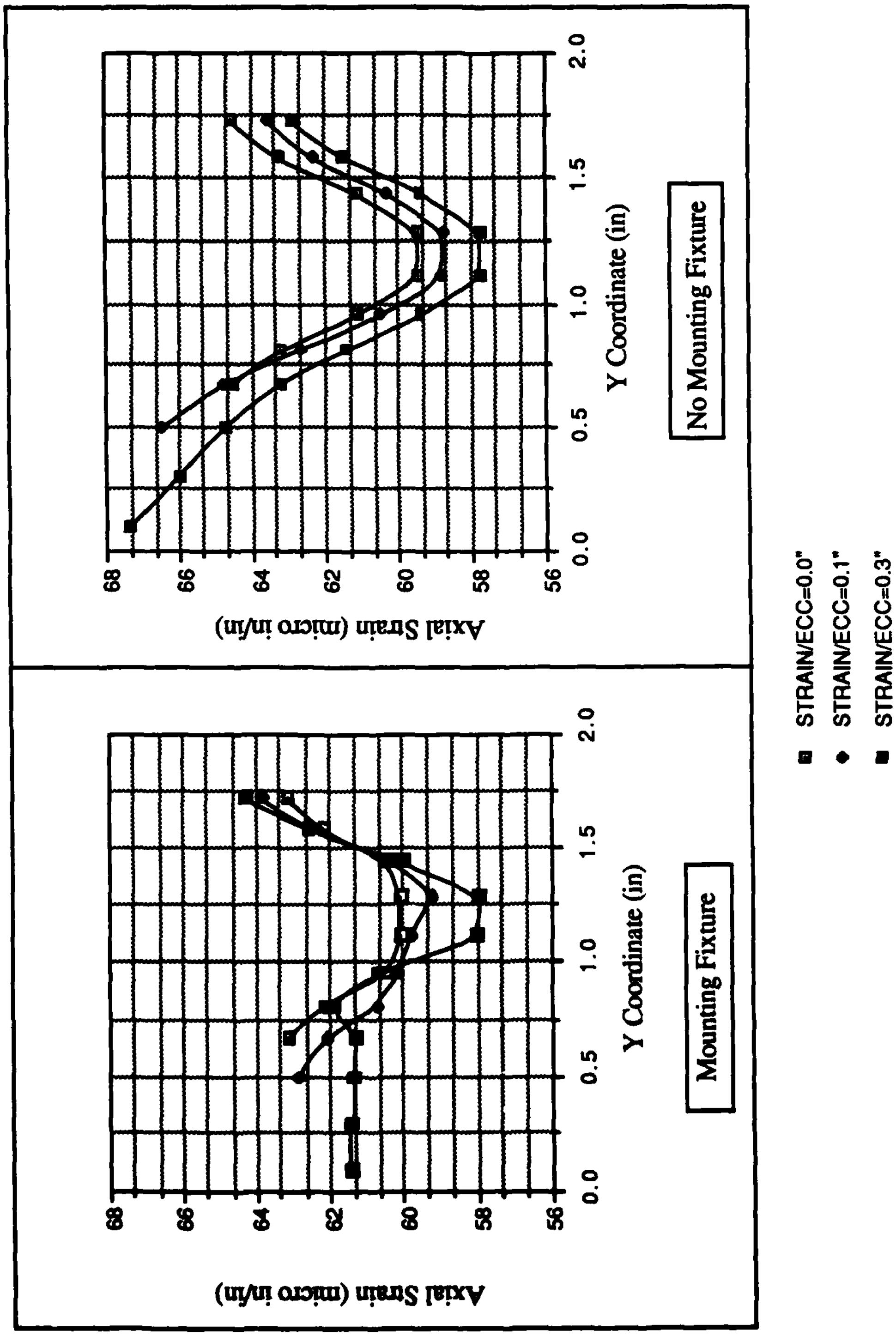

Figure C-7. Far Field Axial Strain Plots (0 degree lay-up)

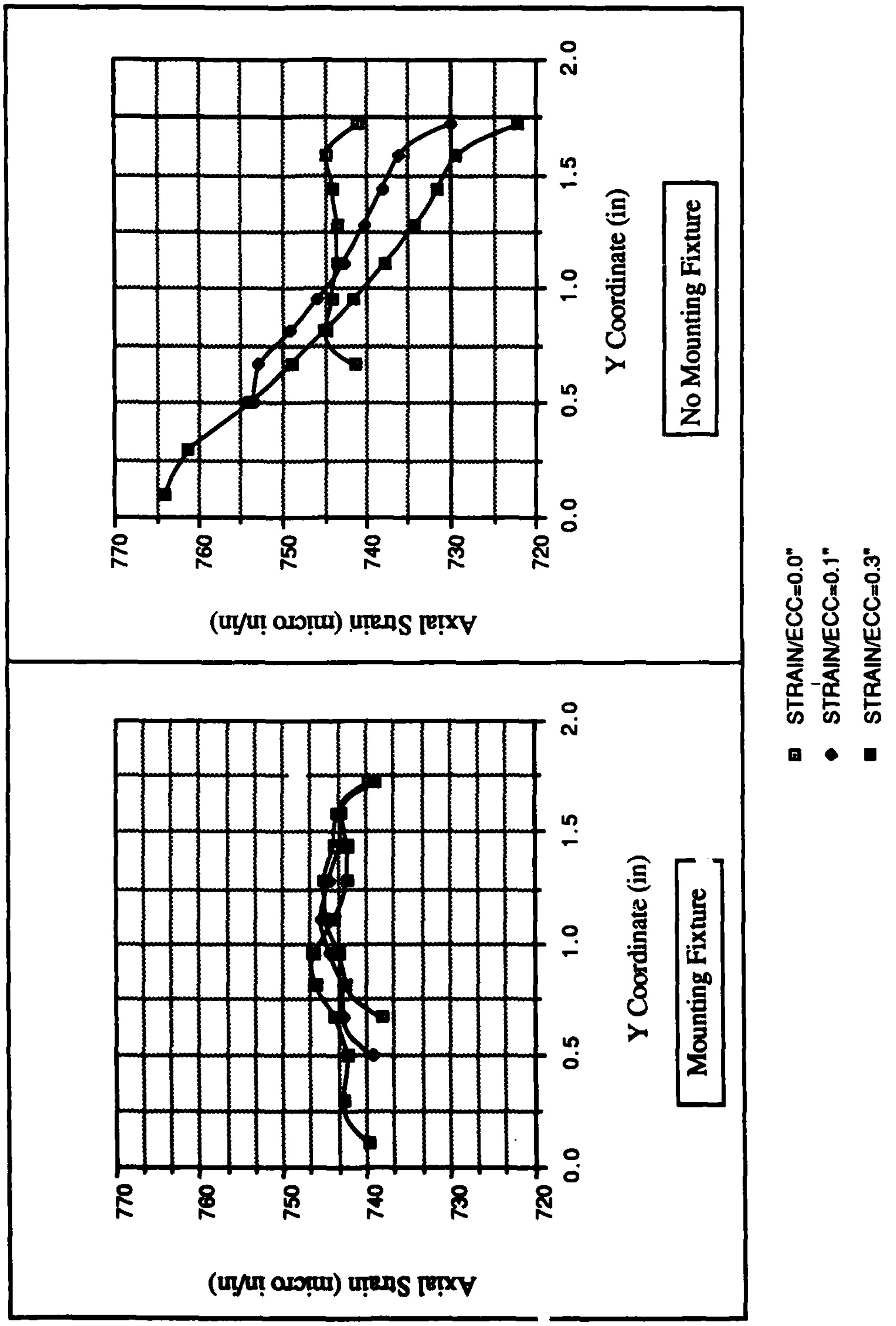

Figure C-8. Far Field Axial Strain Plots (90 degree lay-up)

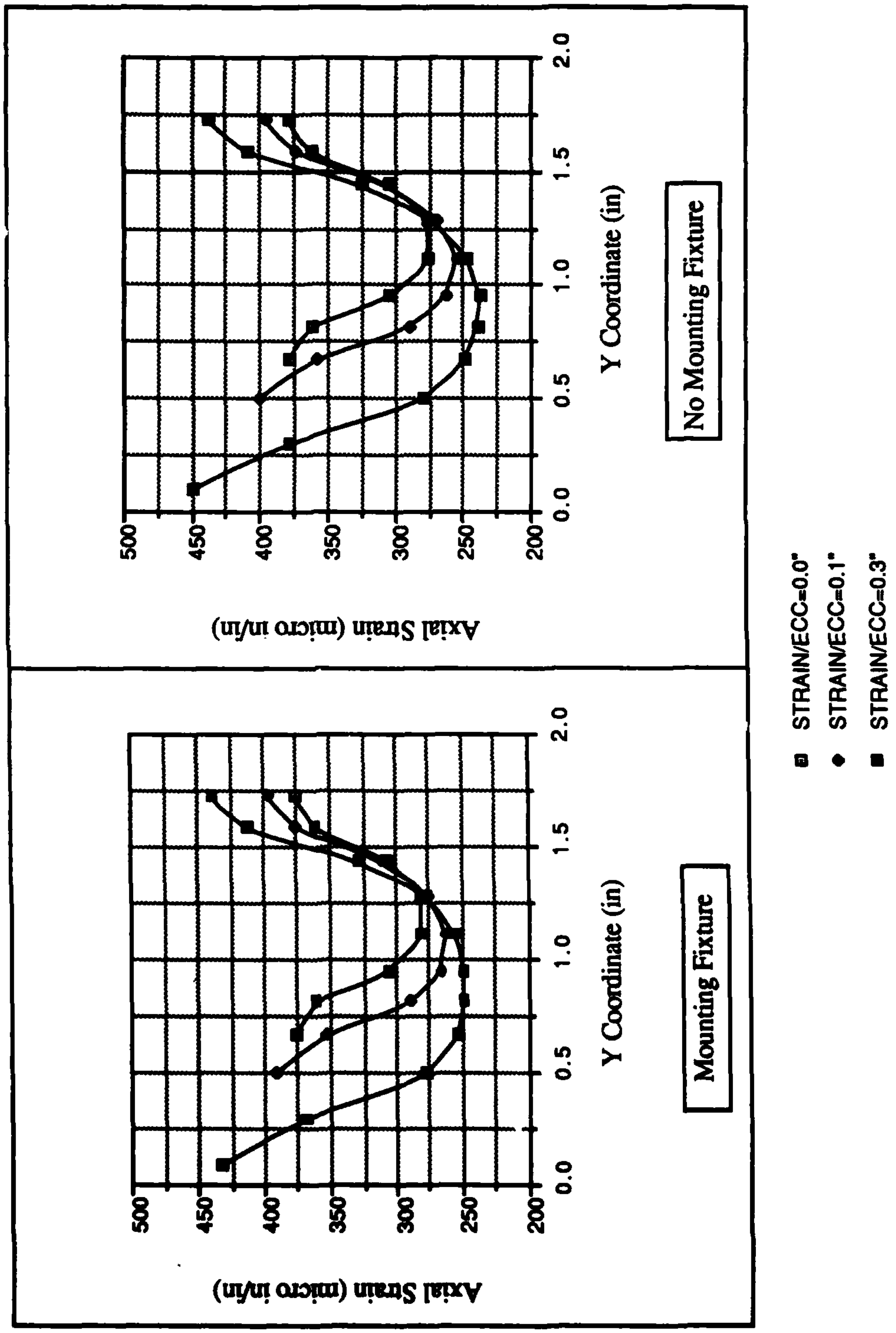

Figure C-9. Far Field Axial Strain Plots (±45 degree lay-up)

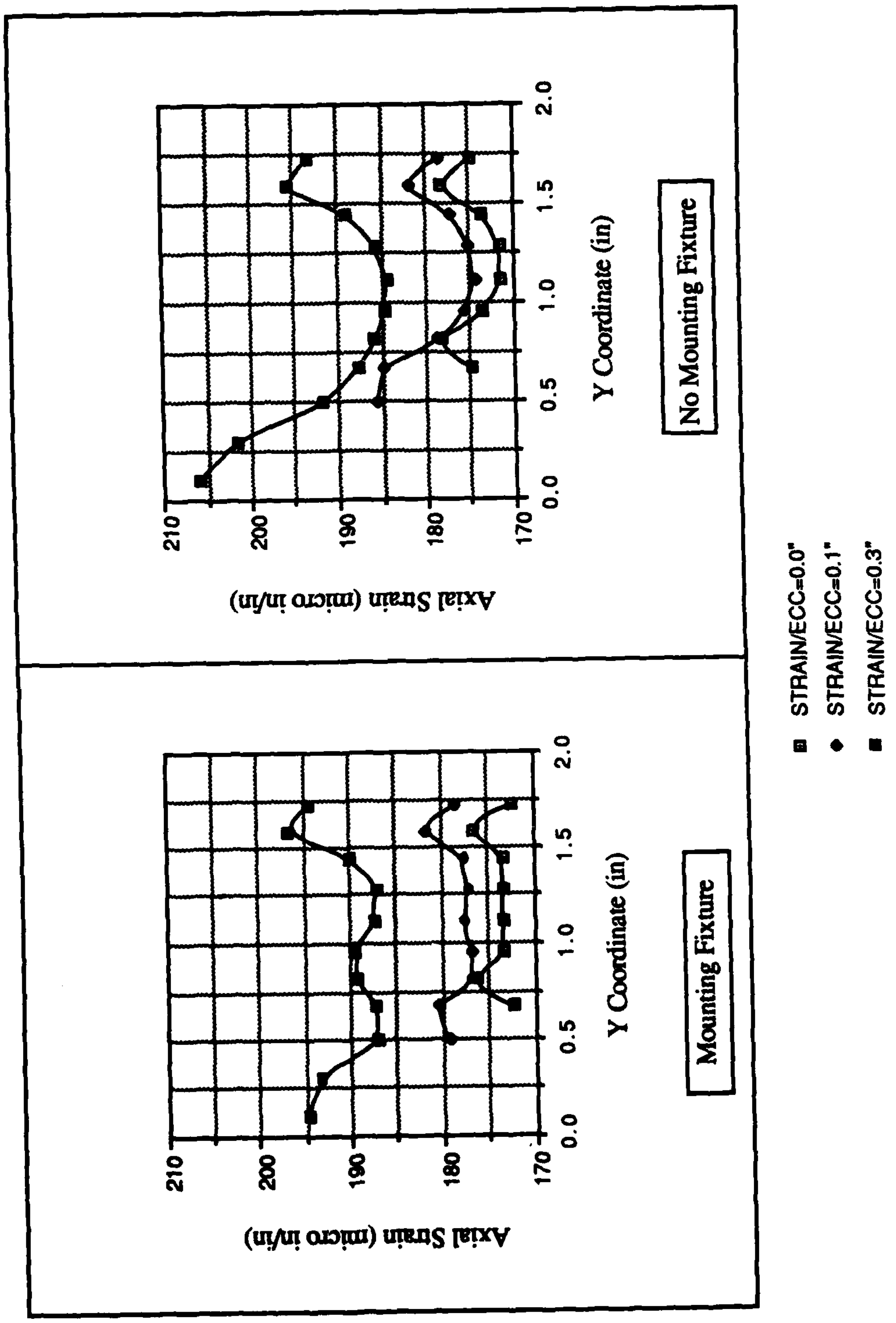

Figure C-10. Far Field Axial Strain Plots (quasi lay-up)

Appendix D. Output Files from Nonlinear Runs

This appendix discusses the output files created during a nonlinear finite element run. Once a nonlinear run had been completed by the CRAY, the following output files were created.

(1) Tape 6 (output data)
(2) Tape 3 (used to restart a run from the point of termination)
(3) Tape 9 (nodal displacement data as a function of the load increment)
(4) Listing (source code listing and any error messages)

(1) Tape 6.

The output file (Tape 6) contained the following information.

a). Summary of input data
  aa). control card summary
  bb). x & y location of nodes
  cc). boundary conditions
  dd). connectivity (nodes surrounding the element)
  ee). material properties
b). For each load increment a summary of
  aa). displacement of each node
  bb). load for each node
  cc). global and local stresses (each element)
  dd). global and local strains (each element)
  ee). strain energy (each element)
  ff). element failure message (if applicable)

(2) Tape 3.

An execution time limit (prescribed by the user) was incorporated in the batch file. This time limit was used to prevent long execution times for input files containing errors. If this time limit was exceeded, execution would be stopped and a Tape 3 produced. This tape could then be used to restart the program from the point of termination. This "restart" capability saved money (by saving computer time) for runs in which the modeled laminate had not failed at the time the program was stopped.

(3) Tape 9.

Tape 9 contained the nodal displacements of each node in the finite element model (for each increment of loading). This file was used for making distorted plots of the model at any increment of loading. After a nonlinear run, this file was transferred to a VAX mainframe computer, and was used as the input data file to a plotting routine (written by Dr. Sandhu). Section V B contains distorted plots (for the various stacking sequences) which were produced from Tape 9 data.

(4) Listing.

The last output file was the listing. This file contained a listing of the source code for the nonlinear program. In addition, this file contained the sequence of steps executed by the CRAY during the run process. This listing was an invaluable source of information (especially to this student) for "debugging" purposes.

Appendix E. Theory of Photoelasticity

Stress-Optics (photoelasticity).

Photoelasticity can be considered an experimental stress analysis technique. The versatility of photoelastic coatings was utilized in this thesis to provide a visible picture of surface stress distribution. Photoelastic fringe patterns were compared to contour plots produced from the analytical solution (see Section V A).

Many materials, notably plastics, are optically isotropic when they are unstressed but become optically anisotropic when stressed. This results in a change in the index of refraction. Therefore, the index of refraction becomes a function of the applied load. In short, this becomes the underlying principal of the theory of photoelasticity. When a polarized beam of light passes through a photoelastic coating, the beam splits and two polarized beams are propagated in the direction of the principal strains.

Brewster's Law states that "The relative change of refraction is proportional to the difference of principal strains." Based upon the strain intensities (in the direction of principal strains), and the speed of light vibrating in these directions, the time necessary for each of the polarized beams to pass through the photoelastic coating will be different. The relative retardation between these beams causes interference and results in visible fringes. Therefore, although photoelastic coatings provide a visible picture of surface stress distribution, the actual fringes observed during photoelastic testing are created by the difference in principal strains. This retardation can be calculated as:

$$\delta = C\left[\frac{t}{V_x'} - \frac{t}{V_y'}\right] = t(n_x - n_y)$$

where:

δ = retardation
C = speed of light
t = photoelastic coating thickness
V_x' = speed of light in direction of the first principal strain

V_y' = speed of light in direction of the second principal strain
$n_x = \frac{C}{V_x'}$
$n_y = \frac{C}{V_y'}$

Furthermore, Brewster's Law can be stated mathematically as:

$$(n_x - n_y) = k(\varepsilon_x' - \varepsilon_y')$$

where:

k = strain-optical coefficient

Therefore, the expression commonly used for strain measurements is given by:

$$\varepsilon_x' - \varepsilon_y' = \frac{\delta}{2+k}$$

where:

ε_x' = first principal strain
ε_y' = second principal strain

Bibliography

1. Adams, D.F. Micro-and Macromechanics Analysis of Composite Materials. North Hollywood, CA: Society of Aerospace Materials and Process Engineers, 1966.

2. Ahlberg, J.H., Nilson, E.N., and Walsh, J.L., Theory of Splines and their Applications. New York: Academic Press, 1967.

3. Awerbuch, J. and M.S. Madhukar. "Notched Strength of Composite Laminates: Predictions and Experiments - - A Review." Journal of Reinforced Plastics and Composites. Vol. 4, January 1985.

4. Broutman, L.J. and Krock, R.H. Composite Materials. New York: Academic Press, 1974.

5. Burden, R.L., and Faires, J.D. Numerical Analysis. Boston: PWS-KENT Publishing Company, 1985.

6. Cook, R.D. Concepts and Applications of Finite Element Analysis. New York: John Wiley & Sons, 1981.

7. Cron, S.M. Improvement of End Boundary Conditions for Off-Axis Tension Specimen Use. MS Thesis, AFIT/GAE/AA/85D-3. School of Engineering, Air Force Institute of Technology (AU), Wright-Patterson AFB, OH. December 1985.

8. Dally, J.W. and Riley, W.F. Experimental Stress Analysis. New York: McGraw-Hill Book Company, 1978.

9. Fiberite Corporation, a subsidiary of Imperial Chemical Industries (ICI). APC-2 PEEK/Carbon Fibre Composite. Manufacturers Data Sheets 1 through 8. Orange, CA, 1986.

10. Fisher, J.M. A Study of Failure Characteristics in a Thermoplastic Composite Material at High Temperature. MS Thesis, AFIT/GAE/AA/88D-15. School of Engineering, Air Force Institute of Technology (AU), Wright-Patterson AFB, OH. December 1988.

11. Frocht, M.M. Photoelasticity. New York: John Wiley & Sons, Inc., 1946.

12. Jones, R.M. Mechanics of Composite Materials. New York: Hemisphere Publishing Corporation, 1975.

13. Martin, J A Study of Failure Characteristics in Thermoplastic Composite Material. MS Thesis, AFIT/GA/AA/88M-2. School of Engineering, Air Force Institute of Technology (AU), Wright-Patterson AFB, OH. March 1988.

14. Palazotto, A.N. Class Handouts and notes in MECH 541, Mechanics of Composite Materials. School of Engineering, Air Force Institute of Technology (AU), Wright-Patterson AFB, OH, January 1989.

15. Peterson, R.E. Stress Concentration Factors. New York: John Wiley & Sons, 1974.

16. Photoelastic Inc. Introduction to Stress Analysis by the Photoelastic Coating Technique. Technical Bulletin TDG-1. Malvern,PA, 1974.

17. Ramey, J.E. Comparison of Notch Strength Between Gr/PEEK (APC-1 and APC-2) and Gr/Epoxy Composite Material at Elevated Temperature. MS Thesis, AFIT/GAE/AA/85D-12. School of Engineering, Air Force Institute of Technology (AU), Wright-Patterson AFB, OH. December 1985.

18. Reed, D.L. Advanced Composite Technology: "Point Stress Laminate Analysis," FZM-5494, Advanced Composites Division, Air Force Materials Laboratory, Wright-Patterson AFB, OH, April 1970.

19. Sandhu, R.S. Analytical-Experimental Correlation of the Behavior of 0^o, $\pm 45^o$, 90^o Family of AS/3501-5 Graphite Epoxy Composite Laminates under Uniaxial Tensile Loading. Air Force Flight Dynamics Laboratory, AFFDL-TR-79-3064, May 1979.

20. Sandhu, R.S. "A Survey of Failure Theories of Isotropic and Anisotropic Materials." Technical Report AFFDL-TR-72-71, AD 756889, Air Force Flight Dynamics Laboratory, Wright-Patterson AFB, OH, January 1972

21. Sandhu, R.S., R.L. Gallo, and G.P. Sendeckyj. "Initiation and Accumulation of Damage in Composite Laminates." Composite Materials: Testing and Design (Sixth Conference), ASTM STP 787, I.M. Daniel, Ed., American Society for Testing and Materials, 1982, pp.163-182.

22. Sandhu, R.S., R.L. Gallo, and G.P. Sendeckyj. "Modeling of the Failure Process in Notched Laminates." Composite Materials: Recent Advances in Mechanics of Composite Material, IUTAM Symposium, August 1983, Pergamon Press, 1983.

23. Sandhu, R.S. "Nonlinear Behavior of Unidirectional and Angle Ply Laminates." Journal of Aircraft, 13, No. 2 (February 1976), pp. 104-111.

24. Sandhu, R.S. and G.P. Sendeckyj. On Delamination of $(\pm 0_m/90_{n/2})_s$ Laminates Subjected to Tensile Loading. Technical Report AFWAL-TR-87-3058, Air Force Wright Aeronautical Laboratory, Wright-Patterson AFB,OH, July 1987.

25. Sandhu, R.S. "Ultimate Strength Analysis of Symmetric Laminates." Technical Report AFFDL-TR-73-137, AD 779927, Air Force Flight Dynamics Laboratory, Wright-Patterson AFB, OH. February 1974.

26. Schwartz, R.T. and Schwartz, H.S. Fundamental Aspects of Fiber Reinforced Plastic Composites. New York: Interscience Publishers, 1968.

27. Tsai, S.W. and Hahn, H.T. Introduction to Composite Materials. Westport, CT: Technomic Publishing Co, Inc., 1980.

28. Whitney, J.M., I.M. Daniel, and R.B. Pipes. Experimental Mechanics of Fiber Reinforced Composite Materials. Society for Experimental Mechanics (SEM) Monograph No. 4, Revised Edition. Brookfield Center, CT: SEM, 1984.

Vita

Captain John A. Daniels [redacted] He graduated in 1977 from high school in Swannanoa, North Carolina. In April, 1979 he enlisted in the USAF and spent the next three years as a crew chief on C-141A aircraft at Charleston AFB, South Carolina. In 1982 he attended North Carolina State University on an Air Force AECP scholarship. Graduating Magna Cum Laude with a Bachelor of Science Degree in Mechanical Engineering in 1984, he then attended Officer Training School and was commissioned in April, 1985. Prior to entering the School of Engineering in May, 1988, he worked as a Project Manager/Engineer in the 4484th Test Squadron, Tyndall AFB, Florida.

[redacted]

REPORT DOCUMENTATION PAGE

Form Approved
OMB No. 0704-0188

1a. REPORT SECURITY CLASSIFICATION UNCLASSIFIED	1b. RESTRICTIVE MARKINGS
2a. SECURITY CLASSIFICATION AUTHORITY	3. DISTRIBUTION/AVAILABILITY OF REPORT Approved for public release; distribution unlimited.
2b. DECLASSIFICATION/DOWNGRADING SCHEDULE	
4. PERFORMING ORGANIZATION REPORT NUMBER(S) AFIT/GAE/ENY/89D-06	5. MONITORING ORGANIZATION REPORT NUMBER(S)
6a. NAME OF PERFORMING ORGANIZATION School of Engineering 6b. OFFICE SYMBOL (*If applicable*) AFIT/ENY	7a. NAME OF MONITORING ORGANIZATION Flight Dynamics Laboratory Wright Research & Development Center, WPAFB
6c. ADDRESS (*City, State, and ZIP Code*) Air Force Institute of Technology Wright-Patterson AFB OH 45433-6583	7b. ADDRESS (*City, State, and ZIP Code*) Air Force Systems Command Wright-Patterson AFB OH 45433-6553
8a. NAME OF FUNDING/SPONSORING ORGANIZATION WRDC 8b. OFFICE SYMBOL (*If applicable*) WRDC/FIBC	9. PROCUREMENT INSTRUMENT IDENTIFICATION NUMBER
8c. ADDRESS (*City, State, and ZIP Code*) Wright-Patterson AFB, OH 45433-6553	10. SOURCE OF FUNDING NUMBERS

PROGRAM ELEMENT NO.	PROJECT NO.	TASK NO.	WORK UNIT ACCESSION NO.
62201F	2401	03	66

11. TITLE (*Include Security Classification*)
A STUDY OF FAILURE CHARACTERISTICS IN THERMOPLASTIC COMPOSITE LAMINATES DUE TO AN ECCENTRIC CIRCULAR DISCONTINUITY

12. PERSONAL AUTHOR(S)
John A. Daniels, Capt, USAF

13a. TYPE OF REPORT	13b. TIME COVERED	14. DATE OF REPORT (*Year, Month, Day*)	15. PAGE COUNT
MS Thesis	FROM ______ TO ______	1989 December	192

16. SUPPLEMENTARY NOTATION

17. COSATI CODES		
FIELD	GROUP	SUB-GROUP
11	04	
11	09	

18. SUBJECT TERMS (*Continue on reverse if necessary and identify by block number*)
Thermoplastics, Composite Materials, Gr/PEEK, Eccentricity
Finite Element Analysis, Nonlinear Analysis

19. ABSTRACT (*Continue on reverse if necessary and identify by block number*)

(see reverse)

Thesis Advisor: Dr. Anthony Palazotto

20. DISTRIBUTION/AVAILABILITY OF ABSTRACT ☒ UNCLASSIFIED/UNLIMITED ☐ SAME AS RPT. ☐ DTIC USERS	21. ABSTRACT SECURITY CLASSIFICATION UNCLASSIFIED
22a. NAME OF RESPONSIBLE INDIVIDUAL Anthony N. Palazotto, Professor	22b. TELEPHONE (*Include Area Code*) 513-255-3517 22c. OFFICE SYMBOL AFIT/ENY

The purpose of this thesis was to determine (both experimentally and analytically) the initiation and progression of failure, stress-strain response, and the failure loads of Graphite/Polyetheretherketone (Gr/PEEK) laminates, incorporating an eccentric 0.4 inch circular discontinuity, loaded in axial tension at room temperature. The ply lay-ups of these specimens were $[0^\circ_{16}]$, $[90^\circ_{16}]$, $[\pm 45^\circ]_{4s}$, and $[0^\circ/\pm 45^\circ/90^\circ]_{2s}$. For each of these ply lay-ups, three values of eccentricity were considered (the three values of eccentricity were determined by the hole location within each specimen). In addition, experimentation was conducted to study the effects of boundary conditions on the failure characteristics of the Gr/PEEK laminates; this was accomplished through the use of a special mounting fixture which allowed in-plane rotation of the specimens. Finally, experimentation was conducted, using photoelasticity, to verify the "gross" stress states of the Gr/PEEK laminates predicted by the analytical study.

Analytically, a nonlinear material finite element program was used to predict the initiation and progression of failure, stress-strain response, and the failure loads of the Gr/PEEK laminates. In addition, the effects of boundary conditions on the failure modes of the Gr/PEEK laminates was studied analytically. And finally, the "gross" stress states of the Gr/PEEK laminates were considered in the analytical portion of this thesis.

The experimental and analytical results were then compared. The initiation and progression of failure, stress-strain response, and the failure loads of the (Gr/PEEK) laminates compared quite well for the $[0^\circ_{16}]$, $[90^\circ_{16}]$, and $[0^\circ/\pm 45^\circ/90^\circ]_{2s}$ laminates. For the $[\pm 45^\circ]_{4s}$ laminates, the analytical predictions for the failure loads underestimated (from 16.6% to 40.5%) the experimentally obtained failure loads. Furthermore, it was observed (both experimentally and analytically) that the failure modes and failure loads for the Gr/PEEK laminates were not appreciably affected by the boundary conditions caused through the use of the mounting fixture (in-plane rotation allowed). Finally, there was good agreement between the experimental and analytical predictions of the "gross" stress states of the Gr/PEEK laminates.

Since eccentricity effects on the failure modes and failure loads of the Gr/PEEK laminates were of interest in this study, the analytical study attempted to predict the behavior of the Gr/PEEK laminates due to an eccentric circular discontinuity. The eccentric circular discontinuity created a centroid (area) shift in the Gr/PEEK laminates. This shift in centroid, combined with the axial loading, created a bending moment which varied depending on the eccentricity of the circular discontinuity. The analytical study was able to accurately predict the failure modes and failure loads resulting from eccentricity effects. Although the final failure mode, and failure load, was available from experimentation, the failure progression resulting from eccentricity effects was not observed during expermentation. All experimentation was recorded on video tape for post failure analysis. However, failure was too rapid to observe failure progression (by viewing the video tape frame-by-frame).